

Towards a bionic bat:
A biomimetic investigation of active sensing,
Doppler-shift estimation, and ear morphology design
for mobile robots.

Jose M. Carmena



Doctor of Philosophy
Institute of Perception, Action and Behaviour
Division of Informatics
University of Edinburgh
2001

Abstract

So-called CF-FM bats are highly mobile creatures who emit long calls in which much of the energy is concentrated in a single frequency. These bats face sensor interpretation problems very similar to those of mobile robots provided with ultrasonic sensors, while navigating in cluttered environments.

This dissertation presents biologically inspired engineering on the use of narrowband Sonar in mobile robotics. It replicates, using robotics as a modelling medium, how CF-FM bats process and use the constant frequency part of their emitted call for several tasks, aiming to improve the design and use of narrowband ultrasonic sensors for mobile robot navigation.

The experimental platform for the work is RoBat, the biomimetic sonarhead designed by Peremans and Hallam, mounted on a commercial mobile platform as part of the work reported in this dissertation. System integration, including signal processing capabilities inspired by the bat's auditory system and closed loop control of both sonarhead and mobile base movements, was designed and implemented. The result is a versatile tool for studying the relationship between environmental features, their acoustic correlates and the cues computable from them, in the context of both static, and dynamic real-time closed loop, behaviour.

Two models of the signal processing performed by the bat's cochlea were implemented, based on sets of bandpass filters followed by full-wave rectification and low-pass filtering. One filterbank uses Butterworth filters whose centre frequencies vary linearly across the set. The alternative filterbank uses gammatone filters, with centre frequencies varying non-linearly across the set. Two methods of estimating Doppler-shift from the return echoes after cochlear signal processing were implemented. The first was a simple energy-weighted average of filter centre frequencies. The second was a novel neural network-based technique. Each method was tested with each of the cochlear models, and evaluated in the context of several dynamic tasks in which RoBat was moved at different velocities towards stationary echo sources such as walls and posts. Overall, the performance of the linear filterbank was more consistent than the gammatone. The same applies to the ANN, with consistently better noise performance than the weighted average. The effect of multiple reflectors contained in a single echo was also analysed in terms of error in Doppler-shift estimation assuming a single wider reflector.

Inspired by the Doppler-shift compensation and obstacle avoidance behaviours found in CF-FM bats, a Doppler-based controller suitable for collision detection and convoy navigation in robots was devised and implemented in RoBat. The performance of the controller is satisfactory despite low Doppler-shift resolution caused by lower velocity of the robot when compared to real bats.

Barshan's and Kuc's 2D object localisation method was implemented and adapted to the

geometry of RoBat's sonarhead. Different TOF estimation methods were tested, the parabola fitting being the most accurate. Arc scanning, the ear movement technique to recover elevation cues proposed by Walker, and tested in simulation by her, Peremans and Hallam, was here implemented on RoBat, and integrated with Barshan's and Kuc's method in a preliminary narrowband 3D tracker.

Finally, joint work with Kim, Kämpchen and Hallam on designing optimal reflector surfaces inspired by the CF-FM bat's large *pinnae* is presented. Genetic algorithms are used for improving the current echolocating capabilities of the sonarhead for both arc scanning and IID behaviours. Multiple reflectors around the transducer using a simple ray light-like model of sound propagation are evolved. Results show phase cancellation problems and the need of a more complete model of wave propagation. Inspired by a physical model of sound diffraction and reflections in the human concha a new model is devised and used to evolve pinnae surfaces made of finite elements. Some interesting paraboloid shapes are obtained, improving performance significantly with respect to the bare transducer.

Acknowledgements

I would first of all like to thank two people to whom I am greatly indebted: John Hallam and Bob Fisher. John, my mentor, believed in me and, with great patience, guided me along these years of exciting research. I was extremely lucky to be supervised by such a bright and multidisciplinary scientist. Thanks John (and the rest of the Hallams) for your friendship and hospitality. Bob very generously fully funded my research (through the SMART-2 grant acknowledged below) as well as several trips to conferences around the world. Without them, the work presented in this thesis would have not been possible.

It was a great experience to work side by side with two truly scientists such as Rolf Müller and Herbert Peremans. Their help and motivation along these years was invaluable, as well as their doses of German and Flemish humor. Thanks also to DaeEun Kim, my officemate, for our fruitful and enjoyable collaborating experience on the artificial pinnae project.

Many thanks to Juan Domingo (Universitat de Valencia, Spain), my first mentor, my friend, and the one who put me on the path to Edinburgh. Despite the physical distance and his busy agenda he was always willing to lend a hand.

Special thanks to Arturo Espinosa, Yiannis Demiris, Yuval Marom, George Maistros, Ignasi Cos, and the rest of the Mobile Robots group for their friendship, support, pub nights (goddess laaaga!), and for making these years in Edinburgh such an enjoyable experience. Thanks also to Ioseba Tena, Angel de Vicente, Gorka Hodson, Jean Buntén, Heba Lakany, Gill Hayes, Chris Malcolm, Judith Gordon, Karen Taylor, Jane Ranking and Tom Nolan.

Many thanks to Bridget Hallam for proofreading the whole dissertation and for giving very useful comments. Thanks also to Paul Crook for proofreading one chapter and to Ashley Walker for lending me some useful papers.

Also thanks to Tim Colles and John Berry for computing support, and to the staff of the electrical and mechanical workshops, namely Sandy Colquhoun, Robert MacGregor, Hugh Cameron and Douglas Howie for their help when needed. Thanks to Olga Franks and Janice Gailani for making the bibliography search process much easier.

Thanks to the European Union TMR Network SMART-2 who provided financial support during these years under contract number FMRX-CT96-0052, as well as the EPSRC (grant number GR/R35515) for providing funding for technical equipment.

Finally, thanks to my parents and friends (they know who they are) for everything. Thanks to Valencia CF (best team in the world) for such an amazing performance during these years. Amunt Valencia! And last, but not least, my warmest thanks to Esther Dura, my girlfriend, who supported with great patience and love these three years of ‘work hard and play not so hard’.

Declaration

I declare that this thesis was composed by myself, that the work contained herein is my own except where explicitly stated otherwise in the text, and that this work has not been submitted for any other degree or professional qualification except as specified.

(Jose M. Carmena)

A Esther.

A María Dolores, que estás en el cielo.

Table of Contents

1	Introduction	1
1.1	The context	1
1.1.1	Back to the early days in Robotics	1
1.1.2	The Physics is out there	3
1.2	Motivation	4
1.2.1	Why Sonar?	5
1.2.2	Why Biomimetic?	5
1.3	Objectives	6
1.4	Structure of the dissertation	6
2	Background and methodology	8
2.1	Introduction	8
2.2	Ultrasonic Sensing in Mobile Robotics	8
2.2.1	Introduction and basic concepts	8
2.2.2	The physics of the ultrasonic transducer	10
2.2.3	The Polaroid range sensor fallacy	14
2.2.4	Other ways of using Sonar	19
2.3	Echolocating bats	22
2.3.1	An introduction to bat echolocation	22
2.3.2	Neurophysiology of the bat's auditory system	24
2.3.3	Ethology	26
2.4	The biomimetic approach	29
2.4.1	Introduction	29
2.4.2	Biorobotics as a methodology	30
2.4.3	Examples of biorobotic research	32
2.4.4	Biomimetic ultrasound	34
2.5	Summary	36

3	The RoBat system	38
3.1	Introduction	38
3.2	RoBat: a biomimetic platform to study perception in bats and robots	38
3.2.1	The biomimetic sonarhead	39
3.2.2	The mobile platform	41
3.2.3	RoBat's modular architecture	42
3.2.4	Software model of the sonarhead	44
3.2.5	Examples of broadband echoes	45
3.3	Research topics	48
3.3.1	Estimation and use of Doppler-shifts.	48
3.3.2	3D tracking methods.	49
3.3.3	Design of artificial pinnae.	49
3.4	Summary	50
4	Inner ear: Cochlear models and Doppler-shift estimation methods	51
4.1	Introduction	51
4.2	Doppler overview	52
4.2.1	Doppler-shifts in a robotic context	52
4.3	Cochlear models	54
4.3.1	Linear (Butterworth) filterbank	55
4.3.2	Gammatone filterbank	55
4.3.3	Other models	56
4.4	Doppler-shift estimation methods	59
4.4.1	Artificial Neural Network	60
4.4.2	Weighted average	61
4.5	Comparison of Doppler-shift estimation methods	62
4.5.1	Design of the experiments	62
4.5.2	Analysis of the results	64
4.5.3	Discussion	65
4.6	Echoes from multiple reflectors	71
4.6.1	The problem of the cross-modulation term	71
4.6.2	Sensing the world through single dominant frequency echoes	72
4.6.3	Discussion	75
4.7	Summary	78

5	Doppler-based behaviours	79
5.1	Introduction	79
5.2	Target recognition through frequency signatures	79
5.3	Doppler-shift compensation	82
5.3.1	Implementation in RoBat	83
5.3.2	Discussion	85
5.4	Convoy navigation controller	88
5.4.1	Discussion	91
5.5	Acoustic flow	91
5.5.1	Discussion	93
5.6	Summary	95
6	Active sensing: Towards a narrowband 3D tracking system	96
6.1	Introduction	96
6.2	Range + azimuth = 2D tracking	97
6.2.1	Implementation of Barshan's and Kuc's model	97
6.2.2	Adaptation to the geometry of the sonarhead	98
6.2.3	Methods	101
6.2.4	Experiments and results	103
6.3	Elevation cues: Arc scanning	106
6.3.1	Methods	107
6.3.2	Experiments and results	109
6.4	Towards a 3D tracking system	113
6.4.1	Discussion	115
6.5	Summary	116
7	Outer ear: from multiple reflectors to surfaces	117
7.1	Introduction	117
7.2	Previous work on artificial pinnae	119
7.3	Exploiting the initial model	120
7.3.1	Results	121
7.4	Computing reflections from finite reflectors	126
7.4.1	Results	127
7.5	Discussion and conclusions	130
7.6	Further work: From multiple reflectors to surfaces	133

8	Conclusions	141
8.1	Thesis summary	141
8.2	Achievements and contributions	144
8.3	Discussion and future work	145
A	Mathematical formulas	147
A.1	Design of acoustic foveas with variable Q values	147
A.2	Derivatives of h with respect to t_r and β	148
A.3	LSE parabola fitting	149
B		150
B.1	ANN parameters	150
B.1.1	Linear filterbank (6-3-1)	150
B.1.2	Gammatone filterbank (9-4-1)	150
B.2	Example of the GA's encoding for a 3-reflector configuration	150
C		152
C.1	Noise removal	152
C.2	Servomotor synchronisation	153
	Bibliography	156

List of Figures

2.1	Polaroid transducer directivity	11
2.2	Echoes from surfaces with different orientation and visibility	13
2.3	Mirror-like T/R configuration of wall, corner and edge reflectors	14
2.4	Time-of-flight (TOF) estimation.	15
2.5	Polaroid (6500 Series) directivity pattern	16
2.6	Photo of <i>Rhinolophus ferrumequinum</i>	23
2.7	Diagram of the mammalian cochlea	25
2.8	Vertical ear movements of <i>Rhinolophus ferrumequinum</i>	28
2.9	From the real world to an artificial model and back to the real world	31
3.1	The robotic platform	39
3.2	Power spectral density of the transfer function	40
3.3	Front view of previous robotic platforms	42
3.4	Block diagram of RoBat's modular architecture	43
3.5	The output of the wideband cochlear model as displayed on the screen of the control computer	45
3.6	The echo from a small object in front of a flat reflecting surface	46
3.7	The echoes reflected off two different types of foliage	47
4.1	Example of Doppler-shift in a robotic context	53
4.2	Diagram of RoBat's "auditory system"	55
4.3	Linear filterbank	56
4.4	Gammatone filterbank	57
4.5	Group delays	58
4.6	Bessel filterbank	58
4.7	Cascade filterbank	59
4.8	Linear filterbank output	60
4.9	ANN fit along the acoustic fovea for different noise levels	61

4.10	The measurement setup	63
4.11	Doppler-shift estimation while RoBat moves at constant velocity orthogonal to a wall	64
4.12	Doppler-shift estimation while RoBat accelerates orthogonal to a wall	65
4.13	Doppler-shift estimation while RoBat decelerates orthogonal to a wall	66
4.14	Doppler-shift estimation while RoBat drives by a post at constant velocity	67
4.15	Relative variance ratio measure for each experimental configuration	69
4.16	Accuracy estimation for each experimental configuration	69
4.17	Varying fit errors found in γ -tone filterbanks	70
4.18	‘Dodgy’ performance	70
4.19	Evolution of estimated Doppler-shift along 300 ms echoes with 2 signals	74
4.20	Doppler-shift estimation error in 50 ms echoes made of 2 signals	76
4.21	Doppler-shift estimation error in 300 ms echoes made of 2 signals	77
5.1	Echo from a rotating fan	80
5.2	Spectrogram comparison	81
5.3	The measurement setup: a ball swinging back and forth in front of the sonarhead	83
5.4	Echoes reflected off the ball swinging back and forth	84
5.5	Doppler-shift estimation while swinging a ball	86
5.6	Full Doppler-shift compensation with different gains	87
5.7	Comparison of call-frequency estimations during Doppler-shift compensation	88
5.8	Block diagram of the convoy navigation controller	89
5.9	Convoy navigation experiment	90
5.10	Müller’s geometrical definition for an obstacle avoidance task by means of acoustic flow	92
5.11	Acoustic flow experiment	93
5.12	Cosine curves showing the angular dependency in Doppler-shift estimation for different velocities	94
6.1	Geometry for obstacle localization with a collinear three-transducer system	98
6.2	Geometry of the sonarhead’s 2D obstacle localization model	99
6.3	Sketch of the sonarhead in unfocused and focused configurations	100
6.4	Parabola fitting for TOF estimation	102
6.5	Echo median controller	103
6.6	Effect of the receivers’ offset	105
6.7	Effect of the servo loop gain on the target range and target angle estimation	106

6.8	Arc scanning for elevation angle estimation	107
6.9	Peak detection process in echoes after arc scanning	108
6.10	Monaural peak-delay profiles	110
6.11	Binaural peak-delay profiles	111
6.12	LSE line fitting to monaural peak-delay profiles	112
6.13	LSE line fitting to binaural peak-delay profiles	113
6.14	Target elevation angle estimated by the 3D tracker	115
7.1	Drawing of <i>Rhinolophus ferrumequinum</i>	118
7.2	IID results	122
7.3	Arc scanning results	123
7.4	Phase effects for 1 reflector	124
7.5	Phase effects for 3 reflectors	125
7.6	Plane wave model with a single reflector and a transducer	127
7.7	2D pressure vs. reflector's effect on transducer for different angles	128
7.8	3D pressure vs. 800 div. reflector's effect on transducer for different angles	128
7.9	Coarse evaluation of the acoustic model in the real world	129
7.10	Comparison between previous acoustic model and current model	131
7.11	Evaluation of the new model	132
7.12	Example of paraboloid surface with transducer at focus position	134
7.13	Comparison between old and new finite element model	134
7.14	IID performance comparison between paraboloid pinna and bare transducer	136
7.15	Performance of arc scanning applied to the bare transducer configuration	137
7.16	Performance of arc scanning using paraboloid pinnae	138
7.17	Paraboloid shape which maximises the gain to 21.56 dB	139
C.1	Example of noise removal in a single echo	154

List of Tables

4.1	Experimental configurations testing linear and gammatone filterbanks with ANN and WA	63
4.2	Experiments with linear filterbank and ANN	66
4.3	Experiments with linear filterbank and weighted average	67
4.4	Experiments with gammatone filterbank and ANN	68
4.5	Experiments with gammatone filterbank and weighted average	68
4.6	Summary of maximum error in Doppler-shift estimation	75
6.1	Comparison of TOF estimating methods	104
6.2	Comparison of the two geometric models	105
6.3	Comparison of peak-delay estimation methods	110
7.1	Comparison of received sound pressure with and without pinna	135
B.1	ANN parameters for linear filterbank for different configurations	150
B.2	ANN parameters for gammatone filterbank	150
B.3	GA encoding for a 3-reflector configuration	151

Chapter 1

Introduction

This work presents biologically inspired engineering on the use of ultrasound in mobile robotics. It replicates, using robotics as a modelling medium, how echolocating bats process and use biosonar for several tasks, aiming to improve the design and use of narrowband ultrasonic sensors for mobile robot navigation.

Echolocation is the ability to localise targets based on the acoustical information contained in the reflections of emitted sound pulses [Suga, 1990]. In nature, there are at least two different creatures who echolocate: bats — in air — and dolphins — underwater. The former are the source of inspiration for this work.

1.1 The context

1.1.1 Back to the early days in Robotics

In the middle eighties, Brooks [1986] introduced the behaviour-based approach which gave a completely different perspective to robotics. The basic idea was to interconnect, at the lowest possible level, the perception (sensors) and action (actuators) of a physical agent interacting with the real world. Brooks invented the “subsumption architecture” which was implemented in physical robots of varying shapes such as wheeled robots or insect-like robots.

A lot of work in robotics was done before the arrival of this approach but relatively few fully integrated robot systems able to run in real time were built. Most of this work was done in the assembly area¹, and only a few places such as Stanford (Shakey [Nilsson, 1984]) and Carnegie Mellon (CART [Moravec, 1979]) experimented with mobile robots. The main prob-

¹Assembly robots are not able to move from the location where they are fixed, in contrast with mobile robots which are able to move around an environment. Relevant examples are the Stanford robot (Stanford University, 1971), the PUMA robot (Unimation, 1978), and the SCARA robot (University of Tokyo, 1979) [Groover et al., 1986].

lem for these experiments was to make the robots perform in real time in a real environment such as a laboratory. Because of the great amount of sensor information provided by cameras and other kinds of sensors, and the way these sensors were interconnected to the actuators, it was (and still is, in some cases) extremely difficult to process all the data and produce an output from the actuators in a short enough time scale to make the robot explore its environment in a reliable way. The generally poor performance of robots in anything approaching an unconstrained environment suggested a fundamental problem existed. Disagreements about the nature of this problem and the best ways of finding a solution arose. The Behaviour-based approach emerged from these disagreements, differing from the Symbolic functionalist approach to intelligence (GOFAI²) [Haugeland, 1985] in claiming that intelligence is not caused by a set of facts and rules explicitly represented and manipulated inside the agent, but by a set of behaviours resulting from the interaction of the agent with the environment [Brooks, 1991]. Brooks' robots were able to perform simple tasks such as collecting empty soda cans in a laboratory, learning to walk, and avoiding obstacles. This, as a first step towards robot autonomy, was a successful start. However, the scalability of this approach is not clear. Besides Brooks' Behaviour-based approach, several other architectures have been implemented such as the RAP system [Firby, 1989], the RUR (Really Useful Robots) project [Nehmzow et al., 1989], Touring Machines [Ferguson, 1992], schema-based control architecture [Arkin and Hobbs, 1993] and tele-reactive architecture [Nilsson, 1994].

Nowadays in the robotics community there is a general agreement about the four *levels* of competence required by a robot in order to navigate autonomously. These competences are obstacle avoidance, map building, localisation and path planning. In other words: a robot capable of surviving and performing some specific task in a dynamic environment — whose structure is being constantly modified in an unpredictable way — without any specific knowledge of it, is “autonomous”.

This is the dream. The reality, as addressed by Hallam [1991], is far away from it, the main problem being the lack of an appropriate methodology for designing robots. Hallam argues that the problem of “intelligence” in an autonomous robot can be analysed as an orchestration of different levels of thought and action such as engineering the environment, altering the robot's morphology, altering the space of actions and altering the control strategy. Though, because of the trade-offs existing among these levels, a different problem arises: how do we choose the “right” level to work in?

Another important issue on the search for a robot design methodology is the lack of complete benchmarking. Hallam and Hayes [1997] explored the possibilities and consequences of

²Good and Old Fashioned Artificial Intelligence.

introducing a benchmarking in the field of robotics research, addressing the implications of standardisation on what they consider to be the three main components of robotic design: *experimental platform* — which constrains the kind of the research tasks that can be performed; *task* — does a suitable set of tasks, neither too generic nor too specific exist?; and *environment* — the implications of the environment’s properties on the performance of the agent are not straightforward. Hallam and Hayes see the problem as how to constrain these components, suggesting the constraint of two of them — task and environment — as the more promising. In fact, as Hallam and Hayes [1997] argue, “the art of robotics is the design of embodied agents that act in physical environments to achieve customer-specified tasks”. This can be seen nowadays in the popular robot contests and games (see, for example [Lund, 1999; Durá and Malcolm, 2000]) from which interesting applications could be scaled up.

1.1.2 The Physics is out there

The environment is full of cues unexploited by the sensors. For instance, most of the commercial robots available come with fixed ultrasonic sensory configurations (*e.g.* the commonly known Walter’s Sonar-ring [Walter, 1987]) which do not allow exploitation of the physics of echolocation (*e.g.* Doppler-shift estimation) as addressed in chapter 2. However, an intelligent use of a single (or limited number of) dynamic sensor(s) rather than the *dumb* use of lots of static sensors would allow these cues to be extracted as will be seen along this dissertation.

One of the pillars in robotics is sensing. Heale and Kleeman [2000] believe in that “map building, localisation and path planning in robotics are not limited by algorithms but by the sensors”. On the same idea, this work is focused at the perceptual level, with the aim of exploiting the sensory capabilities of the robot while keeping the coupling between sensing and action before working at any higher level. Considering the path from the sensors to the actuators as a chain in which every link plays an important role, I believe that perception, the first link of the chain, is the most important. All the information not provided by the sensors will need to be deduced, somehow, by means of a more complex architecture or more processing time. Thus, the aim is to extract all the relevant information from the environment by exploiting the physics of the sensors. The fundamental idea behind this approach is, as stated by Walker et al. [1998a], that “agent-environment interactions should be characterised and investigated in terms of the *physical* principles governing the operation of an agent’s sensors (or, equivalently, actuators) throughout the execution of a specific task. This is somewhat of a departure from other computational approaches which study perception in terms of internal *representational schemes* and *behavioural control architectures*”.

Looking at nature many examples of this can be seen. The example most relevant to our

work and the one which became our source of inspiration is bat biosonar. Bats exhibit navigation and prey-capture skills that if duplicated in a robot would be the envy of any robotics engineer. “All the neural computations needed to perform the estimation tasks underlying the acquisition of vital information about the environment occur within a brain the size of a large pearl” [Suga, 1990]. Stimulus ensembles on which these tasks have to be carried out range from single-target situations (e.g. track an insect in mid-air) to structure-rich environments, where each echo is a superposition of reflections from many reflecting facets.

Another important factor taking part during the bat’s perceptual process is dynamics: bats are mobile animals; they often echolocate on the wing and can move their heads and ears as well as the nose or mouth whenever they emit echolocation signals. As we will see in the background section concerning bats in the next chapter, bat ear dynamics allow environment cue extraction while navigating.

However, how can all this be relevant to robotics? The relationship between bats and robots arises because the sensor interpretation problems of bats, while navigating in cluttered environments such as forests, are very similar to those of mobile robots provided with ultrasonic sensors when navigating in laboratories. Moreover, the constant frequency part of the pulses emitted by narrowband echolocators is analogous to the one typically emitted by robotic ultrasonic sensors in terms of bandwidth. Hence, a better understanding of how these perceptual and motor mechanisms actually work in bats could improve the design of sensors and controllers for mobile robots.

1.2 Motivation

The natural creature which triggers my curiosity is the bat. Hence the aim of this thesis, in a very simple and concise way, is to extract ideas from bat biosonar (the most accurate airborne Sonar system known) and do engineering (*i.e.* replicate these ideas on a robot) with them.

Moreover, the motivation underlying our work is to investigate how simple and dynamic devices, coupled appropriately to their environment through sensors and actuators, can robustly achieve tasks in a noisy auditory environment. To address this issue I use robotics as a modelling medium for studying the role that dynamically generated acoustical cues — such as Doppler-shifts — may play in bats’ 3D acoustic perception.

To do this, I use a sensor consisting of one emitter and two receivers (as the ears) provided with independent panning and tilting and located one on each side of the emitter, devised by Peremans et al. [1997]. The emitter and receivers are mounted on a head which can also pan and tilt, providing the sensor with 4 independent degrees of freedom (DOF) in total. This

biomimetic sensor, henceforth called the sonarhead, allows modeling different strategies that might be used by bats to actively explore their environment as we will see, together with the rest of the platform used in this work, in chapter 3.

1.2.1 Why Sonar?

Sonar, which stands for Sound Navigation And Ranging, has been widely used in the robotics community as a means of range measurement. However, despite some successes, results have been disappointing as pointed out by McKerrow and Hallam [1990], Leonard and Durrant-Whyte [1992] and Peremans et al. [1993] among others.

As we will see in detail in the next chapter, we believe that the reason for this bad performance is due to the fact that most research on ultrasonic sensing in mobile robots has suffered from the ‘ultrasonic sensor = Polaroid range sensor’ fallacy. This sensor, by extracting Time-Of-Flight (TOF) for the first echo only, discards most of the information present in the echo signal. Thus it is necessary to perform extensive post-processing on a large number of range readings in order to construct consistent and reliable environment models from them.

It is the author’s belief that Sonar for mobile robotics has not been fully exploited. The motivation for this work is therefore to show how current ultrasonic sensing in mobile robotics can be improved using Sonar in an *intelligent* way instead of using more powerful — and expensive both in terms of cost and of processing time — equipment, such as vision cameras or laser range sensors.

1.2.2 Why Biomimetic?

“How do they do that?” is a common question when wondering about how a living creature performs a particular task. In fact this curiosity, arising from the incredible versatility, reliability and adaptiveness of animal behaviour, is the reason why we decided to follow a biomimetic approach, *i.e.* extract ideas from nature on how bats use biosonar and implement them on a robot. However, it is important to clarify that nature does not always provide the best solution to an engineering problem. For instance, aircrafts fly much faster using engines than birds do by fluttering their wings.

Recently there has been an increase in researchers of different areas of Artificial Intelligence and Computer Science following this biomimetic approach or relating somehow their work to it. As Lee [1996] says,

“...there is a recent ‘back to nature’ trend: Supporters of Artificial Neural Networks continue to cite neuroscience as their inspiration and justification; genetic

algorithms evolve problem solutions in a Darwinian way; the new field of ‘Artificial Life’ is concerned with the study of artificial systems which exhibit lifelike behaviours...”

From the other side, as a Robotics approach to Biology, biologists are becoming interested in creating tools that will allow them to explore the sensory world of animals with synthetic observers and test hypotheses for adaptive sensing behaviour in real-world conditions. Hence, Biorobotics, as a direct link between biology and robotics at the level of real sensori-motor systems and robotic hardware, is a novel and interesting field of research which is aimed at contributing to both science and engineering. We will go back in detail to the biomimetic approach in chapter 2.

1.3 Objectives

The main objective of this work is to improve the design and use of narrowband ultrasonic sensors for mobile robot navigation by applying ideas from bat biosonar.

More specifically, these ideas are related to

- the estimation and use of Doppler information in mobile robotics.
- the implementation of active sensing methods in a physical robot for 3D object localisation.
- ear morphology design for improving the capabilities of a biomimetic Sonar sensor using evolutionary techniques.

Also, a secondary objective of this work is to develop a robotic tool which will provide useful insight into animal feedback and control systems, complementary to those from a direct biological investigation.

1.4 Structure of the dissertation

This dissertation is structured in eight chapters (including this one) in the following way:

Chapter 2 gives a review of the fields of ultrasonic sensing in mobile robotics — from the physics of the transducer to robot navigation — bat biosonar — only the topics relevant to this work — and the biomimetic approach — a novel methodology for both science and engineering.

Chapter 3 describes RoBat, the biomimetic platform with which the experiments described in this work were performed. It also summarises the research topics investigated in this dissertation.

In Chapter 4, two models of the signal processing performed by the bat's cochlea, together with two methods of estimating Doppler-shift from the return echoes after cochlear processing, are implemented and compared. It also addresses the problem of multiple reflectors in terms of error in Doppler-shift estimation and discusses the reliability of assuming a single wider reflector.

Chapter 5 investigates how Doppler can be used in indoor environments as a frequency cue for robotic tasks taking inspiration from bat behaviours. A Doppler-based controller suitable for collision detection and convoy navigation in robots is devised and implemented in RoBat.

In chapter 6, the 2D object localisation method devised by Barshan and Kuc [1992] is adapted to the geometry of the sonarhead and implemented on RoBat. The ear movement technique to recover elevation cues proposed by Walker [1997] and tested in simulation by her, Peremans and Hallam [Walker et al., 1998b], is also implemented and tested on RoBat. Both techniques are finally integrated in a preliminar 3D tracker system.

Chapter 7 presents a joint work with Kim, Kämpchen and Hallam on designing optimal ear morphology, inspired by the CF-FM bat's large *pinnae*, for improving the echolocating capabilities of the sonarhead.

Finally, chapter 8 summarises and discusses the contributions of this work, drawing conclusions and outlining areas for further work. Formulas, parameters and technical information are included in appendices A, B and C.

Chapter 2

Background and methodology

2.1 Introduction

It is the intention of this chapter to give an overview of the different disciplines related to this work. For the sake of clarity, this chapter has been divided into three main parts that will be briefly summarised next.

The first part covers the field of ultrasonic sensing in mobile robotics, from the physics of ultrasound to the *intelligent vs. dumb* uses of the Polaroid range sensors. It also describes other approaches to the use of Sonar and, finally, advocates exploiting physics, taking inspiration from the behavioural aspects of bat biosonar, as the intelligent way of using these sensors. Bat biosonar is visited in the second part, in which an overview of bat echolocation — the most accurate existing airborne Sonar system — is given, covering some neurophysiology and ethology, and pointing out some aspects from which to extract ideas that can be applied to ultrasound-based navigation in mobile robots.

Finally, the third part of the chapter introduces the biomimetic approach as the methodology used in this work, *i.e.* the way in which to integrate the two previous sections and do both science and engineering with them. Examples of biorobotics work in general, and biomimetic Sonar in particular, will be given. Some of the concepts covered in this chapter will be extended in subsequent chapters.

2.2 Ultrasonic Sensing in Mobile Robotics

2.2.1 Introduction and basic concepts

A conventional review of mobile robot navigation would consist of a list of referred work divided into several sections according to the different competences with respect to mobile robot

autonomy, that is, obstacle avoidance, map building, localisation and path planning. Very complete surveys can be found in [McKerrow, 1991; Leonard and Durrant-Whyte, 1992; Lee, 1996]. However, in this section we will focus on the engineering goal of this work, *i.e.* exploiting the physics of the ultrasonic sensors, taking ideas both from engineering and nature in order to improve mobile robot navigation. Therefore this section is organised in terms of the different kind of approaches to and uses of Sonar sensing in mobile robotics.

Despite the different architectures, algorithms and sensor configurations, most of the authors of the extensive ultrasound literature somehow coincide in focusing on reliability problems when using ultrasonic sensors for navigational tasks. In fact, the use of ultrasonic sensors for mobile robot navigation has been under-rated for many years. As suggested by Lee [1996], “many researchers, frustrated by problems of wide beam width and unwanted reflections, have decided that ultrasonic sensing is only suitable for short-range obstacle avoidance.”. This resulted in the use of other sensors such as vision cameras — which are more expensive and require much more processing time — laser range sensors and also new sensors such as LIDAR — an acronym for *light detection and ranging* — [Adams, 2000].

A *good* approach to ultrasonic sensing in mobile robots involves using a realistic model of the sensor, as described in section 2.2.3. Extensions of this approach (including ours) which acquire and post-process the echoes in different ways will also be introduced there.

Non-contact sensors used for measuring the distance from the body of the robot to any object within a specific range are called range sensors. These sensors are based on two physical principles: the time-of-flight (TOF) of a pulse and triangulation. TOF sensors measure the time between the pulse is emitted and when the return echo is detected. Half this time is multiplied by the speed of the pulse in the medium (air or water) to calculate the distance to the object [McKerrow, 1991]. Radar (an acronym for *R*Adio *D*etection And *R*anging) is the most common example of TOF range measurement. It uses reflected electromagnetic radiation to estimate the velocity and location of a targeted object. In indoor mobile robotics, Radar is not used because its wavelength is too long for the distances involved. Ultrasound¹ is used instead because its much slower speed makes TOF measurements over short distances feasible.

Triangulation sensors (such as laser sensors) measure range by geometry using two different view-points at a known distance from each other. The two view-points can be achieved using multiple sensors or a single mobile sensor exploited in an intelligent way *e.g.* as described in [McKerrow, 1991].

Combining these two principles — TOF and triangulation — intelligent ultrasonic sensors for mobile robotics can be built, relevant examples being [Peremans et al., 1993, 1998a;

¹Any acoustic wave above the normal range of human hearing, *i.e.* above 20000 Hz.

McKerrow, 1993; Stanley and McKerrow, 1997; Kuc, 1993, 1996, 1997] amongst others.

There are several ultrasonic transducers available on the market from different manufacturers. As we will see in this section, the Polaroid ultrasonic range sensor² has the greatest market penetration in the mobile robotics community. In this work, all the assumptions made and the uses of the word *transducer* relate to the Polaroid 6500 electrostatic version [Biber et al., 1980; Maslin, 1983].

2.2.2 The physics of the ultrasonic transducer

As we aim to exploit the physics of our sensor (the biomimetic sonarhead described in the next chapter), the first thing to do is to understand how the ultrasonic transducers contained on it actually work.

Peremans [1994] investigated the linearity assumption of Anke's multiple electrostatic transducer model [Anke, 1974] for the Polaroid transducer. If Anke's assumption holds true, *i.e.* the transducer behaves like a linear system in which the emitter and receiver are perfectly co-located, the spectrum should be equal to the product of the transfer function and the spectrum of the input signal:

$$|Y(f)| = |H_e(f)H_r(f)||X(f)|$$

From the experimental results described in [Peremans, 1994], despite some nonlinear effects around the 100 kHz part of the spectrum — due to the high signal amplitudes at emission time — we can assume the linearity of the system. The nonlinear effects — 2nd harmonic distortion which contains approximately 0.29% of the energy of the signal — can be ignored because almost all acoustic energy is concentrated around the 50 kHz frequency band, which is the one we are going to work with.

Continuing with the physics of the transducer, the Polaroid can be considered as a moving piston and therefore its radiation pattern will be (*e.g.* [Braddick, 1965])

$$D_{piston}(\theta) = \frac{J_1(ka \sin(\theta))}{ka \sin(\theta)},$$

with θ as the directivity angle, a the radius of the transducer (13 mm in our system), J_1 a first order Bessel function, and $k = 2\pi f/c$, being f the frequency at which the transducer is going to be used (50 kHz in our system) and c the speed of sound in air (approx. 345 m/s in indoor environments³).

In our system, the first three zeroes of the Bessel function: $ka \sin(\theta) = 3.8317, 7.0156$ and 10.1735 correspond to the angles $\theta = 18.8^\circ, 36.3^\circ$ and 59.2° . These zeroes, which correspond

²It is important to differentiate between *sensor* and *transducer*. The latter is part of the former, which as a whole returns a sensed value, *e.g.* the measured range in the case of the Polaroid range sensor.

³ $c = 331 + 0.6T$ (m/s), T being the temperature in the Celsius scale.

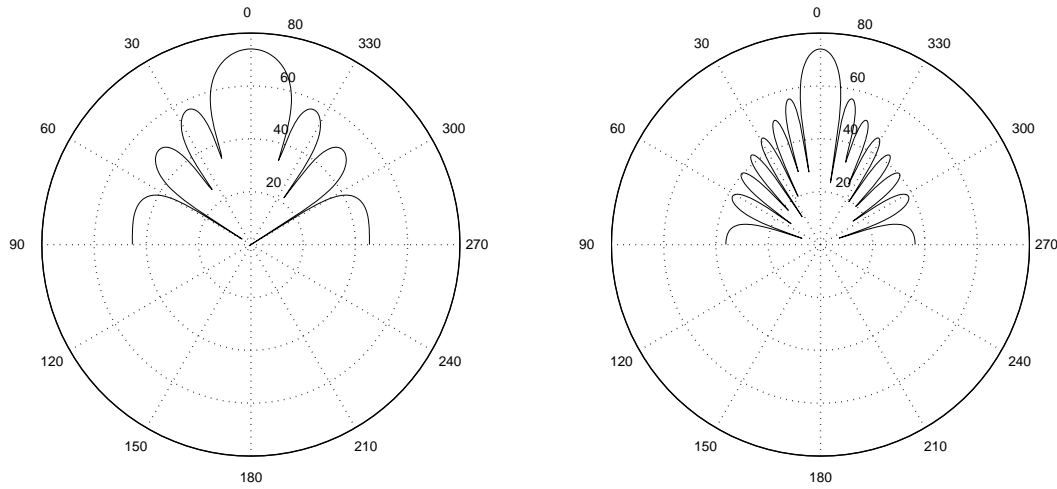


Figure 2.1: **Polaroid transducer directivity** (simulated data) for radius=13mm (left) and radius=26mm (right) at $f = 50 \text{ kHz}$ (radial units in dB).

to the transition between lobes in the directivity pattern (as seen in figure 2.1 (left)), introduce “blind spots” that result in the impossibility of detecting a reflector if positioned at any of these angles. Figure 2.1 shows two different simulated directivity patterns for transducers of different size.

For circumventing this constraint, some systems use chirped-pulses instead. In that case, there will be multiple radiation patterns due to the many frequency components of their spectra. Since our system sends constant frequency pulses of 50 kHz, its radiation pattern will be the one shown in figure 2.1 (left).

The half-width of the main lobe of our system is

$$\Theta = \arcsin(\lambda/a) = 15^\circ$$

λ being the wavelength (approximately 7 mm for $f = 50 \text{ kHz}$) and a the diameter of the transducer (26 mm in our system). However, as can be seen in figure 2.5, the radiation pattern is not perfectly symmetrical. Due to this small asymmetry, an average value for the main lobe width of roughly 26° can be taken. This is clearly seen in figure 2.5, which shows the directivity pattern of the Polaroid transducer normalised to 0 dB. As seen in the figure, the energy of the main lobe decreases 40 dB at approximately 13° .

There is also a physical effect in the airborne ultrasound that we should not forget about, which is the atmospheric absorption of sound. The absorption of sound in air H_{air} is frequency dependent and is given in [Peremans, 1994] by the transfer function

$$H_{air}(f) = 10^{-\frac{\alpha(f)r}{10}} \exp(-j2\pi f \frac{2r}{c}),$$

where $\alpha(f)$ is the absorption coefficient in dB/m at a frequency f , $2r$ the distance between transmitter and receiver and c the speed of sound in air. In his thesis, Peremans [1994] used the approximate analytical expression for $\alpha(f)$ derived in [Bass et al., 1972] to calculate $|H_{air}(f)|$ for objects at different distances (assuming a temperature of 20° , pressure of 1 atm and a relative humidity of 50%). In his experiments, as expected, absorption increased as distances grew larger. An important effect of the strong frequency dependence of absorption is that it can distort a large bandwidth pulse shape considerably. Fortunately, this distortion does not affect the system used in this work which operates at narrowband signals of 50 kHz. From the data in [Peremans, 1994] we can estimate an attenuation factor of roughly 0.3 at 3 meters distance for this frequency.

Finally, summarising this section on the Polaroid transducer's physics, we saw that almost all acoustic energy is concentrated around the 50 kHz frequency band. In addition, the transducer acts as a notch filter (figure 2.1), the notches depending on the angle of the radiation pattern which depends on the radius as seen before.

2.2.2.1 Types of reflectors in indoor environments

According to the size of the emitted pulse wavelength we can classify different types of objects into two main groups with respect to their surface radius:

- **Reflecting objects:** for which the surface radius is larger than the wavelength of the emitted pulse (6.9 mm in our case). The reflection may be specular (*i.e.*, mirror-like) or diffuse.
- **Diffraction objects:** with a surface radius smaller than the wavelength of the emitted pulse.

In indoor environments, *e.g.* robotics laboratories, most objects produce reflecting echoes except for particular cases such as facets of some objects, edges and the textures of some surfaces which can introduce diffraction. In particular, large and acoustically smooth reflecting objects produce specular reflections which maintain the integrity of the incident wavefront. These objects produce loud echoes which are highly directional — determined by the angle of incidence with respect to the surface — and independent of the pulse frequency. Some examples from a transducer in which the transmitter (T) and receiver (R) are co-located (like the Polaroid transducer) are illustrated in figure 2.2 and analysed next.

Figure 2.2 (a) shows a transducer emitting with incidence angle of 5° and receiving an echo with intensity

$$I \propto \frac{\exp^{-2mr} \sigma_{wall}}{r^2},$$

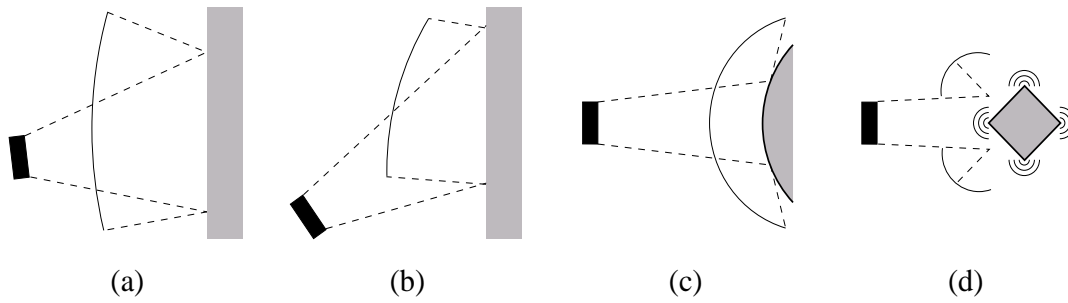


Figure 2.2: **Echoes from surfaces with different orientation and visibility.** (Adapted from [Walker, 1997] with permission.)

σ being the effective target radius, m the energy attenuation constant — inversely proportional to frequency — used for calculating the atmospheric absorption, and r the frequency independent beam spreading term. In figure 2.2 (b), however, there is no echo received because the reflected beam misses the receiver. In figure 2.2 (c) a reflection produced by a cylindrical reflector can be seen. These kind of convex specular surfaces, typical of metal posts, introduce beam spreading such that the incoming spherical waves are scattered to form new waves, centered at the point of reflection and with intensity proportional to

$$I \propto \frac{\exp^{-2mr} \sigma_{convex}}{r^3}.$$

Finally, diffuse reflections, which are produced by diffracting objects, can be seen over a wide area (figure 2.2 (d)). In this case, the object of the figure produces scattering through both reflection of the planar faces (specular) and spherical facets (diffuse) and through diffraction at the surfaces in the shadow region. In this case, the intensity of the received echo is

$$I \propto 3 \frac{\exp^{-2mr} \sigma_{sphere}}{r^4}.$$

An attempt at modelling diffuse reflections of TOF Sonar was presented in [Gilkerson and Probert, 1999]. However, after the paper was published, the authors found that in airborne Sonar using Polaroid transducers and smooth targets, a diffuse model was not useful. The experimental results described in [Gilkerson and Probert, 1999] were more likely to be due to interference from small reflections from the edges of the planar targets⁴.

Researchers agree about the three main groups of objects — depending on the type of echo they produce — that can be found in indoor environments [Kuc and Siegel, 1987; Bozma and Kuc, 1991; Leonard and Durrant-Whyte, 1991; Sabatini, 1992; Peremans, 1994; Kleeman and Kuc, 1995]:

⁴Personal communication from Paul Gilkerson.

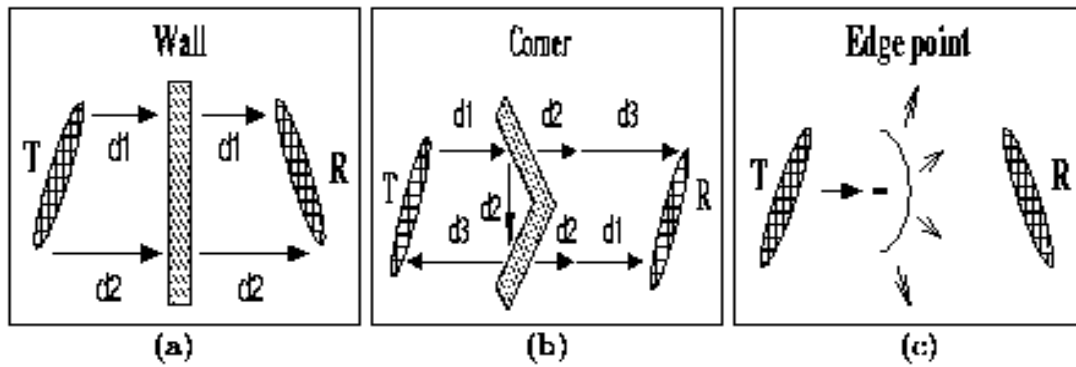


Figure 2.3: **Mirror-like T/R configuration of wall, corner and edge reflectors.** (Reproduced from [Walker, 1997] with permission.)

- **Walls** produce lossless reflections that appear like a perfect mirror to the acoustic waves. The T/R transducer can be modelled by separate transmitter and receiver aperture (figure 2.3 (a)).
- **Corners** are defined as the line between two perpendicular walls forming a concave dihedral. The angle of inclination of the equivalent receiver aperture is the negative of that for the wall (figure 2.3 (b)). There is also a diffracted signal — originating from the line of intersection between the two walls defining the corner — which is much smaller than the reflection and thus can be ignored.
- **Edges** usually have dimensions smaller than the pulse wavelength and therefore produce a diffracted echo. These echoes are characterised by a cylindrically diverging wave emanating from the edge location (figure 2.3 (c)) which has very low amplitude and, in most cases, is invisible to the robot.

Despite the difficulty for being detected from a single echo, corners and walls can be detected from several consecutive echoes providing reliable cues as we will see in section 2.2.3.2.

2.2.3 The Polaroid range sensor fallacy

As mentioned at the beginning of this chapter, unsatisfying results were obtained by the robotics community using ultrasonic range sensors. What was wrong with these sensors? In our opinion, most research on ultrasonic sensors for mobile robots has suffered from the ‘ultrasonic sensor = Polaroid range sensor’ fallacy [Peremans, 2000]. This sensor [Biber et al., 1980], which is used in mobile robotics for determining the proximity of objects, converts the time of the first amplitude measurement greater than a threshold into a distance value.

This operation mode discards most of the information present in the echo signal such as Doppler-shifts and incoming echoes from further reflectors. Even worse, wide beam-width (due to the piston-like transducer's radiation pattern), unwanted reflections (*e.g.* when approaching a concave reflector such as a corner) and diffracted reflected problems contribute to worsen performance when operated in this way. Hence extensive post-processing has to be performed on large numbers of range readings to construct consistent and reliable environment models out of them [Moravec and Elfes, 1985; Leonard and Durrant-Whyte, 1991]. From the study of biological acoustic sensorimotor systems [Popper and Fay, 1995; Nachtigall and Moore, 1988], however, we believe that much more information can be extracted from these echoes. Doing so leads to improved robotic ultrasonic sensors [Peremans et al., 1998a].

An illustration of the performance of the Polaroid range sensor can be seen in the sketch of figure 2.4 (left). In this figure, the sensor measures time t_1 which is the time for the sensor to detect the first echo exceeding the threshold value, ignoring a second echo from a further reflector. Figure 2.4 (right) shows a real example in which incoming echoes from three reflectors at different ranges are plotted.

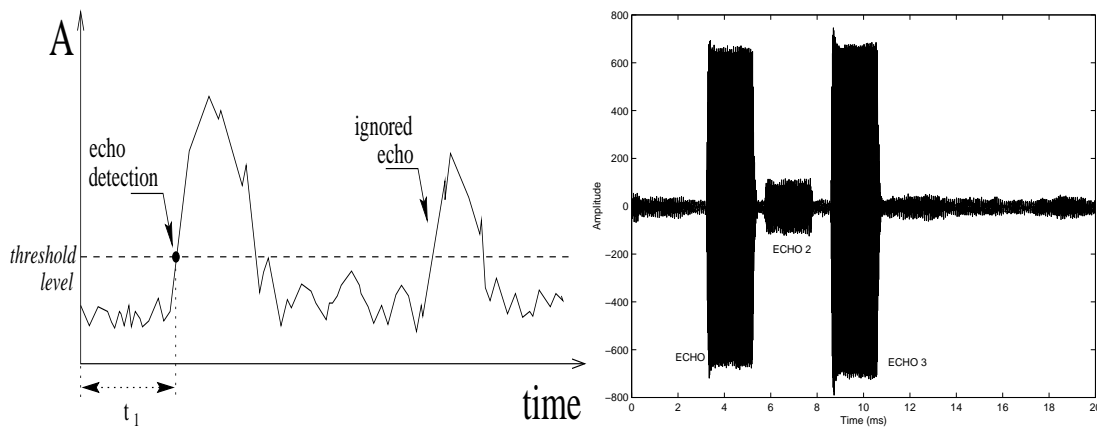


Figure 2.4: **Time-of-flight (TOF) estimation.** Left plot: sketch of the conventional TOF ultrasonic sensor performance showing the envelope of an echo detected at time t_1 and a further ignored echo. Right plot: real data showing an echo from a close reflector (echo 1) and incoming echoes from further reflectors (echoes 2 and 3).

The old Polaroid range sensor — the one implemented in cameras — used to send 1 ms chirps — containing 56 pulses from 60 to 50 kHz — every 200 ms. These multi-frequency chirps were used because the absorption coefficients of some materials at specific frequencies can result in the lack of an echo. Also, a textured surface can produce echo cancellation by producing sufficient phase shift for some parts of the reflected signal resulting in a destructive interference [McKerrow, 1991]. The problem with this configuration was that the Polaroid

electrostatic transducer is made of a capacitor which is charged with a bias voltage by transmitting a pulse. This voltage starts decreasing with time which affects the frequency resonance of the transducer working in receiver mode. This resulted in false readings since in most cases the 60 kHz part of the echo was missed because of the transducer frequency response at that specific time, receiving only the lower frequency — near to 50 kHz — components of the chirp. In other words, the decay of the bias voltage affected reception resulting in erroneous range estimations.

The newer Polaroid 6500 Series range transducer [Polaroid, 1982] sends 16 cycles of a 49.4 kHz square wave pulse and therefore the frequency response problem does not exist anymore. However, there is another false readings problem (as addressed by Lee [1996] among others) when the reflector is located in a low-amplitude part of the polar directivity pattern (see figure 2.5). In such cases, the capacitor which measures the TOF takes longer to charge and reach the threshold, resulting in a wrong estimation of the range.

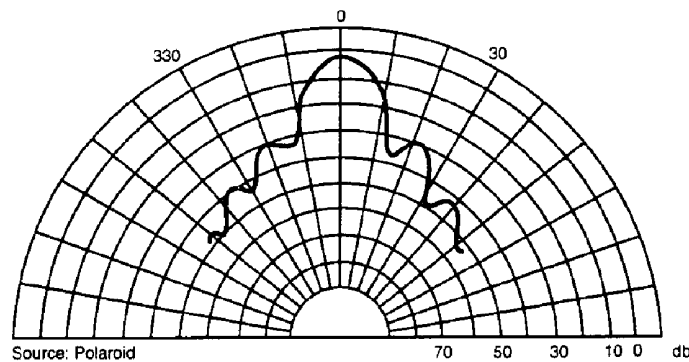


Figure 2.5: **Polaroid (6500 Series) directivity pattern** at 50 kHz.

The only advantage of the TOF implementation is its simplicity of use since multiple reflections from the same object (occurring at later times than the first reflection) are ignored. However, as we stated at the beginning of this section, there is an important drawback: the fact that the sensor fires as soon as an echo reaches the threshold level results in the rest of the incoming data from that echo being lost. This data is necessary for determining properties of the reflector such as shape, motion, etc.

Another problem with the Polaroid transducer which affects all configurations is *ringing*, consisting of the reverberations produced when the transducer is acting as an emitter. In such case, false readings at very short distances could happen. The Polaroid sensor circuitry prevents this problem by disconnecting the receiver circuitry for 2.38 ms on echo reception resulting in a “blind-zone” for the transducer of approximately 30 cm [Polaroid, 1982].

How has the Polaroid transducer been used? In the literature we can find, at least, two well known approaches to the use of ultrasound sensors for navigation in mobile robots: The *grid-map* approach and the *feature-based* approach. These will be reviewed next.

2.2.3.1 Dumb sensing

The grid-map approach, which uses rectangular cells as map primitives whose value denotes whether the cell is occupied or empty, was originally proposed by Moravec and Elfes [1985]. This idea used a Sonar beam modelled by probability distribution functions defined on a discrete grid. Since then, a large number of papers have further elaborated on the basic ideas [Elfes, 1987; Matthies and Elfes, 1988; Elfes, 1989, 1992].

Using the same idea, Borenstein and Koren [1989] developed the Virtual Force Field (VFF) method in which the target applied an attractive force to the robot and obstacles applied repulsive forces. This approach had severe problems with motion stability when travelling within narrow corridors, because of the severe repulsive effect of both walls being easily unbalanced.

Later, Borenstein introduced the Vector Field Histogram (VFH) method which aimed to achieve a smooth motion of the robot among densely cluttered and unexpected obstacles [Borenstein and Koren, 1990]. This method used a similar approach to the certainty and occupancy grids used by Moravec and Elfes [1985], although it worked faster since it incremented only one cell per range reading instead of all the cells affected by the range reading.

The grid-map approach is theoretically fairly well founded and has been widely used. However, there are several weaknesses which lead us not to support this approach. The main one is that the grid cell does not correspond with an acoustically meaningful feature of the environment. Even worse, the updating of the grid cells requires constant localisation. Also, due to the low information rate provided by the Polaroid range sensor, many measurements have to be collected in order to build usable maps [Peremans, 2000]. In our opinion, a higher level of autonomy — *e.g.* path planning — can be easily executed by a robot from a grid-map. However, the difficult part is getting the grid-map from Sonar readings because of the problems stated above.

Many of the people who followed Elfes's grid-map approach used different models for the range sensors (applicable to both ultrasonic and infra-red (IR) sensors) [Oriolo et al., 1995; Matia and Jimenez, 1998; Pagac et al., 1998; Urdiales et al., 1998, 1999] in order to work out which cell was the cause of the range echo. These models arose as an attempt to deal with the uncertainty of these kind of sensors. They estimate, by means of more or less complex functions, the space occupancy probability from the readings of the sensor, *i.e.* the probability of a given cell is occupied.

2.2.3.2 Intelligent sensing

As in [Walker, 1997], we will use the definition of “intelligent sensor” given by Barshan and Kuc [1990]: “Intelligent sensors are sensors in which the signal processing algorithms interpret the observed data, the interpretation being based upon the *physical principles* governing the sensor and a *model* of the environment that is being examined”.

In such terms, people such as Hallam [1984], Kuc and Barshan [1989], Leonard and Durrant-Whyte [1992], Kleeman [1992], McKerrow [1993], Lee [1996] and Peremans et al. [1993] among others suggested that reliable range readings can be obtained from Sonar if a realistic model of the sensor is used. At this point, the feature-based approach emerged, converting range measurements into features available in man-made environments, such as walls, edges, corners, cylinders, etc., using such features as building blocks for constructing maps [Peremans, 2000]. This is what we consider the beginning of the *good* approach to *intelligent* ultrasonic sensing in mobile robots. Some of the above researchers used the Polaroid range sensor whereas others used more advanced sensor configurations as we will see in section 2.2.4.

The Edinburgh feature-based navigator [Hallam, 1984; Hallam et al., 1989; Nehmzow et al., 1989] assumed no *a priori* map, taking account of explicit environmental motion which was being used for predicting future states determined by a Kalman filter as in [Hallam, 1984]. Using the same idea but with the limitation that the environment was needed to be known *a priori*, a sonar based localisation algorithm for known indoor environments containing geometric beacons tracked using an extended Kalman filter was presented in [Leonard and Durrant-Whyte, 1991]. The algorithm was implemented in two different configurations: a vehicle equipped with a rotating sonar and a mobile robot using a ring of six static sonar transducers. From the results obtained Leonard and Durrant-Whyte addressed the tradeoffs between the use of servo-mounted sonars versus a ring of fixed sonars, the main advantage of the servo-mounted sonar being the *local support* inherent in a densely sampled scan which makes data interpretation easier compared with a single range measurement obtained by an isolated sensor in a ring.

McKerrow [1993] describes a mobile robot provided with a conventional ring of ultrasonic sensors capable of mapping a room. The sensors are modelled with an arc model which allows an object to be detected inside an arc with radius equal to the range and arc angle equal to twice the beam angle. As a result of fusing the readings from the sensors with the motion of the robot, a surface can be detected as a sequence of arcs.

Lee [1996] exploited the map-building and exploration capabilities of a simple mobile robot equipped with just one ultrasonic transducer. In that work Lee successfully investigated

different methods for map-building, localisation and path planning. He also tested several exploration strategies, obtaining his best results with hybrid architectures combining reactive navigation with map-based strategies.

All the work on ultrasound for mobile robots seen so far has something in common: Since the sensor used is the Polaroid range sensor there is no opportunity for acquisition and post-processing of the echoes. Instead, a semi-reliable range value is obtained. Amongst the information missed by using this sensor configuration are true-TOF (*i.e.* a more reliable range), Doppler-shifts, and phase.

2.2.4 Other ways of using Sonar

Next we will see other ways of using Sonar in mobile robots with respect to sensor configurations: call emissions, phase coherence⁵ and echo processing.

Kuc and colleagues exploit the physics of sound propagation using the Polaroid transducer in different configurations, extracting range and amplitude information from the received echoes.

Kuc and Barshan [1989] started working on a physically based model of acoustic sensor robot navigation by addressing the problem of differentiating reflections from different objects as walls, corners and planes. In [Barshan and Kuc, 1990] they showed that planes and corners cannot be differentiated using a single transducer with the transmitter and receiver co-located (T/R) as in the Polaroid. They suggested using an array of two transducers (both in T/R mode) instead. With such a sensor configuration, corners and planes can be discriminated by exploiting the difference in sign of the virtual receiver characterising these surfaces as seen in figure 2.3 (a) and (b).

Kuc and Viard [1991] developed a strategy for guiding an autonomous vehicle equipped with a Polaroid ultrasonic sensor through an unstructured environment composed of specular surfaces. Their system avoids collisions with obstacles using a scanning procedure which exploits the physics of sound propagation, being capable of differentiating between the echoes reflected from surfaces and those diffracted from edges. Further work by Kuc and colleagues, this time using a biomimetic approach, will be analysed in section 2.4.4 of this chapter.

Other researchers used Barker codes or perfect codes (pseudo-random binary coded waveforms imported from RADAR theory [Berkowitz, 1965; Burdic, 1968]) in conjunction with matched filters for accurate estimation of target range.

Peremans and colleagues used Barker codes and matched filters in their work. After successfully experimenting with a single Polaroid sensor [Audenaert et al., 1992], they built a

⁵Regarding Sonar systems, a coherent system is a system which keeps records of the phase of the received echo.

high-resolution sensor based on tri-aural perception capable of determining the position of objects in 2D (distance and bearing angle) using the information contained in one single snapshot of a moderately complex scene such as an office environment [Peremans et al., 1993; Peremans, 1994]. The sensor, which was composed of three ultrasonic sensors (one transmitter/receiver and two extra receivers), could also discriminate between different types of reflectors such as walls and edges. They also employed sensor movement for distinguishing between corners and planes. The results were obtained through determining the arrival times of the echoes arriving at the three receivers. This differs from the conventional TOF ultrasonic sensor which processes only the first echo to arrive at the receiver as we saw earlier in this section. They also compared their sensor performance with those of Matthies and Elfes [1988] and Moravec and Elfes [1985], arguing that the main performance difference lies in the number of measurements required to arrive at comparable results.

DSPs are very powerful tools for signal processing applications, performing operations such as FFT and convolution products extremely fast. These operations have direct application in Sonar processing. For example [Heale and Kleeman, 2000]’s system consists of a real time DSP Sonar echo processor mounted on a mobile robot which allows *on-the-fly* map building with a 0.1 degree error in bearing estimation. This high map-building speed is possible because their system permits repetition rate of 27 Hz for ranges up to 5.4 meters ⁶.

Another way of using Sonar is the CTFM (Continuous Transmission Frequency Modulated) sensor, which emits a sawtooth frequency modulation pattern that allows mapping range into frequency by mixing the echo with the emission. This kind of sensor permits efficient pattern classification based on sound *signatures* as demonstrated by McKerrow’s group in plant species classification [Harper and McKerrow, 1995; McKerrow and Harper, 2001] and landmark-based navigation in outdoor environments [Ratner and McKerrow, 1998, 2000].

Along the same lines, Politis and Probert [2001] did interesting work on textured surface classification for robot navigation based on a geometric scattering model. Among the different surfaces their system recognised were hard smooth floors, carpets, asphalts and tile patterns.

One particular usage of CTFM Sonar has been in the development of prosthetic devices for the blind [Kay, 1980, 1999]. CTFM systems allow the patient to classify different objects and find their way by distinguishing different sound signatures. However, a common problem with this kind of application is that the disabled patient tends to reject the prosthetic device because it interferes with the sense they rely on most: hearing.

Another interesting example is the work done by Blanes and colleagues [Blanes et al., 1998;

⁶Our system (RoBat) can achieve repetition rates of 18 Hz (monaural) or 12 Hz (binaural) for 3 meter ranges as we will see in the next chapter.

[Blanes, 2000]. Their system consists of a sensor which can rotate 360° made of cheap piezo-ceramic transducers. The two emitters and two receivers are located in such a way that they can be used in two different configurations: single emitter and double emitter. The former generates pulses with a main lobe of 30° whereas the latter, due to the superposition of both directivity patterns when both transducers emit synchronously, generates a much narrower (5°) lobe. Their system uses a coherent demodulator which extracts the phase and quadrature components from the echoes reducing the bandwidth of the signal from 40 kHz to 4 kHz and therefore reducing the number of samples needed.

In the literature we also find examples of target localisation and classification using artificial neural networks. Barshan continues her previous work with Kuc on feature-based target differentiation from amplitude and range values [Barshan et al., 2000]. These values are now fed into a neural network which allows a more robust differentiation of objects. This increase in robustness suggests that using neural networks to process Sonar data and the exploitation of amplitude measurements may be useful in future applications.

Ecemis and Gaudio [2000] used an ultrasonic transducer mounted on a mobile platform to perform object recognition in two different ways: first, using the power spectral density of the echoes, and second, using the envelope function. They trained a fuzzy ARTMAP neural network [Carpenter et al., 1992] to recognise different types of objects, such as a 1-litre plastic water bottle, a metal trash can and a LEGO wall, from different ranges. The envelope function proved to be better for almost all the cases. From our point of view, these results make sense since not much frequency information — apart from Doppler shifts, which they do not use because of taking static measurements — can be expected from the Polaroid transducer when sending constant frequency pulses. Despite good results, Ecemis and Gaudio note the difficulty of recognising objects using Sonar if they are approached from arbitrary positions because of the great rate of change in the echo envelopes.

2.2.4.1 Our approach

In this work we also advocate an intelligent sensing approach, *i.e.* exploiting the physics of the agent and the environment as in some of the work reviewed above. Our system, which is fully described in chapter 3, has control of the emitted call and echo reception, and can be phase coherent if necessary. Thus our system is conceived to be:

- **simple:** using one single dynamic sensor instead of several static sensors (as in the sonar-ring of most commercial robots).

- **embedded:** because of the design and configuration of the sensor and the way it is appropriately coupled to the robot’s body.
- **informative:** the whole echo is acquired and post-processed in search of valuable information (cues from the environment) instead of only the first peak as in the Polaroid range sensor.

At this point, there is a significant difference in the way we make use of Sonar with respect to the different uses previously described in this section. The previous approaches apply engineering techniques such as Radar theory, Barker codes, matched filtering and CTFM Sonar among others for the sake of improving performance. In contrast, in this work, because of our interest in how bats echolocate, we use biologically-plausible models — which do not necessarily provide the fastest performance — instead. Thus we take a different approach *i.e.*, biomimetic, as a way of implementing in artificial devices ideas extracted from nature.

2.3 Echolocating bats

2.3.1 An introduction to bat echolocation

Bat biosonar has been widely studied since Griffin [1958] demonstrated how bats can orient themselves by Sonar. In fact, bats can successfully locate and hunt insects in acoustically cluttered environments (*e.g.* forests and caves) with extreme accuracy by the use of echolocation.

Echolocation is the ability of bats to localise targets based on the acoustical information contained in reflections of their own emitted ultrasound pulses [Suga, 1990]. In nature we can find examples of underwater echolocation, such as that performed by dolphins, and airborne echolocation as in the case of bats. However, among the more than 800 different species of bats, not all can echolocate. Focusing on the echolocating ones, these can be divided into two broad non-taxonomic groups based on the time-frequency-structure of their echolocation pulses: For FM bats (FM = frequency modulated), such as the big brown bat *Eptesicus fuscus*, echolocation calls are multi-harmonic chirps. The duration and bandwidth of the frequency sweep as well as the shape of the instantaneous frequency as a function of time vary between species. The frequency range covered extends up to approximately 200 kHz. In CF-FM bats, echolocation pulses are often dominated by prolonged CF (= constant frequency) signal portions, although frequency-modulated “tails” are always present as well. Allocation of energy to the CF and FM portions of a signal varies with behavioral context [Tian and Schnitzler, 1997]. In this work, we focus on the latter group *i.e.*, the CF-FM bat.

Two families of CF-FM bats, Rhinolophidae and Hipposideridae, have been the most extensively studied. Well known examples are the Greater Horseshoe bat *Rhinolophus ferrumequinum* and the Mustached bat *Pteronotus parnellii*. Instead of emitting their calls through the mouth as most FM bats do, Rhinolophids emit through their nostrils, which change shape for focusing and directing the ultra-sound waves as desired [Nowak, 1994].



Figure 2.6: *Rhinolophus ferrumequinum* (Photos from [Nowak, 1994]). Copyright by W. Wisenbach and P. Rödl.

The fact that sound waves are attenuated as they travel through air suggests that echolocation is a short ranging localisation system. At higher frequencies, as in the case of *Rhinolophus ferrumequinum* which emits a 83 kHz frequency pulse [Pye and Roberts, 1970], the attenuation effect is even more significant although the target resolution increases and smaller prey become detectable [Walker, 1997; Jones, 1999]. After arriving at the target, the bat's emitted sound wave is reflected by the surface of the object. The surface of a reflector plays an important role: convex and rough surfaces spread the sound front in all directions, the amplitude of the echo decreasing proportional to $\frac{1}{r^3}$ or faster, where r is the range of the target. In contrast, the attenuation of the echo reflected by a scattering surface such as a large wall is proportional to $\frac{1}{r^2}$ [Walker, 1997]. Also, if points on the surface have different distances to the bat, the echo will be the summation of all reflections. Phase cancellations and amplifications can occur, in which case duration of the echo is elongated. The information — cues from the environment — that can be obtained from an echo by an echolocating bat can be summarised as:

- **Range.** The delay of the echo gives the range (distance) of the bat to the reflector.
- **Azimuth angle.** Given by differences in the arrival time, phase and amplitude between

the two ears.

- **Elevation angle.** Given by interference patterns of sound waves reflected within the structure of the pinna. This happens only in FM bats like the big brown bat *Eptesicus fuscus* in which target elevation estimation relies on pinnae morphology instead of pinnae motion as in the CF-FM bat.
- **Relative speed.** Moving targets such as flying insects produce a Doppler-shift in the echo's carrier frequency which provides the relative velocity between the bat and the prey (target).
- **Shape.** The amplitude of the echo can provide information about the shape and size of the reflector, as described above.
- **Frequency patterns.** The wing movements of insects modulate the frequency of the emitted call producing energy patterns along the frequency spectrum which can be used for detecting specific fluttering prey.

In the next two sections we will see how these cues are extracted and used from neurophysiological and ethological points of view.

2.3.2 Neurophysiology of the bat's auditory system

The bat's auditory system is structured in the same way as that of other mammals having an external, a middle and an inner ear (see e.g., [Pickles, 1982]). Incident sound is directed towards the ear canal by the pinna, a cartilaginous flap of the external ear which is very mobile and has a highly convoluted surface in many bat species. This mobility plays an important role since the bat's ears have a directional sensitivity, *i.e.* the same echo is perceived by each ear with different amplitudes as the angles of the incoming sound differ between the ears.

As seen in figure 2.6, CF-FM bats have large pinnae. This might compensate for the loss of intensity in the echo due to the high frequency of their call. With large pinnae, the perceptual volume gain — the increase of sound pressure — of the ear can be maximised [Obrist et al., 1993]. Moreover, muscles in the inner ear can regulate the size of its aperture for reducing the amplitude of loud sound [Nowak, 1994].

The ear canal ends up at the tympanic membrane which passes the acoustic signals to the cochlea's oval window membrane through the ossicle bones. These small bones are in charge of adapting (matching) impedances between the air and the cochlea. The cochlea, located in the inner ear, is a fluid filled, spiral apparatus that transforms the physical motion of the

oval window membrane into neuronal response. At the base of the cochlea there are two membrane-covered holes, the oval window and the round window, which function to relieve the fluid pressure. Figure 2.7 shows a cut-away cross section of a cochlear duct. The dashed lines indicate fluids paths from the input at the oval window and back to the round window [Lyon and Mead, 1988].

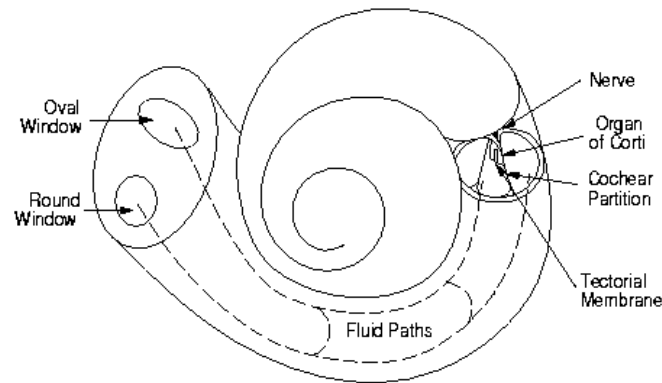


Figure 2.7: **Diagram of the mammalian cochlea** (adapted from [Lyon and Mead, 1988]).

Inside the cochlea there is a partition called the basilar membrane (BM) which is a flexible membrane that bends in response to sound. The BM is wider at the apex than at the base and its response to sound waves travelling along it establishes a code in which different locations of membrane are maximally deformed at different sound frequencies. Thus, low-frequency sound will propagate all the way to the apex of the BM before dissipating while high-frequency sound will dissipate near the base. The BM holds the *hair cells*, the mechanical-neural transducers of the auditory system. These cells detect the bending motion of their hairs and respond both by changing an internal voltage and by releasing a neurotransmitter [Bear et al., 1996].

The transduction processing in the cochlea performs a joint time-frequency analysis of the incoming signal. A simple model of this analysis is a bandpass filter bank with subsequent demodulation in each channel by a combination of full-wave rectification and lowpass filtering. In the FM bat the layout of the auditory filter bank follows the general mammalian pattern of keeping filter quality constant as center frequency varies. CF-FM bats deviate considerably from this pattern by forming an *auditory fovea* in the frequency range where the carrier frequencies of the echoes are kept by the Doppler-shift compensation behavior of these animals [Behrend et al., 1999]. Towards the center of the fovea, filter qualities rise steeply to the highest values known (maximum $Q_{10dB} \sim 400$ in *Rhinolophus ferrumequinum*); outside this frequency band the CF-FM bats follow the general mammalian pattern.

The neural phase of transduction is rather complicated comprising several auditory path-

ways which converge into the inferior colliculus before ascending to the auditory cortex. What happens in this part of the bat's brain is still a matter of research, not much being known so far. An exception is the relatively well-researched mapping system in the auditory cortex of the moustached bat for representing echo delay and Doppler-shift [Suga and Jen, 1977; Suga et al., 1981].

2.3.3 Ethology

It is quite interesting, and not completely understood, the way in which Rhinolophids and Hipposiderids, which use narrow-band call structures, perform echolocation.

They may, similarly to FM bats, determine target range through echo delay. However, since CF-FM bats emit long pulses of up to 100 ms, this can result in an overlap of these pulses with the received echoes if the target is within a range of 5 m [Griffin et al., 1962]. One way in which CF-FM bats seem to solve this problem is by decreasing the duration of the pulse as the target comes nearer to it. At the same time, the rate at which these pulses are sent increases resulting in a quicker update of perceptual information. Recent studies showed that only the terminal FM component of a call changes for very low target ranges. This may indicate the importance of the FM component for the estimation of target range and for a refinement in calculating prey spatial orientation when hunting [Tian and Schnitzler, 1997].

Auralisation — the ability to locate and identify a sound source — is a perceptual mechanism which echolocating bats exploit in a very impressive way. In order to estimate the target position in 3D, the bat must be able to extract the target's range and 'solid' angle from the echo. This angle is defined by the azimuth — horizontal direction — and elevation — vertical direction — of the echo. In the case of the horizontal angle, interaural intensity (IIDs), time (ITDs) and phase (IPDs) differences are powerful lateralisation cues that can be used by binaural auditory systems, *i.e.* when having a receiver placed on each side of the head (as in bats).

From sound localisation theory (see *e.g.* [Handel, 1989]) it is known that IPDs and ITDs are used in the case of low frequencies while IIDs are used with high frequencies. The border line between these two depends on the size of the subject's head (distance between the ears) and on sound wavelength. If the latter is bigger than the former ITDs or IPDs can be used, otherwise IIDs are used. Experiments with crickets [Webb, 1993] and some passive listener bats — bats which use the sound emitted by the prey — [Heffner et al., 1999] have indicated the use of IPDs.

With respect to the CF-FM bats, it has been demonstrated that in *Rhinolophus ferrume-*

quinum, whose call frequency of 83 kHz has a wavelength of approximately 4.2 mm smaller than the distance between its ears, IIDs play a role in obstacle avoidance [Flieger and Schnitzler, 1973]. This is valid also for our sonarhead for which the 50 kHz call frequency wavelength of approximately 7 mm is also much smaller than the distance between the two “ears” as we will see in chapter 3.2.

However, how can the target’s elevation angle be estimated from an echo consisting of a monochromatic tone *i.e* when spectral cues are unavailable? It is known that narrowband echolocators such as the CF-FM bat move the pinna to alter the directional sensitivity of their perceptual systems whereas broadband listening systems (*e.g.* humans and broadband emitting bats) rely on pinna *morphology* to alter acoustic directionality at different frequencies [Walker et al., 1998b]. Moreover, biologists have investigated the importance in Rhinolophids and Hipposiderids of pinna motion along vertical arcs of about 30° as shown in figure 2.8, observing a high correlation between the emitted pulses and these ear movements [Griffin et al., 1962; Pye et al., 1962; Pye and Roberts, 1970]. In the behavioural studies performed by Griffin [1958], Gorlinsky and Konstantinov [1978] and Mogdans et al. [1988], the ears of a *Rhinolophus ferrumequinum* were impaired by immobilization. These results showed that ear movements play a greater role in localising a sound source in the vertical plane than in the horizontal one. The vertical movements are performed in the following way: while one ear is moved in the positive vertical direction the other ear performs the same motion in the opposite angular direction, the frequency of these movements increasing as the target range decreases. These pinna movements, named ‘arc scanning’ by Walker [1997], alter the directional sensitivity of the auditory system so as to make it possible for a narrow-band echolocator to collect and compare interaural intensity disparities collected from several regions of the frontal sound field. Moreover, they produce local Doppler-shifts and thus create additional directivity information, as the magnitude of the Doppler-shift is dependent on the target’s elevation [Walker, 1997; Walker et al., 1998b; Peremans et al., 1998a]. Effective use of these spatio-temporal cues would require pinna movement and echo arrival to be highly synchronised, but could give rise to powerful directional cues even under conditions of monaural hearing [Walker et al., 1998b].

Arc scanning also allows the bat to simultaneously obtain the amplitude of the echo, which is important for the calculating the IID. Thus, arc scanning, combined with azimuth angle estimation by means of IIDs and target range by echo delay, provides a narrow-band echolocator with a 3D estimation of an insonified target’s relative position.

The fact that the CF-FM bat modifies the carrier frequency of its own calls, compensating the Doppler-shift produced when bat, reflector or both are moving, indicates the importance of the Doppler-shift information in the received echoes [Roverud and Grinnell, 1985; Kobler

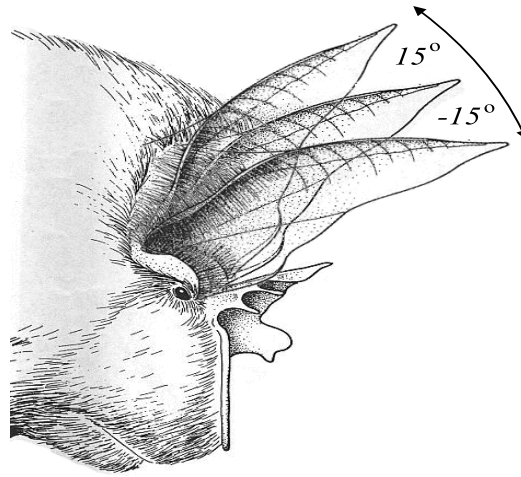


Figure 2.8: **Vertical ear movements of *Rhinolophus ferrumequinum*.** Adapted from [Schnitzler and Grinnell, 1977].

et al., 1985; Keating et al., 1994; Tian and Schnitzler, 1997; Behrend et al., 1999]. Moreover, frequency modulation patterns in the echo produced by the flutter of some insect wings allow the bat to hunt for a specific prey, *e.g.* by distinguishing between insects which are part of their daily diet and the ones which are not [Goldman and Henson, 1977; Schnitzler and Flieger, 1983; Ostwald, 1987; Kober and Schnitzler, 1990; Walker, 1997]. We will go back to these issues in chapter 5.

Lee et al. [1992, 1995] suggested that bats perform braking control using echolocation in the same way as birds and humans do using vision, proposing the tau function⁷ to describe this behaviour. Lee was one of the first authors to address the concept of acoustic flow, which was then investigated by Müller [1998]. Müller advances an interesting hypothesis about how CF-FM bats perform obstacle avoidance when tracking an insect in presence of multiple reflectors (*e.g.* foliage, tree branches, etc.). He suggests that CF-FM bats use an acoustic flow analog to optic flow in which Doppler shift and echo amplitude constitute two perceptual dimensions which bats may employ for the extraction of two-dimensional spatial information.

A hot topic in current biosonar research and in the audition research community in general is binaurality, *i.e.* how the different perceptual information provided by each ear is combined at higher levels of the auditory system and how this *data fusion* affects behaviour. A relevant example can be given with acoustic flow: Since Doppler shifts and echo amplitude are monaural cues, what role does binaurality play in acoustic flow as described by Müller? In other words, how do bats combine this monaural perceptual information? In the next section we will

⁷The tau function of a variable x is x divided by the rate of change of x .

see how this and other scientific questions can be investigated with synthetic models such as robots.

2.4 The biomimetic approach

2.4.1 Introduction

With the arrival of the technological era, computers started playing an essential role in the development of science. People like Marr [1982] advocated the use of computational theory as a tool for empirical investigation, giving emphasis to the importance of the *levels of description* idea for studying perception. Perception, in his opinion, can not be understood without explanations of a system at three different levels of abstraction: computational (*why?*), algorithmic (*what?*) and implementational (*how?*). Marr's levels idea forms the base of new emerging methodologies such as the biomimetic approach.

An early definition of *biomimetic* was given by Walter [1950] as “synthetic Biology”. In fact, biomimetic comes from biomimesis, *i.e.* to mimic life, the imitation of biological systems. In such terms, biomimetic sensing systems are man-made systems which implement functional principles of their biological counterparts, either as a research tool for biology or as an engineering application. Moreover, biomimetic systems do not violate any of the known constraints on biological function. However they do forgo replicating any detail of biological structure irrelevant to the problem under study [Peremans et al., 2000].

The biomimetic approach arises as an alternative to more traditional approaches to the study of perceptual mechanisms in animals such as direct investigation, *via* psycho-physical and neuro-ethological experiments, and theoretical investigation, *via* mathematical and computational simulation of aspects of those mechanisms described in the biological literature.

Horiuchi [2000], in an attempt to define *neuromorphic engineering*, differentiates between biomimetic and biomorphic, the latter being “the engineering or scientific effort to copy and utilise what we understand about the functional benefits of physical bodies of creatures, such as the utility of arms, hands, fingers, legs, and feet”. As a result, Horiuchi sees the synergy of biomimetic and biomorphic as neuromorphic engineering, defining it as “the construction of computational devices that utilise the physical structure and/or representations found in biological nervous systems”. In such terms, we define Biorobotics as the biomimetic approach to Robotics, which will be followed as a methodology for this work.

2.4.2 Biorobotics as a methodology

The analysis and modelling of natural sensorimotor systems, as a biological approach to robotics, has been gaining momentum during recent years. This multi-disciplinary field of research aims at both a better understanding of how these mechanisms actually work in nature as well as improvements in the design of mobile robot controllers. In addition, biologists are becoming interested in the implementation of sensorimotor systems in hardware as such physical models complement the more traditional mathematical models. These new tools, i.e. a robotics approach to biology, allow them to explore the sensory world of animals with synthetic observers and test hypotheses for adaptive sensing behaviour in real-world conditions. From the merger of these two disciplines, biology and robotics, biorobotics arises.

A point suitable for discussion is whether the use of a computer-based simulation instead of a physical (robotic) implementation of the animal as the model to work with, is sufficient or not. Computer simulations tend to simplify the interactions between the animal and its environment while focusing on particular aspects of behaviour. These disembodied models often fail to replicate the essential details of an agent-environment interaction. On the other hand, the construction of a robotic model requires the formation of a complete and explicit hypothesis about the mechanisms underlying the generation and use of cues in the perception task, but at the same time offers a cost-effective way of exploring a biological feedback and control system without the need to simulate complex interactions with the environment [Kuc, 1996; Walker, 1997; Lund et al., 1998]. Hallam [1997] extends this argument:

“for experiments of certain kinds, robotics models offer advantages that outweigh the difficulty of working with them. There is no question of the completeness or validity of a simulation in such experiments, as the real world is being used”.

In the same way, Rucci believes that since perceptual processes have evolved to adaptively control interactions with the environment, they must be studied in conjunction with motor behavior and learning. In his research, Rucci uses robotic systems to expose neural models to the non-idealized characteristics of real environments [Rucci et al., 1999].

This argument can be summarised in the diagram of figure 2.9 given by Webb [1993] who is, together with Hallam, one of the pioneers in this field. In such diagram we can see a system S (*e.g.* an animal) producing a behaviour B which is studied by an experimenter. This experimenter has an hypothesis (step 1) about how this system works (S_H) and by a formal method demonstrates that it produces a behaviour B_H . These, the hypothesised system and behaviour, are considered equivalent to the real system and behaviour by the experimenter. Now (step 2), the experimenter builds an artificial model (*e.g.* a real or a simulated robot) to investigate the hypothesis practically. This new system is called S_H^* and the behaviour it

produces B_H^* . At this point (step 3), the experimenter claims that the artificial model S_H^* is a valid representation of the formal model of the system (S_H) and therefore the same for the behaviour B_H^* produced by the artificial model. Finally, the experimenter concludes that this behaviour (B_H^*) is equivalent to that in the real world (B).

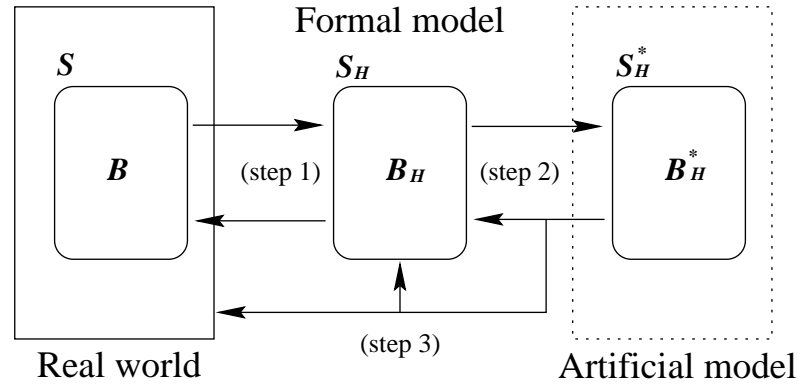


Figure 2.9: **From the real world to an artificial model and back to the real world.** (Adapted from [Webb, 1993].)

Hence, because of the physical interaction of the real system (S) with the world, a real robot instead of a simulated robot is needed as the artificial agent to work with since a simulated robot will need to simulate all the relevant physics of the real world, which is impractical because of both the ignorance of all relevant factors and the computational cost.

Webb [1993] proposes a methodology for investigating perception which was later adopted by Walker [1997] and which will be adopted in this dissertation as well. Such a methodology can be summarised in the following points.

- **Target system.** Choose a particular biological sensory system as a target.
- **Physical characterisation.** Characterise the relevant physics of the biological sensor and sensor motion in sufficient detail to facilitate the generation of hypotheses about the perceptual mechanisms underlying the animal's behaviour.
- **Implementation.** Build a model of the sensory mechanism in which to test behavioural hypotheses. Such a model must capture, realistically, the problems of interacting with the real world.
- **Evaluation.** Carry out experimental tests to evaluate the performance of the model system and examine the hypotheses embedded therein.

As a result of her work, Walker [1997] pointed out an interesting conclusion:

“building models of the evolved perceptual mechanisms of particular animals is a fruitful way to approach the difficult robot design problem of identifying the task and environmental factors which act to constrain and simplify this process of sense-information extraction”.

This is exactly the motivation of our work, in which as a *target system* we have chosen the bat’s echolocation ability for navigation and prey capture tasks. This is based on Walker’s *et al.* *physical characterisation* of the CF-FM bat and in its *implementation* (robotic model).

Webb’s contribution towards a biorobotic methodology has continued since then. In [Webb, 1999] and [Webb, 2000], a framework for describing the process of modelling is presented. Webb explains how models of biological systems can vary along a number of different dimensions and how controversy about the ‘correct’ way to model is often simply confusion among these dimensions.

Webb describes eight dimensions on which models of biological behaviour can differ in what they represent and how they represent it, arguing that any model has a position in a multidimensional space, in which the origin for all dimensions is the system itself. These dimensions are: realism (can the target system be identified?), level (what are the base units of the model?), generality (how many systems has the model targeted?), abstraction (how many elements and processes are in the model, compared to the target?), accuracy (does the model represent the true mechanisms of behaviour in the target?), medium (what is the simulation built from?), match (in what way does the model behave like the target?) and utility (is our understanding improved by the model?).

2.4.3 Examples of biorobotic research

Many people have built robot “animals” with greater or lesser faithfulness to the underlying Biology. Many more have built robots which use a sometimes vague form of “biological inspiration”. Robots which are truly biomimetic are much more rare and generally very recent. Some examples from the biorobotics literature are summarised below:

- **The cricket robot.** At Edinburgh University, Webb [1993, 1995] and Lund et al. [1998] built a robotic model of the *Grillus bimaculatus* auditory system. The model implemented a simple neural controller which performs phonotaxis using songs of real male crickets. The cricket robot behaved as female crickets do in identical experimental conditions. The authors claim that the cricket robot could be used for further exploration of the mechanisms controlling recognition and choice behaviour in real female crickets.

- **The cockroach robot.** At Case Western Reserve University, Beer, Quinn and colleagues built an hexapod robot that can successfully walk, turn, run and climb in a cockroach-like manner [Beer et al., 1998; Quinn and Ritzmann, 1998]. This project aims benefits for Robotics — investigating the advantages of biological emulation of cockroach kinematics and applying it to hexapod robots— and Biology — providing a platform on which biologists can test hypotheses about cockroach posture and locomotion.
- **Shabot.** Möller and his colleagues at Zurich investigated visual homing strategies in the desert ant using a mobile robot [Möller et al., 1998]. Their navigation behaviour strategies were reproduced by a “snapshot model” based on the assumption that insects store a visual snapshot of the surroundings at the target location, deriving a home direction from a comparison of the current image with this snapshot. Their results confirm that the snapshot model is a plausible model of insect navigation which can provide new ideas in mobile robots research.
- **Robolobster.** Grasso’s research at Northeastern University in chemo-orientation in marine environments [Grasso et al., 1999] involved understanding how lobsters locate odour sources in turbulence. In their experiments, the underwater robot approaches an odour source under turbulent conditions which disperse the odour similarly to turbulence in the real world.
- **The barn owl robot.** Rucci adapted a computer model of the auditory and visual stimulation of the barn owl to the control of the orienting behaviour of a robotic system equipped with a camera and two lateral microphones [Rucci et al., 1999]. The results showed that an architecture specifically designed to account for biological phenomena can improve the motor control of a mobile robot performing in the real world.
- **VLSI fly motion sensor.** Harrison and Koch [1999] built a hardware model of the fly optomotor control system which uses visual flow information to estimate self-rotation as flies do. The model was implemented on a chip that receives input directly from the real world via on-board photoreceptors and generates motor commands in real time. The silicon system exhibited stable control sufficiently analogous to the biological system to allow for quantitative comparisons.
- **Honeybee navigation.** Srinivasan and colleagues at the Australian National University investigate different aspects of insect vision and navigation, such as how honeybees communicate optic flow measured distances by dancing, and how can the arising principles be embodied in autonomously navigating robots [Srinivasan et al., 2000].

2.4.4 Biomimetic ultrasound

Animal acoustic sensorimotor systems, like the ones found in bats or crickets, have the potential to become model systems for studying the principles of biological sensing and sensorimotor integration starting from clearly defined behavioural tasks.

Having seen different examples of biorobotic applications we will focus on those more directly related to this work — which will be introduced in chapter 3. For example Walker et al. [1998b]’s research on biomimetic sonar resulted in successful single target tracking in clutter. They also investigated the spatio-temporal acoustic cues generated by scanning the receivers of the biomimetic sonarhead described in chapter 3 and used in my work also, using a simplified version of the opposing pinna movements (arc scanning) employed by *R. ferrumequinum*. As described in section 2.3, sweeping the sonarhead receivers through opposite vertical arcs creates dynamic cues in the form of amplitude modulations which vary systematically with target elevation, suggesting at least one possible source of information the bats could use. Walker’s motivation was that “if neurons exist to represent moving targets — as measured by stationary pinnae — then the apparent motion of a stationary target — as measured by moving pinnae — may be similarly encoded” [Walker, 1997].

Walker also investigated the possibility addressed by [Pye et al., 1962] of Rhinolophids and Hipposiderids moving their ears in order to exploit the cosine-law dependence of the Doppler effect, whose continuous change in echo frequency encodes target angle, to create frequency modulations whose magnitude will depend systematically upon relative target bearing [Walker, 1997].

The results of this research gave insights for understanding how a dynamic sensory device can perform accurate target localisation in a cluttered environment using both binaural and monaural sensor mechanisms. They also experimented with simulation, building a software model of an echolocation system [Walker et al., 1998a]. This simulation was used for investigating behaviours for localising moving targets in the presence of strong stationary reflectors. The simulator was also used together with a genetic algorithm to investigate the role of pinna shape during target localisation in broad-band bats, particularly for determining the target’s elevation [Peremans et al., 1998b]. The genetic algorithm was used to evolve different pinna shapes which were tested on the simulator afterwards. They also proposed building the pinnae and attaching them to the sonarhead to improve target localisation. This artificial pinna project has been extended by us as part of the RoBat project as we will see in chapter 7.

Other examples of biomimetic sonar follow. Teimoorzadeh [1995]’s model of bat obstacle avoidance and prey recognition behaviours is another example of work done in simulation. He investigated bat mental representation of acoustic images by modelling a memorisation circuit

of sensory expressions based on feedback and association of sensory phenomena. However, despite the results of this work there is no evidence of further work done with this simulator nor of a robotic implementation of it.

Barshan and Kuc [1992] present an active wide-beam Sonar system that mimics the sensor configuration of echolocating bats is presented. This system provides 2D (range and azimuth) estimation of an object, located along the system line-of-sight, which improves with decreasing range. This work is continued in [Kuc, 1993] in which *ROBAT*^{3D}, a robot driven by four air jets and provided with a Sonar system consisting of five transducers configured in the form of a cross, is used for tracking moving objects in the space using qualitative interpretation of sonar signals. Kuc's system, instead of using TOF measurements for computing the location of the object by triangulation, extracts qualitative information from a sequence of pulses, basically determining which receiver detected the echo first using ITDs.

As we saw earlier in this chapter, intelligent ultrasonic sensors for mobile robotics can be built by combining TOF and triangulation. Using these two principles, Kuc [1996] implemented an active Sonar system capable of changing its configuration in response to observed echoes as biological systems do. This approach calculates the true range and bearing angle of a target assuming it is on the same elevation plane as the transmitter and receivers. Then, each of the receivers defines with the transmitter an ellipse of possible locations of the target. The target is assumed to be located at the intersection of these two ellipses. The method uses ellipses assuming a target at 0° in elevation instead of ellipsoids, hence being valid for large and specular objects such as walls and posts but not for tracking smaller objects in the space. In chapter 6 we will go back to Barshan and Kuc [1992] and Kuc [1996] works.

More recently, Kuc extended his work to object identification. In [Kuc, 1997], a biomimetic sonar system consisting of a central transmitter with two rotating receivers on each side is situated at the end of a 5 DOF robot arm. This configuration maximises the SNR of the echoes, whose bandwidth extends from 20 to 130 kHz, allowing better performance of the learning module. The system learns to identify small objects (smaller than 2.5 cm) by extracting vectors of 32 envelope values at different bearing angles and forming a data base. The whole process consists of two different phases: first the system approaches the object using TOF information to focus the system as in [Kuc, 1996]. Then, the evolution of the echo energy with time is used for object identification. Also, Kuc [1994] proposes a sensorimotor model for prey capture in the big brown FM bat *Eptesicus fuscus*. The model shows (in computer simulation) how successful non-predictive tracking of an ideal prey can be performed with a simple system using a pair of controllers that apply yaw and pitch corrections to alter the bat's heading while pursuing a prey. Kuc's model is continued by Erwin et al. [2000] who disagree with Kuc's

claim that only azimuth and elevation are necessary for non-predictive tracking. According to Erwin and colleagues, the use of distance (range) information is crucial for a complete model of prey hunting by bats. Moreover, their results suggest that realistic aerodynamics constrain the bat's behaviour more than was suggested by Kuc.

2.4.4.1 Discussion

As McKerrow [1991] said a decade ago, “we have a long way to go before our sensors will even approach the echolocation ability of a bat”. Since then, the small but active biomimetic Sonar community has achieved some important issues, heading towards the development of a bionic bat.

Despite the different examples of work following a biomimetic approach seen in this section, it is important to notice its scarcity in the scientific community. Müller, a relevant example in the use of biomimetic ultrasound technology for scientific purposes [Müller and Schnitzler, 1999, 2000; Müller and Kuc, 2000], gives the following illustrative example: “If research is like a multi-player jigsaw puzzle, biomimetic ultrasound is a small research area which requires an agreement in the shape of the pieces and the regions of the image to be used among the scarce *players* in order to get fruitful results”. By contrast, in big research businesses such as Human Genome, Aids, Alzheimer's, etc, random synergy is sufficient because of the large number of research groups involved. Müller [2000] proposes focusing on, among others, binaurality in active Sonar, stimulus ensembles and where they come from, adaptive mobility, neural and signal representations and an inventory of ultrasonic tasks in Biology.

2.5 Summary

This chapter has given an overview of the two disciplines relevant to this work, the use of ultrasound in robotics and bat biosonar, as well as introduced the biomimetic approach as the methodology to follow in this work.

After explaining the physics of the Polaroid transducer and the problems arising when using it as a simple range sensor, two different approaches — the grid-map approach and the feature-based approach — to the use of ultrasound for localisation and sensing in mobile robots were introduced. Next, other ways of using the ultrasonic transducer with respect to sensor configuration, structure of the call and the processing of the received echoes were presented, as well as our interest in how bats exploit the physics of echolocation. An overview of some aspects of the CF-FM bat neurophysiology and ethology was given, pointing out ideas suitable for application to ultrasound-based navigation in mobile robotics. Finally, the biomimetic approach

to Robotics was introduced followed by some examples of biomimetic work. At this point we are ready to present RoBat, the biomimetic platform used in the experiments described in this work.

Chapter 3

The RoBat system

3.1 Introduction

The RoBat¹ project aims to investigate bat biosonar as a biomimetic approach to mobile robot navigation, *i.e.* it tries to understand how echolocating bats perform navigation tasks such as obstacle avoidance and prey capture, and how this can be applied to ultrasonic-based navigation in mobile robots.

Thus the motivation for creating a tool such as RoBat is twofold:

- to help engineers to better understand the relationships existing between environment features and their corresponding acoustic images in a dynamic context.
- to help biologists studying echolocation in bats to better understand what type of information is available to the bat while performing particular tasks.

This chapter is structured in two main parts: section 3.2 describes RoBat and shows examples of performance under different configurations (as a FM bat and a CF-FM bat). Section 3.3 describes the topics of interest investigated in this work as part of the RoBat project.

3.2 RoBat: a biomimetic platform to study perception in bats and robots

RoBat consists of three main components: a biomimetic sonarhead (described below); a 3 DOF mobile platform (described in section 3.2.2); and a modular architecture (described in section 3.2.3) which integrates a processing module and several behaviours in a reactive way

¹The name RoBat was previously used by R. Kuc as *ROBAT*^{3D} in [Kuc, 1993].

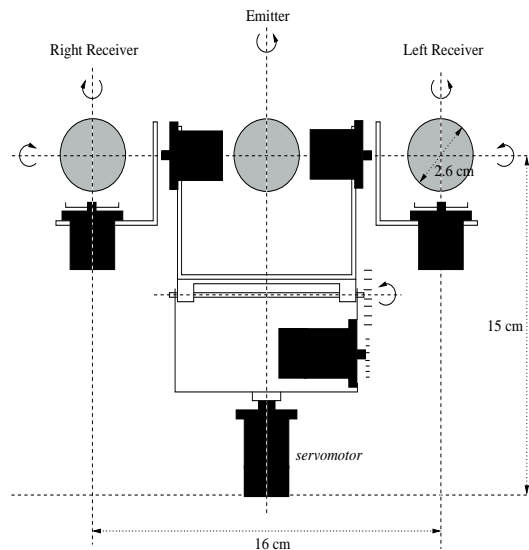


Figure 3.1: **The robotic platform.** Front view of the sonarhead consisting of the central transmitter fixed to the head and the two receivers each independently orientable (left). RoBat, a biomimetic sonarhead mounted on a mobile base (right).

(see figure 3.4). These three components are all controlled and integrated into a single system by software running on a 1 GHz Athlon PC computer under Linux. In addition to this hardware platform there is also a software model of the biomimetic sonarhead, for testing signal processing algorithms, which incorporates the physics necessary to simulate realistic experiments.

3.2.1 The biomimetic sonarhead

The biomimetic sonarhead used in this research was originally devised by Peremans et al. [1997]. As indicated in figure 3.1 (left), the sonarhead allows panning and tilting of the neck, and independent panning and tilting of each of the two ears (receivers). The ultrasonic transducers are Polaroid electrostatic transducers. The motors driving the different axes are standard radio-control servomotors².

This setup, when mounted on the mobile platform as in figure 3.1 (right), allows insonification of arbitrary points in space independent of the orientation of the mobile platform. Taken together with the capability of the sonarhead to independently orient the ears as well it allows us to model different strategies that might be used by bats to actively explore their environment [Peremans et al., 2000]. An example of such an active exploration strategy used by real CF-FM bats is the arc scanning behaviour described in chapter 2.

²These kind of motors do not provide position encoders and therefore it is not possible to know the position of the servo at a time along its trajectory. A model of the servo (described in chapter 6) was devised to solve this constraint.

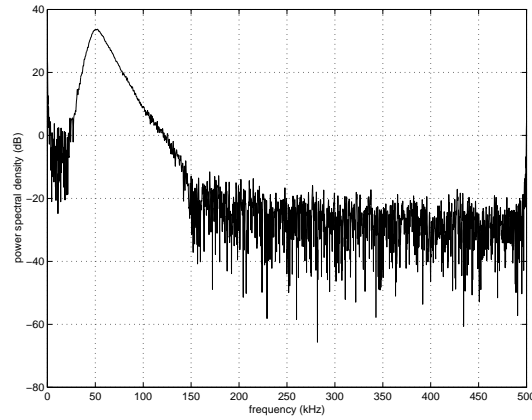


Figure 3.2: **Power spectral density of the transfer function** describing the transmitter-transducer-transducer-receiver system.

The transmitter is mounted at the centre of the head, moving along with the pan and tilt movements of the neck. The transmitter electronics allows the transmission of waveforms generated by the D/A converter board at 1 Msample/s (Gage CG1100 2 channel/12 bit/80 Msample/s D/A card) in the control computer. The D/A converter noise floor is $1/4096$ of the peak signal, *i.e.* 72dB below the maximum signal amplitude. This noise floor is low enough for the measurements taken in this work. The output voltage of the transmitter consists of a bias voltage of 150V upon which the transmit waveform, amplitude 150V, is superposed. We have chosen this transducer because its large bandwidth (figure 3.2), after removal of the protection grid, allows the modelling of both broadband echolocation and narrowband echolocation.

Detection and amplification of the reflected echoes is performed by the receiver electronics, which is mounted, together with the transducers, on pan/tilt servos. As above, the output signals from the receivers are sampled at 1 Msample/s by the A/D converter board (Gage CS512 2 channel/12 bit/5 Msample/s) in the control computer. All further processing of the received data is performed on the control computer which communicates with the robot through a 18 meter long coaxial umbilical.

3.2.1.1 Noise

The electronics of the sonarhead are susceptible to different noise sources such as electronic pick-up from the transmitter, a low frequency component from the mains, the DC/DC converter and some noise because of the umbilical. These noise sources are reduced by a pre-filtering module (described in section C.1 of appendix C) applied to every echo before entering the filterbank.

In further versions of the sonarhead, and providing that the echo processing could be implemented in hardware, the noise sources could be dramatically decreased using an integrated system in which acquisition and processing would be integrated in the same insulated box as in *e.g.* Heale and Kleeman [2000].

3.2.2 The mobile platform

During different stages of the RoBat project, different mobile platforms have been used for providing the required mobility to the sonarhead.

The current platform is “Bill”, a 12 inch diameter off-the-shelf mobile platform from Real World Interface (RWI), model B12 [RWI, 1994]. Bill (figure 3.1 (right)) has three wheel steering and three wheel drive. The three wheels are driven synchronously and remain parallel at all times. Good positional accuracy is achieved due to the separation of the steering system from the drive system.³ Since all wheels are driven, the B12 has excellent traction. This 3 DOF platform has an on-board controller that receives motion-commands from and sends back status information to a control computer through its serial port.

The mobility offered by this robot base is used to generate dynamically varying acoustic images, *i.e.* the acoustic flow mentioned in chapter 2, that correspond, at least in principle, with the *images* bats get while flying through their environments.

3.2.2.1 Previous mobile platforms

The main difference between the current platform and the previous ones resides in the way the echoes coming from the sonarhead are processed. The previous platforms used a network of transputers whereas the current platform uses a state of the art microprocessor under Linux.

“Ben Hope” In previous work [Walker, 1997; Walker et al., 1998b,a], the sonarhead was mounted on “Ben Hope”, a mobile robot made of a RWI-B12 base (similar to Bill’s) and an enclosure which hosted a transputer-based computer on which all the echo processing was carried out (see figure 3.3 (left)). Control of the sonarhead’s servomotors was performed by the transputer server, installed in a desktop PC, which communicated with Ben Hope through an umbilical. Ben Hope was 50 cm tall, providing the sonarhead with a different perspective of the world than Bill’s or the LEGO platform described below.

³This platform provided the motion required for Doppler-shift estimation. True-Doppler (see chapter 4), was calculated from the readings of the wheel encoders without previous calibration of the platform.

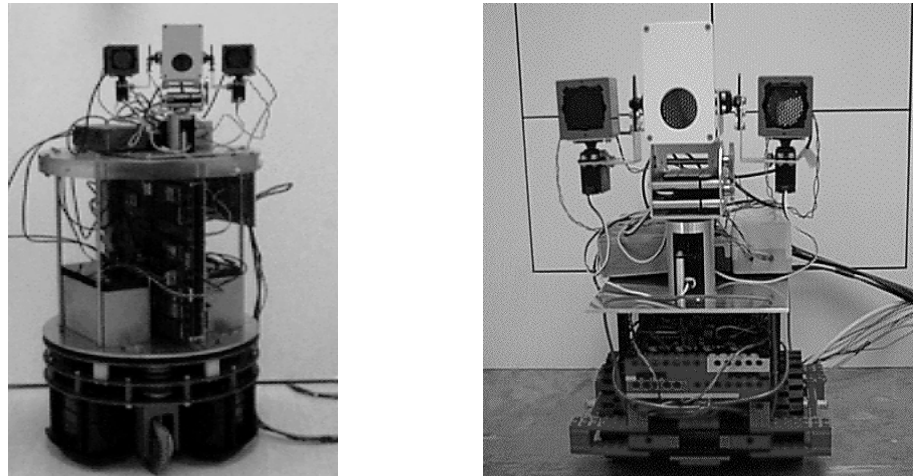


Figure 3.3: Front view of **previous robotic platforms**. Ben Hope (left) and the LEGO robot (right).

LEGO robot. A mobile robot was built from scratch using LEGO pieces and some electronics developed at the Division of Informatics for controlling the actuators. The reason for using LEGO was because of its flexibility and modularity as a design and implementation medium, as well as familiarity from using it in previous work [Carmena, 1998; Carmena and Hallam, 1999].

The robot was a simple and flat platform as seen in figure 3.3 (right), strong enough to carry the sonarhead on board. It was 12 cm tall and consisted of 3 wheels (2 driven wheels and 1 free wheel) with a gear reduction big enough to provide the robot with a fast response despite the sonarhead's weight. The robot's brain-brick hosted a simple program which drove the motors according to the commands sent by a desktop PC. The transputer network was installed on this PC, carrying out all the processing tasks of the sonarhead and communicating with the robot through an umbilical. Despite the inaccuracy of the LEGO driving mechanisms, lack of speed and torque, and unrepeatability of the whole platform, fairly good preliminary results on estimating Doppler-shift were obtained as reported in [Carmena and Hallam, 2000].

3.2.3 RoBat's modular architecture

A block diagram of the modular architecture can be seen in figure 3.4. As seen in the figure, all the monaural modules, such as signal processing and cue extraction, are duplicated because of the two receivers.

Next, some of these modules are briefly described. A full description is given in chapters 4, 5 and 6.

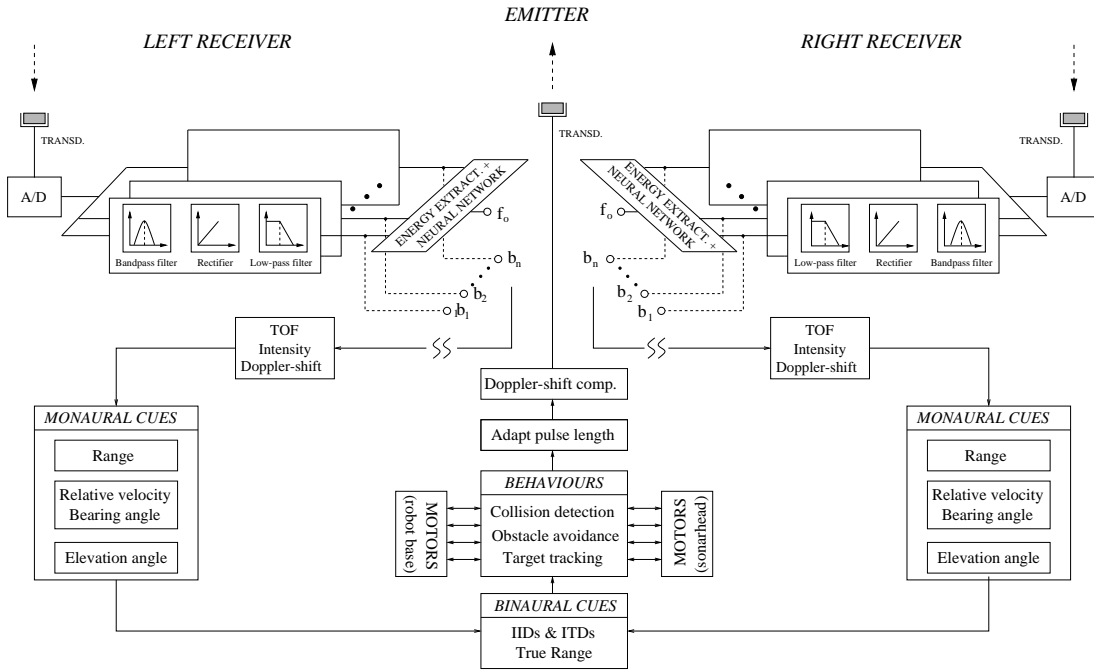


Figure 3.4: **Block diagram of RoBat’s modular architecture.** The signal processing module together with the TOF and Doppler estimation modules coming from each of the two receivers are connected to a binaural module in charge of the motor and emission tasks (see text).

3.2.3.1 Signal processing module

Bats (and mammals) surely do not perform Fast Fourier Transforms (FFTs) for the frequency discrimination of the incoming sound. Instead, their inner ear performs an approximation of an FFT through the basilar membrane inside the cochlea.

In RoBat, the received echoes are sampled by an A/D converter and fed into a signal processing module whose operations are based upon a filterbank model of the processing performed by the mammalian cochlea [Slaney, 1993]. Two different kinds of filterbank — linear and gammatone — were investigated in detail. Preliminary study of other models (*e.g.* cascade filterbanks) was also carried out. From the output of the filterbank, two different methods — a neural network and a weighted average — were used for extracting Doppler-shifts which, together with the TOF, form the monaural cues extracted from each individual echo.

The RoBat system can be configured for being phase coherent. However, since there is no evidence of bats having a coherent detector implemented in their auditory system, we decided not to make use of phase information.

3.2.3.2 Behaviours

The processed data coming from each of the monaural modules is then integrated by the binaural module, resulting in behaviours such as obstacle avoidance, motion detection, Doppler-shift compensation and target tracking. These behaviours will be described in chapters 5 and 6.

Also, the length and call-frequency of the emitted pulses are recalculated at the end of each loop depending on the behaviour being performed by the robot. During most of the experiments performed in this work the length of the pulses was kept constant. However, the call-frequency was modified during the Doppler-shift compensation experiments described in chapter 5.

All processing and interpretation of the received data is performed on the control computer. The operating speed of this computer is 12 Hz, *i.e.* 12 complete *sense-and-act* loops per second including a spectrogram-like display of the received echo at each ear was normally obtained⁴. This performance makes it possible to investigate the dynamics of a number of acoustical phenomena in real-time conditions.

3.2.3.3 Visualisation module

A visualisation module⁵ allows interactive exploration of echoes from echolocation scenarios, and seeing them through a model of the auditory base representation of bats. This provides quick, intuitive access to biosonar problems [Peremans et al., 2000].

This module takes the logarithms of the outputs of the different channels of the filterbank which are shown in a spectrogram-like display on the screen of the control computer. Figure 3.5 shows an example of the output of the visualisation module when processing the echo of a frequency swept transmit pulse (from 120kHz down to 40kHz) reflected from a stationary flat surface oriented towards the sonarhead. The white lines in the figure are two mobile cursors which allow visualisation of arbitrary slices of the display parallel to the time or frequency (filterbank channel) axes.

Other examples of the type of echolocating scenarios that can be seen with the visualisation module will be presented in section 3.2.5 and in chapter 5.

3.2.4 Software model of the sonarhead

The *3D Echolocation Simulator*, a software model of the sonarhead, was developed by Herbert Peremans and Ashley Walker (see Appendix C in [Walker, 1997] for a detailed description) as

⁴This depends, among other factors, on the number of channels in the filterbank and on the number of acquired samples, as we will see in chapter 4.

⁵This module, described in [Peremans et al., 2000], was mainly developed by Müller with contributions from Peremans and myself.

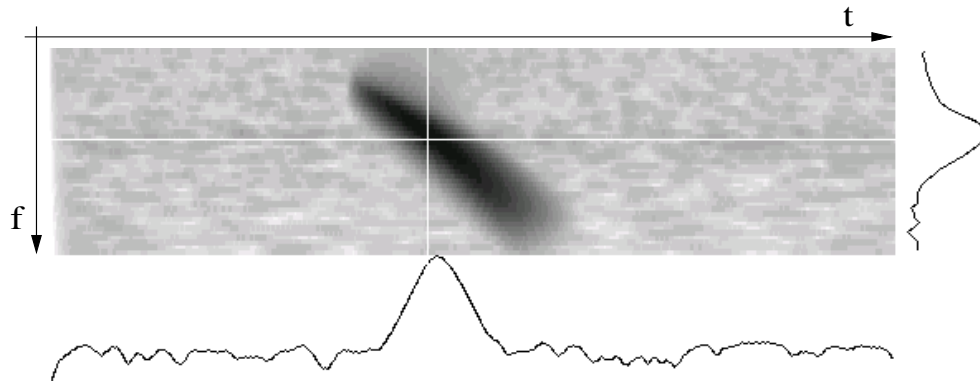


Figure 3.5: **The output of the wideband cochlear model as displayed on the screen of the control computer.** The source is a frequency swept from 120kHz down to 40kHz reflected on a stationary flat surface (one ear only).

a tool for simulating signal processing algorithms before implementing them in the sonarhead. Moreover, the simulator can host experiments that can not be carried out with the existing hardware *e.g.* those using different sensor morphology or transducer size. It also incorporates the physics necessary to simulate realistic experiments, for instance allowing the use of oscillating targets with different geometries and motions.

With respect to the RoBat project, the *3D Echolocation Simulator* was used for testing and evaluating the pinna-like reflector configurations and finite element surfaces evolved by a genetic algorithm, as will be seen in chapter 7. For such work, the simulator was modified as needed to suit the requirements of the different experiments.

3.2.5 Examples of broadband echoes

As we saw in chapter 2, CF-FM bats have both a narrowband, *i.e.* constant frequency component as well as a broadband, downward frequency sweep component in their call. Furthermore, they vary the importance of each component dynamically depending on the task, by varying the energy in each of them. Due to our interest in the constant frequency component of the call — which, according to the literature, is the component relevant to the sort of tasks we are interested in such as obstacle avoidance — we do not include FM tails at the end of RoBat's calls in the experiments presented in this work.

By contrast, in this section we will show pilot data obtained with the biomimetic platform exploring examples of broadband echolocation tasks faced by FM bats. It is clear that everything said about these examples applies equally well to the FM portion of the call of CF-FM bats. The following content of this section is extracted from [Peremans et al., 2000].

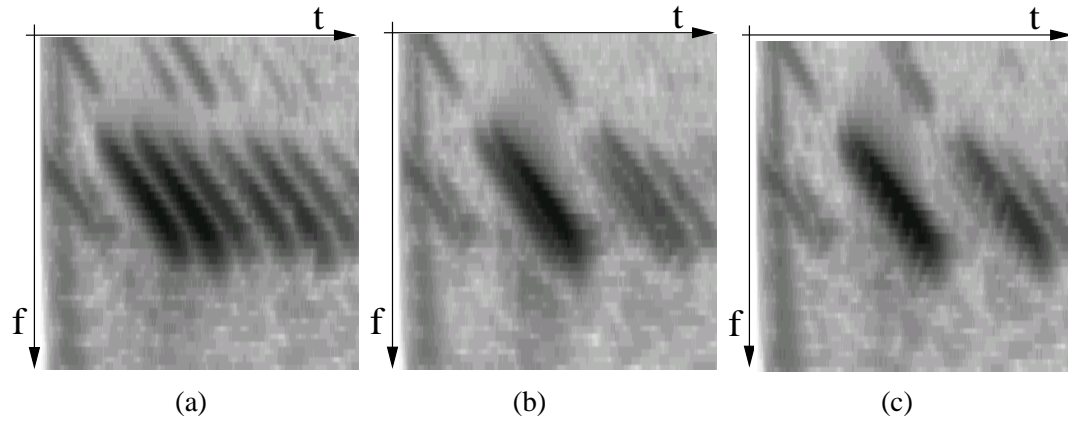


Figure 3.6: **The echo from a small object** (cylinder $\varnothing=1.5$ cm) **in front of a flat reflecting surface:** (a) 10 cm separation; (b) 4 cm separation; (c) 2 cm separation. The first two echoes correspond to the reflections from the cylinder and the surface respectively. Subsequent echoes are generated by multiple bounces between the transducers and the targets.

Resolution versus system-identification. Resolution is hardly ever a critical constraint in natural biosonar tasks performed on FM signals. Even with the incoherent, low-pass filtered time-frequency representations, which bats have at their disposal and which were modelled here, resolving echoes from reflectors separated by a few centimeters or even less is a fairly simple task. Such a resolution should suffice for the survival of a bat. The ease of achieving centimetre resolution is illustrated by the following examples: A biomimetic broadband echolocation system, *i.e.* a transmit pulse with frequency sweeping down from 120 kHz to 40 kHz in 3 ms analysed with the broadband cochlear model, was used to examine the echoes generated by a cylinder (with 1.5 cm diameter) placed in front of a flat surface. Distances from the sensor were 10, 4 and 2 cm. The echoes generated by these two objects are clearly distinguishable (figure 3.6), even with the significant overlap which occurs at the smallest separation (plot c).

It should be noted that the total bandwidth of the echolocation system is not the relevant factor in determining whether we can visually discern the two echoes in the spectrogram. It is the bandwidth of the individual bandpass filters that make up the cochlea that determines the minimal duration of the response, *i.e.* the smearing, in each frequency channel.

When FM bats hunt in a cluttered environment the sonar problem is not a problem of resolving different scatterers, but it is a problem of target identification. For example, if certain species of FM bats were indeed capable of finding arthropods on foliage with sonar, the problem would not be to tell that there are two scatterers close to each other, but to tell that the first one is a prey item and the second one a leaf, rather than just two leaves or a small branch in

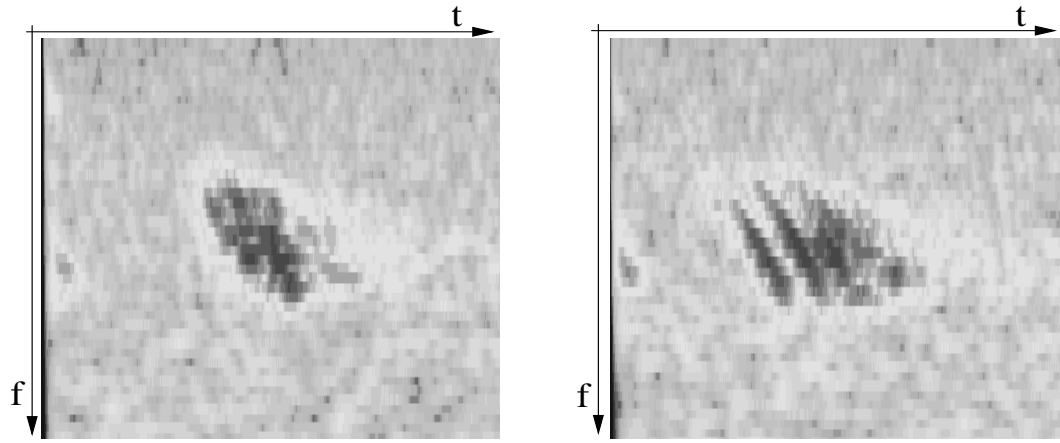


Figure 3.7: **The echoes reflected off two different types of foliage** (see text for explanation).

front of a leaf [Peremans et al., 2000]. As we will see in chapter 5, this point is nicely illustrated by the case of CF-FM bats where resolution, by virtue of the long CF components, is very poor indeed but the target identification task can be solved nevertheless.

Echoes from extended, natural targets. Many species of echolocating bats encounter not only isolated “point” scatterers (*e.g.* when tracking a prey some distance away from clutter-producing obstacles), but frequently receive echoes generated by extended targets consisting of anything ranging from a few to a great many reflecting facets. Their sensing capabilities, as well as the behaviours which may be enabled by these capabilities, remain largely unexplored. Müller believes that echoes composed of contributions from many scatterers are best treated as random processes in the sense that the resulting waveforms are prohibitively hard to predict as a function of position and orientation of the sonarhead. This is for instance true for ubiquitous natural textures like foliage [Müller and Kuc, 2000]. It is therefore important to characterise how the statistical properties of echoes from such targets change as a function of position and orientation. A first impression of the behaviour of such echoes is readily gained using an interactive tool like the one described in this chapter.

Examples of echoes from foliage insonified with a broadband call, *i.e.* a pulse with frequency sweeping down from 120 kHz to 40 kHz with a duration of 3 ms, are shown in figure 3.7. Obvious properties of these echoes are a fairly long duration ($\sim 3 - 4$ ms), compared with the duration of the echo from the flat reflecting surface shown in figure 3.5, as well as a random pattern of peaks and notches in the time-frequency plane. Furthermore realistic filterbank parameters result in a considerable smearing of the echoes. However, the loss in fine structure information that is associated with this smearing does not seem to prohibit obtaining

biologically meaningful information, *e.g.* target class, from these echoes, since bats seem to be capable of distinguishing between different types of foliage. Müller conjectures that this is so because most of the fine structure present in the echo is likely to reflect irrelevant structural detail, *e.g.*, the current properties and placement of all leaves within the sonar footprint, which is likely to change with the next gust of wind anyway [Peremans et al., 2000].

3.3 Research topics

Now that the biomimetic platform has been described, the research topics addressed in this work can be introduced. From all the interesting topics suitable for being investigated with a synthetic tool such as RoBat, this dissertation contains investigations in the estimation and use of Doppler-shifts for echolocating tasks, in 3D tracking methods exploiting the dynamics of the sonarhead, and in artificial pinna design.

3.3.1 Estimation and use of Doppler-shifts.

As mentioned in the literature review of chapter 2, CF-FM bats use Doppler-shifts for several tasks such as obstacle avoidance and prey capture. Moreover, this rich source of information is not exploited by commercial ultrasonic range sensors for robots, hence our motivation for incorporating the use of Doppler-shifts in mobile robot navigation.

The literature on Doppler-shift estimation using Sonar, for engineering applications, is very scarce. With respect to biosonar, it is even more scarce. Müller [1998] contributes with an acoustic flow for obstacle avoidance hypothesis in the CF-FM bat. Müller's work, a good example of a scientific contribution using synthetic tools, gave us the motivation for investigating the use of Doppler-shifts in mobile robotics.

Thus, as a starting point towards Doppler-based navigation, we are interested in implementing and comparing models of the signal processing performed by the bat's cochlea with methods for extracting Doppler information from echoes. The cochlear models — named filter-banks — are based on sets of bandpass filters followed by full-wave rectification and low-pass filtering. This will be seen in chapter 4.

In chapter 5, some Doppler-based behaviours — such as Doppler-shift compensation, convoy navigation and acoustic flow — will be implemented, discussing to what extent they can be useful in sonar-based mobile robotics.

3.3.2 3D tracking methods.

As we saw in chapter 2, Walker [1997] investigated, by means of static and dynamic cues, different ways in which pinna movements may be used for 3D target localisation in CF-FM bats. She hypothesised a dynamic approach based on temporal cues. By sweeping their pinnae through vertical elevation arcs, CF-FM bats may create dynamic cues in the form of amplitude modulations which vary systematically with target elevation in the form of:

1. **IID rates of change:** obtained by measuring variations in IID over time while the ears perform arc scanning. However, this will fail for 0° elevation since IIDs are constant throughout the duration of the measurement.
2. **Peak delays:** the delay between echo arrival time and peak time in each ear (*i.e.* monaural timing cues) encode target elevation. It is possible to determine the target's elevation position by measuring the separation of these measured peak delays between the two ears (*i.e.* binaural timing cues).

With respect to the bearing angle and true range of the target, we are interested in the method devised by Barshan and Kuc [1992]. This method considers the target to be located in the intersection of the two ellipses defined by each of the receivers with the transmitter, assuming the target is in the same elevation plane as the co-linear emitter and receivers. Our intention, as we will see in chapter 6, is to implement and test both methods in RoBat, and to integrate them afterwards in a bat-inspired 3D tracking system.

3.3.3 Design of artificial pinnae.

The inspiration for evolving artificial ears comes from our belief of the important role the large size and mobility of the pinnae — compared to the size of their head — plays in *Rhinolophus ferrumequinum*. As seen in chapter 2, large pinnae can maximise the perceptual volume gain (the ratio of sound pressure when a pinna is present as opposed to its absence) by increasing the sound pressure arriving at the inner ear. Even more, the pinna mobility of CF-FM bats suggests the important role the pinna plays during specific behaviours such as arc scanning.

In fact, one of the long-term goals of the RoBat project is to build and attach artificial pinnae to the sonarhead. The motivation for this is twofold:

- to improve the directional sensitivity of the sonarhead's receivers (*i.e.* maximise the angular resolution of the receiving transducers) and the perceptual volume gain.

- to get insights on the role that dynamic reorientation of the head and pinnae may play in the creation of cues essential for sound source/reflector localisation.

In addition, the fact of being an unexplored field makes it more interesting. Papadopoulos [1997] and Peremans et al. [1998b] were the only references relevant to evolving bat pinna morphology available in the literature at the beginning of this work, as far as the author is aware.

3.4 Summary

In this chapter we have presented RoBat, a biomimetic platform that allows the study of ultrasonic perception in realistic dynamic environments. This tool makes visible a biologically plausible representation, *i.e.* the outputs of the cochlear model, of the acoustic flow field in real-time as the biomimetic platform moves through its environment, thereby making it much easier for human experimenters to detect the salient features in these acoustic images and investigate their relationship with environmental features. The usefulness of the biomimetic platform is related to four essential features: its mobility allows the study of sequences of echoes in the context of different behaviours; the active sonarhead allows the study of active sensing strategies; the biologically plausible representation of the echoes allows the cross-fertilisation of biology and robotics; and real-time operation allows the study of acoustic flow fields.

In order to demonstrate the capabilities of the system, we also explored example issues of biosonar tasks faced by FM bats. The ease with which range resolution on the scale of a few centimeters can be achieved was demonstrated, thereby highlighting that much of the difficulty of biosonar tasks lies in system identification rather than in resolution. For extended scatterers target identification has to be carried out under the constraint of a strong ill-posedness of the inverse problem and hence is best treated as a random process classification task [Peremans et al., 2000].

Finally, following the description of RoBat, the three research topics covered in this work — estimation and use of Doppler-shifts, 3D tracking methods and design of artificial pinnae — were introduced. These topics have two things in common: the exploitation of the physics of echolocation and the fact of not being deeply explored before — except for some of the tracking methods — in the mobile robotics community.

Chapter 4

Inner ear: Cochlear models and Doppler-shift estimation methods

4.1 Introduction

This chapter explores how continuous estimates of Doppler-shifts can be derived from physical echoes seen through two different models of a cochlear representation of the CF-FM bat.

Why Doppler? As we already saw in chapters 2 and 3, the Doppler effect plays a very important role in the echolocating behaviours of the CF-FM bat. Moreover, this rich source of information is not exploited by commercial ultrasonic range sensors for robots, hence our motivation for investigating the use of Doppler to mobile robot navigation.

At this point, the importance of both a biologically plausible — to keep our biomimetic approach — and computationally reliable — to perform real time processing in RoBat — model of the bat cochlea is clear. Also, such a model will also facilitate future analysis of the involved biological sensing problems faced by bats.

The chapter is structured in the following way: after giving a short overview of Doppler theory and applications, we compare two parsimonious models of the auditory fovea of the CF-FM bat — a linear and a gammatone filterbank — and two methods — an artificial neural network and a weighted average — for estimating Doppler-shift from the output of these models. Finally, a discussion supported by simulated data on how realistic our system is for dealing with real world scenarios, including more than one dominant frequency in the echoes, will close the chapter.

4.2 Doppler overview

In the nineteenth century Christian Doppler described how the observed frequency of light and sound waves was affected by the relative motion of the source and the detector. Since then many applications of this so-called *Doppler effect* have arisen. Common examples are meteorology — in which a Doppler radar is used as a forecasting tool (see, for example [Snyder et al., 1989]) — and biomedical applications (see, for example [Bøe and Kristoffersen, 1995]).

In mobile robotics, the Doppler-effect has not been extensively used, perhaps because of a lack of sensors in the market that allow this physical effect to be estimated. An exception are microwave radar sensors used for reducing errors commonly found in dead reckoning navigation due to factors such as wheel slippage and tread wear. Most implementations of these sensors employ a single forward-looking transducer to measure ground speed in the direction of travel [Borenstein et al., 1996].

There is not much work in the literature on Doppler-shift estimation using narrowband Sonar signals. One of the few references available is the work done by Dooley and Nandi [1999] in which a computationally cheap adaptive algorithm for estimating pure time delays is used for both time delay and Doppler-shift estimation, considering the latter as a linearly time-varying delay and so reducing the problem of Doppler estimation to a linear regression problem. Even though it is an interesting and apparently efficient method for Doppler-shift estimation, we did not take this or a similar engineering approach because of its not being biologically plausible. The same applies to fast Fourier transforms (FFTs); obviously bats do not perform FFTs *per se* but an approximation of it in the form of a filterbank as will be seen in section 4.3.

To the author's knowledge, there is no previous work on the use of Doppler-shifts from ultrasonic sensors in robotic applications. The context in which these Doppler-shifts are estimated and used in this work will be introduced next.

4.2.1 Doppler-shifts in a robotic context

Doppler-shifts can be very well estimated when the emitted call is a monochromatic tone — *i.e.* a CF signal — of a fairly long duration. However, it is not trivial to estimate Doppler-shift from a chirped call — like the one emitted by FM bats — because of the more complex echoes with multiple frequency components varying over time. In fact, as we saw in the literature in chapter 2, there is evidence of the use of Doppler only in CF-FM bats. These bats can reach up to 2500 Hz Doppler-shift when flying at speeds of 5 ms^{-1} as in the case of *R. ferrumequinum* whose call frequency is 83 kHz. However, in the robotics domain, assuming a call frequency

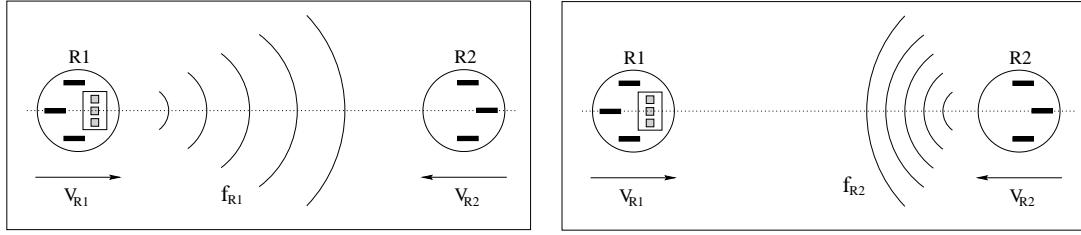


Figure 4.1: **Example of Doppler-shift in a robotic context.** Emitted Doppler-shifted call by $R1$ (left) and reflected Doppler-shifted echo by $R2$ (right).

of 50 kHz and a static reflector, Doppler-shifts will be below 300 Hz for maximum robot speed of 1 ms^{-1} as we will see in this chapter.

From physics theory we know that Doppler-shift is produced when sound waves are squeezed or stretched depending on the relative velocity between the sound emitter and an observer. In our case this is translated to the emitter and observer being located at the same place (*i.e.* the robot) and the sound source (ultrasonic pulse) being reflected by a static object — waves stretching — or a moving object — waves stretching or squeezing depending on the relative velocity between both emitter and reflector. Next we will define the concept of Doppler-shift in the context of our work using the example of figure 4.1.

Let's consider two robots, $R1$ and $R2$, approaching each other in a straight line (relative angle $\simeq 0$) at speeds V_{R1} and V_{R2} . If f is the frequency emitted by $R1$ ¹, c the speed of sound in air (approx. 345 m/s) and ϕ the angle between the relative velocities of $R1$ and $R2$, we can define the Doppler-shifted f because of V_{R1} as

$$f_{R1} = f \left(1 + \frac{V_{R1}}{c} \cos \alpha \right)$$

with $\cos \alpha \simeq 1$ because of $\alpha \simeq 0$. Hence the frequency arriving at $R2$, because of V_{R2} , will be

$$f \left(1 + \frac{V_{R1}}{c} \right) \left(1 + \frac{V_{R2}}{c} \right) = f \left(1 + \frac{V_{R1} + V_{R2}}{c} + \frac{V_{R1} * V_{R2}}{c^2} \right) \simeq f \left(1 + \frac{V_{R1} + V_{R2}}{c} \right)$$

and therefore, the Doppler-shifted frequency of the reflected echo will be

$$f_{R2} = f \left(1 + \frac{V_{R1} + V_{R2}}{c} \right) \left(1 + \frac{V_{R2}}{c} \right) \left(1 + \frac{V_{R1}}{c} \right) \simeq f \left(1 + \frac{V_{R1} + V_{R2}}{c} \right)^2 \simeq f \left(1 + 2 \left(\frac{V_{R1} + V_{R2}}{c} \right) \right)$$

Defining the relative velocity between $R1$ and $R2$ as $v = V_{R1} - (-V_{R2}) = V_{R1} + V_{R2}$, the Doppler-shift (δf) is then defined as

$$\delta f = 2f \frac{v}{c} \cos \alpha. \quad (4.1)$$

¹We consider $R2$ not emitting, or emitting at a different frequency which will not interfere with the call emitted by $R1$ (our system allows this).

In the case of $R2$ moving in the same direction as $R1$, the relative velocity will be then $v = V_{R1} - V_{R2}$. The sign of the relative velocity will determine the sign of the Doppler-shift, *i.e.* positive Doppler if above the call frequency or negative Doppler if below.

4.3 Cochlear models

As stated by Lyon and Mead [1988], “a good cochlear model should take real sound as input, in real time, and product output that resembles the signals on the cochlear nerve”. In our case, real time is a determinant factor which will affect the cochlear design dramatically as we will see in this chapter.

As we saw in chapter 2, the bat’s auditory system is structured in the same way as that of other mammals. Incident sound is directed towards the ear canal by the pinna. After an impedance matching between the middle and inner ear, the transduction stage located in the cochlea performs a joint time-frequency analysis of the incoming signal. A simple model of this analysis is a bandpass filterbank with subsequent demodulation in each channel by a combination of full-wave rectification and lowpass filtering. This model assumes roughly between 10 and 30 hair cells in the bat per channel in the filterbank. In the FM bats the layout of the auditory filterbank follows the general mammalian pattern of keeping filter quality constant as center frequency varies. CF-FM bats deviate considerably from this pattern by forming an auditory fovea in the frequency range where the carrier frequencies of the echoes are kept by the Doppler-shift compensation behavior of these animals [Behrend et al., 1999]. Towards the center of the fovea, filter qualities rise steeply to the highest values known (maximum $Q_{10dB} \sim 400$ in *Rhinolophus ferrumequinum*). Outside this frequency band the CF-FM bats follow the general mammalian pattern.

In this work, the cochlear models investigated are conventional digital analysis filterbanks whose frequency response characteristic splits, by a set of parallel bandpass filters following a particular distribution, the incoming signal into a corresponding number of sub-bands. The transduction of the movement of the basilar membrane into neural activity, implemented biologically by the hair cells of the cochlea, is modelled fairly well by processing the outputs of these sub-bands (or channels) with a full-wave rectifier and a low-pass filter [Schroeder and Hall, 1974]. These last two steps are equivalent to a simple amplitude demodulation scheme that approximately recovers the envelope of the outputs of the bandpass filters in the filterbank. This scheme gives the experimenter complete control over the parameters, *i.e.* central frequencies and Q-factors, defining the behaviour of the filters in the filterbank.

A diagram of a generic cochlear model is shown in figure 4.2. Next we will describe the

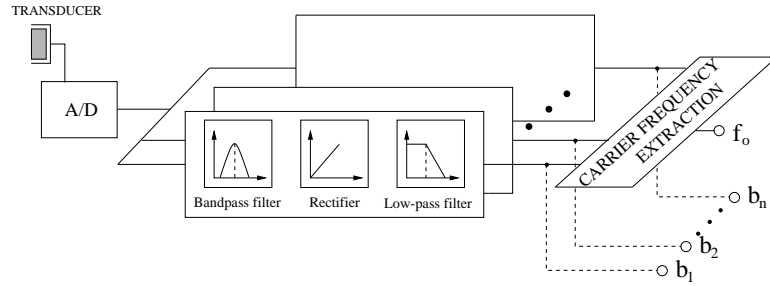


Figure 4.2: **Diagram of RoBat’s “auditory system”** consisting of the ultrasonic transducer connected to an A/D card the output of which is fed to a software model of the bat cochlea.

two filterbanks assessed in this work together with some preliminary investigation of other models.

4.3.1 Linear (Butterworth) filterbank

The linear filterbank has a uniform distribution of the center frequencies of the channels. These channels are located at center frequencies d Hz apart across the band from $f - \frac{n}{2}d$ to $f + \frac{n}{2}d$ Hz, f being the frequency of the center of the “acoustic fovea” (50kHz for our system), n the number of channels and d half of the single channel 3dB bandwidth. Thus the larger the d is, the smaller the n of the filterbank. The frequency range determined by n suffices for the range of Doppler-shifts received by RoBat. Three different configurations of 4, 7 and 16 channels, with filter-band widths for 3dB loss of 200, 100 and 40Hz respectively, were investigated.

Because of the real time performance constraint, the type of filters chosen need to be cheap computationally and provide a good response. The bandpass and low-pass filters are 2nd and 1st order Butterworth respectively. The reasons for using this type of filter are a flat pass band — needed for estimating Doppler-shift — and a moderate group delay²[Proakis and Manolakis, 1996]. Figure 4.3 shows the filter response and the distribution of the center frequencies for a linear filterbank with 16 channel for filter-band widths for 3dB loss of 40Hz.

4.3.2 Gammatone filterbank

This filterbank has a gammatone (*i.e.* non-uniform) distribution of the center frequencies of the channels as seen in the right plot of figure 4.4. It can be designed to facilitate the extraction of particular features of the echoes as testified by the presence of the fovea in CF-FM bats which greatly enhances those bats’ capability to accurately estimate Doppler-shifts around the central frequency of the fovea [Peremans et al., 2000]. The filterbank consists of a user-specified set

²The group delay of a filter at a particular frequency is the time that such frequency component of the signal is delayed by filtering.

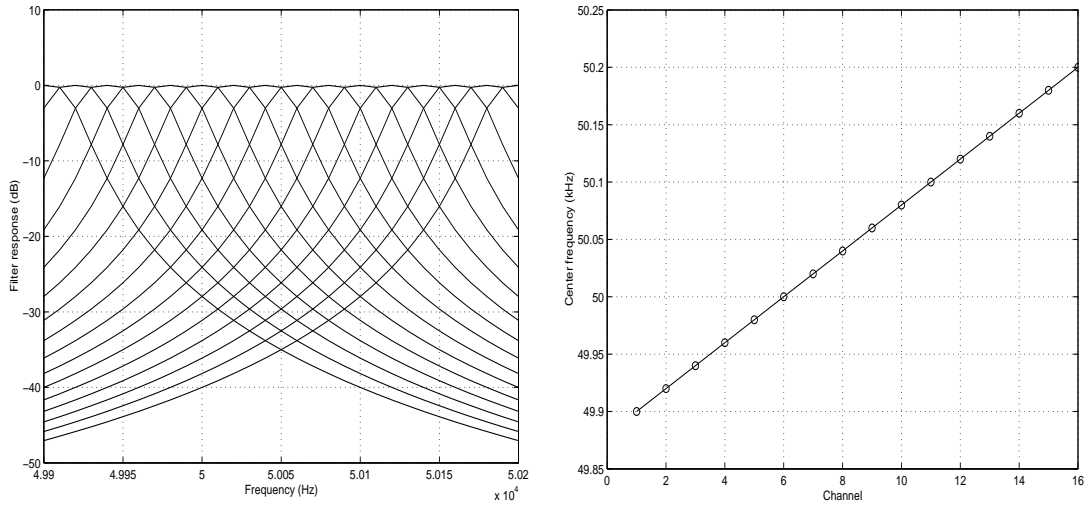


Figure 4.3: **Linear filterbank**: configuration with 16 channels for filter band-widths for $3dB$ loss of $40Hz$ (left); linear distribution of the center frequencies of the 16 channels (right).

of gammatone filters, 9 and 29 being the size of the two different configurations investigated in this work (see section 4.5).

For modelling the narrowband fovea of the cochlea of the CF-FM bats we have concentrated the central frequencies of the bandpass filters symmetrically around the call frequency of 50 kHz. In order to provide a simple, tractable model rather than a detailed copy of the biological system, the relationship between the quality factor Q of the bandpass filter and its central frequency f is chosen to be

$$Q = \frac{Q_{max}}{\frac{|f - f_{fovea}|}{W_{fovea}} + 1}, \quad (4.2)$$

with f_{fovea} and W_{fovea} denoting respectively the central frequency of the fovea and its width (see section A.1 of appendix A for more details).

Filters are also spaced for equal overlap between neighbouring filters which results in a wider spacing of filters as bandwidth increases, thereby mirroring the over-representation property of the biological fovea [Slaney, 1993]. Figure 4.4 shows the quality factor as a function of the central frequency in the fovea (left) and the distribution of these center frequencies (right) for a 29 channel configuration.

4.3.3 Other models

For the purpose of exploring alternative faster methods of cochlear processing, an undergraduate project was proposed and supervised simultaneously with this work. The results [McCormick, 2000] are summarised below.

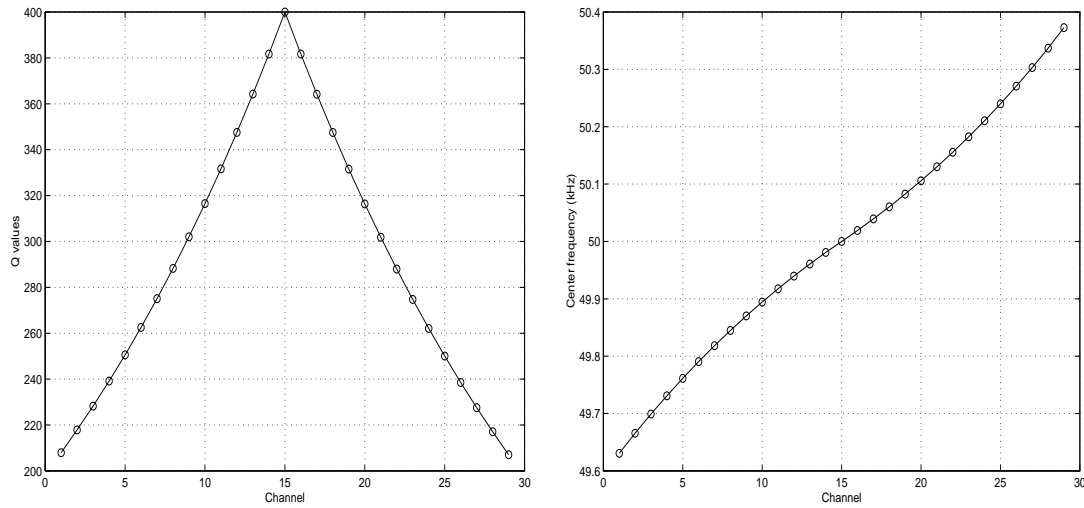


Figure 4.4: **Gammatone filterbank**: Quality factor as a function of the central frequency in a 29 channel gammatone filterbank (left); non-linear gammatone distribution of the center frequencies along the 29 channels (right).

Bessel filterbank

The first alternative method replaced each of the bandpass filters of a generic linear filterbank with two low-pass filters as in [Cavaco and Hallam, 1999]. The difference between two low-pass filtered signals was used in place of the output of a bandpass filter. It was hoped that this would reduce the computational cost: low-pass filters are about half as expensive to compute as bandpass filters and, to gain the equivalent of N bands, only $N+1$ low-pass filters are needed.

Bessel filters were used due to their group delay properties. In Butterworth filters, the group delay changes dramatically over the frequency range whereas in Bessel filters, the group-delay is fairly flat as seen in figure 4.5 (left). However, while the group-delay is fairly constant for a single filter, that constant is dependent on the cut-off frequency. This resulted in the output from one filter being delayed slightly longer than that from the other. To correct this problem, both signals were delayed after filtering trying to give them both the same net delay at the point where they were subtracted. This is illustrated in figure 4.6.

It was found that, with large differences in filter cut-off frequency such as those used in [Cavaco and Hallam, 1999], the variation in the group-delays had no significant effect and could be eliminated as in figure 4.6. However, with smaller differences such as those used in our work, serious problems remain. As can be seen in figure 4.5 (right), the group-delays do not have a constant difference and in fact the 60kHz curve crosses the 50kHz, so a constant post-filtering delay only moves the problem a little and does not solve it. Hence the Bessel approach was rejected.

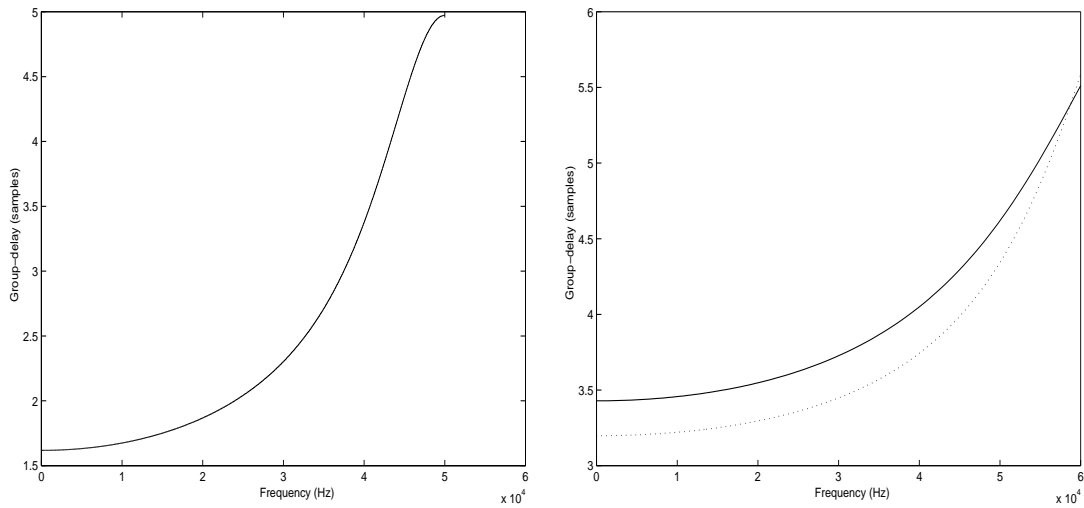


Figure 4.5: **Group delays.** Left plot: Group-delay of Butterworth (solid) vs. Bessel (dotted) low-pass filters with cut-off frequency 50kHz. Right plot: Group-delays of two Bessel low-pass filters with 50 kHz (solid) and 60 kHz (dotted) cut-off frequencies (adapted from [McCormick, 2000]).

Cascade filterbank

An alternative to the parallel filterbank model is the model devised by Lyon and Mead [1988]. This configuration consists of N low-pass filters in series, the output of the first filter being fed to the next filter and so on. After every N filters a “tap” allows the output so far to be measured. This corresponds more directly to the physical organisation of the cochlea and the basilar membrane: the cascade of filters equates to the membrane while each tap corresponds to a hair cell on the membrane. Figure 4.7 outlines the operation of this model.

Lyon and Mead [1988] used analogue electronics to make the filter cascade. Watts et al. [1992] and van Schaik et al. [1995] improved the model while remaining within the domains of

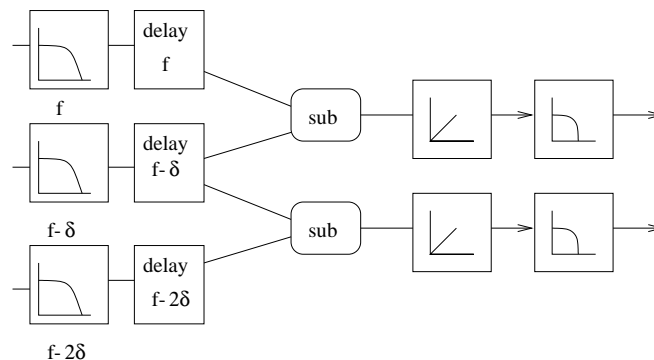


Figure 4.6: **Bessel filterbank** in which a delay is being applied to each filter output before subtraction (adapted from [McCormick, 2000]).

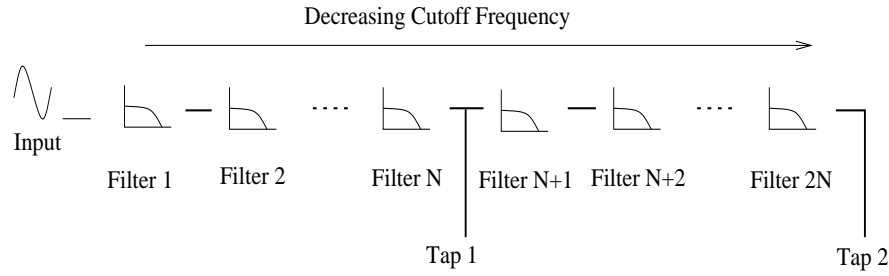


Figure 4.7: **Cascade filterbank** with 2 taps and N filters per tap (adapted from McCormick [2000]).

solid-state circuits and analogue filters. The implementation here attempted to create the same model of the cochlea but in a digital framework using software filters.

Implementing the actual filters used by Lyon and Mead [1988] in the digital domain caused problems. However, it proved possible to replace them with digital low-pass Butterworth filters while allowed the main features of this cochlear model to be preserved, namely the cascaded nature of the filterbank, with the output of one tap being affected by the outputs of the previous taps.

The operation of the filterbank was analysed calculating the transfer function of the whole cascade together with the frequency response for each tap. The results reported in [McCormick, 2000] showed that while the cascade can accurately identify pure tone signals, its performance is much reduced by real (noisy) signals. Thus, for an application which does not require much accuracy, the cascade is a computationally cheap model. However, when a highly tuned fovea is required — as in our case — the reduction in performance for real signals is too great.

4.4 Doppler-shift estimation methods

For Doppler-shift estimation, we need a higher frequency resolution than that provided by a single channel of a normal n channel filterbank. This is analogous to the sub-pixel resolution problem in machine vision [Marr, 1982]. Two different methods for increasing resolution by extracting the carrier frequency from the output of the filterbank models: an artificial neural network (ANN) and a weighted average (WA); are described next. It is important to clarify that in both methods we are assuming Doppler-shifted echoes comprising a single dominant frequency component.

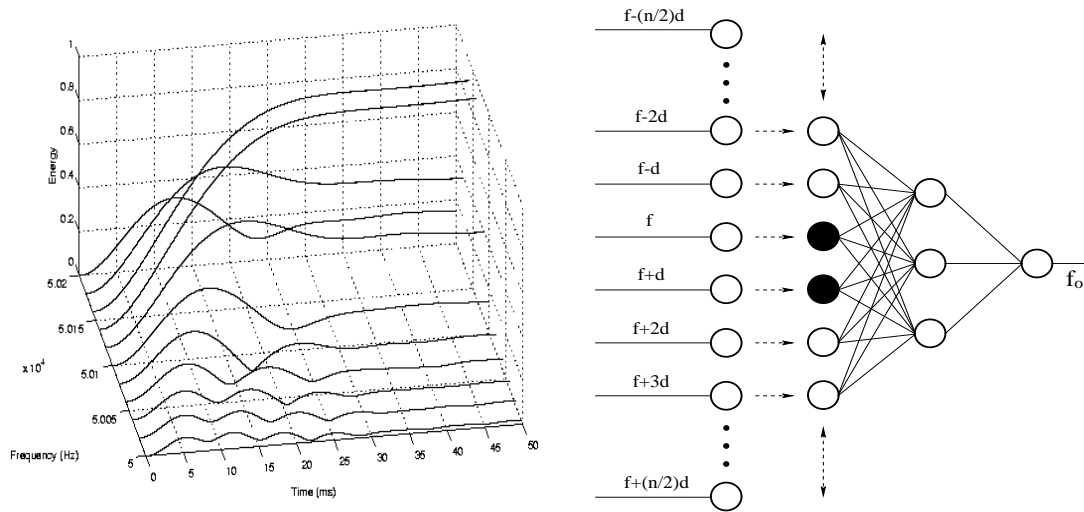


Figure 4.8: **Linear filterbank output** for a 150 Hz shifted echo (left). **Sliding ANN** for frequency estimation (right).

4.4.1 Artificial Neural Network

To perform frequency discrimination using the filterbank outputs we need to interpolate the frequency of the echo. An ANN which will determine the value of the principal harmonic of the echo is therefore applied to the output of the filterbank as shown in the example of figure 4.8. The left plot shows a 150 Hz Doppler-shifted echo (made using a 50150 Hz noisy sinusoid) coming out from a linear filterbank (only selected channels plotted) before being fed to the ANN. Then (right plot), the ANN performs as a sliding window containing channels centered on the two channels of the filterbank that bracket the frequency of the echo (50140 and 50160 Hz in this case) and therefore have the highest energy. The energy of these 2 channels (at centre frequencies f and $f + d$ in the right plot) feed the 2 black-filled input units of the ANN. The interpolated frequency f_o will be somewhere between the centres of these 2 channels.

Two different topologies of backpropagation ANNs, chosen after pilot experiments looking for the minimum number of input and hidden units³ needed, were tested: 6–3–1 for the linear filterbank and 9–4–1 for the gammatone filterbank. In the latter case, there was no “sliding” behaviour since the number of inputs of the ANN matched the number of channels of the gammatone filterbank and the intrinsic symmetries of the linear filterbank, which permit sliding, do not obtain for the gammatone. No ANN was used with the 29 channel gammatone filterbank because of being too computationally expensive and therefore too slow for real time applications.

³After several attempts it was found impossible for the ANN to learn the whole set of data without a hidden layer.

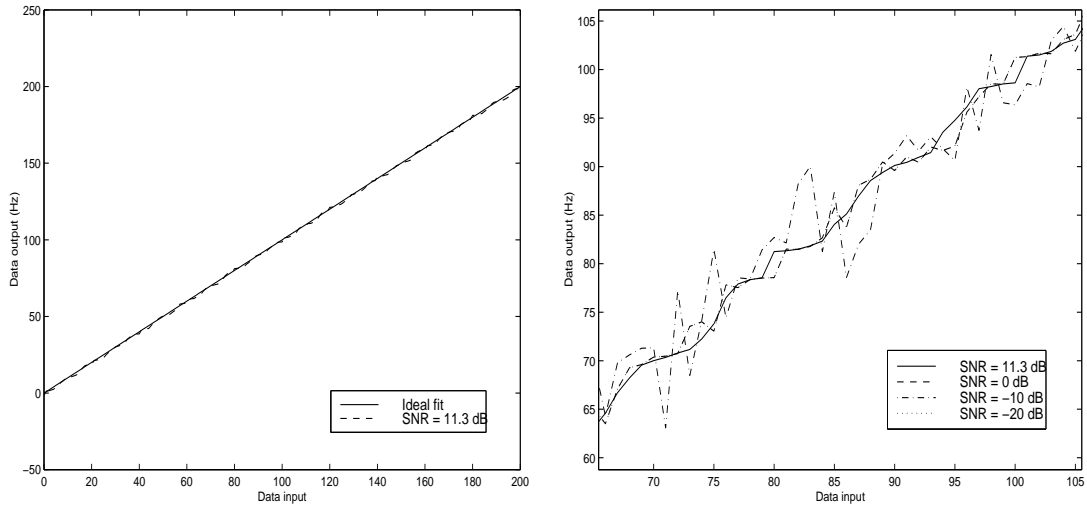


Figure 4.9: ANN fit along the acoustic fovea for different noise levels. Whole acoustic fovea (left), magnification of part of the fovea (right).

The ANNs were trained using simulated noisy signals, a learning rate of 0.1 or smaller and no momentum (see Appendix B for a complete parameter list). The signals were made of a sinusoid of given frequency – the frequency to be estimated – added to uniformly distributed random noise. Figure 4.9 (left) shows a comparison of the ANN’s performance along the acoustic fovea with an ideal fit for simulated noisy data (SNR=11.3dB). As can be seen, the ANN’s output fits the line quite satisfactorily, with an estimated error of ± 2 Hz. In figure 4.9 (right), a comparison among different levels of noise is shown. As can be seen there, the ANN is quite robust to high levels of noise (SNR=-10dB).

4.4.2 Weighted average

The other method used was a weighted average (WA) of the filterbank’s output, with each channel’s center frequency receiving a weight proportional to that channel’s output level.

Thus in this method Doppler-shifts are calculated as follows:

$$f_d = \frac{\sum_{i=1}^n (a_i * f_i)}{\sum_{i=1}^n a_i}, \quad (4.3)$$

where a_i is the output of the filterbank’s i^{th} channel, f_i the carrier frequency for that channel and n the number of channels of the filterbank.

Apart from its simplicity, this method has the *a priori* advantage — compared with the ANN — of not requiring any training at all and being independent of the number of channels in the filterbank. This method was suggested by Müller who previously used it for Doppler-shift estimation in Müller [1998].

4.5 Comparison of Doppler-shift estimation methods

4.5.1 Design of the experiments

Four different kinds of experiment were designed for each of the methods under test. The first three experiments consisted in moving RoBat orthogonally towards a smooth wall as in figure 4.10 (left) under the following conditions:

- **Constant velocity** — since the Doppler-shift depends on the cosine of the bearing angle, it is comparatively insensitive to small fluctuations in bearing around zero. Therefore, Doppler-shift in this scenario should be fairly constant once the desired speed has been reached.
- **Acceleration** — the Doppler-shift should increase as the velocity of the robot increases.
- **Deceleration** — opposite behaviour, *i.e.* the Doppler-shift should decrease along with the robot's velocity.

In the fourth experiment, RoBat was moving at constant velocity through an uncluttered environment containing a 5 cm diameter post positioned to one side of its path, as in figure 4.10 (right). As the mobile base moves, a tracking behaviour makes the sonarhead point always at the post hence guaranteeing its insonification. When the robot is far from the post, a maximal Doppler-shift is obtained since the bearing angle between the robot and the post is close to 0° (α_1 in the figure). However, as the robot nears the post, this Doppler-shift starts decreasing.

Each of the experiments was run 10 times. Different configurations were tested during the above experiments for the gammatone filterbank and the ANN. For the linear filterbank a fixed configuration was used. All these configurations are summarised in table 4.1. Configuration 2 was the same as configuration 1 but with the ANN trained in increments of 0.5 Hz instead of 1 Hz as in the rest of the configurations. In total, 40 experiments were performed in 400 trials.

The experimental conditions, such as the starting position of the robot and the position of the wall and post, were kept constant among trials. This resulted in a very good repeatability, as proven by the very low error bars of the robot's velocity when averaging all the data points among the 10 trials of a single experiment. Figures 4.11, 4.12, 4.13 and 4.14 show a single trial of each of the four different cases from the whole set of experiments which will be discussed in section 4.5.3. For each plot, the Doppler-shift estimated by the method under test *vs.* the true Doppler-shift is plotted.

As in equation 4.1, true Doppler-shifts (f_{t-d}) are calculated by the following equation:

$$f_{t-d} = 2f_s \frac{v}{c} \cos \alpha$$

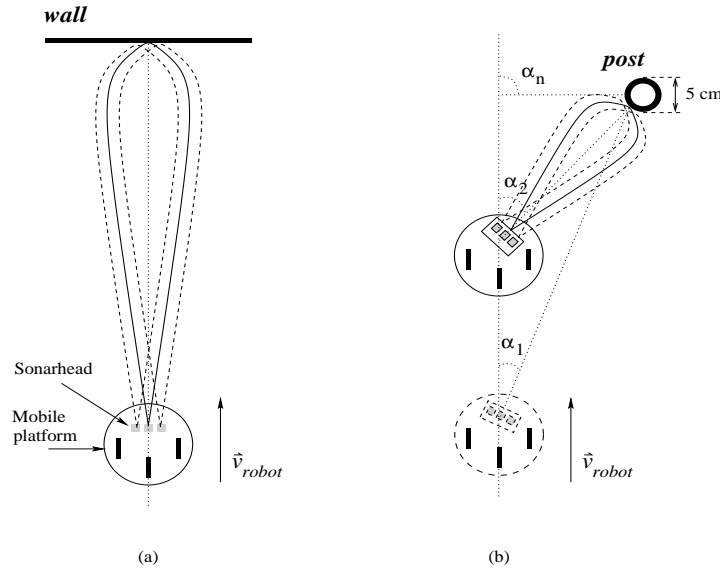


Figure 4.10: **The measurement setup:** (a) RoBat driving straight up to the wall; (b) RoBat driving by a post.

Config.	Description
1	40 Hz, linear, ANN
2	same as (1) but 0.5 Hz inc.
3	100 Hz, linear, ANN
4	200 Hz, linear, ANN
5	40 Hz, linear, WA
6	100 Hz, linear, WA
7	200 Hz, linear, WA
8	9 channels, γ -tone, ANN
9	9 channels, γ -tone, WA
10	29 channels, γ -tone, WA

Table 4.1: **Experimental configurations** testing linear and gammatone filterbanks with ANN and weighted average (WA) estimation methods.

where f_s the source frequency (50 kHz), v the relative velocity between the robot (estimated from the readings of the wheel encoders) and the reflector, c the speed of sound in air (approximately 345 m/s) and α the relative bearing angle. In the experiments with the wall $\alpha \simeq 0$ whereas with the post α is estimated by trigonometry given that the positions of both the post and the robot are known (the latter through the TOF of each echo) and knowledge of the robot path for each of the data points of a single trial.

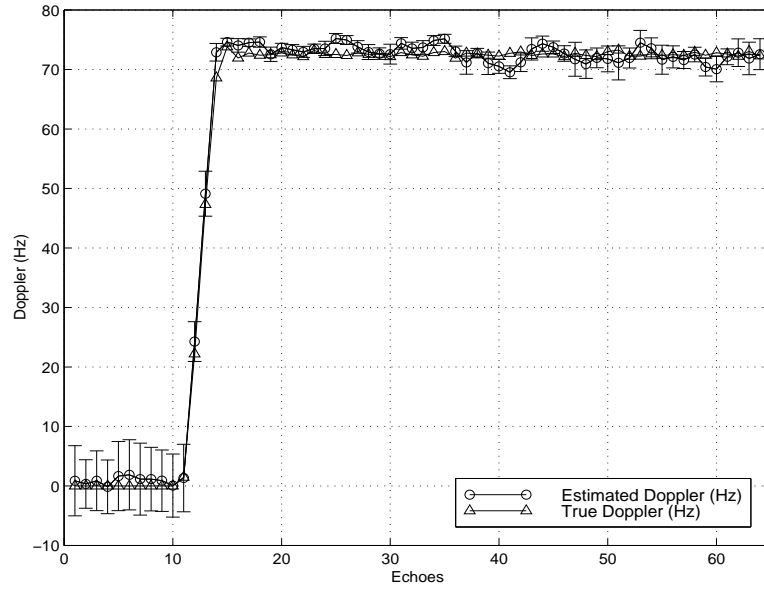


Figure 4.11: **Doppler-shift estimation while RoBat moves at constant velocity orthogonal to a wall** (configuration 1).

4.5.2 Analysis of the results

For assessing performance in each experiment, the following four measures were calculated:

1. Accuracy — mean difference between the Doppler value calculated by the method being tested and the value calculated from the measured robot speed (Hz).
2. Standard deviation of the accuracy differences (Hz).
3. RMS standard deviation of the Doppler calculated by the method under test (Hz).
4. Ratio of the standard deviations calculated above, 2 divided by 3, expressed as a relative percentage. This measure indicates the extent to which the method amplifies or reduces the measurement noise (%).

To see the utility of this last measure, consider a situation where the true Doppler is constant. In that case, the variation in the difference measure 1 is due solely to the measurement variation in the Doppler values produced by the method being tested, and the relative standard deviation measure will be 0. In the real experiment, the true Doppler varies somewhat in response to robot velocity errors caused by bumps in the floor (for example). If the method is good, the computed Doppler and the true Doppler should co-vary, and the variance of the accuracy differences may thus be less than the variance of the computed Doppler itself; measure

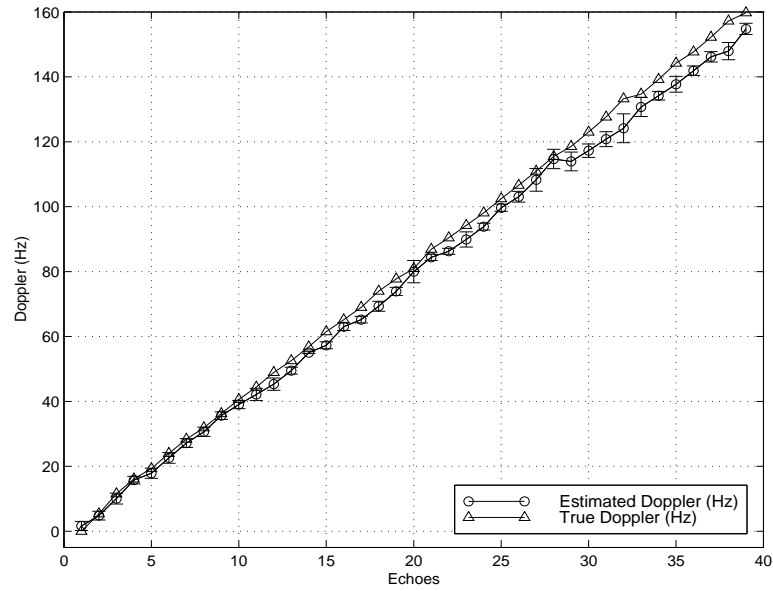


Figure 4.12: **Doppler-shift estimation while RoBat accelerates orthogonal to a wall** (configuration 6).

4 will then be negative. On the other hand, if the method being tested de-correlates the variations or suffers from a substantial and varying fit error between computed and true Doppler, the accuracy difference variation will be bigger than that in the computed Doppler alone and the relative variation measure, 4, will be positive.

Tables 4.2, 4.3, 4.4 and 4.5 show the values of the four measures in the order given as above for each of the experiments. The numbers in parentheses in the first column of the table are the experimental configurations from table 4.1. Measures 1 and 4 for all the experiments are plotted in figures 4.15 and 4.16.

4.5.3 Discussion

From the analysis of the results some interesting things can be seen. In figure 4.15 the ANN has consistently good noise performance on both filterbanks with worst case in configuration 4 (linear filterbank) reaching roughly double the noise level in the Doppler accuracy data. The weighted average method performed worse than the ANN, configuration 7 being the worst case because of the small number of channels (4). Figure 4.16 shows fairly good accuracy in all cases except for configurations 2, 7, 9 and 10.

It was interesting to find overall good performance in most of the cases of the post as a reflector, despite being a much weaker reflector compared to a wall. This can be seen in, for example, figure 4.14, in which the performance is quite good despite some small fitting errors

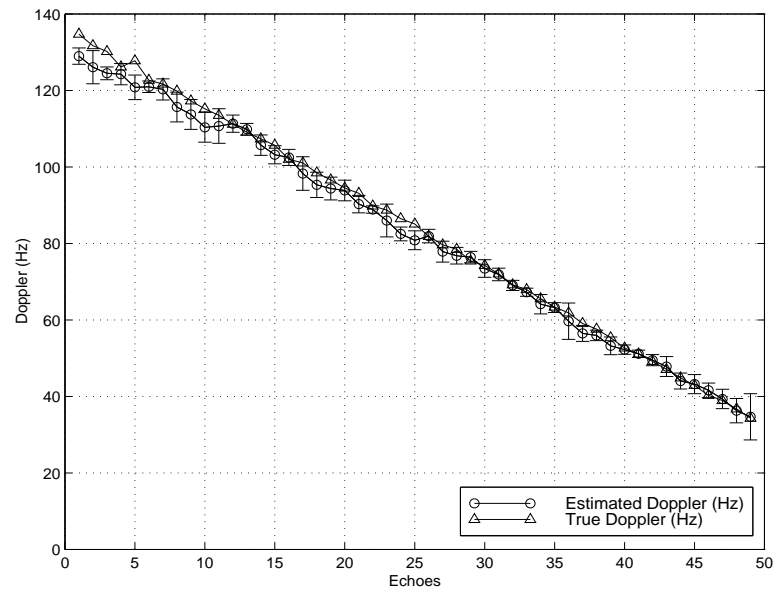


Figure 4.13: **Doppler-shift estimation while RoBat decelerates orthogonal to a wall** (configuration 6).

	WALL			POST
Config.	Const. vel.	Acceleration	Deceleration	Const. vel.
(1)	-0.44 Hz	1.36 Hz	-1.19 Hz	3.36 Hz
	1.43 Hz	2.57 Hz	2.47 Hz	4.69 Hz
	2.70 Hz	4.91 Hz	3.66 Hz	9.07 Hz
	-47.08 %	-47.55 %	-32.52 %	-48.31 %
(2)	1.93 Hz	4.37 Hz	1.86 Hz	4.73 Hz
	2.58 Hz	3.02 Hz	3.41 Hz	3.53 Hz
	2.92 Hz	3.31 Hz	3.17 Hz	6.19 Hz
	-11.65 %	-8.91 %	7.18 %	-42.87 %
(3)	3.45 Hz	2.74 Hz	0.03 Hz	1.36 Hz
	1.64 Hz	2.55 Hz	2.27 Hz	2.11 Hz
	1.59 Hz	2.35 Hz	3.69 Hz	2.23 Hz
	3.28 %	8.87 %	-38.54 %	-5.69 %
(4)	-0.23 Hz	2.88 Hz	1.47 Hz	0.66 Hz
	3.53 Hz	4.92 Hz	3.95 Hz	2.33 Hz
	2.26 Hz	2.63 Hz	4.12 Hz	2.78 Hz
	56.85 %	86.92 %	-4.22 %	-16.17 %

Table 4.2: Experiments with **linear filterbank** and **ANN**. The first column indicates the experimental configuration under test (see table 4.1). The four measures inside each cell are (top to bottom): accuracy; standard deviation of the accuracy differences; RMS standard deviation; relative variance ratio (see text).

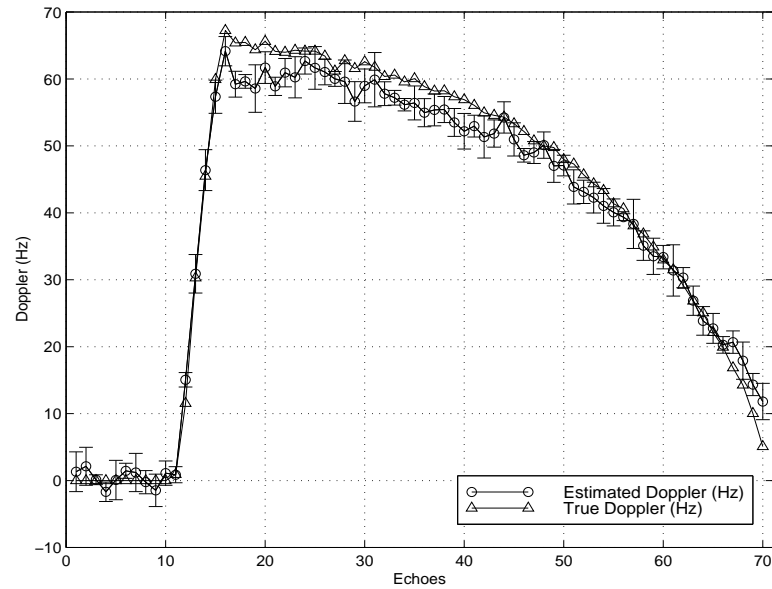


Figure 4.14: **Doppler-shift estimation while RoBat drives by a post at constant velocity** (configuration 9).

	WALL			POST
Config.	Const. vel.	Acceleration	Deceleration	Const. vel.
(5)	1.92 Hz	3.64 Hz	3.18 Hz	3.19 Hz
	2.24 Hz	2.95 Hz	3.74 Hz	3.29 Hz
	1.65 Hz	2.01 Hz	2.37 Hz	4.53 Hz
	35.53 %	46.55 %	58.19 %	-27.42 %
(6)	1.41 Hz	3.37 Hz	1.69 Hz	3.06 Hz
	1.54 Hz	2.37 Hz	1.99 Hz	2.82 Hz
	1.64 Hz	1.96 Hz	2.76 Hz	3.88 Hz
	-5.62 %	20.98 %	-28.14 %	-27.12 %
(7)	2.86 Hz	3.99 Hz	5.76 Hz	0.16 Hz
	3.89 Hz	4.37 Hz	4.04 Hz	4.47 Hz
	1.45 Hz	1.99 Hz	2.28 Hz	2.70 Hz
	168.19 %	119.17 %	77.31 %	65.26 %

Table 4.3: **Experiments with linear filterbank and weighted average.** The first column indicates the experimental configuration under test (see table 4.1). The four measures inside each cell are (top to bottom): accuracy; standard deviation of the accuracy differences; RMS standard deviation; relative variance ratio (see text).

at the beginning of the Doppler-shift curve and close to the end (almost at 90° relative position). The former are due to the long distance (*i.e.* lower SNR) from the post during that period whereas the latter are due to the fact that, at that point, the robot is about to pass by the post having reached the maximum turning angle of the sonarhead's pan servomotor. Overall, the

	WALL			POST
Config.	Const. vel.	Acceleration	Deceleration	Const. vel.
(8)	0.46 Hz	2.81 Hz	-0.99 Hz	0.79 Hz
	2.28 Hz	3.71 Hz	3.34 Hz	2.63 Hz
	2.47 Hz	3.03 Hz	3.26 Hz	4.12 Hz
	-7.77 %	22.34 %	2.66 %	-36.11 %

Table 4.4: Experiments with **gammatone filterbank** and **ANN**. The first column indicates the experimental configuration under test (see table 4.1). The four measures inside each cell are (top to bottom): accuracy; standard deviation of the accuracy differences; RMS standard deviation; relative variance ratio (see text).

	WALL			POST
Config.	Const. vel.	Acceleration	Deceleration	Const. vel.
(9)	3.37 Hz	5.54 Hz	4.59 Hz	1.42 Hz
	1.89 Hz	3.51 Hz	2.54 Hz	2.54 Hz
	1.85 Hz	1.89 Hz	2.46 Hz	2.30 Hz
	2.53 %	86.02 %	3.19 %	10.58 %
(10)	4.49 Hz	6.22 Hz	7.51 Hz	0.83 Hz
	2.02 Hz	3.17 Hz	4.17 Hz	5.33 Hz
	1.59 Hz	2.13 Hz	2.32 Hz	2.72 Hz
	26.46 %	49.28 %	79.72 %	96.25 %

Table 4.5: Experiments with **gammatone filterbank** and **weighted average**. The first column indicates the experimental configuration under test (see table 4.1). The four measures inside each cell are (top to bottom): accuracy; standard deviation of the accuracy differences; RMS standard deviation; relative variance ratio (see text).

performance of the linear filterbank is more consistent than the gammatone. Similarly, the ANN gave consistently better noise performance than the weighted average.

It is important to mention that, during the pilot experiments, we found a strange behaviour in the Doppler-shift estimate when gammatone filterbanks and specular reflectors (such as walls) were used. This behaviour resulted in substantial varying fit errors — Doppler-shifts decreasing dramatically instead of keeping constant — as the robot got closer to the wall (see figure 4.17). The fact that moving the robot orthogonally towards a post did not result in this behaviour suggested a dynamic range problem. Since the electronics of the sonarhead do not include a time-varying gain (as the commercial Polaroid sensor does), we need to adjust the output amplitude of the D/A card to maximise dynamic range without saturating the input channels of the A/D card. This saturation occurs when the combination of sound pressure and D/A card output voltage is higher than the voltage range of the A/D card. When an echo saturates, the portions of it that are above the input range of the A/D card are clipped resulting in a square

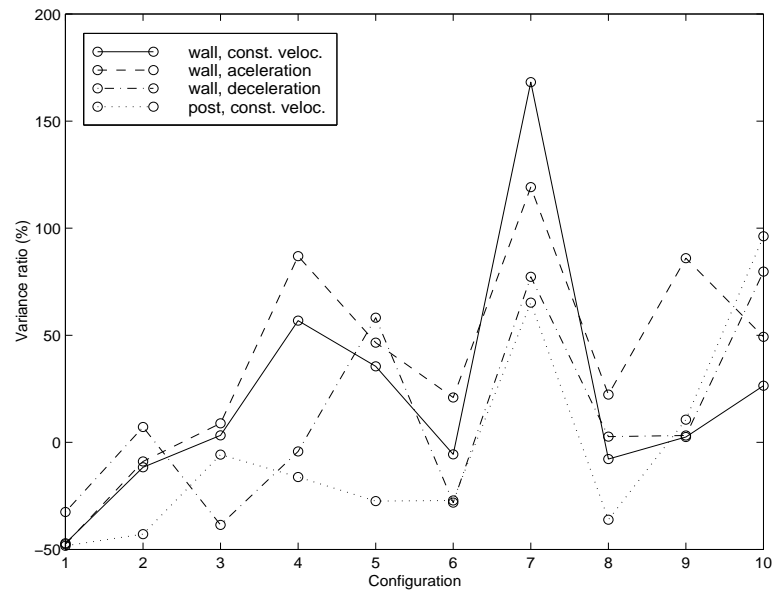


Figure 4.15: **Relative variance ratio measure** for each experimental configuration (see table 4.1).

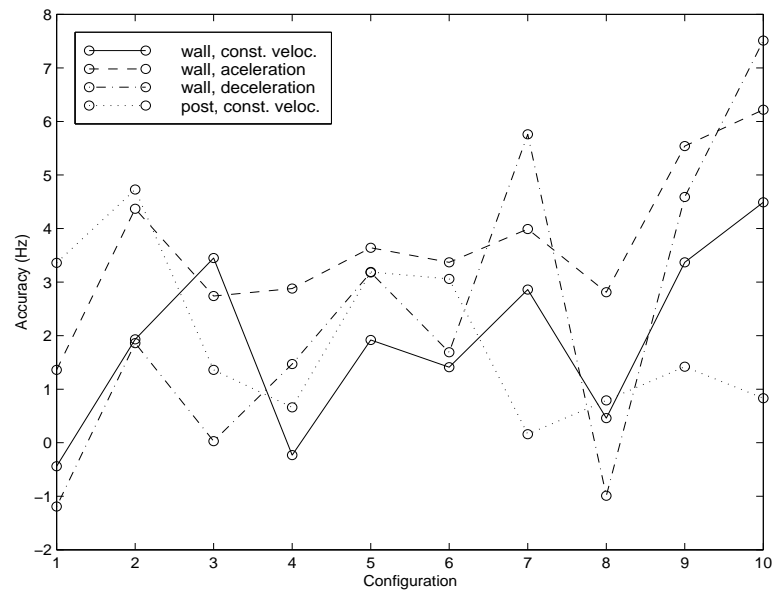


Figure 4.16: **Accuracy estimation** for each experimental configuration (see table 4.1).

wave-like pulse. This can be seen in the left plot of figure 4.18, in which the envelope of a weak (normal) echo has the amplitude modulation characteristic of a Doppler-shifted echo whereas the saturated (dodgy) echo looks like a pure simulated signal because of the A/D clipping (grey echo in the figure). The square wave-like behaviour as a result of this clipping appears in the spectrum as a significant aliased 3rd harmonic of the echo, the 49.8 kHz peak of figure 4.18

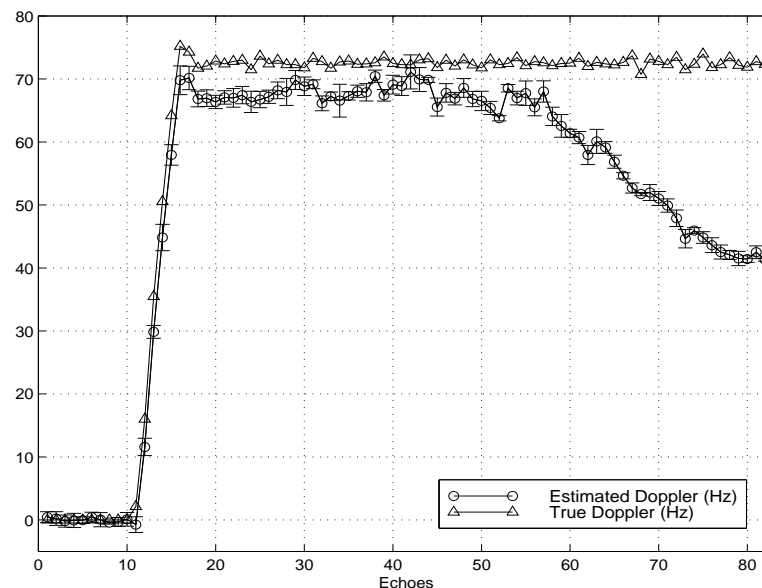


Figure 4.17: **Varying fit errors found in γ -tone filterbanks** when RoBat was driving towards a wall (configuration 10).

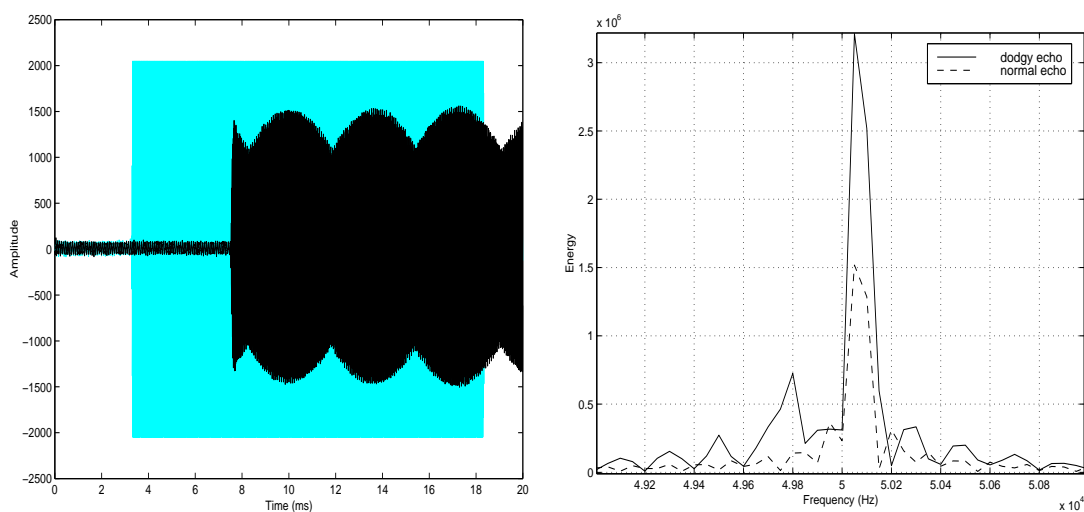


Figure 4.18: **‘Dodgy’ performance.** Left plot: amplitude comparison between dodgy (grey) and normal (black) echos. Right plot: frequency spectra of both echos.

(right).

The reason why this affects gammatone filterbanks only is because of the length of the acoustic fovea, which is larger than in the linear filterbank. Thus the energy of the echo’s 3rd harmonic — which is aliased below the carrier frequency but still within the fovea— is being combined with the echo’s fundamental and therefore pulling down the computed Doppler estimate. To eliminate this behaviour in the experiments performed in this chapter, two different

D/A output values — 5V and 1V — were chosen for the post and the wall respectively.

However, since it is more practical to use a fixed configuration (RoBat is not supposed to know a priori which type of feature it will encounter), a linear filterbank was used for the rest of the experiments reported in this dissertation. Possible long-term solutions to this dynamic range problem are: implementing a time-varying gain as in the Polaroid sensor, dropping the noise floor by improving the sonarhead electronics, or including some form of automatic gain control.

4.6 Echoes from multiple reflectors

So far we have successfully achieved a system capable of estimating Doppler-shifts in the echoes received by RoBat. However, these echoes, despite coming from real reflectors within a real environment, are made of a single dominant Doppler-shifted frequency hence implying a single significantly reflecting target moving at some relative velocity⁴ with respect to the robot.

Thus, the next step is to assess our system in a more realistic environment with more than one dominant frequency in the echoes. This is a much more severe test which might cause the model fail. But, how could this happen? This is addressed in the following section.

4.6.1 The problem of the cross-modulation term

According to Martin [1995], there are several approaches for extracting the envelope of a band-pass signal such as the Hilbert transform method, rectification-and-smoothing and squaring-and-smoothing. The cochlear models used in our system perform rectification-and-smoothing because of the biological properties described in section 4.3.

By definition rectification is a non-linear process and, as a result, cross-modulation terms will be introduced when more than one signal is simultaneously fed into the filterbank. These terms will make the system not satisfy the superposition principle [Proakis and Manolakis, 1996], which would require the response of the filterbank to a weighted sum of signals to be equal to the corresponding weighted sum of the outputs of the filterbank to each of the individual input signals.

Let us illustrate this with an example. Given a periodic signal Y with amplitude A and frequency ω , and assuming the signal has been bandpass filtered through one of the filterbank's channels, the expression obtained after full-wave (by squaring) rectification (Y_r) will be:

$$Y_r = (A \cos \omega t)^2 = A^2 \cos^2 \omega t = \frac{1}{2} A^2 (1 + \cos 2\omega t) = \frac{A^2}{2} + \frac{A^2}{2} \cos 2\omega t$$

⁴Obviously, this also applies to the case of a static target and a moving robot, or both moving simultaneously.

Next, applying the low-pass filter (Y_{lp}) with a cut-off frequency $f_c \ll \omega$, the following output is obtained:

$$Y_{lp} = \frac{A^2}{2}$$

Considering now two signals with different amplitude (A, B) and frequency (ω_1, ω_2), and the signal Y the sum of A and B , the rectification after the bandpass filtering will be:

$$\begin{aligned} Y_r &= (A \cos \omega_1 t + B \cos \omega_2 t)^2 = A^2 \cos^2 \omega_1 t + B^2 \cos^2 \omega_2 t + 2AB \cos \omega_1 t \cos \omega_2 t \\ &= \frac{1}{2}(A^2 + B^2) + \frac{1}{2}A^2 \cos 2\omega_1 t + \frac{1}{2}B^2 \cos 2\omega_2 t + AB \cos(\omega_1 + \omega_2)t + AB \cos(\omega_1 - \omega_2)t \end{aligned}$$

Finally, after low-pass filtering, the obtained signal will be

$$Y_{lp} = \frac{1}{2}(A^2 + B^2) + AB \cos(\omega_1 - \omega_2)t$$

which, as expected, contains a cross-modulation term not eliminated by the low-pass filtering if $\omega_1 - \omega_2 \ll \omega_1 \omega_2$.

Considering the possibility of getting rid of this term, a non-biologically plausible way of doing it could be by low-pass filtering with a very small cut-off frequency (*e.g.* 1 Hz or 0.1 Hz). The problem then, however, would then be the huge group delay of such a low-pass filter, which would need at least 500000 samples ($fs = 1MHz$) worth of echo⁵ to being useful. This would not be practical because of the huge size of the time window needed for both the call — which will affect the number of pulses sent per second — and the echo processing along the filterbank channels.

4.6.2 Sensing the world through single dominant frequency echoes

Having seen the cross-modulation problem introduced by other signals in the echo, the following questions arise: How likely is this situation to happen in our system? If common, how will this affect Doppler-shift estimation? In order to try to answer these questions, a set of rules of thumb about the coupling between our system (RoBat) and the world sensed will be presented next.

1. Doppler depends on call frequency, speed of sound, relative velocity and bearing angle.

The last two play an important role since

⁵This is a rough estimation after pilot experiments with simulated data.

- at small bearing angles (*e.g.* $\pm 15^\circ$), because of the cosine dependency of Doppler, and the relatively low velocity of the robot, the frequency separation between different reflectors decreases dramatically. In other words, the other frequency components (if any), will be almost overlapping with the control frequency.
 - at larger bearing angles the frequency separation increases but the importance of the target decreases since the robot is about to pass it already.
2. Long echos are needed for Doppler-shift estimation, therefore the time domain scenario in which non-overlapping echoes from different reflectors can be detected is not valid.
 3. If the control reflector is situated in the middle of the robot's path (*i.e.* maximum Doppler-shift), any other static reflector nearby the control will reflect an echo with a lower Doppler-shift.

Hence, the natural question here is whether it possible to sense the world in terms of a single main frequency component at a time or not. The relatively narrow main lobe given by the radiation pattern of the Polaroid transducer — approximately 25° at -20 dB (see figure 2.5) compared to the 100° of *R. ferrumequinum* [Schnitzler and Grinell, 1977] — does not leave much *room* for other reflectors to be fitted within the lobe. This results in either a single reflector or a small number of reflectors so close together that can be ‘seen’ as a single larger reflector.

This 25° beam width has been a common problem with the Polaroid sensor when determining the true range of an object, as discussed in the literature reviewed in chapter 2. However, with respect to Doppler-shifts, rather than being too big, the 25° lobe is too small for discriminating other frequencies in a single echo. Even more, this is worsened by the small velocity of robots in indoor environments (approx. 0.5 ms^{-1} or even lower) compared to real bats which can fly up to 5 ms^{-1} .

In addition, the echo generated by any reflector situated at a bigger range than the control reflector (*i.e.* behind) will be weaker than this one because of atmospheric attenuation. Some of the facts addressed above can be seen in figure 4.19 in which the evolution of Doppler-shift in 300 ms simulated echoes containing two signals — control and interference — is shown. The frequency of the interference signal is separated 5 Hz (left plot) and 25 Hz (right plot) from the 50145 Hz of the control signal. The control frequency is the maximum expected Doppler-shift when RoBat moves at 0.5 ms^{-1} towards a reflector at bearing angle $\alpha = 0^\circ$. The amplitude A of the interference signal is increased from 0.25 to 1 to see the effect in the compound signal. For all the curves, the compound signal is fed through a 16 channel linear filterbank and Doppler-shifts are estimated at every echo sample ($f_s = 1\text{ MHz}$), *i.e.* 300000 estimations per echo.

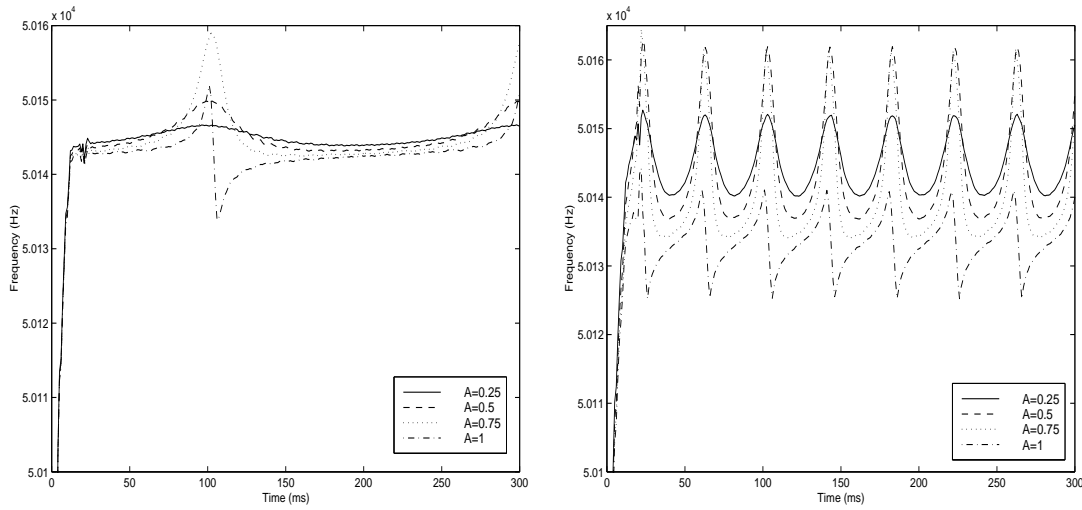


Figure 4.19: **Evolution of estimated Doppler-shift along 300 ms echoes** with 2 signals separated by 5 Hz (left) and 25 Hz (right) for different amplitudes.

As seen in figure 4.19, the effect of the interference signal is a modulation in the Doppler curve which increases in peak-to-peak amplitude as A increases. This modulation shows a periodic behaviour with frequency equal to the separation frequency between the two signals, *i.e.* 5 Hz in the left plot and a 25 Hz in the right plot. Also, the mean value of the Doppler curve decreases from the control frequency because of the interference signal, this effect being much more significant in the right plot because of the bigger frequency separation. The question now is: How much is the mean Doppler-shift value affected by the interference signal?

During the experiments described in this chapter, Doppler-shifts were estimated as the mean of several estimations along an echo. Hence, this final estimation should be the one to consider, *i.e.* to investigate how much the Doppler-shift value estimated from the mean of the 300000 estimations along an echo is affected by the interference signal. On such terms, the experiments shown in figure 4.20 were designed, measuring the error as the variation in Hz of the Doppler-shift estimations with respect to the control signal. The scenario simulates RoBat sending 50 kHz calls, 50 ms long, while moving at 0.5 ms^{-1} towards two reflectors — control and interference — under different situations. In the top plots, the control reflector is positioned at $\alpha = 15^\circ$ hence generating a 50140 Hz Doppler-shifted echo, whose amplitude is assumed to be constant ($A = 1$). The interference reflector's position is changed $\pm 15^\circ$ with respect to the control, *i.e.* generating Doppler-shifted echoes from 50145 to 50126 Hz. In the bottom plots, the control reflector is positioned at a $\alpha = 45^\circ$ (50102 Hz Doppler-shifted echo), whereas the interference reflector position varies $\pm 15^\circ$ as above, generating Doppler-shifted echoes from 50126 to 50073 Hz. The left column plots show the frequency variations

described before versus amplitude variations ranging from 0.05 to 1 in 0.05 increments. The right column plots show the same frequency variations versus relative signal phase along a whole period (20 samples at $f_s = 1\text{MHz}$).

As seen in the top plots of figure 4.20, for small bearing angles (control reflector at $\alpha = 15^\circ$) the maximum error occurs when the interference reflector is located at $\alpha = 30^\circ$ (frequency 50126 Hz) with maximum amplitude and is phase-shifted 180° , as expected. In the rest of the cases, the Doppler-shift estimation fluctuates around values close to the control signal (error 0). With respect to the bottom plots (control reflector at $\alpha = 45^\circ$), the error follows similar behaviour as in the top plots although in this case, due to the larger frequency separation — because of the cosine behaviour — the error range is slightly larger (see table 4.6).

The results shown in figure 4.21 are from experiments identical to the ones in figure 4.20 except for the echo length which in this case is 300 ms. Despite the unrealistic length of these echoes — too long for real time robotic applications — the experiment was carried out to investigate whether there are significant differences with respect to smaller echo lengths such as the 50 ms of figure 4.20. A summary of the maximum error in Doppler-shift estimation of figures 4.20 and 4.21 is shown in table 4.6. As can be seen, there are no significant differences in the error between 50 and 300 ms, which validates the assumption of using 50 ms as a realistic call length.

Experiment	50 ms	300 ms
$\alpha = 15^\circ$, freq. vs. amp.	5.59 Hz	5.94 Hz
$\alpha = 15^\circ$, freq. vs. phase	9.44 Hz	6.44 Hz
$\alpha = 45^\circ$, freq. vs. amp.	12.99 Hz	13.20 Hz
$\alpha = 45^\circ$, freq. vs. phase	15.16 Hz	13.48 Hz

Table 4.6: Summary of **maximum error** in Doppler-shift estimation.

4.6.3 Discussion

In the top plots of figures 4.20 and 4.21 the error is consistently smaller than in the bottom plots. This was expected, since the frequency separation — due to Doppler being cosine dependent — is larger in the latter case than in the former. Nevertheless, except for very specific situations in which the interference signal is phase-shifted 180° and has the same amplitude as the control signal, the error is fairly small and therefore it may be reasonable to consider only a single reflector when there is more than one and they are very close to each other. Otherwise, reflectors separated by more than the 25° of the main lobe width will not produce significant error and we could consider them as separated reflectors. A scanning behaviour along the robot's path

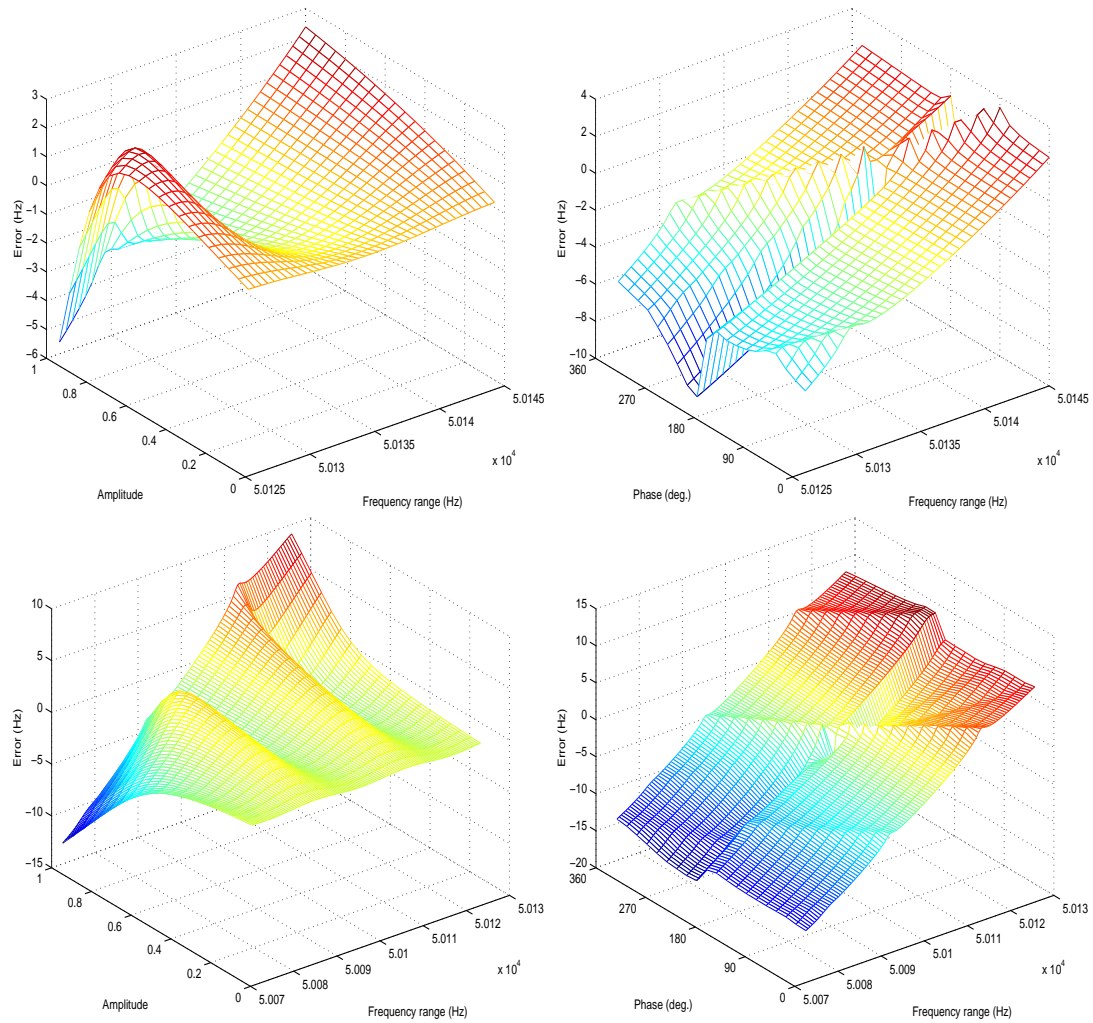


Figure 4.20: **Doppler-shift estimation error in 50 ms echoes made of 2 signals** (simulated data); top plots show a 50140 Hz control signal with interference signal varying from 50145 to 50126 Hz; bottom plots show a 50102 Hz control signal with interference signal varying from 50126 to 50073 Hz; left column plots show amplitude *vs.* frequency variations; right column plots show phase *vs.* frequency variations.

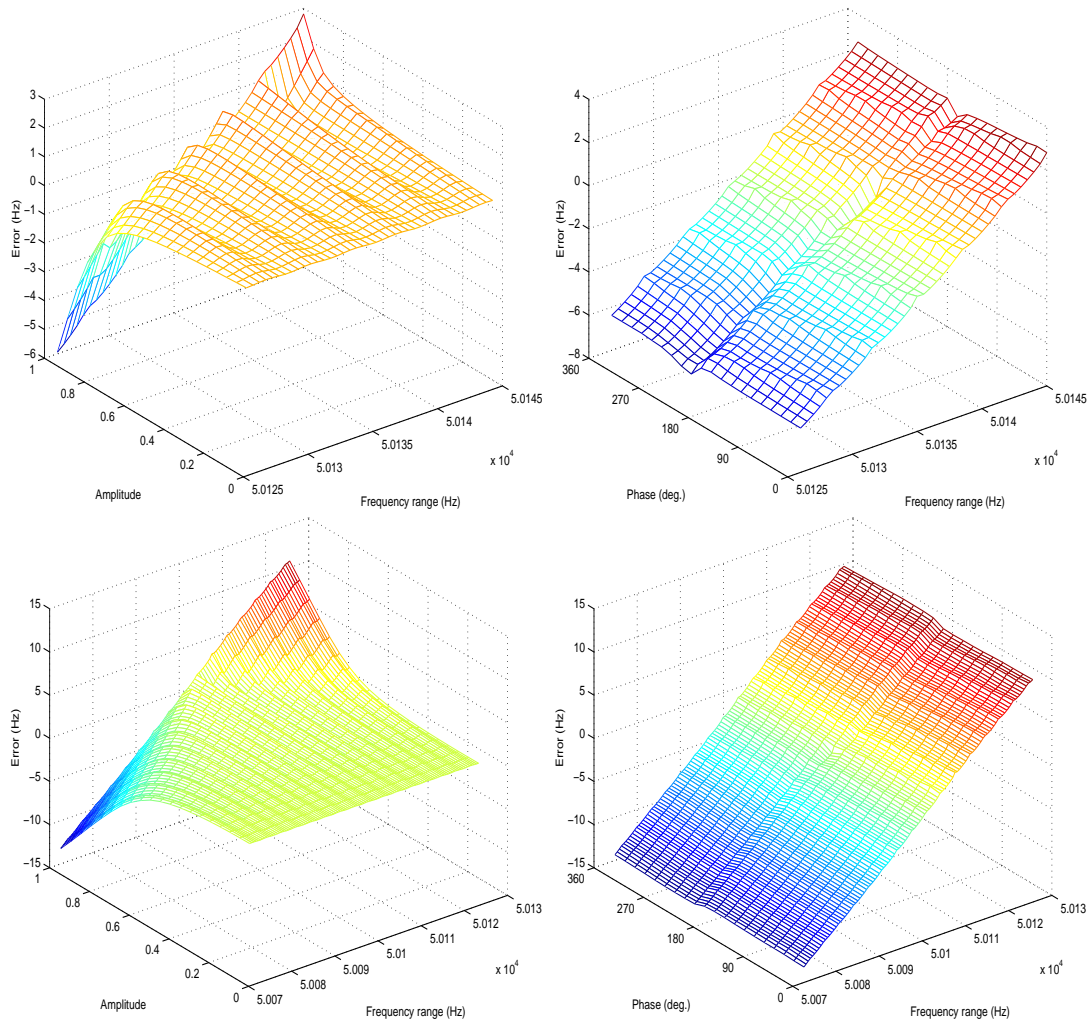


Figure 4.21: **Doppler-shift estimation error in 300 ms echoes made of 2 signals** (simulated data); top plots show a 50140 Hz control signal with interference signal varying from 50145 to 50126 Hz; bottom plots show a 50102 Hz control signal with interference signal varying from 50126 to 50073 Hz; left column plots show amplitude *vs.* frequency variations; right column plots show phase *vs.* frequency variations.

could also improve this close-but-not-overlapped reflector assumption.

An interesting topic for taking this work further would be to investigate the variation in the Doppler-shift estimation error from two or more reflectors as the robot passes by, searching for patterns in the evolution of the error as the bearing angle — and thus the separation among frequencies — increases.

4.7 Summary

This chapter showed how continuous estimates of Doppler-shifts can be derived from physical echoes seen through two different models of a cochlear representation of the CF-FM bat. Two parsimonious models of the auditory fovea of these bats — a linear and a gammatone filterbank — and two methods for estimating Doppler-shift from the output of these models — an artificial neural network and a weighted average — were tested under different experimental conditions.

It was interesting to see how Doppler-shift can be reliably estimated despite the limitations of the robotics domain — specifically robot velocity and transducer characteristics — compared to real bats in their own domain, *i.e.* nature.

The problem of multiple reflectors when estimating Doppler-shift was addressed in a qualitative way, *i.e.* how much our Doppler-shift estimation deteriorates when another signal was introduced in the echo, investigating how likely the problem applies to robotics provided with Polaroid electrostatic transducers and up to what extent the problem can be ignored when assuming a single dominant frequency echoes in indoor environments.

Chapter 5

Doppler-based behaviours

5.1 Introduction

Müller's work on the hypothesis of CF-FM bats using acoustic flow for obstacle avoidance [Müller, 1998] motivated the author to investigate the utility of Doppler-shifts for ultrasound-based robotic navigation which, to the author's knowledge, has not been explored yet. This is not surprising given that the ultrasonic sensors used in robotics (like the Polaroid) do not provide this Doppler information nor permit extracting it by means of further processing. Thus extra hardware, which currently is quite expensive, is needed as seen in the description of RoBat in chapter 3.

In the previous chapter it was shown how Doppler-shifts can be reliably estimated from the echoes. What sort of Doppler-based applications can then be implemented in mobile robots provided with ultrasonic sensors? Furthermore, what can be learnt from Biology regarding the use of Doppler? These questions are addressed in this chapter, in which Doppler-based behaviours found in bats such as target recognition through frequency signatures, Doppler-shift compensation, and obstacle avoidance by means of acoustic flow will be implemented in RoBat and their performance discussed. Moreover, a convoy navigation controller inspired by Doppler-shift compensation is devised and performance results presented.

5.2 Target recognition through frequency signatures

CF-FM bats can hunt insects in clutter, although the spatial resolution achievable with the narrow-band portions of their biosonar pulses is poor. This clutter is mainly composed of dense foliage, trees, other bats and also other preys flying around which will interfere with the pursued prey. So, how can they recognise their preys in such clutter? They do so by utilising

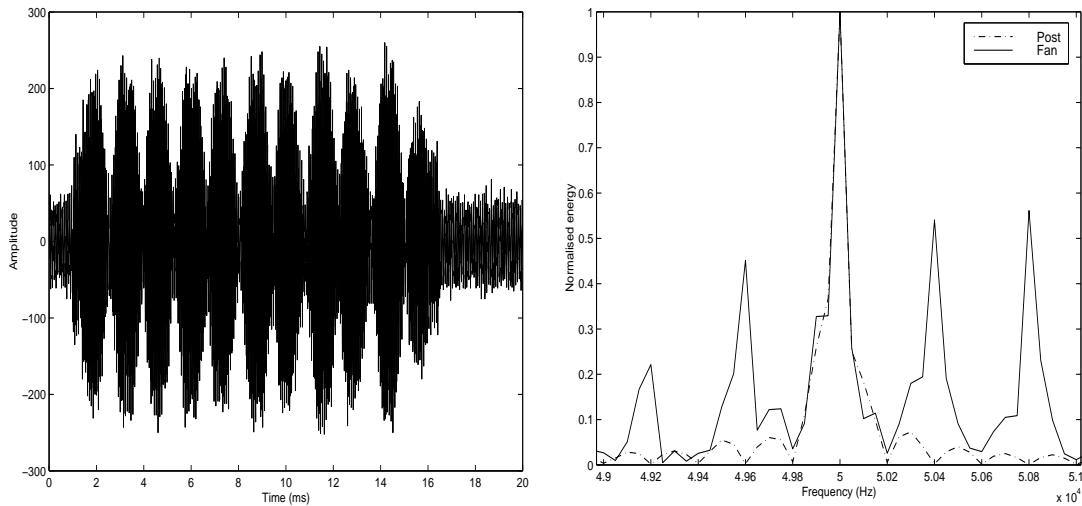


Figure 5.1: **Echo from a rotating fan.** Time domain plot (left); spectrum analysis of such echo vs. an echo from a post (right).

the distinctive patterns of amplitude peaks and spectral broadenings introduced by the insects' wing-beat, which are known as glints [Schnitzler and Ostwald, 1981; Kober and Schnitzler, 1990]. It has been noted before that the echoes generated by echolocating off a small computer fan resemble those generated by flying, *i.e.* wing flapping, insects quite closely, in fact, so much so that bats have been known to actually attack these fans.

These patterns introduced by a computer fan are illustrated in figure 5.1. The left plot shows the amplitude modulations introduced by the reflection off the blades of the rotating fan. The right plot shows the spectrum analysis (FFT) of such echo versus an echo from a post. As seen in the figure, the fan introduces frequency patterns beside the 50kHz component that are missing in the echo from the post.

Putting the fan in front of a flat reflecting surface — such as wall — separated by $\sim 4\text{ cm}$, can be used as a model for a flying insect in front of a large reflecting structure. The echo, when analysed with a narrowband cochlea, $f_{fovea} = 80\text{ kHz}$, $W_{fovea} = 5\text{ kHz}$, $f_{min} = 78\text{ kHz}$ and $f_{max} = 82\text{ kHz}$, and visualised with the interactive display tool described in chapter 3, results in the spectrogram shown in figure 5.2.

The spectral broadening and the amplitude peak of the glint can be seen by comparing the left and right plots of figure 5.2. Here the frequency and the amplitude modulations are introduced by the reflection off the rotating blades of the fan. The amplitude modulations are due to the periodically changing orientations of the reflecting surfaces of the blades whereas the frequency modulations are due to the periodic movement of the blades producing Doppler shifts.

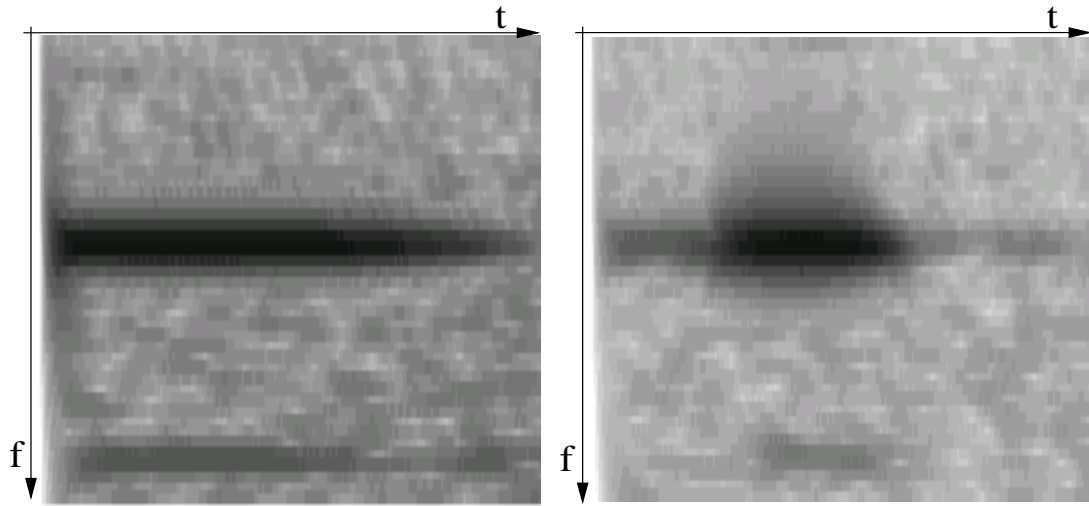


Figure 5.2: **Spectrogram comparison:** echo from a flat reflecting surface (left); echo from a rotating fan held in front of the flat reflecting surface (right).

Based on these spectrograms one can easily distinguish between the two experimental setups, therefore it seems to us that bats also will have no difficulty in distinguishing between the two cases. Hence, this result indicates that correctly interpreting the scene, *i.e.* a flying insect in front of a large reflecting structure, is not so much a resolution problem, *i.e.* distinguish two closely spaced echoes, as it is a pattern recognition problem, *i.e.* classify the ‘glint-spectrogram’ as a ‘prey-in-front-of-large-reflector’ situation [Peremans et al., 2000].

Walker et al. [1998a] successfully implemented this behaviour in a previous version of RoBat (Ben Hope, described in chapter 3), in which the robot was set to track a target fan in a cluttered environment — a robotics lab — in presence of other clutter fans. However, the tracking behaviour was performed with the robot halted, *i.e.*, Ben Hope was moved a pre-set distance, echo measurements and processing were performed and, following by a control law depending on the echo spectrum signatures, Ben Hope turned to one side and moved again. Real bats often perform this ‘pattern recognition through frequency signatures’ on the wing, resulting in Doppler-shifts being introduced when there is relative velocity between the bat and the prey. An interesting question arises: How the bat manages to recognise the spectral glints in its narrowly tuned acoustic fovea if the echo is Doppler-shifted? This is addressed in the next section.

5.3 Doppler-shift compensation

As we saw in chapter 2, the CF-FM bat modifies — increasing or decreasing — the carrier frequency of its own calls, compensating the Doppler-shift produced when the bat, the reflector or both are moving. This echolocating behaviour, called Doppler-shift compensation, has been deeply investigated.

Keating et al. [1994] collected quantitative data in the mustached bat moving at velocities ranging from 0.1 to 5 m/s while compensating Doppler-shift. Interesting results showed bats holding the value of the reference frequency (the echo) between the resting frequency and the cochlear resonance value, the mean frequency reference being always an undercompensation, in other words, compensation in echolocating bats is not perfect. According to the data in Gaioni et al. [1990], mustached bats compensate for an average of 80% of the echo Doppler-shift, *i.e.* 20% undercompensation, whereas Keating et al. [1994] found 15.8% undercompensation for the same bats.

From [Kobler et al., 1985] we know that *Pteronotus parnellii* compensates simultaneously for Doppler and echo intensity during forward swings of a pendulum. Surprisingly, they only compensate for Doppler during backward swings. Perhaps, this might be due to the lesser importance of a target which is getting away — negative Doppler-shift — from the bat. Moreover, by behaving in this way, a saving in energy can be made.

Roverud and Grinnell [1985] showed evidence of joint frequency tracking and Doppler-shift compensation behaviours in the CF-FM bat *Noctilio albiventris* when flying towards an artificial CF-FM sound. The reason for the bat performing frequency tracking is so far unknown. However, the fact that *N. albiventris* hunts in groups suggests a frequency shift in their call relative to surrounding bats in order to avoid jamming in the identification of individual echoes [Roverud and Grinnell, 1985].

Also, from [Behrend et al., 1999] we know that for Doppler-shift compensation bats depend on binaural cues. They arrive at this conclusion after experimenting with healthy and impaired (deaf) bats, reporting better performance for the former. This is an interesting fact given the monaural nature of Doppler. In other words, after Doppler-shifts are calculated in the lower auditory system of each ear, the information is presumably combined at higher levels in the auditory cortex before action is taken.

From all these interesting findings it can be argued that Doppler-shift compensation is an important behaviour from which bats benefit in several ways some of them summarised below:

- Accurate target recognition, as described in section 5.2, allowing the echo to fall closer

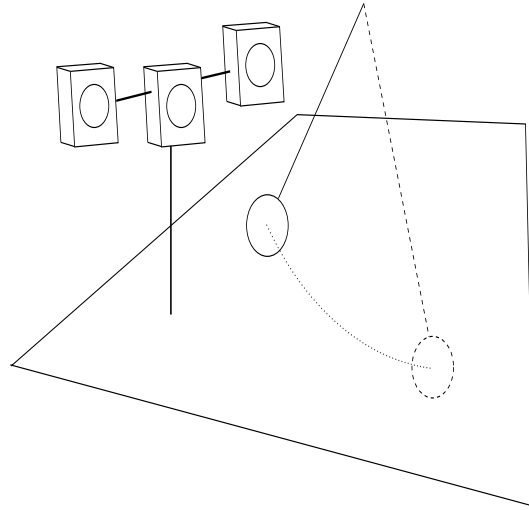


Figure 5.3: **The measurement setup:** a ball swinging back and forth in front of the sonarhead.

to the middle of the fovea.

- Smaller size of the fovea, as a consequence of the above, since less high-quality filters are needed.
- Faster sense-and-act cycle, again as a consequence of the above, allowing realistic performance when operating in high duty cycle mode.

5.3.1 Implementation in RoBat

The aim of the following experiment was to see to what extent the RoBat system allows accurate Doppler-shift compensation like that performed by bats. In order to introduce relative movement between RoBat and a reflecting target, a swinging ball experiment was designed. The chosen object was a plastic ball of 8 cm diameter suspended from a 50 cm long thin nylon wire, putting the ball to swing back and forth in front of RoBat as illustrated in the cartoon of figure 5.3.

Figure 5.4 (left) shows a time domain plot consisting of 20 consecutive echoes corresponding to half of a swinging cycle, *i.e.* the ball starts far from the robot at zero velocity, swings towards RoBat, reaches its maximum Doppler-shift at the lowest point of the trajectory and ends up at the closest position but with low amplitude because of an unfavourable directivity gain for this position, and then swings back. Figure 5.4 (right) shows the spectrogram, *i.e.* the output of the fovea-part of the cochlea, of a whole experiment. The constant frequency at 50 kHz is due to the crosstalk during pulse emission. In the figure, a sinusoidal change in the received carrier frequency over time is clearly visible. The extrema of this curve represent the

ball swinging forward or backward at maximum speed, resulting in maximal Doppler-shifts of positive and negative sign, respectively.

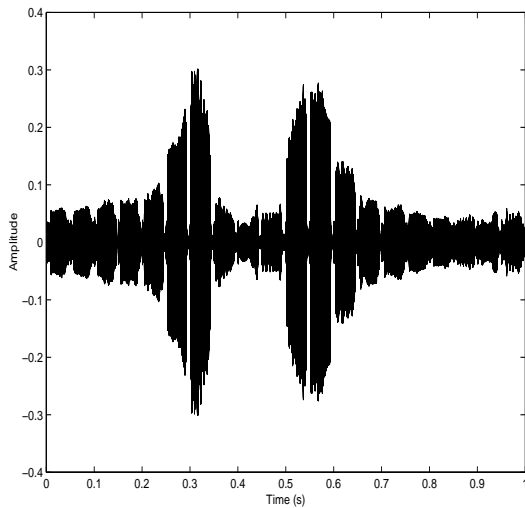


Figure 5.4: **Echoes reflected off the ball swinging back and forth:** time domain plot (left); spectrogram (right).

Having seen how Doppler-shift can be extracted fast enough from a swinging ball, the experiment is now extended. Figure 5.5 shows experiments in which the ball was put to swing back and forth in front of RoBat, starting at a pre-set height and recording data until the swing attenuated almost completely. The left column plots show Doppler-shift estimation throughout the experiment whereas the right column plots show a zoomed call frequency versus Doppler-shifted echo comparison.

In the experiment shown in the upper plots of figure 5.5, no Doppler-shift compensation was applied, as can be inferred from the harmonic simple oscillatory movement envelope of the left plot. In the right plot, the call remains at the resting frequency (50 kHz) whereas the frequency of the echo is Doppler-shifted according to the swinging ball. The middle plots show half compensation, *i.e.* compensating only for positive Doppler-shifts — ball swinging forward — as *P. parnellii* does [Kobler et al., 1985]. This is clearly seen in the right plot, in which the call remains at the resting frequency during negative Doppler-shift whereas it changes its frequency to compensate for positive Doppler-shifts. Finally, the lower plots show full (positive and negative) compensation. The compensation effect can intuitively be seen by comparing top-left with bottom-left plots (note that all the left column plots are equally scaled). The phase-shift between the echo and call curves seen in the bottom-right plot is due to the *a posteriori* compensation, *i.e.* the call frequency being modified according to the last Doppler-shift estimation, which introduces underdamping for a gain $K = 1$. This also applies to the half

compensation case (middle plots). In both cases, RoBat undercompensates by approximately 30% as a result of this underdamping. This is close to the 20% undercompensation reported by Gaioni et al. [1990].

Figure 5.6 shows the same experiment as figure 5.5 but with different gain values. For the upper plots, the gain was set to 0.25, resulting in a highly underdamped behaviour with very low compensation (approx. 15%). Also, because of the underdamping, the phase-shift worsens as seen in the right plot. In the middle plots, increasing the gain to 1.25 starts worsening performance due to overshoot in earlier stages of the trial. Nevertheless there are small improvements with respect to $K = 1$ at the final stage of the trial as seen in the left plot. Finally, the lower plots show unstable performance because of the overshoot introduced by a $K = 1.75$ gain. The phase-shift between the call and echo curves (right plot) is significantly decreased although at the cost of overshoot.

5.3.2 Discussion

We have seen how the Doppler-shift of the echoes reflected by a swinging ball in front of RoBat can be successfully compensated by adapting the frequency of the call using the last Doppler-shift estimation. Different gain values have been tried, the best being $K = 1$ for a 70% compensation as shown in the middle plots of figure 5.5. This compensation factor is constrained by the computational time required for a complete sense-and-act cycle. By implementing this behaviour, the size of the acoustic fovea could be reduced and therefore higher duty cycles could be achieved as previously discussed in section 5.3.

In order to see the effect of varying the Doppler-shift compensation gain in different scenarios, experiments in which RoBat was moving orthogonally towards a wall as in chapter 4 were performed. The plots in figure 5.7 show the behaviour of the call frequency while compensating for Doppler-shift when RoBat was moving at constant velocity (left plot) and accelerating (right plot). As can be seen in the figure, optimal values for K are found between 0.75 and 1. Below this range, the response of the system is too underdamped whereas above this range it becomes unstable because of overshoot as in the swinging ball experiment. This overshoot is very clearly seen in the constant velocity experiment for $K = 1.75$.

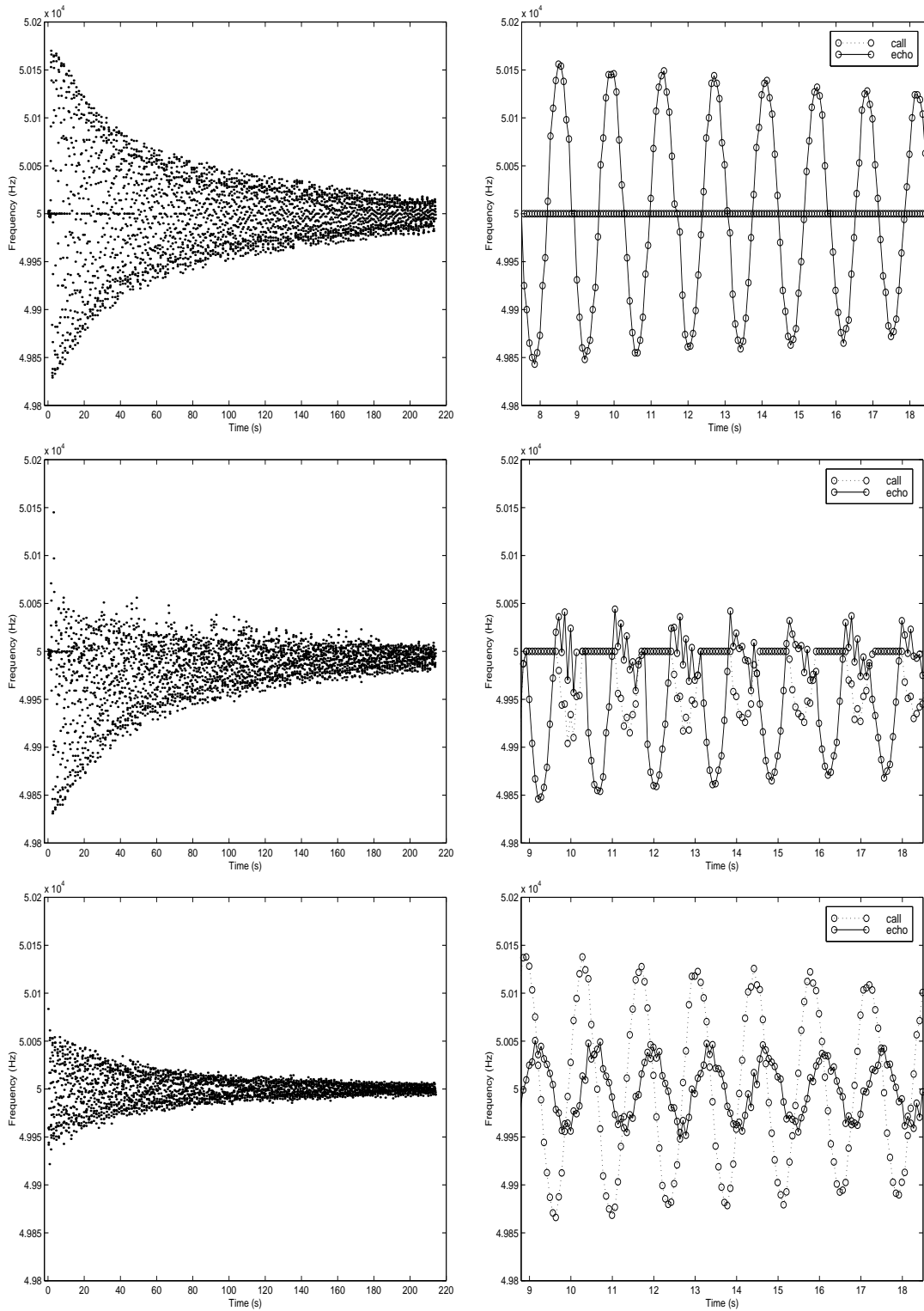


Figure 5.5: **Doppler-shift estimation while swinging a ball** without compensation (top), half compensation, $K = 1$ (middle) and full compensation, $K = 1$ (bottom). Left plots (equally scaled) show Doppler-shift estimation along the whole experiment. Right plots show zoomed call vs. echo curves.

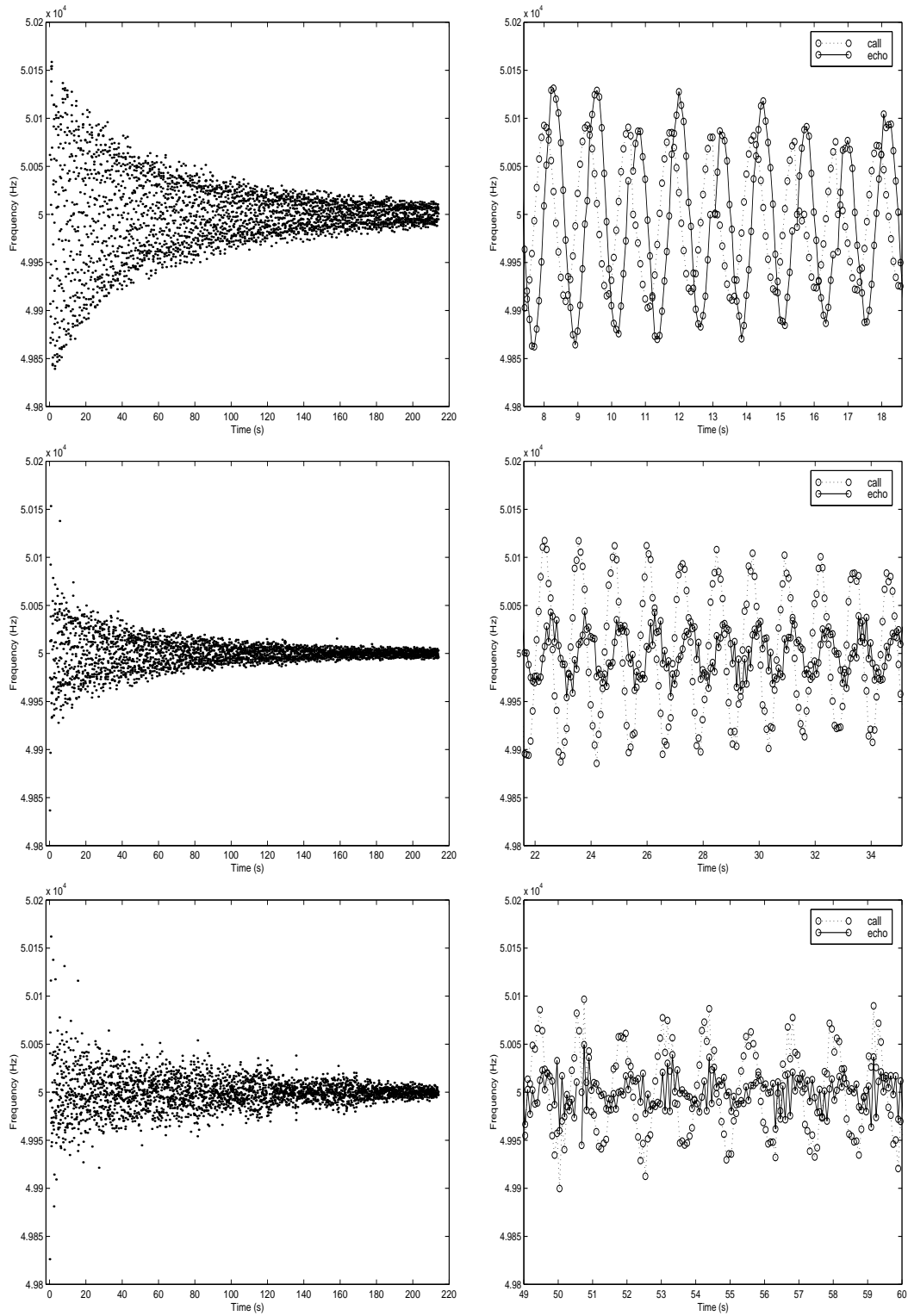


Figure 5.6: **Full Doppler-shift compensation with different gains:** 0.25 (top), 1.25 (middle) and 1.75 (bottom). Left plots (equally scaled) show Doppler-shift estimation along the whole experiment. Right plots show zoomed call vs. echo curves.

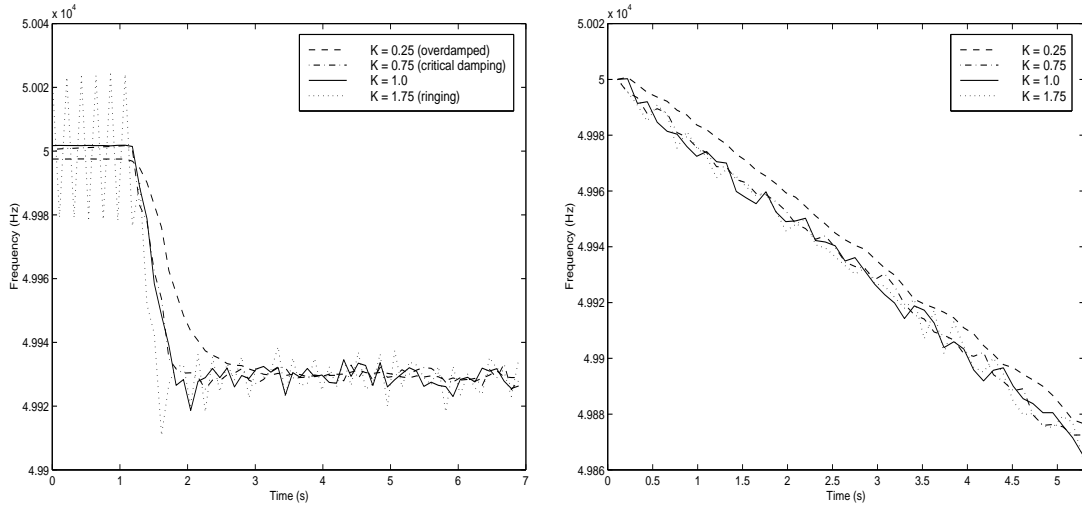


Figure 5.7: **Comparison of call-frequency estimations during Doppler-shift compensation** for different gain (K) values while RoBat moved towards a wall at constant velocity (left) and accelerating (right).

5.4 Convoy navigation controller

In dynamic environments where several physical mobile agents can be found such as laboratories, automated factories, and also in travelling group applications such as [Melhuish et al., 1999], situations in which convoy navigation is required are commonly found.

In such terms, Han et al. [2001] recently showed how using a pair of ultrasonic sensors, a moving object can be tracked by estimating its relative velocity from the trajectory followed by the robot. Despite successfully achieving its task, the method does not exploits the physics of echolocation, *e.g.* by taking advantage of the monaural characteristic of Doppler which allows the relative velocity of an object to be estimated with a single transducer and from a single echo under certain conditions as we shall see below.

In a real robotic environment, we can find at least three different Doppler-dependent situations while navigating. In this context, *maximum Doppler* refers to the maximum Doppler-shift the robot could observe for a given velocity assuming a static reflector at 0° bearing angle.

- **Doppler ≤ 0** There is no reflector in the way or there is a moving reflector whose relative velocity with respect to our robot is zero or negative. In this case the robot can navigate safely within its perceptual range¹.
- **$0 < \text{Doppler} < \text{Max. Doppler}$** There is either a static reflector in the way or a moving

¹The maximum range from which the robot can accurately sense the environment. In RoBat this range is 3 m.

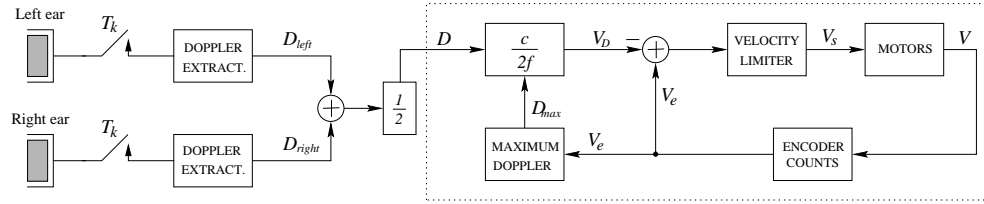


Figure 5.8: **Block diagram of the convoy navigation controller.**

reflector with a positive relative velocity with respect our robot but with a bearing angle sufficient to avoid a collision.

- **Doppler \geq Max. Doppler** There is a moving reflector in the way with a positive relative velocity with respect our robot and its bearing angle is 0 or close to 0. In this case the robot should change its path immediately for avoiding collision.

Inspired by the Doppler-shift compensation behaviour, and applying these Doppler-dependent rules, a simple controller suitable for use in convoy navigation is devised. The main difference with respect to Doppler-shift compensation is that it is the velocity of the robot, instead of the call frequency, that is the variable altered by the controller to keep the Doppler-shift close to 0. The controller assumes a moving reflector (*e.g.* another robot) within the robot's perceptual range and at a small bearing angle (close to 0). A block diagram of this controller is shown in figure 5.8.

As seen in the figure, the average Doppler-shift (D) from the individual Doppler-shifts received by each of the transducers is estimated, *i.e.* a binaural estimation as suggested in [Behrend et al., 1999]. Then the velocity of the robot (V_D) is estimated according to the sign and value of D . In case where D is greater than the maximum Doppler (D_{max}), *i.e.* reflector moving towards the robot, an immediate escape maneuver such as turning to one side would be adopted for avoiding collision. Next, the velocity is set to its new value (V_s) which is limited by a preset value (60 cm/s). Finally, from the readings of the wheel encoders, the current velocity (V_e), which is used for both calculating the new velocity and the maximum Doppler, is estimated.

The experiment designed for assessing the performance of this controller consisted in Ro-Bat moving along a corridor right behind “Gillespie”, a RWI-B21 robot moving in the same direction (figure 5.9 (upper-left)). Three different cases were tested: In the first case, Gillespie starts moving keeping its velocity constant at 35 cm/s (upper-right graph). In the second case, Gillespie starts moving and keeps accelerating until reaching the maximum allowed velocity of 60 cm/s (lower-left graph). Finally, in the last case, Gillespie starts moving with high acceleration until reaching the maximum speed of 60 cm/s and then decelerates smoothly to 30 cm/s before stopping (lower-right graph).

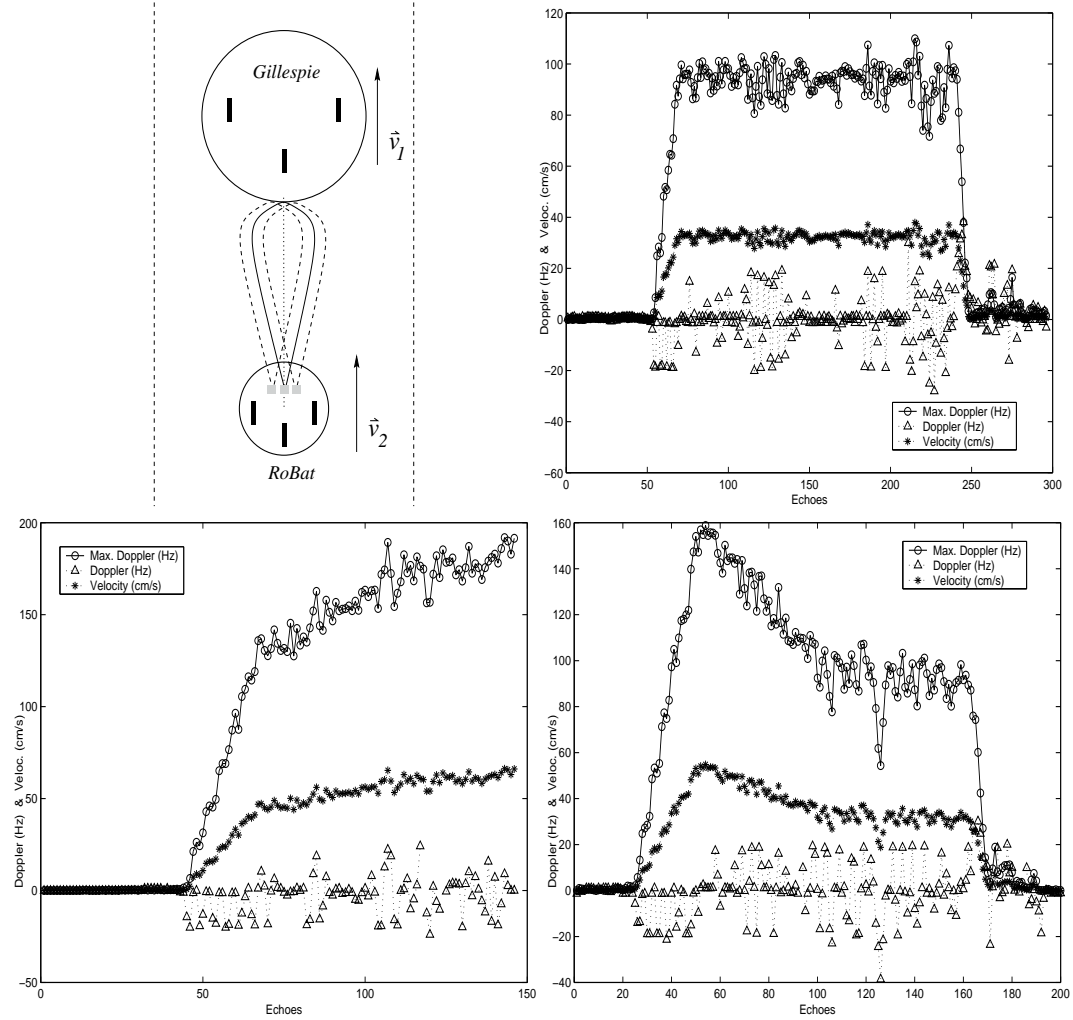


Figure 5.9: **Convoy navigation experiment.** Measurement setup for the motion detection task (upper-left). Doppler-shifts and velocity values estimated by RoBat while Gillespie was moving at constant velocity (upper-right), accelerating (lower-left) and decelerating (lower-right).

The controller performed satisfactorily well. For each of the three cases, the Doppler-shift, maximum Doppler and RoBat's velocity were estimated for every echo, as shown in the graphs of figure 5.9. Because of the large size and weight of Gillespie, the irregularities of the floor affect its velocity more drastically. Interestingly, the system is sensitive enough to pick up these irregularities resulting in a small ripple in the velocity curves. This can be clearly seen in the Doppler-shift and maximum Doppler curves.

5.4.1 Discussion

The real world is dynamic: things move and change their position. We believe that for efficient navigation, an agent must take into account other agents moving around in the same environment, and likewise this should be done at the lowest level and, therefore, in the simplest way, before going to higher levels of abstraction.

In this section we have seen how a simple and efficient controller for smooth convoy navigation and collision detection can be devised taking advantage of Doppler. Since Doppler-shifts depend on the cosine of the bearing angle between the robot and the reflector, and given the flatter portion of the cosine curve at small bearing angles as seen in figure 5.12, an angle close to 0° for situations in which a moving reflector — *e.g.* another robot — is moving in the same direction within its perceptual range can be assumed. In such situations, the controller showed how the relative velocity of the other agent can be estimated, resulting in smooth navigation while keeping the relative velocity close to 0, as seen in the results of the experiments using RoBat and Gillespie.

5.5 Acoustic flow

In their work, Müller and Schnitzler [1999, 2000] present an acoustic flow hypothesis for obstacle avoidance in the CF-FM bat. This type of acoustic flow provides crude localisation information which suffices for tasks like obstacle avoidance in which as high accuracy is not needed as in other tasks, *e.g.* prey capture.

Müller bases his acoustic flow hypothesis on two perceptual dimensions: Ψ (changes in Doppler shift) and Θ (changes in sound pressure amplitude) which CF-FM bats may employ for the extraction of two-dimensional spatial information. For obtaining such perceptual dimensions, Müller considers translational movements — in Cartesian coordinates (d, h) with the heading (h) always aligned with the bat's velocity — as shown in figure 5.10. Ψ and Θ are calculated from the following equations [Müller, 1998]:

$$\Psi(d, h) = \frac{\partial f_d}{\partial h} / f_d = \frac{d^2}{h(d^2 + h^2)} \quad [m^{-1}] \quad (5.1)$$

$$\Theta(d, h) = \frac{\partial P}{\partial h} / P = -\frac{2h}{d^2 + h^2} - \frac{m(f)/10 \ln(10)h}{\sqrt{d^2 + h^2}} + \frac{\partial \Phi}{\partial h} / \Phi \quad [m^{-1}] \quad (5.2)$$

In equation 5.1, the Doppler effect is modeled as a frequency shift

$$f_d = 2f_e \frac{v}{c} \frac{h}{\sqrt{d^2 + h^2}},$$

whereas in equation 5.2, $m(f)$ [dB/m] is the absorption coefficient, P is the pressure amplitude obtained from a simplified scene model of the animal and Φ is the directivity of emitter and receiver calculated from the model proposed in [Schnitzler and Grinell, 1977].

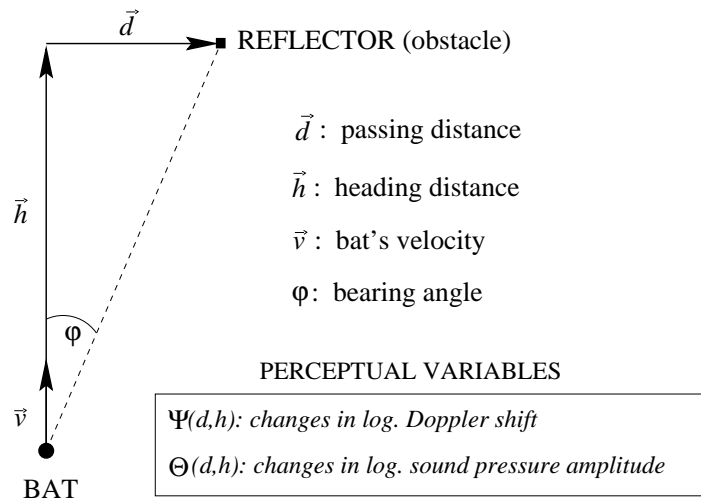


Figure 5.10: **Müller's geometrical definition for an obstacle avoidance task by means of acoustic flow** (adapted from [Müller, 1998]).

As seen in equation 5.1, Müller skips the calculation of the velocity, assuming that bats do not calculate it. In this work, for the sake of simplicity and utility — as an extra source of information — the velocity of the robot, estimated from the readings of the wheel encoders, will be used. Thus, the bearing angle will be estimated from equation 4.1. In addition, TOF will be used instead of changes in sound pressure amplitude because of being more reliable and easy to calculate in our system.

We aim to investigate whether the accuracy of this crude estimation suffices for an obstacle avoidance task in a robotic context. Acoustic flow is monaural, *i.e.* intensity differences (TOFs

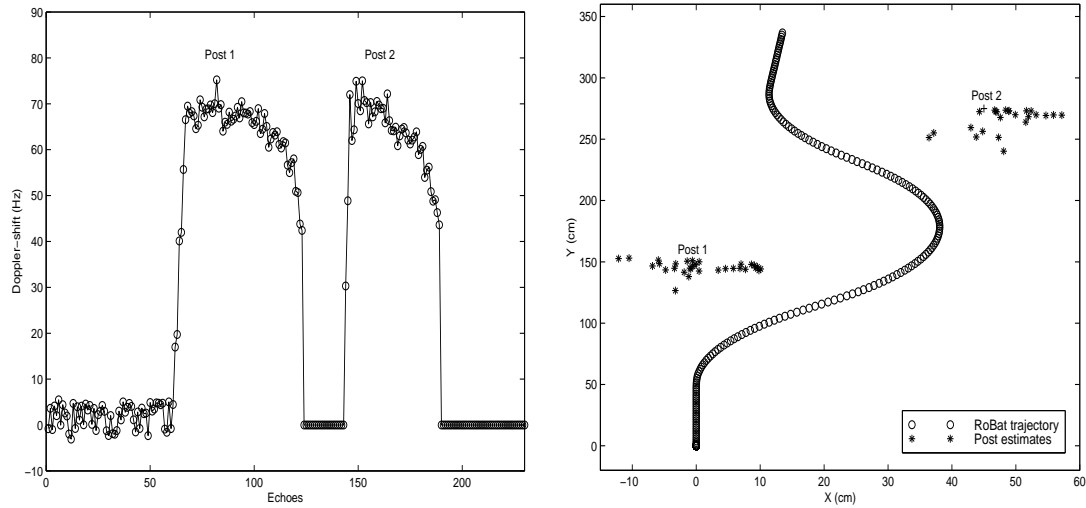


Figure 5.11: **Acoustic flow experiment.** Estimated Doppler-shifts of the two posts (left). Posts position estimations along RoBat's trajectory through acoustic flow (right).

in our system) and Doppler-shifts can be extracted independently by each of RoBat's ears. The way this information is combined at higher levels of the bat's auditory system (binaurality) is currently a matter of investigation by biologists, as seen in [Behrend et al., 1999]. In our system we simply take the averages of the two TOF and Doppler estimations.

An experiment in which RoBat had to avoid two obstacles (posts) on its path was performed, obtaining a crude estimation of the cartesian position of the two posts as shown in figure 5.11. In the left plot we can see the Doppler-shift estimations of the two posts from the cochlear model. The first wiggling part of the plot is due to noisy estimations when the robot is not moving yet, having the first post in front of it. As soon as RoBat starts moving, the post is detected and RoBat starts turning until the bearing angle increases — Doppler-shift decreases — up to a desired value (in our system this was set to 50°) when the second post was detected, making the avoiding process start again. The 0 Hz Doppler-shifts between posts and after the second post are due to the lack of echoes at that particular moment. A crude position estimation of the two posts along the robot's trajectory is shown on the right plot of figure 5.11.

5.5.1 Discussion

The aim of this section was to investigate whether the crude position estimation provided by the acoustic flow suffices for an obstacle avoidance task in a robotic context. RoBat was set to perform such task by means of acoustic flow, *i.e.* estimating the Cartesian coordinates of the obstacles from the TOF and bearing angle — calculated from the Doppler-shifts — of the received echoes along its trajectory.

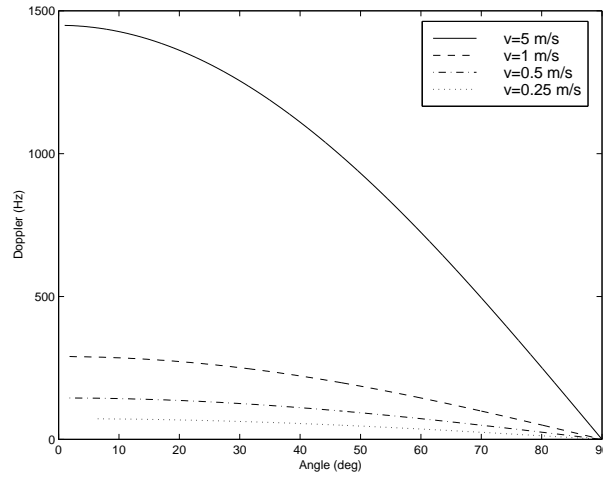


Figure 5.12: **Cosine curves showing the angular dependency in Doppler-shift estimation for different velocities** ($f_c = 50000 \text{ kHz}$, $\varphi = 0^\circ$).

The results suggest a Doppler-shift resolution problem from the rather small velocities of the robot compared with real bats. This is illustrated in figure 5.12, in which the angular dependency of Doppler is plotted for different velocities for the same call frequency of 50 kHz and assuming a reflector target located at bearing angle $\varphi = 0^\circ$. As seen in the figure, a velocity of 5 ms^{-1} — perfectly reachable by bats — introduces a Doppler-shift of almost 1500 Hz^2 resulting in a much steeper curve (*i.e.* higher resolution) than the ones resulting from realistic velocities for indoor mobile robots³ (*i.e.* 0.25 to 1 ms^{-1} in figure 5.12).

The sensitivity to Doppler depends on the sine of the angle between passing and heading distances to the target (as seen in figure 5.10). However, as seen in equation 4.1, the Doppler itself has a cosine dependence. Thus there is a trade-off — the closer to zero bearing, the larger the Doppler but the worse the sensitivity, while the closer to 90° , the better the sensitivity but the poorer the Doppler. This can be seen in the acoustic flow task in terms of a poor position estimation of the reflector at small bearing angles. As a consequence, Doppler sensitivity depends on $\sin \theta \cos \theta = \sin 2\theta$. In a point-like transducer, *i.e.* no beam-forming, this results in maximum Doppler sensitivity at 45° .

In addition, the 83 kHz carrier frequency of the CF-FM bat is higher than RoBat's 50 kHz . As a result, the range of Doppler-shifts obtained by RoBat is much smaller than by the real bat and, therefore, the bearing angle estimation will be worse. The effect of this poor resolution was shown in the non-consistent position estimation of the two posts of figure 5.11. Nevertheless, it suffices for avoiding the posts as demonstrated by the trajectory performed by the robot. This

²Actually this will be around 2400 Hz for *R. ferrumequinum* because of its call frequency of 83 kHz .

³In the author's opinion, velocities higher than 1 ms^{-1} for indoor environments would be highly dangerous.

is not very far from Müller's acoustic flow hypothesis in that it provides crude localisation information in tasks demanding low accuracy such as obstacle avoidance.

5.6 Summary

In this chapter we have seen how Doppler-shifts, a rich source of information which is not exploited by commercial robotic ultrasonic range sensors like the Polaroid, can be used in several ways in a robotic context. The biological inspiration came from CF-FM bats, creatures that fully exploit the physics of echolocation, some of whose behaviours, such as target recognition through frequency signatures, Doppler-shift compensation and acoustic flow, have been implemented in Robat, demonstrated and discussed.

From Doppler-shift compensation, inspiration for a convoy navigation controller following a set of simple Doppler-dependent rules has been successfully implemented. This controller takes advantage of the flat portion of the cosine curve at small bearing angles which allows small fluctuations in bearing angle around 0° without worsening performance.

On the other hand, an implementation of Müller's hypothesis on acoustic flow for obstacle avoidance resulted in a poor estimation of the target's passing distance at small bearing angles which improved as the angle increased, nevertheless sufficing for avoiding the two reflectors of the experiment. The reason for this poor estimation is the low resolution caused by the relatively low velocity and call frequency of the robot.

Chapter 6

Active sensing: Towards a narrowband 3D tracking system

6.1 Introduction

3D object localisation using sonar has normally been achieved using ultrasonic sensor systems — made of, at least, three receivers — in which the differences in arrival times of echoes among the receivers are used for calculating the position of the reflector in the space [Delepaut et al., 1986; Kuc, 1993; Akbarally and Kleeman, 1995; Hong and Kleeman, 1995]. Alternatively, Peremans et al. [1998a] presented a method based exclusively on amplitude measurements which facilitates very small head size. This method, implemented in the biomimetic sonarhead, used interaural amplitude differences measured at different frequencies.

Recently, Han et al. [2001] used a pair of ultrasonic sensors for tracking a moving object by estimating its relative velocity from the trajectory followed by the robot. The position of the target (range and azimuth) is estimated using the triangulation method [Sabatini and Benedetto, 1994]. Their method — defined as the virtual ultrasonic image — does not take into account target elevation.

In chapter 2 we saw how Rhinolophids and Hipposiderids move their pinnae along vertical arcs for estimating a target's elevation. These ear movements, named 'arc scanning' by Walker [1997], are highly correlated with the emitted pulses [Griffin et al., 1962; Pye et al., 1962; Pye and Roberts, 1970]. Moreover, while performing arc scanning, the bat can simultaneously obtain the amplitude of the echo, which is important for the calculating IID. Thus, arc scanning, combined with azimuth angle estimation by means of IIDs and target range by echo delay, provides a narrow-band echolocator with a 3D estimation of an insonified target's relative position [Walker et al., 1998b].

In this work, active sensing means

1. changing the configuration of the system in response to the observed echoes as biological systems do, and
2. exploiting the dynamics of the sonarhead for extracting cues from the environment,

as a mean of achieving narrowband 3D object localisation. In section 6.2, Barshan and Kuc's [1992] method for obstacle localisation (extended afterwards in [Kuc, 1996]) is adapted and implemented in RoBat. Then, in section 6.3, arc scanning is implemented in RoBat as a way to provide elevation cues. Section 6.4 integrates both techniques in an attempt to obtain reliable 3D target position estimation. Finally, section 6.5 summarises the achievements of the chapter.

6.2 Range + azimuth = 2D tracking

6.2.1 Implementation of Barshan's and Kuc's model

As seen in chapter 2, Barshan and Kuc's [1992] bat-like adaptive system allows 2D obstacle localisation. The system is composed of a wide-beam Sonar sensor with a receiver-transmitter-receiver configuration that mimics, in the same way as the sonarhead used in this work, the echolocating system of bats. The system allows true range and azimuth estimation of an object, located along the system line-of-sight, which improves with decreasing range.

Figure 6.1 illustrates Barshan's and Kuc's geometric model for obstacle localization. If a reflector located at a range r and azimuth angle θ is inside the active region — defined by the intersection of the radiation pattern main lobes of the emitter and receivers — two TOF measurements will be obtained from R1 and R2. In addition, if the reflector is located in the same elevation plane (*i.e.* 0° elevation), each of these TOFs will define an ellipse of possible object locations for which the transmitter and the respective receiver are the foci [Kuc, 1996].

From the geometric model of figure 6.1, the following equations are obtained [Barshan and Kuc, 1992]:

$$\sqrt{x^2 + y^2} + \sqrt{(x - D)^2 + y^2} = cT_R \quad (6.1)$$

$$\sqrt{x^2 + y^2} + \sqrt{(x + D)^2 + y^2} = cT_L, \quad (6.2)$$

in which D is the separating distance between transducers, c the speed of sound in air, and T_R and T_L the round-trip distances (estimated from the TOF) from the transmitter to each receiver. Thus, from equations 6.1 and 6.2, the range r and azimuth angle θ of the reflector can be calculated [Barshan and Kuc, 1992]:

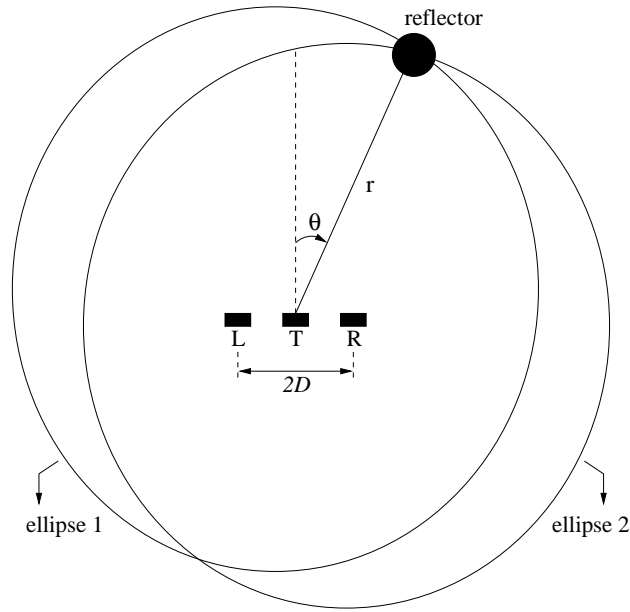


Figure 6.1: **Geometry for obstacle localization with a collinear three-transducer system.** Ellipse 1: foci at L and T; ellipse 2: foci at T and R (adapted from [Barshan and Kuc, 1992]).

$$r = \frac{(cT_L)^2 + (cT_R)^2 - 2D^2}{2c(T_L + T_R)} \quad (6.3)$$

$$\theta = \sin^{-1} \left[\frac{(c^2 T_L T_R + D^2) c(T_L - T_R)}{D(c^2 T_L^2 + c^2 T_R^2 - 2D^2)} \right] \quad (6.4)$$

In [Kuc, 1996], the system incorporated motors in the receivers which allowed independent receiver orientation towards the reflector by the simple relation

$$\gamma_L = \tan^{-1} \left[\frac{r}{D} \right], \quad (6.5)$$

where γ_L is the steering angle of the left receiver (defining its rotation towards the transmitter as positive). By symmetry, γ_R is the complement of γ_L . This maximises echo amplitude and bandwidth [Kuc, 1996].

6.2.2 Adaptation to the geometry of the sonarhead

The geometry of the sonarhead is slightly different from the collinear sensor used by Barshan and Kuc [1992]. The main difference lies in the offset of the receivers' position with respect to the transmitter. This is illustrated in figure 6.2.

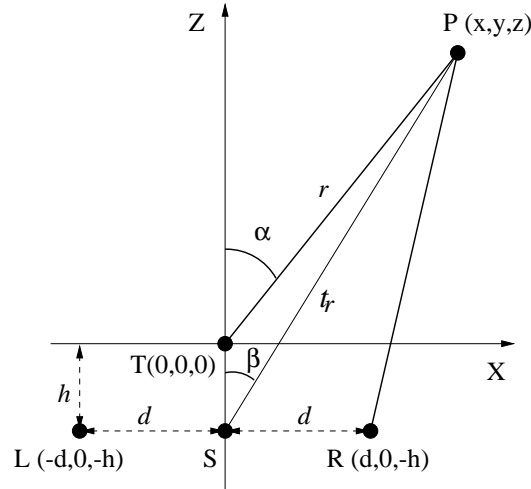


Figure 6.2: **Geometry of the sonarhead's 2D obstacle localization model** (top view). Right (R) and left (L) receivers are located in the horizontal plane at an offset h from the transmitter's (T) horizontal axis and a distance d from its vertical axis. T is the origin of coordinates in the model from which the distance r and angle α to the reflector P are calculated. S is the sonarhead's rotation axis from which the target's true range t_r and azimuth angle β with respect to P are calculated.

Since the transmitter and receivers are in the same vertical plane (*i.e* Y axis), the equations from the geometric model of the sonarhead are:

$$\sqrt{x^2 + y^2 + z^2} + \sqrt{(x-d)^2 + y^2 + (z-h)^2} = cT_R \quad (6.6)$$

$$\sqrt{x^2 + y^2 + z^2} + \sqrt{(x+d)^2 + y^2 + (z-h)^2} = cT_L \quad (6.7)$$

where $h = 3 \text{ cm}$ and $d = 7.5 \text{ cm}$ (as described in [Peremans et al., 1997]). As in Kuc [1996], the reflector is assumed to be at 0° elevation hence we can get rid of the y coordinate. From figure 6.2, using polar instead of Cartesian coordinates, and given $r = \sqrt{x^2 + z^2}$, equations 6.6 and 6.7 become

$$cT_R = r + \sqrt{(r \sin \alpha - d)^2 + (r \cos \alpha + h)^2} \quad (6.8)$$

$$cT_L = r + \sqrt{(r \sin \alpha + d)^2 + (r \cos \alpha + h)^2} \quad (6.9)$$

Resolving equation 6.8 for

$$r = \frac{(cT_R)^2 - d^2 - h^2}{2(cT_R - d \sin \alpha + h \cos \alpha)}, \quad (6.10)$$

and substituting in equation 6.9 after calling $a = cT_R$ and $b = cT_L$, we get

$$h(b^2 - a^2) \cos \alpha - d(a^2 + b^2 - 2d^2 - 2h) \sin \alpha = (a - b)(ab + d^2 + h^2)$$

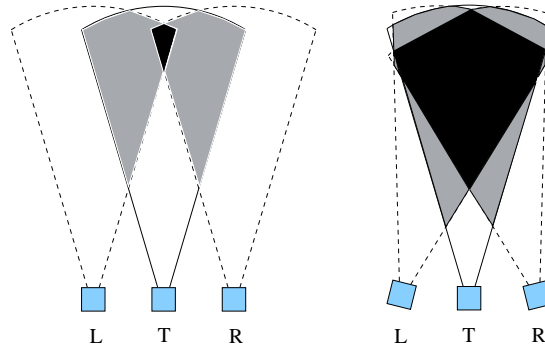


Figure 6.3: **Sketch of the sonarhead in unfocused and focused configurations.** The black shadowed area delimits the active region. Once the range and orientation of the target is determined, the unfocused sonarhead (left plot) focuses on the target (right plot) by panning the ears. This increases the active region and therefore maximises echo amplitude and bandwidth.

For the sake of clarity we will also call $A = h(b^2 - a^2)$, $B = -d(a^2 + b^2 - 2d^2 - 2h)$, and $C = (a - b)(ab + d^2 + h^2)$. If $R^2 = A^2 + B^2$ we get:

$$R \sin \theta \cos \alpha + R \cos \theta \sin \alpha = C,$$

and given $\sin(\theta + \alpha) = C/R$, and $\theta = \tan^{-1} \left[\frac{A}{B} \right]$, we can calculate

$$\alpha = \tan^{-1} \left[\frac{A}{B} \right] - \sin^{-1} \left[\frac{C}{R} \right] \quad (6.11)$$

Knowing r and α , we can finally obtain the expressions for the true range t_r and azimuth angle β by trigonometry (figure 6.2):

$$t_r = \frac{r \sin \alpha}{\sin \beta} \quad (6.12)$$

$$\beta = \tan^{-1} \left[\frac{r \sin \alpha}{r \cos \alpha + h} \right] \quad (6.13)$$

Focusing the receivers towards the reflector maximises echo amplitude, allowing estimation of t_r and β more accurately. Figure 6.3 shows a sketch of the sonarhead in unfocused and focuses configurations. Following the same criteria as in equation 6.5, the orientation of the left receiver with respect the reflector's true range is given by:

$$\gamma_L = \tan^{-1} \left[\frac{t_r}{d} \right], \quad (6.14)$$

and γ_R is the complement of γ_L as in [Kuc, 1996].

6.2.3 Methods

In the experiments reported in this chapter, the reflectors used are of two kinds: cylindrical (4 cm diameter plastic post) and spherical (8 cm diameter plastic ball). The range interval is between 20 to 60 cm for azimuth angles of $\pm 15^\circ$ with respect to the emitter axis. The pulses emitted in the experiments of this section are made of a 4 ms long sinusoid of 50 kHz frequency (sampling frequency $f_s = 1 \text{ MHz}$) with rectangular envelope (*i.e.* no amplitude modulation as in [Barshan and Kuc, 1992]). Echoes modulated with a Gaussian-like envelope allow TOF estimation by applying optimal correlation detectors (*i.e.* matched filters). This method needs the reception of the whole echo, resulting in a longer delay and more processing time. Even worse, the echo could also be overlapped with other incoming echoes in which case the TOF estimation would be more complicated. In our case we are forced to use a rectangular envelope because of the amplitude modulation introduced by arc scanning, as we will see in section 6.3.

Prior to applying the TOF estimation methods (except for the zero-crossing method described below), the echoes are squared for full-wave rectification followed by a low-pass filter for envelope extraction. The reason for squaring instead of using the absolute value is to increase the differences between small and large sample values. Initially, a 1st order Butterworth low-pass filter (cut-off frequency 1 kHz) was used. However, the noise ripple was quite high — compared to the results reported in [Barshan and Kuc, 1992] — resulting in a poor TOF estimation (using the thresholding method described below) reaching standard deviation errors — on a 1000 echo set of data — of up to 5 samples (sampling frequency $f_s = 1 \text{ MHz}$) for each receiver. Increasing to a 2nd order filter solved the problem as seen in the smooth envelope of figure 6.4.

Three methods for TOF estimation, similar to those used in [Barshan and Kuc, 1992] and [Kuc, 1996], described below, were implemented and tested.

Zero crossing Since the frequency of the emitted pulse and the sampling frequency are known, a zero-crossing method can be applied. This method subtracts the number of samples of a half period (10) from the sample index given by the first zero crossing after a sample has exceed a pre-set threshold value. This method has the a priori advantage of not requiring either echo rectification or envelope extraction.

Thresholding A threshold value (τ) above the noise level, high enough to avoid spurious readings, is pre-set. The first echo sample whose value is above τ will determine the TOF. This is a common method used by most sonar ranging systems. In the case of the Polaroid sensor, the threshold is not accurately calculated as we saw in chapter 2. However, in systems in

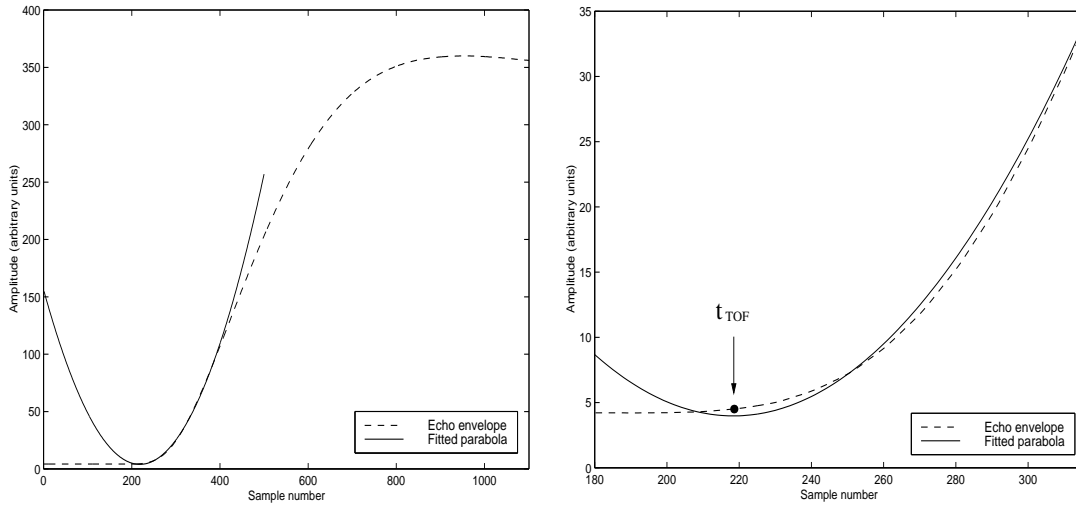


Figure 6.4: **Parabola fitting for TOF estimation.** Left plot: Parabola fitted to an echo envelope. Right plot: Zoom showing the estimated TOF (t_{TOF}) from the parabola vertex.

which the echo is acquired and post-processed, such as RoBat, the accuracy can be acceptable. Nevertheless, as addressed by Barshan and Kuc [1992], the TOF estimation will be affected by other factors such as the clock resolution and the different locations of the reflector within the active region. The latter results in variations in the part of the echo envelope which exceeds the threshold.

Parabola fitting This can be considered as an extension of the thresholding method and is intended to remove the bias introduced by the difference between the time when the threshold is exceeded (t_x) and the time when the echo arrives (t_{TOF}). After t_x is estimated, the next N samples are stored in memory and the following least squared error (LSE) method for fitting a parabola to the echo envelope is applied:

$$E = \sum_{i=1}^N (ax_i^2 + bx_i + c - Y_i)^2 \quad (6.15)$$

where E is the pre-calculated LSE fitted parabola defined by the parameters a , b , and c , x_i is the sample index, $N = 201$ is the number of samples, and Y_i is the data (echo samples). For the whole set of equations of the LSE parabola fitting see section A.3 of appendix A.

From the intrinsic properties of the parabola, the vertex, defined by

$$x_i = \frac{-b}{2a}, \quad (6.16)$$

defines the arrival time (t_{TOF}) of the echo, *i.e.* the true TOF. This is illustrated in figure 6.4.

The servomotors [Futaba, 2001] in charge of tilting the receivers of the sonarhead sometimes oscillate, especially when not in their resting position. These small oscillations are caused by the mass of the box hosting the transducer and its electronics which is a bit heavy for servomotors designed for driving light mechanisms in hobby applications. Pilot experiments suggested the need of a method for getting rid of the erroneous TOF estimations produced by these oscillations. A controller which takes the median of the last three echos (shown and described in the block diagram of figure 6.5) was devised. Using the median instead of the mean avoids components of large errors being introduced as an average.

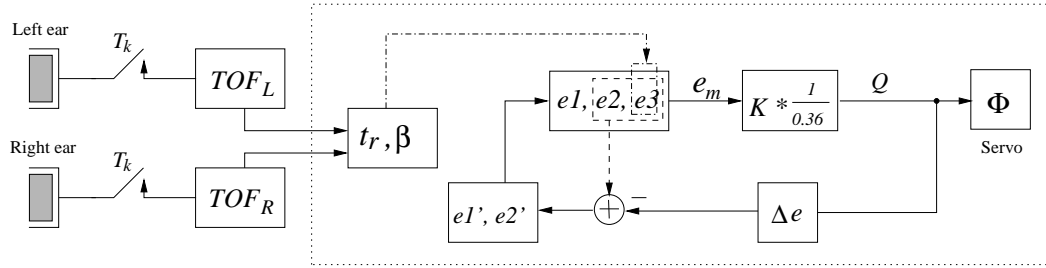


Figure 6.5: **Echo median controller.** Block diagram of the method for decreasing the noise effect in TOF estimations produced by the servomotor oscillations. True range (tr) and azimuth angle (β) of the last received echo are estimated (e_3) and combined with the two previous echoes (e_1, e_2). The median (e_m) is quantised (Q) — with both gain K and 0.36° servo resolution — as a servo command (ϕ) and subtracted (the non-quantised part Δe) from the two latest echoes of the triplet which become the new previous two (e'_1, e'_2).

Finally, the main sources of noise in our system are acoustic — coming from the environment — and thermal — intrinsic to the electronics of the sonarhead. As in [Barshan and Kuc, 1992], if we assume acoustic noise being dominated by thermal noise, the error component in each of the receivers ($e(r, \theta)$), which depends on the range and azimuth angle, can be considered uncorrelated (*i.e.* white Gaussian noise).

6.2.4 Experiments and results

For evaluating the three TOF estimation methods, 1000 consecutive echos from a reflector (post) positioned at approximately¹ 40 cm range and 0° azimuth were acquired and the TOF from each of the receivers estimated. Table 6.1 shows the comparison of the three methods.

As seen in the table, zero-crossing resulted in the worst of the three methods despite being the cheapest with respect to CPU time. Zero-crossing proved to be an effective method in [Kuc, 1996]. However, RoBat's long umbilical (mentioned in chapter 3) incorporates extra noise

¹We lack an accurate way of measuring the position of the reflectors in the space (*e.g.* laser pointer based equipment).

Method	μ_{tof-l}	σ_{tof-l}	μ_{tof-r}	σ_{tof-r}	μ_{time}
Zero-crossing	2153.31	10.46	2173.95	10.36	129.77
Thresholding	2115.39	0.77	2106.49	0.66	767.04
Parabola fitting	2117.57	0.71	2119.77	0.61	770.91

Table 6.1: **Comparison of TOF estimating methods.** Mean and standard deviations of TOF estimated by the receivers (units in samples) for each method along 1000 consecutive echoes from a reflector (post) positioned at approximately 40 cm range and 0° azimuth. Mean of the CPU time for each method (units in μs).

which results in an unreliable TOF estimation. Thresholding and parabola fitting performed very similarly both in TOF estimation and CPU time although the latter performed slightly better than the former (TOF-wise) as expected and with very little extra cost in CPU time. The reason of this small difference in CPU time between thresholding and parabola fitting is because of the pre-calculation of the LSE fitted parabola, *i.e.* a generic parabola is used for all echoes.

Having selected parabola fitting as the method for estimating TOF, experiments comparing the two geometric models — the collinear approximation and the real geometry model — were performed, together with a second version of the real geometry model upgraded with the median controller. The collinear approximation assumes a three-transducer array positioned on the same vertical and horizontal axes, as in [Barshan and Kuc, 1992]. The real geometry model introduces the offset of the receivers with respect to the emitter (see figure 6.2). ‘Real + median’ is the real model upgraded with the median controller method. The results of the experiments are summarised in table 6.2.

Surprisingly, the real model performed slightly worse than the collinear approximation for the angle estimation (σ_{angle}). The median method improved a bit with respect to the real model. The range estimation was slightly better in the real model than in the collinear approximation. Introducing a new parameter (h) in the model makes it a bit more complex, resulting in an extra source of noise.

To see the effect of h on the true range and azimuth angle estimation in the real model, the partial derivatives $\left(\frac{\partial r}{\partial h}, \frac{\partial \beta}{\partial h}\right)$ were calculated. For details of the derivative calculations see section A.2 of appendix A. The partial derivatives were evaluated in simulation with the TOFs T_L and T_R from a reflector positioned in the different cells of a grid defined along the transmitter-right ear semi-plane. The results are shown in figure 6.6.

In the figure, the Y axis corresponds to the heading distance (range) between the sonar-head’s origin and the target. The X axis corresponds to the passing distance (azimuth angle). Note the much smaller scale (10^{-3}) of the azimuth angle compared to the range. For both

Model	μ_{range}	σ_{range}	μ_{angle}	σ_{angle}
Collinear approx.	36.23	0.022	0.43	0.152
Real model	37.99	0.021	0.46	0.162
Real + median	37.99	0.021	0.46	0.155

Table 6.2: **Comparison of the two geometric models.** The table shows mean and standard deviations of the range (units in cm) and azimuth angle (units in degrees) of 1000 consecutive echoes from a reflector (post) positioned at approximately 40 cm range and 0° azimuth. ‘Real + median’ is the real model upgraded with a method for discarding erroneous measurements (see text).

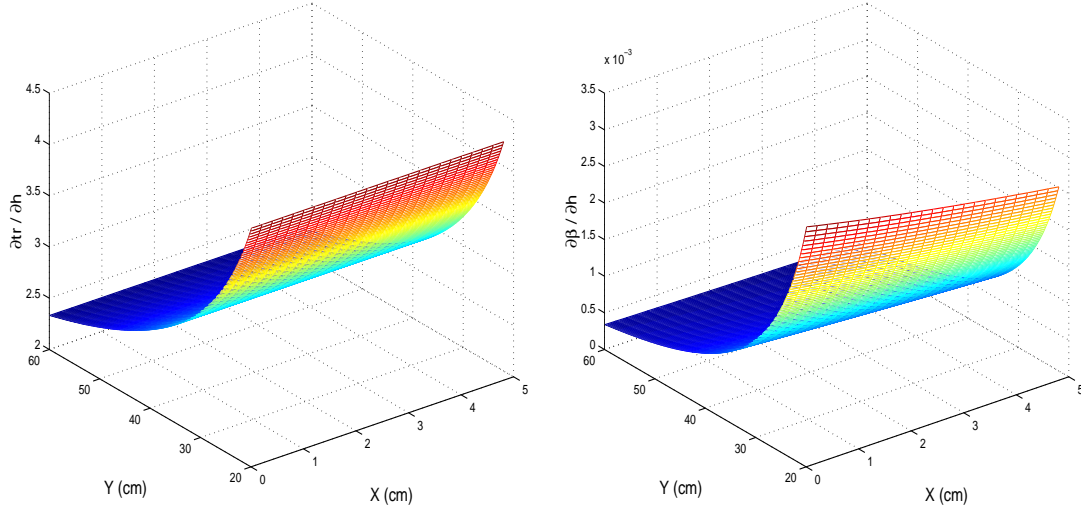


Figure 6.6: **Effect of the receivers’ offset (h) on range (left plot) and azimuth (right plot).** The plots show simulated experiments performed in the active region of the transmitter-right ear semi-plane. (Note the $\frac{1}{1000}$ scale of the right plot.)

cases, and within the portion of space evaluated, the derivative decreases with range and remains almost constant for azimuth angle, suggesting that the error depends more on the range than on the azimuth angle, *e.g.* at 60 cm range (left plot), an error in h of 1 cm will result in a 2.4 cm error in range measured.

To choose a suitable gain (K) for the servomotor in charge of panning the sonarhead (see figure 6.5), a comparison of range and azimuth angle estimation across different K 's using the real model — with and without the median controller — was done. A proper gain is necessary for adjusting the response of the system to its sense-and-act requirements and also for compensating the error introduced by quantising the azimuth angle in a servo command. The resolution of the servos is 0.36° per servo count for a 90° range. Alternatively, as we will see in next section, the range can be doubled to 180° at the cost of a 0.72° resolution. For the orientation angle of the receivers (γ) a gain of $K = 1$ can be chosen without specific experimentation

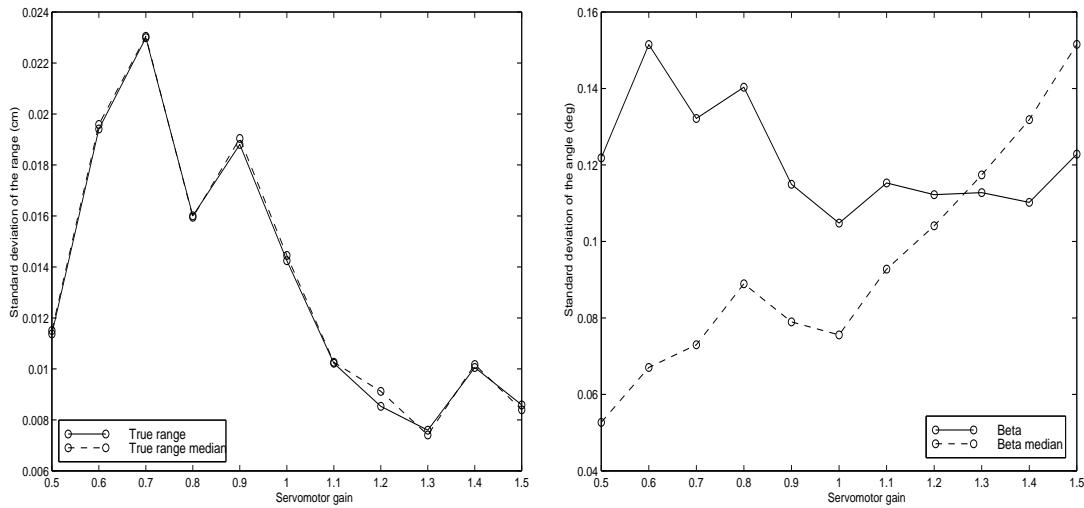


Figure 6.7: **Effect of the servo loop gain** on the target range (left plot) and target angle estimation (right plot) for the real model and the real model with the median method incorporated. (Note the $\frac{1}{10}$ scale of the left plot.)

because its dependency with the target's range results in small angle increments.

RoBat was set to focus on a post positioned at an arbitrary range and azimuth angle for 1000 echoes, repeating the experiment for K values ranging from 0.5 to 1.5. In figure 6.7, the standard deviation of the true range (left plot) and azimuth angle (right plot) versus the servo loop gain K is shown.

As seen in the figure, the performance of the real method with and without the median controller is practically the same for the range estimation, the error being minimum for K values between 1 and 1.5. For the azimuth angle, the median controller improves performance significantly in almost all the cases, the error being minimum for K values between 0.5 and 1. Thus, from the intersection of these intervals, a gain of $K = 1$ is chosen. The next step is to devise a method for estimating the elevation angle, described in the next section.

6.3 Elevation cues: Arc scanning

In chapter 2 we saw the importance in Rhinolophids and Hipposiderids of pinna motion along vertical arcs for recovering elevation cues [Griffin et al., 1962; Pye et al., 1962; Pye and Roberts, 1970]. This is crucial when spectral cues in the echoes are unavailable because of emitting a narrowband call.

More recently, Walker [1997] hypothesised that by sweeping their pinnae through opposite vertical arcs (as in figure 6.8), CF-FM bats may create dynamic cues (in the form of frequency and amplitude modulations) which vary systematically with target elevation. As seen in chapter

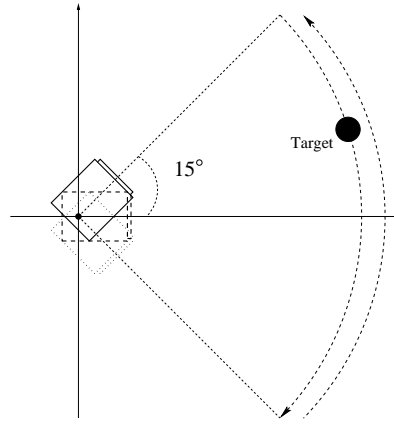


Figure 6.8: **Arc scanning for elevation angle estimation.** Sketch showing the side view of a receiver performing arc scanning along 30° arcs.

3, Walker proposed two methods in which the cues obtained from these pinna movements — named ‘arc scanning’ — could be extracted: IID rates of change, and peak delays. In this work we pay attention to the latter. Two main properties of this method are its independence of TOF, and monaurality. The former allows us to estimate the elevation angle of a reflector providing that the time at which the receivers start moving is known and the echo is long enough for the receivers to point at the reflector’s elevation during the echo arrival interval. The latter allows elevation estimation with only one receiver, *i.e.* using monaural peak-delays. Moreover, if two receivers moving in opposite directions are used, elevation can be estimated from the relative difference between the monaural peak-delays, *i.e.* from binaural (or inter-aural) peak-delays.

6.3.1 Methods

The receivers start moving synchronously with call emission. This guarantees peak estimation for targets positioned in the vertical border of the sound field, whose limits ($\pm 12.5^\circ$) are constrained by the main lobe of the Polaroid’s radiation pattern. Moving asynchronously — *e.g.* before call emission — could result in a receiver missing the peak of the echo, *i.e.* scanning the target before being insonified. The same applies for peak estimation at the end of the scan. This, which depends on echo length, is constrained by the angular velocity of the servos. Pilot experiments proved echo lengths of 140 ms sufficient for a complete coverage of the frontal sound field by a receiver scanning 30° . To guarantee synchronisation of the receivers with call emission, precise timing of the servos in charge of tilting the receivers is needed. This was performed by directly reading from the servo controller through the serial port, as described in section C.2 of appendix C.

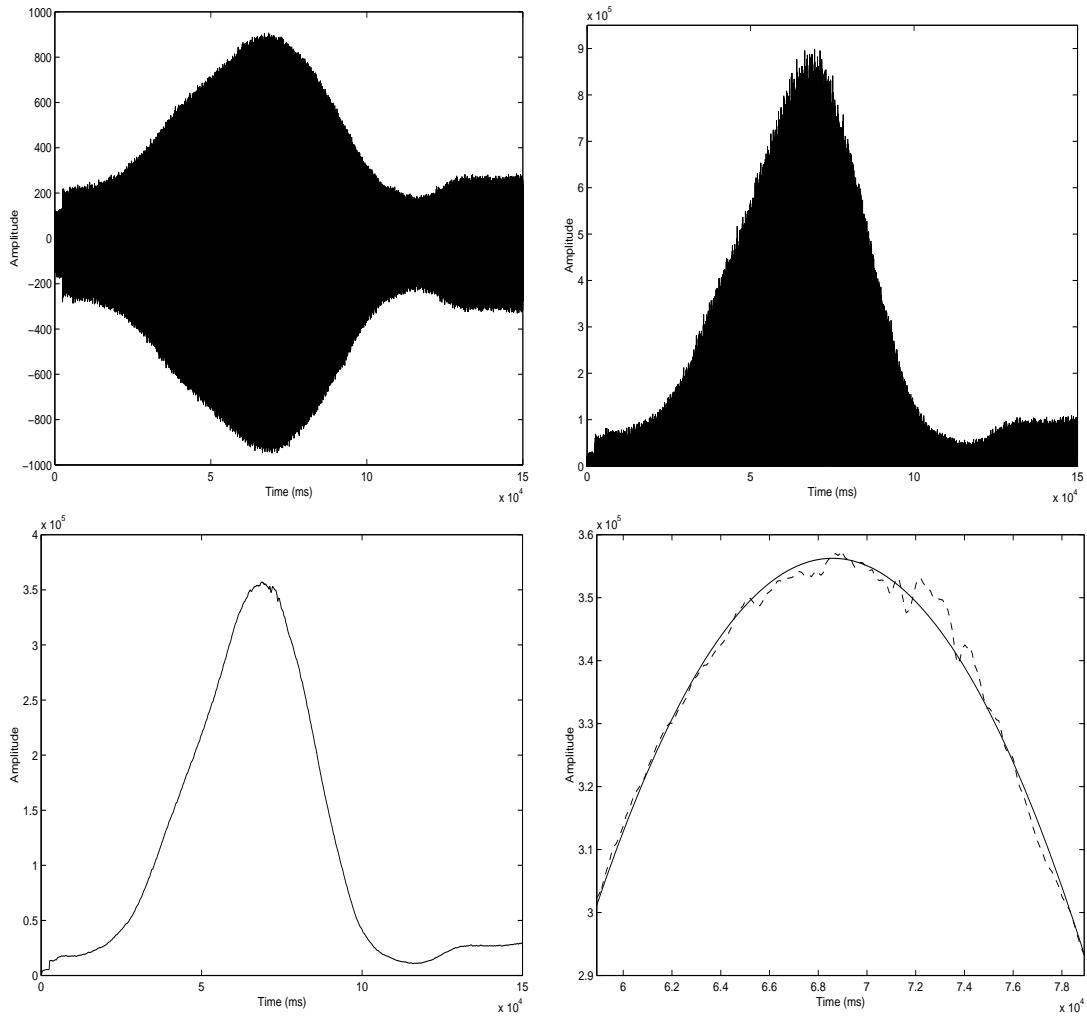


Figure 6.9: **Peak detection process in echoes after arc scanning.** Received echo shows amplitude modulation as a result of arc scanning (top-left). Full-wave rectified echo by squaring (top-right). Echo envelope after low-pass filtering and rough peak detection (bottom-left). Parabola fitting for accurate peak detection (bottom-right).

Peak detection was performed by two different methods after full-wave squared rectification and low-pass filtering (as in TOF estimation) of the arc scanned echo: echo peak and parabola fitting. The former simply stores in memory the maximum sample value (*i.e.* the peak) across the whole echo envelope. The latter aims to compensate the error of the echo peak method due to noisy envelopes. The envelope of the arc scanned echo (see bottom-left plot of figure 6.9) resembles a parabola, thus the motivation for applying a curve fitting technique — as in TOF estimation — for accurate peak detection. After the “noisy” peak is estimated, a number ($N' = 5000$) of echo envelope samples prior and posterior to the peak are stored. For speeding up the process, a decimation by a factor of 50 is applied, ending with a set of samples

of size $N = 201$, whose index is given by $x_i = [-100, \dots, +100]$ where 0 is the noisy peak. Then, applying the LSE method of equation A.13, a parabola which fits the decimated data is obtained (see bottom-right plot of figure 6.9). Finally, the vertex of the parabola given by equation 6.16 defines the true peak, whose true sample index is then recovered by interpolation.

For calculating the monaural and binaural peak-delay versus elevation angle profiles, an accurate method for estimating the elevation of the reflector under test is needed. Since we lack this method, an alternative method in which the receivers' elevation axis was tilted instead of the sonarhead's was used. The post reflector was put in front of the sonarhead, whose emitter was fixed at 0° elevation, and the receivers' elevation axis tilted according to the elevation angle measured. Thus the 30° scans were performed over different elevation axes while the emitter insonifies the post. This method also guarantees proper target insonification for all elevations, which is necessary for a reliable estimation of the profiles. The median controller used for the azimuth and range experiments is also used in the arc scanning experiments.

For the arc scanning experiments, the resolution of the servos was set to 0.72° per servo count, permitting a servo range of 180° . This is because the range of the servos went beyond the 90° allowed by the previous 0.36° resolution when performing the profile estimation method described above. In the experiments described in the next section, the terms positive and negative arc scanning are used. We define 'positive' arc as ear_L scanning upwards while ear_R scans downwards, and negative arc as the inverse case.

6.3.2 Experiments and results

A comparison between the two methods for peak-delay estimation described in the previous section was done. The experiment consisted of the sonarhead continuously performing positive and negative scans while insonifying a reflector (post) positioned at approximately 40 cm range and 0° elevation. The mean and error of the peak estimated by each ear over 100 echoes (50 echoes scanning upwards and 50 scanning downwards), and the mean of the CPU time required for a complete scan by each method are shown in table 6.3.

Since the reflector is at 0° elevation, the peak-delay estimated by both ears should be the same if the servos are correctly calibrated and have the same response (*i.e.* behave similarly). As seen in the table, both servos performed similarly when scanning downwards (peak-delays of 67 ms). However, when scanning upwards, the right ear behaved quite differently with respect to the left ear. Moreover, the latter keeps very close to the downward scans (peak-delays of 68 ms) suggesting a decent calibration of the servos. The large variation of peak-delay estimation of the right ear when scanning upwards is due to a malfunctioning of its servo. As seen from the error values in the table, the parabola fitting method performed better than the

	LEFT EAR		RIGHT EAR		TIME
	upwards	downwards	upwards	downwards	
METHOD	$\mu \pm \sigma$	$\mu \pm \sigma$	$\mu \pm \sigma$	$\mu \pm \sigma$	μ
Peak	68.19 ± 0.21	67.85 ± 0.27	58.48 ± 0.48	67.27 ± 0.24	14.22
Parabola	68.63 ± 0.08	67.24 ± 0.19	58.28 ± 0.21	67.82 ± 0.13	24.62

Table 6.3: **Comparison of peak-delay estimation methods.** Mean and error of the peaks estimated by the two methods while each ear scans upwards and downwards (units in ms). Mean CPU time needed for a whole arc for each method (units in ms). Data from 50 echoes (for each case) from a reflector (post) positioned at approximately 40 cm range and 0° elevation.

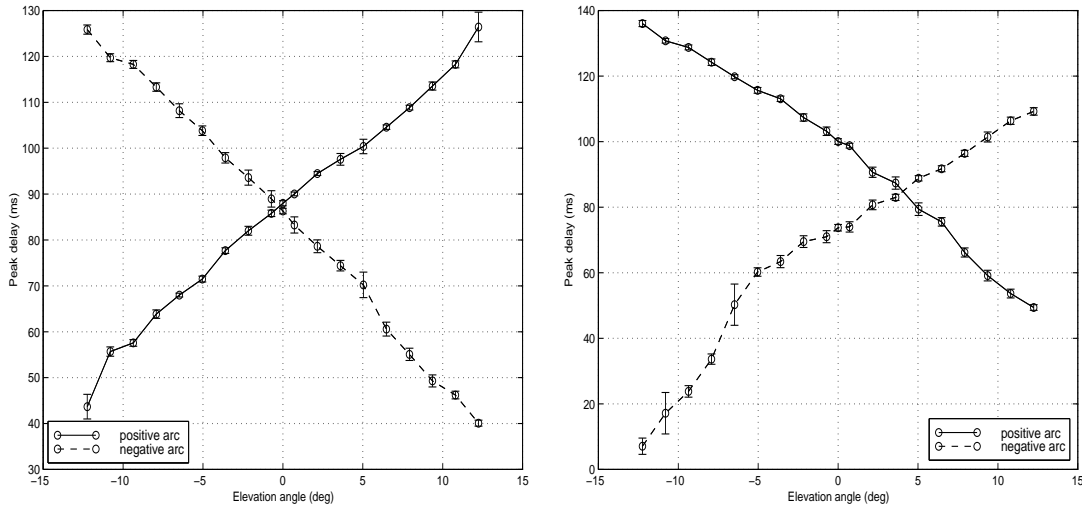


Figure 6.10: **Monaural peak-delay profiles** for the left receiver (left plot) and the right receiver (right plot) along positive and negative arcs of 30° . Blobs represent mean of 50 echoes, error bars show standard deviation.

simple peak method in all the cases, as expected. The former method has an extra cost in CPU time of roughly 40% with respect to the latter.

The next step was to estimate the peak-delay vs. elevation angle profiles for both monaural and binaural arc scanning using the method in which the receivers' elevation axis is tilted, as described in the previous section. Figure 6.10 shows the monaural peak-delay profiles estimated by each ear along positive and negative scans of 30° . The blobs indicate the elevation angle of the target given by the tilt of the receivers' elevation axis. This axis is tilted at increments of twice the resolution of the servos selected for these experiments, *i.e.* 1.44° , from -12.24° to 12.24° .

As seen in the figure, the left ear's profile is quite linear for both positive and negative arcs, specially between -11° and 11° . Moreover, both profiles cross the 0° elevation coordinate very closely (offset of 0.6 ms) as expected from the data in table 6.3. The right ear's profiles

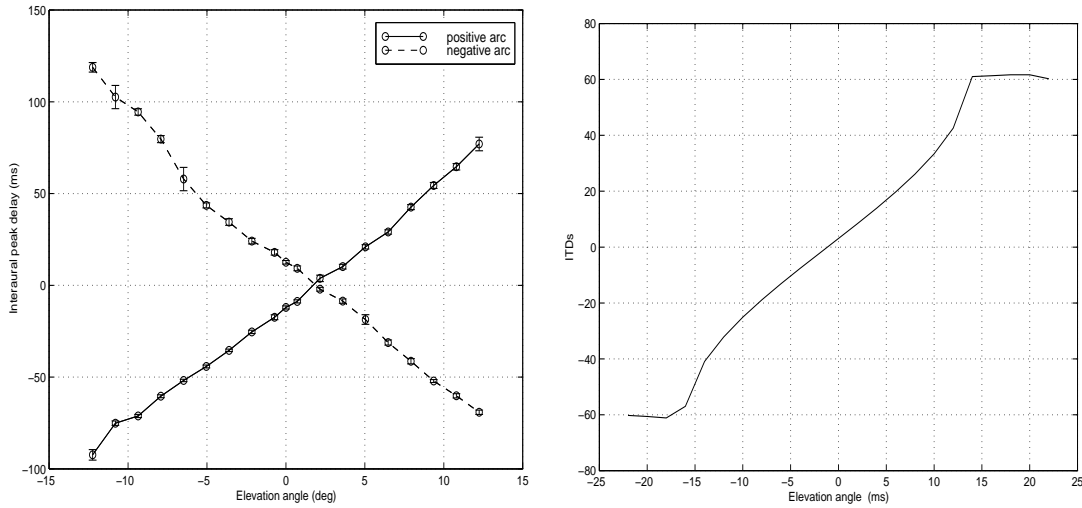


Figure 6.11: **Binaural peak-delay profiles.** Left plot: Real data obtained with the sonarhead while scanning along 30° arcs. Blobs represent mean of 50 echoes, error bars show standard deviation. Right plot: Simulated data obtained with the software model of the sonarhead (only positive arc shown).

are, as expected from table 6.3, not as good as the left ear's. The strange behaviour of the servo when scanning upwards (*i.e.* during the negative arc) is clearly seen in the figure. It has a faster response than the other servo, reaching -12.24° elevation in roughly 8 ms whereas the right servo takes 42 ms. This affects both linearity (specially between -12.24° and $-6.48.24^\circ$ as indicated by the larger error bars) and the 0° elevation crossing point.

The binaural peak-delay profiles for both positive and negative arcs are shown in the left plot of figure 6.11. The bad performance of the right receiver's servo can be appreciated, although its effect is slightly compensated by the better performance of the left receiver's servo. The low error bars of the profiles (except for the upwards scan of the right ear) indicate good repeatability of the servos while performing arc scanning. The right plot shows the binaural positive arc profile obtained from simulated data using the software model of the sonarhead, showing linear behaviour in the same interval as the real data profiles.

Once the monaural and binaural arc scanning profiles have been obtained, the next step is to find the line which best fits them in order to obtain a peak-delay per elevation angle linear relation. These lines are estimated applying the same LSE method as with the parabola (described in section A.3 of appendix A), the number of points ($N = 29$) given by the different elevation angles at which the measurements were taken. Figure 6.12 shows the line fitting of the monaural profiles. The left ear fittings suggest a better monaural arc scanning performance than the right ear (specially when scanning upwards). Figure 6.13 shows the line fitting of the binaural profiles for positive and negative arcs. The fitting of the positive arc is better than the

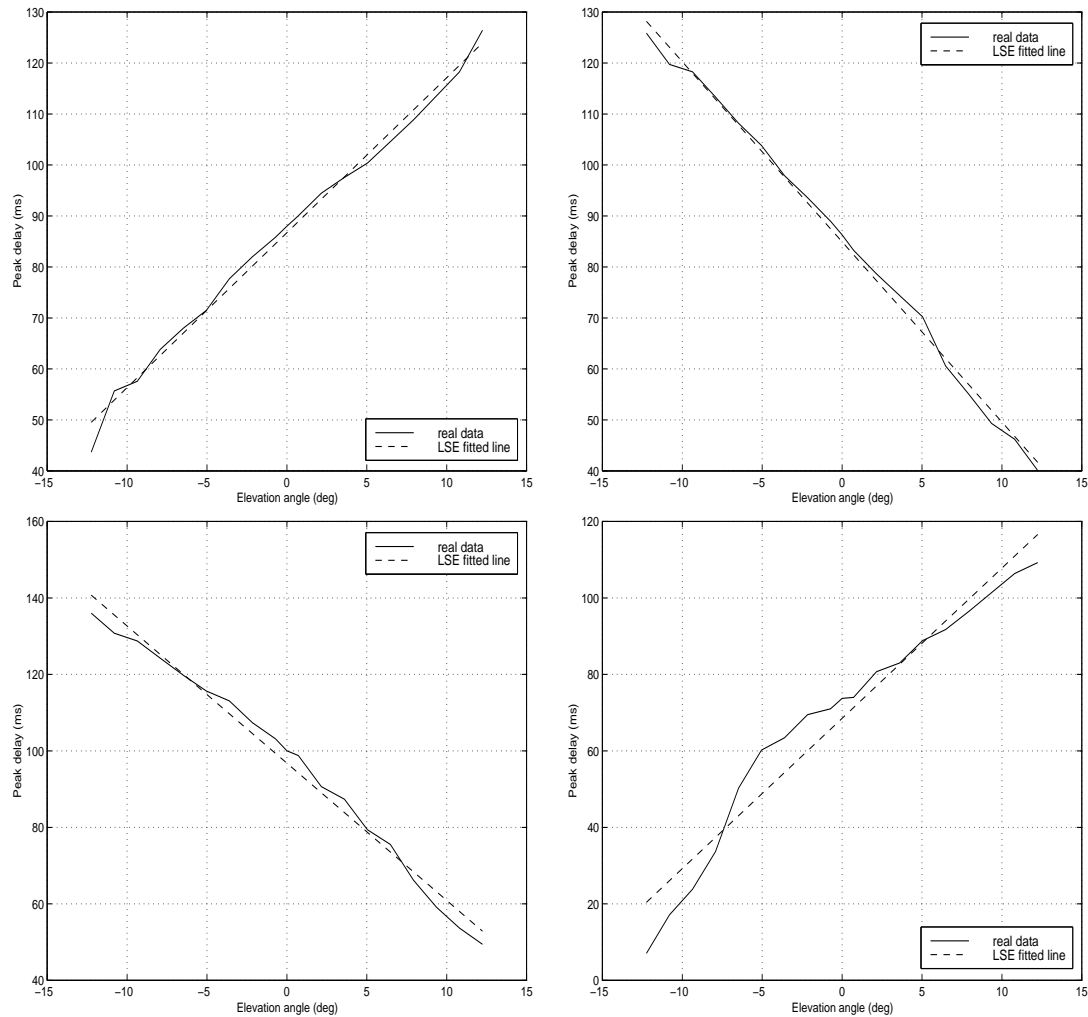


Figure 6.12: **LSE line fitting to monaural peak-delay profiles.** Top plots: Left ear during upwards (left) and downwards (right) scans. Bottom plots: Right ear during downwards (left) and upwards (right) arcs.

negative arc as expected.

At this point, the equations of the lines fitting the different profiles can be used conveniently depending on the location of the target with respect to the active region. This could lead to situations in which one ear receives signal from an echo while the other does not. In such case, the insonified ear's monaural profile is used for estimating the elevation of the target. Otherwise, the binaural profiles can be used. As seen in table 6.3, the CPU time required to compute a whole binaural arc is about 25 ms. Adding this to the approximately 400 ms required by the PC to transfer the 150 ms echo from the acquisition board to memory positions, we end up with approximately 425 ms per binaural scan, *i.e.* 2.3 sense-and-act cycles per second.

In this section we have seen how Walker's [1997] arc scanning hypothesis can be imple-

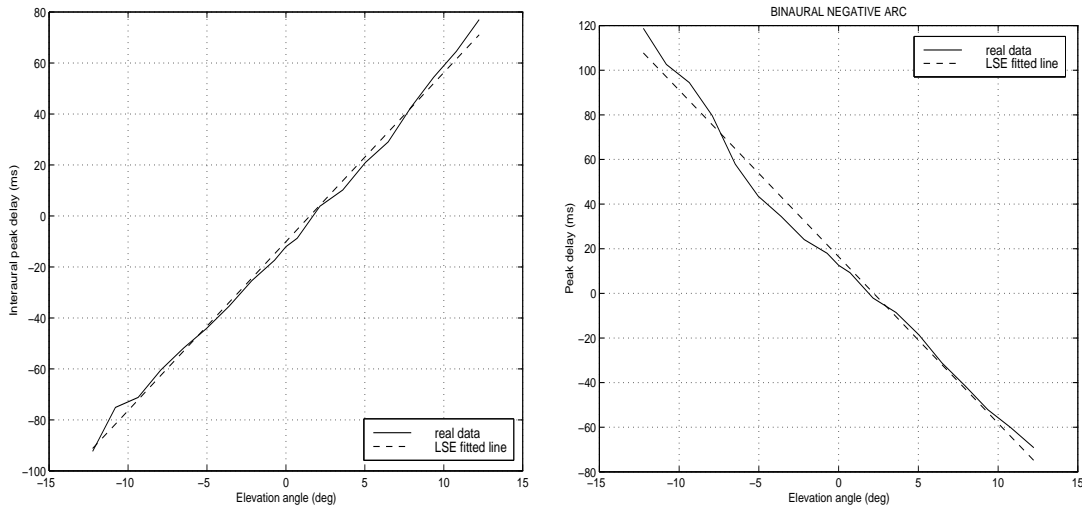


Figure 6.13: **LSE line fitting to binaural peak-delay profiles** for positive (left) and negative (right) arcs.

mented and executed in real time in RoBat. In the next section we discuss methods for integrating both arc scanning and the adaptation of the 2D geometric model of Barshan and Kuc [1992] in a 3D tracking system.

6.4 Towards a 3D tracking system

In this section we introduce and discuss the way for integrating the methods for object localisation in the azimuthal and elevation planes seen in the chapter.

As we mentioned in section 6.2, Barshan and Kuc [1992] system allows true range and azimuth estimation of an object located along the system line-of-sight, *i.e.* elevation 0. Hence, the further the target is from this elevation, the less reliable is the method. However, as long as one of the receivers gets insonified, arc scanning does not depend on azimuth. When this is the case, monaural cues are used for estimating the elevation angle and tilting the sonarhead to the target's elevation. At this point, and assuming sense-and-act loops fast enough to cope with real world situations (*i.e.* a moving target), the erroneous azimuth and range estimation of the previous echo will be corrected. Conversely, the azimuth and range estimation method — even when the target is at an elevation different than 0° — will help to better estimate the elevation angle by making the target fall in the active region, thereby allowing binaural elevation estimation. This permits the choice of monaural or binaural cues.

The simplest way to integrate the azimuth and elevation estimation methods is to alternate them one at a time. From the results in section 6.3 we chose to use the positive arc binaural

profile. Thus, the sonarhead will start with the right receiver pointing at 15° and the left receiver at -15° . A positive scan will be performed next at the same time the call is being sent (in analogy to the correlation between pinna movements and call emission in CF-FM bats). After estimating the elevation — either by monaural or binaural cues — and updating the sonarhead tilting axis, the receivers return to point at the 0° default position for azimuth and range estimation. The individual orientation of the receivers (γ) is also performed. This is expected to increase the SNR in the echoes and therefore allow more accurate peak-delay estimation. After the sonarhead updates the new azimuth angle, the receivers return to positive scan position and a new elevation-azimuth estimation cycle begins.

An experiment in which an 8 cm diameter plastic ball was positioned in front of RoBat at, approximately, 35 cm range, -1° azimuth and 8° elevation, was performed. The aim was to see how the tracker performs when RoBat, starting at coordinates (0,0) in azimuth and elevation, modifies its coordinate system (*i.e.* tracks) to the target's and has to remain stable on it.

The spatial location was subject to small variations during the experiment due to a smooth swinging of the ball, caused by its very light weight being affected by normal air flow in the laboratory. The short range of the target (which also applies to maximum distances of 1 m *i.e.* 6 ms worth of echo) and the minimum time required by the servos to reach the $\pm 12.24^\circ$ maximum elevation from the original $\pm 15^\circ$ position (8 ms for the right ear scanning upwards according to figure 6.10), guarantees echo arrival — and therefore peak-delay estimation — even in the worst case, *i.e.* when the target is at $\pm 12.24^\circ$ elevation. The length of the call and the echo reception time window are adapted according to the cue being estimated, *i.e.* 150 ms call for elevation estimation and 4 ms call for azimuth and range.

Figure 6.14 shows the estimation of the ball's elevation angle for different servomotor gains along 45 echoes. This angle is not the elevation angle at which the sonarhead was pointing — which is constrained by the 0.72° resolution of the servos — but the angle estimated by the tracker. Hence, the sonarhead tilt axis fluctuates between the two closest multiples of 0.72° surrounding the estimated elevation, *i.e.* 7.92° and 8.64° for the target's 8° elevation in the experiment. These fluctuations are also due to the error in the LSE line fitting of the profiles and to the smooth swinging of the ball. As seen in the figure, a gain of $K = 0.5$ over-damps the response of the tracker whereas a gain of $K = 1.3$ produces overshooting. A compromise gain value of $K = 0.9$ gives a fast response (reaching 8° elevation in 3 echoes) and remains between $\pm 0.72^\circ$ of such elevation.

One of the drawbacks of this tracker implementation is the time spent in moving the receivers to the starting position of both the azimuth and elevation estimation methods. A more sophisticated and complex tracker would integrate range, azimuth and elevation in a single

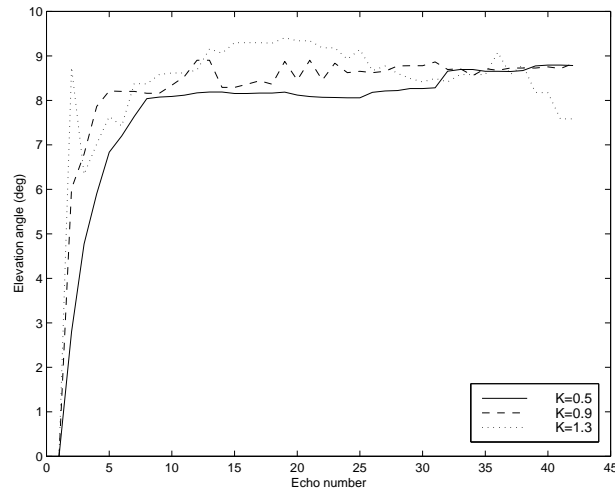


Figure 6.14: **Target elevation angle** estimated by the 3D tracker for different servomotor gains along 42 echoes (target positioned at approximately 35 cm range, -1° azimuth and 8° elevation).

scan, as CF-FM bats seem to do [Griffin et al., 1962; Pye et al., 1962; Pye and Roberts, 1970]. In such case, the arc scanning method would be no longer TOF independent, as azimuth and range would be estimated as the ears move. Moreover, the geometric model would no longer be valid since the y coordinate of the receivers' origin (see figure 6.2), which will be different than 0 at the starting position, will vary along time. Hence the angle at which the receiver is pointing when TOF is being estimated will be needed. This could be provided by more accurate motors (*e.g.* stepper motors) with absolute encoders.

A pilot experiment similar to the one in figure 6.14 resulted in a severely unstable performance. Looking at the data we found another pitfall of this tracking method: erroneous TOF estimations arising from the adverse SNR conditions introduced by arc scanning, *i.e.* when the receivers do not point at the target on echo arrival. This suggested the need of a better method for simultaneously estimating TOF with arc scanning.

6.4.1 Discussion

At this point we have seen how arc scanning can be simply combined with a 2D object localisation model which exploits the geometry of the sensor for performing 3D target tracking. In this tracker system, temporal cues have been used for estimating the range, azimuth and elevation of a target in the space, however, it is important to note the possibilities of amplitude cues which have not been exploited in this work. For instance, using IIDs would allow the building of a smaller sensor whose accuracy will depend only upon the sensitivity of the receivers and

their relative orientation. In such case, IIDs could be combined with arc scanning as the IID rates of change proposed by Walker et al. [1998b]. For range estimation, differences in sound pressure can be used provided that the system has a priori knowledge of the target shape and size.

Moreover, adding artificial pinnae to the receivers can improve their directional sensitivity — by maximising the angular resolution of the transducers — and echo amplitude. As we will see in chapter 7, by using artificial pinnae, echolocating behaviours such as arc scanning and IIDs could be replicated more successfully than using only bare transducers.

6.5 Summary

In this chapter we have seen how the spatial position of a target reflector can be estimated by exploiting both the physics of narrowband echolocation and the dynamics of the sensor. Moreover, instead of using extra receivers to measure target elevation (as in *e.g.* [Kuc, 1993]), we employ the sensor's motion to create additional virtual receivers.

First, Barshan and Kuc's [1992] active method for estimating the azimuth and range of a target was adapted to the geometry of RoBat's sonarhead. Different TOF estimation methods were tested, the LSE parabola fitting being the most accurate. A comparison of the original (collinear) geometric model with the adapted (real) model, and an upgraded version incorporating a median based controller for removing the effect of erroneous TOF estimations was implemented. Surprisingly, the real model performed slightly worse than the collinear approximation for estimating the azimuth angle, although the differences in performance were minimal.

Walker's [1997] arc scanning hypothesis for elevation cue extraction in CF-FM bats was implemented in RoBat for estimating the elevation angle of a reflector. Peak-delays were chosen as the temporal cue to be extracted from the arc scanned echoes. Peaks were accurately estimated from the vertex of an LSE fitted parabola. Monaural and binaural arc scanning profiles were obtained experimentally and peak-delay per degree transformations were calculated by LSE line fitting for all of the cases.

The integration of both techniques in a 3D tracking system was performed in the simplest way, *i.e.* applying both methods independently. A more sophisticated method in which the TOF of both receivers is estimated at the same time than performing arc scanning was proposed. The method, which needs the geometric model to be revisited and a better TOF estimation method, would allow estimation of range, azimuth and elevation in a single scan.

Chapter 7

Outer ear: from multiple reflectors to surfaces

7.1 Introduction

This chapter describes a joint investigation with Kim, Kämpchen, and Hallam on designing artificial pinnae for RoBat using genetic algorithms (GAs). The aim of this investigation is twofold: to improve the echolocating capabilities of the biomimetic sonarhead, and to obtain insights on the role of pinnae in CF-FM bats for specific echolocating behaviours such as arc scanning and IIDs.

Nature is full of impressive examples of how evolution has exploited new sensory channels. Nowadays, the topic of sensor evolution, situated among biology, robotics and artificial life, is becoming a very modern and promising field of research (see *e.g.* [Kortmann et al., 2001; Liese et al., 2001]). From this new discipline, new concepts for the design of sensors for adaptive robots can be gained. Also, it can help understanding the relationship between the information available to an agent and the way it is processed. In animals, adding pinnae to ears creates directional cues which enable them to do more than simply lateralise a sound source/reflector but to “project” the source out to a well-defined location. This allows the perceiver to determine attributes of front-back-above-below for the incoming sound. In many species, mechanisms underlying 3D target perception are believed to employ the passive acoustic filtering properties of the head and pinnae to provide spectral cues which encode 3D target angle [Shaw, 1974; Obrist et al., 1993; Fay and Popper, 1996]. However, less attention has been focussed on the role that dynamic reorientation of the head and pinnae may play in the creation of cues essential for sound source/reflector localisation.

As we saw in chapters 2 and 6, in several narrow-band emitting microchiropteran species

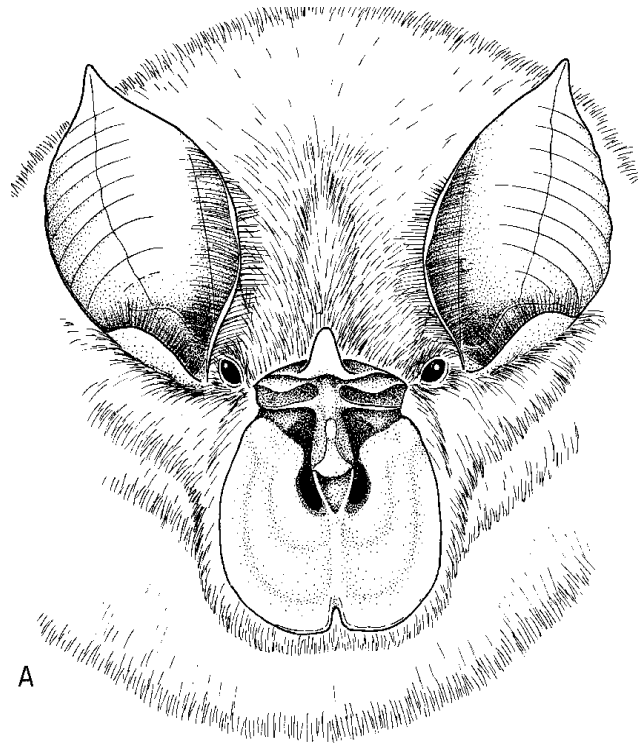


Figure 7.1: Drawing of *Rhinolophus ferrumequinum*. (Copyright by Martin Trappe)

(mainly species in the families Rhinolophidae and Hipposideridae) spectral cues are unavailable and systematic pinnae movements are heavily employed in the perceptual mechanisms underlying 3D target localisation and tracking [Griffin et al., 1962; Pye et al., 1962; Pye and Roberts, 1970]. This was investigated in chapter 6, showing — with a robotic implementation — how the elevation angle of a reflecting target insonified with a narrowband call can be estimated.

As part of the RoBat project, we pursue improvement of the directional sensitivity of the sonarhead's receivers (*i.e.* maximise the angular resolution of the receiving transducers), as well as the echo amplitude, by adding artificial pinnae to them. As a result of this increased discrimination, echolocating behaviours such as arc scanning and IIDs could be replicated in the sonarhead more successfully than using only bare transducers. Thus, as a target system, we choose *Rhinolophus ferrumequinum* which has large and highly mobile pinna compared to the size of its head as can be appreciated in figure 7.1.

This chapter is structured in two main and differentiated parts: the first, from section 7.2 to 7.5, describes joint work with Kim and myself, supervised by Hallam. The second part (section 7.6) summarises the continuation of the first part, done by Kämpchen [2000] during his Master's project, which I proposed, co-supervised with Hallam, and in which I was much

involved. The whole joint work was finally published as [Carmena et al., 2001].

7.2 Previous work on artificial pinnae

First attempts in evolving bat pinna morphology [Papadopoulos, 1997; Peremans et al., 1998b] used genetic algorithms (GAs) to evolve simple pinna shapes for broadband echolocators because of the difficulty of designing a pinna model by an analytical approach. The evolved solutions were evaluated on the *3D Echolocation Simulator*, a software model of the biomimetic sonarhead presented in chapter 3 (for a fully description of the simulator see [Walker, 1997]).

The pinna was modelled by up to three disc reflectors whose position and orientation angle around the receiving transducer were determined by a GA, using a chromosome with the following structure,

$$(x_1 \ y_1 \ z_1 \ \alpha_1 \ \beta_1 \quad x_2 \ y_2 \ z_2 \ \alpha_2 \ \beta_2 \quad \dots \quad x_n \ y_n \ z_n \ \alpha_n \ \beta_n)$$

where x, y and z are cartesian position coordinates and α, β are azimuth and elevation angles. The GA comprised a population of candidate sets of reflector positions, whose fitness was determined by simulating their effect on the acoustic signals transduced by the receiver. 2-point crossover and a mutation rate of 0.03 were used with a population of 100. This was found a suitable size given the existing computing facilities and the number of parameters to be evolved. A tournament-selection scheme of size 8 wherein a set of genomes is randomly selected from the population was used. The fittest genome in the set was chosen with a given probability; if not selected, then the second best is selected with the same probability, and so on. Experiments were run for 1000 generations. An example of the GA's encoding for a 3-reflector configuration can be seen in section B.2 of appendix B.

The GA in [Peremans et al., 1998b] was set two tasks: first, to deploy reflectors in a monaural system so as to maximise the displacement between the axes of maximal sensitivity at 30 kHz and 90 kHz (thereby allowing target elevation to be most accurately inferred from the different amplitudes of the echo at these frequencies); and second, to deploy reflectors in a binaural system to produce a maximally steep IID curve with respect to target angular position (thereby maximising the angular resolution of the binaural system and allowing the target's position to be most accurately estimated from the IID). In the binaural case, the left ear was symmetrical with the right ear, *i.e.* the two pinna configurations were derived from the single disposition of reflectors indicated by the GA. The results for the first experiment were reasonable, but for the second experiment no significant improvement of the IID performance could be obtained with up to three reflectors.

7.3 Exploiting the initial model

Such work was continued by us [Kim et al., 2000] applying similar model considerations as [Peremans et al., 1998b], that is: disc-shaped specular reflectors were used to modify the directionality characteristics of a dynamic binaural echolocation system. The differences with respect to [Peremans et al., 1998b] were the consideration of sound losses in the reflectors due to absorption, instead of considering perfect reflection, and the way in which the phase cancellation phenomena was calculated. An absorption rate of the reflectors of 20% of the incident sound was assumed. Phase cancellation among different echos from the reflectors when arriving at the transducer was also considered. As in [Peremans et al., 1998b], neither the diffraction and diffusion phenomena around the edges of the reflector discs nor multiple reflections were taken into account, *i.e.* each reflector introduced one additional echo path. The reflectors' radii were constant and equal to that of the receiver and their orientation angles varying between -90 and +90 degrees with a resolution of 2 degrees.

In [Kim et al., 2000], two different methods were considered, a signal based method and a region coverage method, the latter being the chosen one because of its smaller processing time.

Signal based method This method was based on the one used in [Peremans et al., 1998b] for IID behaviour. In our case, because of the arc scanning behaviour, we were seeking a high amplitude-modulated signal with sharp peaks for a better delay-per-degree estimation. For that purpose, a fitness function $F = A/\sigma$, where A is the maximum amplitude value during the arc scanning and σ is the standard deviation of the time-varying amplitude along time during the arc scanning, was used. This fitness function would possibly guarantee clarity of target position. The method was finally rejected because of the high amount of computational time required.

Region coverage method This was based on the following assumption: having an ear morphology whose left ear focuses on the left side of the target's position along azimuth angle and the right ear on the right side, a broader range of IIDs can be obtained. In this method we also sought to evolve a reflector formation for both a good IID range and arc scanning. For the IID case, targets at every azimuth and elevation angle were considered while for the arc scanning case we only considered *slices* of the vertical plane, *i.e.* all elevation positions for a fixed azimuth.

The fitness function aimed to combine this covered region method with the phase cancellation constraint, thus no reflector should be positioned in a location where, from any of the possible target positions, phase cancellation happens. Based on this criterion, our fitness

function was defined as

$$L = \alpha \left| \sum_{k=0}^N e^{-i(\omega t + \theta_k)} \right| + \beta \left(\sum_{i=1}^N \sum_{k=1}^M r_{ik} \right)$$

where N is the number of reflectors, M is the target position, θ_k is the phase of the wave coming from reflector k and r_{ik} is set to 1 if the i -th reflector can reflect the left-sided target k on the left transducer (otherwise it is set to 0). This will allow the reflectors around one transducer to focus on the side of it. As a result, it should improve IID range by increasing the echo intensity of one ear with respect to the other.

7.3.1 Results

When using this fitness function, results for IID using 10 reflectors¹ were very little improved from those in [Peremans et al., 1998b]. In figure 7.2, a reflector distribution around the transducer (a) and the region covered by these reflectors (b) is shown.

As can be seen, the middle part of the IID profiles, *i.e.* the part related to the main lobe of the transducer directivity, is quite similar to the bare transducer and to the 3 reflector case (figure 7.2(c)) in terms of steepness and linearity and therefore there is no improvement. However, there is a small improvement in the side lobe parts of the IID profile, for a target at 2 deg. elevation angle, in the form of smoothness of the peaks of such side lobes. A smoother performance along these lobes (*i.e.* removing the peaks) offers an improvement of the angular range along the horizontal plane. Arc scanning behaviour with this reflector configuration (d) performs fairly well, that is, there is some distortion in the wave peaks (continuous line) which is the significant part for arc scanning, but this could be resolved by a suitable curve-fitting process, *e.g.* using the bare transducer curve (dotted line).

When evolving a reflector configuration for arc scanning behaviour (figure 7.3), results were slightly more satisfactory than in figure 7.2(d)). In figure 7.3(b), there is an improvement in amplitude (continuous line), despite some distortion at the middle part of the scan, compared with bare transducer (dotted line). From these results, it is clear that there were no big improvements in a 10 reflector configuration with respect to [Peremans et al., 1998b].

The reason why there was no big improvement in performance is the effect that phase cancellation produces in the final wave. Because of the difficulty of finding an optimal position for all the reflectors in all the target possible positions, final performance does not significantly improve with respect to a bare transducer configuration, as the analysis below suggests.

¹This was decided to be the maximum number of reflectors because of the high computational cost introduced by each reflector.

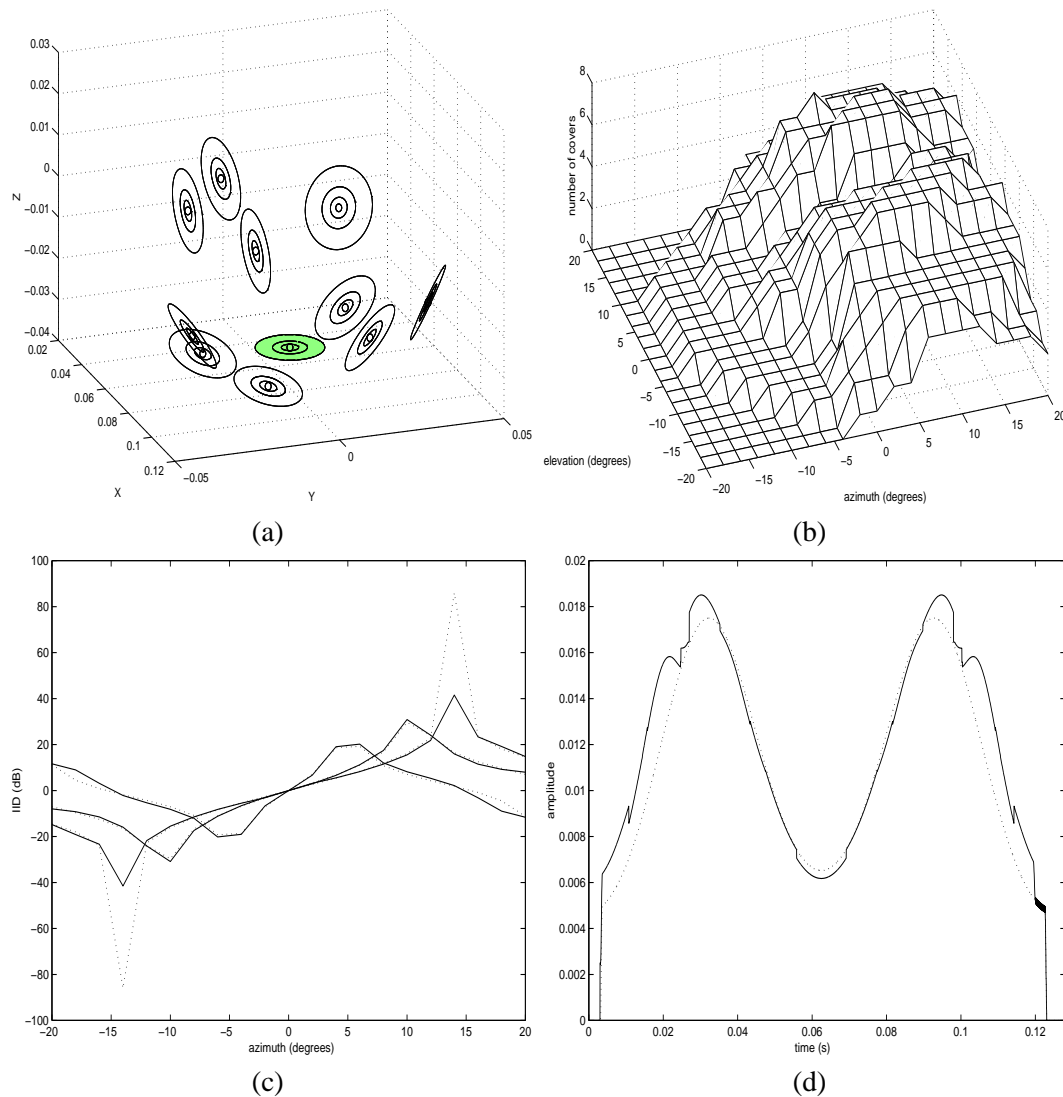


Figure 7.2: **IID results:** (a) reflector formation (b) region covered by reflectors (c) IID at elevation 2, 13, and 18 degrees (d) arc scanning at azimuth 0 degree (dotted: bare transducer; solid: transducer with reflectors).

For investigating the effect of phase cancellation, a static transducer with a fixed reflector was evaluated for all the possible target positions, that is, an array of 21×21 positions representing a range of -20 to $+20$ degrees in both horizontal and vertical planes.

As seen in figure 7.4(a), the reflector is positioned beside the transducer on the right ear. The reflector can be effective only in target positions at azimuth angle ranging from -20 to -14 . Figure 7.4(b) shows the region covered by this reflector; each cell shows a phase diagram of how much signal of the reflector's echo is phase-shifted from the transducer's direct echo signal. The reflected signal is about 235 degree phase-shifted at -20 degrees in azimuth and

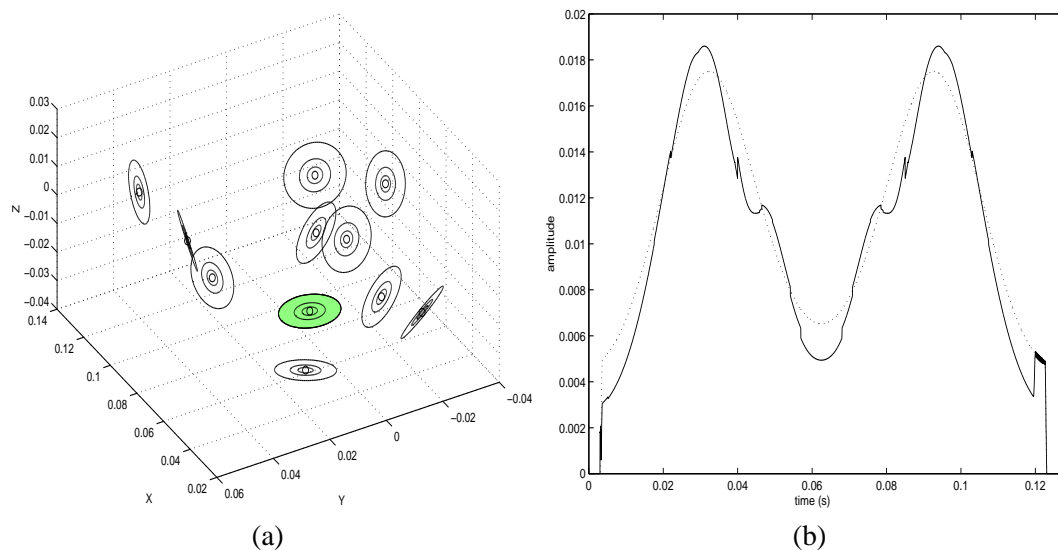


Figure 7.3: **Arc scanning results:** (a) reflector formation (b) arc scanning at azimuth 0 degree (dotted: bare transducer; solid: transducer with reflectors).

-18 degrees in elevation (c), and about 180 degrees at -16 degrees in azimuth and -6 degrees in elevation (d). The net effect of the signals into the transducer is the superposition of all the incoming signals and we can see the result of echo interference.

Next, the reflector configuration was scaled up to three reflectors (figure 7.5(a)). The regions coverage of each reflector (b), are located on the right side as expected. The echo interference becomes more complex when we have more reflectors. As a matter of fact, echo interference occurs with a large number of signals from any surface around the transducer position. In some cases the net echo signal is overwhelmed by the direct signal to the transducer (d), and in other cases the reflected signals greatly influence the net echo becoming unpredictable for a target position. Thus, it is not possible to focus on all target positions with a good reflector formation. Even a slight movement of target position makes a phase shift signal for one reflector as in 7.4(b). This results in our objective being a very difficult problem to solve with a genetic algorithm.

In summary, from the results obtained in [Kim et al., 2000], we realised that increasing the number of reflectors from three to ten did not improve performance enough, because of the adverse effect of multipath *phase cancellation* phenomena. Experiments with one and three reflector models showed how the effect of phase cancellation for a fixed reflector configuration varies for different target positions. Our conclusion from these results were that we were using too simple a model of the pinnae, *i.e.* using small reflectors instead of surfaces. Hence, to evolve an optimal reflector configuration which will improve performance for every target

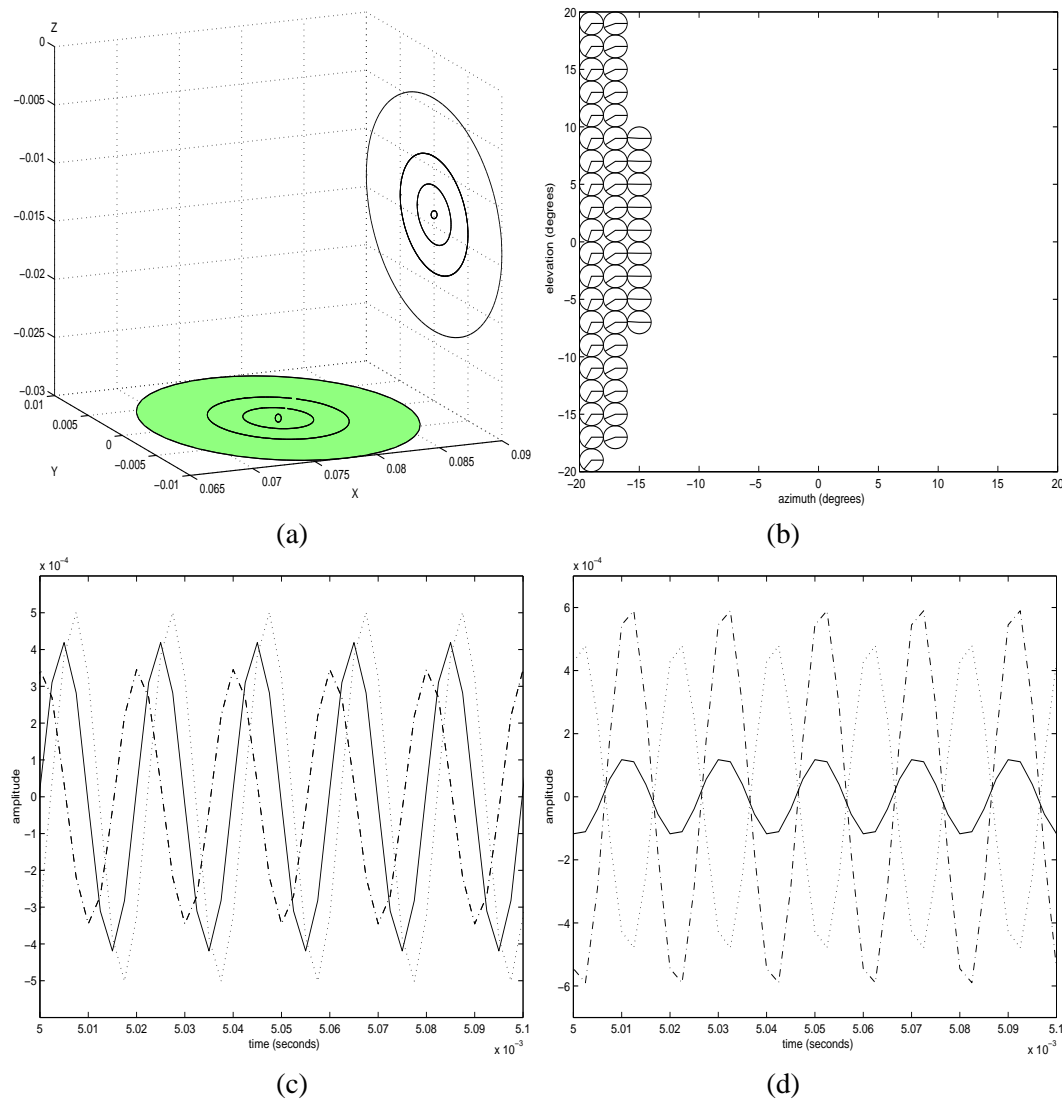


Figure 7.4: **Phase effects for 1 reflector:** (a) reflector formation (b) cover region and phase shift (c) echo signals at azimuth -20, elevation -18 (d) echo signals at azimuth -16, elevation -6 (dotted: transducer; dashed: reflector; solid: superposition of signals).

position using this simple model seemed to be a very difficult task. This suggested that a more realistic model of the bat's pinna would be a fruitful avenue to explore. However, the problem with a more realistic surface-based model is the substantial increase in parameters required and hence in the space to be searched by the GA. At this point, the necessity of a more realistic model of wave propagation which could be applied to complex surfaces therefore arose. We also proposed as further work to investigate good compromises for the tradeoff mentioned above, giving parabolic surfaces, in which many small reflectors would be placed around the

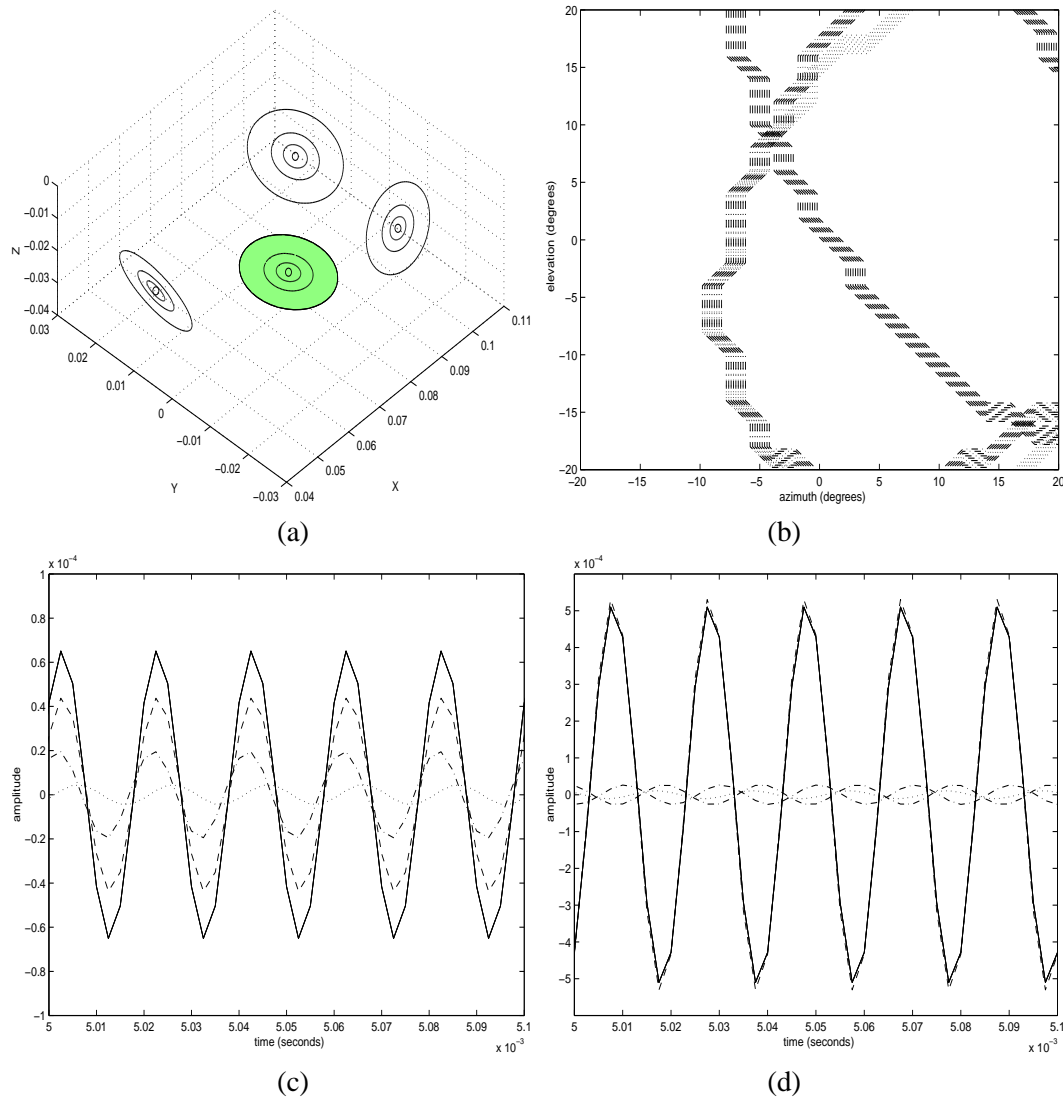


Figure 7.5: **Phase effects for 3 reflectors:** (a) reflector formation (b) contour of cover region (c) echo signals at azimuth -2, elevation -20 (d) echo signals at azimuth 20, elevation 14 (dash: transducer; dashdot: reflector 1 and 3; dot: reflector 2; solid: superposition of signals).

focus point², an example to start with.

Thus, an acoustic model inspired by a physical model of sound diffraction and reflections in the human concha [Lopez-Poveda and Meddis, 1996], was the next step taken [Carmena et al., 2000]. Such a model will be described next.

²Because of the inherent properties of the parabola equation, all the reflections will direct to the focus, *i.e.* the transducer.

7.4 Computing reflections from finite reflectors

If we assume that the echo source is in the far field of the transducer and reflector system, the incoming echo will have planar wavefronts. (The near field case can be modelled similarly, with different assumptions about the incident waves.) The incident sound insonifies the transducer and reflectors, generating a pressure at each point \vec{r} on their surfaces which is given by

$$p_0(\vec{r}, t) = p_0 e^{j(\vec{k} \cdot \vec{r} - \omega t)} \quad (7.1)$$

where \vec{k} is the wave vector of the incident wave.

The total sound pressure field at the transducer is given by the direct path field, given by the equation above, and by the contributions from the reflectors. The reflector contributions can be calculated using Kirchhoff's diffraction theory [Braddick, 1965] — each point on the reflector surface is taken to be an acoustic source radiating sound in all directions. The sound pressure on any surface element of the transducer is then the integral of the contributions from each surface element of the reflector system. Using the diffraction theory model allows us to take account of the finite size of the reflector.

The reflected pressure generated at a point by a surface element on a reflector depends on the incident sound pressure, the distance to the point and the angle between the surface normal and the direction to the point. The relationship is defined by

$$dP_R(\vec{p}, t) = \frac{R(d, \gamma_0) p_0(\vec{r})}{d} e^{jk d - j\omega t} ds, \quad (7.2)$$

where $p_0(\vec{r}, t)$ is the incident sound pressure at position \vec{r} on the reflector surface (where the element ds is), d is the distance from the reflector surface element ds to the transducer (that is, $\|\vec{p} - \vec{r}\|$), k is the magnitude of the wave vector (that is, $\frac{2\pi}{\lambda}$ for a wave with wavelength λ) and γ_0 is the angle between the surface normal at \vec{r} and the line joining the surface element to the point \vec{p} for which the pressure is being calculated.

The directional factor for reflection is given by the reflector obliquity function [Lopez-Poveda and Meddis, 1996]:

$$R(r, \gamma_0) = \frac{\cos \gamma_0}{4\pi} \left(-jk + \frac{1}{r} \right). \quad (7.3)$$

Therefore, integrating over the whole transducer surface S_T and the whole reflector surface S_R , we can obtain the total pressure contributed to the transducer which is given by the equation:

$$P_T = \iint_{S_T} \iint_{S_R} \frac{R(\|\vec{r} - \vec{p}\|, \gamma_0) p_0(\vec{r})}{\|\vec{r} - \vec{p}\|} e^{jk\|\vec{r} - \vec{p}\| - j\omega t} ds_r ds_t \quad (7.4)$$

A diagram of the plane wave model used for a transducer and reflector system is shown in Fig. 7.6. In the figure, a plane wave arriving at a surface element \vec{r} of the reflector (R)

insonifies a surface element \vec{p} of the transducer (T) along path $\vec{p} - \vec{r}$. Note, however, that each of the reflector's surface elements will behave as an acoustic source radiating sound in all directions, not only along $\vec{p} - \vec{r}$, as explained above.

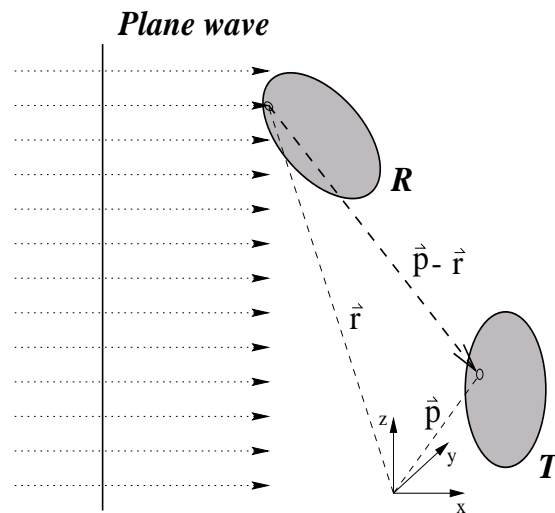


Figure 7.6: **Plane wave model** with a single reflector (R) and a transducer (T).

7.4.1 Results

A 2-dimensional adaptation of the model was tested first because of the simplicity of calculation. Figure 7.7 shows the curves obtained for a reflector held at different positions (0.5, 0.75 and 1 cm) and positioned along different angles (0 to 90 degrees). As expected, maximum amplitude is obtained at 45 degrees and with the reflector at the closest position of the transducer, *i.e.* 0.5 cm.

Because of the plausible results obtained with the 2D adaptation, the next step was to scale up to 3D. For the sake of simplicity the model was applied numerically instead of analytically. The reflector and transducer surface pressures were calculated as the sum of contributions of finite elements (FE) as an approximation to the surface integral. The division into elements was calculated using polar coordinates, varying the radius and angle according to the number of desired surface segments. Since the larger the number of divisions, the more accurate the calculation is, 2000 vs. 800 divisions were tested, resulting in a not very significant difference as seen in the overlapping dotted curve in Fig. 7.8. Hence for the rest of the experiments 800 divisions were used.

Also, as evidence of plausibility of the simulation work, a coarse evaluation of the acoustic model in the real world was performed experimenting with one single reflector (Fig. 7.9 left). The receiver to which the reflector was attached was turned 90 degrees (facing the ceiling). In

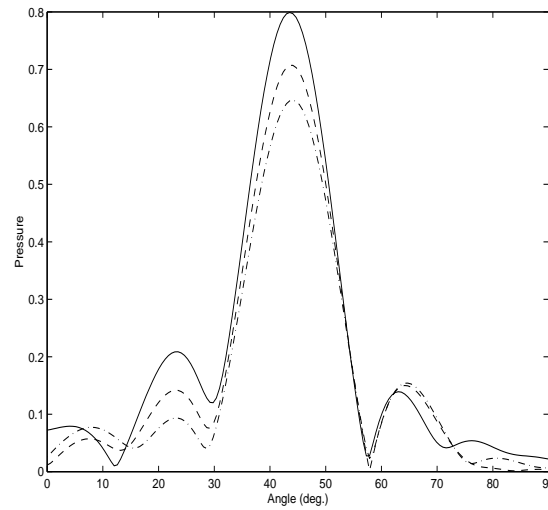


Figure 7.7: **2D pressure vs. reflector's effect on transducer for different angles** (distances: 0.5 cm (solid), 0.75 cm (dashed), 1 cm (dashdot)).

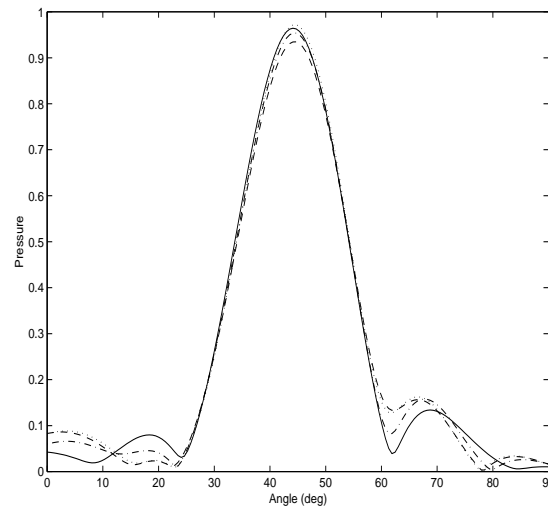


Figure 7.8: **3D pressure vs. 800 div. reflector's effect on transducer for different angles** (distances: 0.5 cm (solid), 0.75 cm (dashdot), 1 cm (dashed)); 2000 div. reflector at 1 cm (dotted).

such a position, the bare receiver is not insonified by the echo and, therefore, a better estimation of the reflector's effect can be obtained. Measurements were taken in increments of 7.5 degrees (from 90 to 0 degrees) with an estimated error of ± 1 degree along yaw (α) and pitch (β) angles. The reason for this sparse angular sampling was the difficulty for positioning the attached reflector. With respect to Cartesian coordinates a positioning error of ± 1 mm was assumed. For each measurement, 1000 consecutive pulses were sent by the emitter to a post located 30 cm in front of RoBat. The mean value of the echo energy was calculated for each of the pulses.

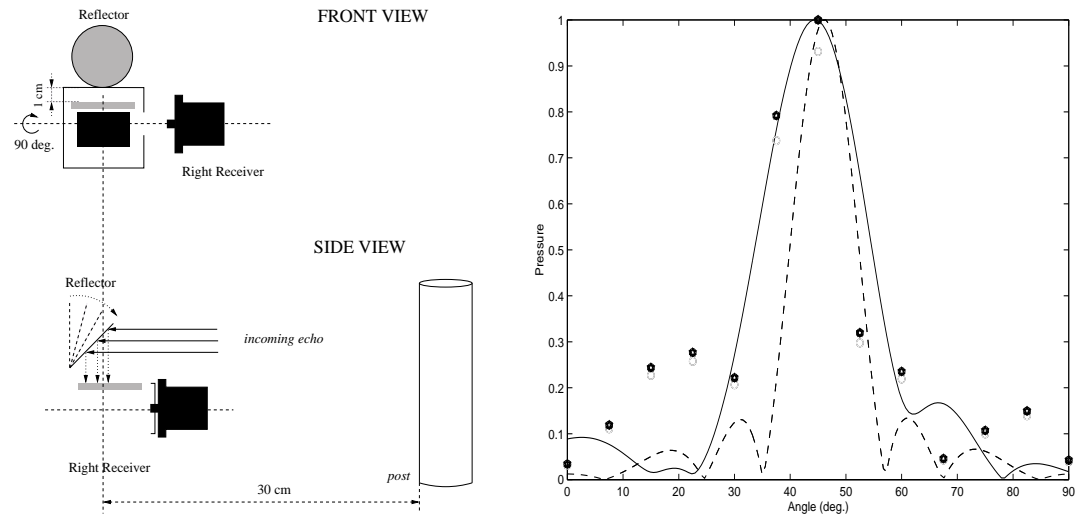


Figure 7.9: **Coarse evaluation of the acoustic model in the real world.** Left plot: Experimental set-up for one reflector. Right plot: Results comparison between simulation work (previous model (dashed) and plane wave model (solid)) and real world (blobs).

As seen in Fig. 7.9 (left), the reflector's vertical distance with respect to the transducer is 1 cm because of the gap between the transducer and the grid covering it.

Figure 7.9 (right) shows a comparison between simulation and real echo amplitude. In the figure, the solid line represents the plane wave model, the dashed line represents the previous model [Peremans et al., 1998b] and the blobs represent the mean of 1000 echo energy values. When the real measurements were taken, the physics of the transducer-reflector configuration was not as simple as the model described in section 7.4. As can be seen in Fig. 3.1, each of the transducers is inside a square box covered by a grid³. Some of the effects of this modified model can be appreciated in the interval between 10 and 30 degrees (Fig. 7.9 (right)) as a pressure offset value with respect to the simulated data. Another factor is the very low standard deviation (whose maximum value is 0.0042 in the scale of Fig. 7.9) obtained from the 13 sets (from 0 to 90 degrees in increments of 7.5) of 1000 samples. Thus, despite the physical differences of the real model, the data fitted encouragingly well for the preliminary experimental conditions in which the measurements were taken.

It is also worth mentioning the preliminary experiments done with 2 reflectors in order to see the sensitivity of multi-reflector echos to reflector position. Two reflectors in symmetric positions were placed on the two rear corners of the receiver's box at an angle α of 45 degrees. Then, the position and orientation of one reflector, the other, and the two of them together was slightly modified, obtaining big energy variance in the final echo as a consequence of phase

³This is to prevent accidental touching of the transducer (which is charged at 200 V) by the user's fingers.

cancellation and shadowing effects. This suggests that for further complex experiments with several reflectors, an accurate way of positioning the reflectors in the space (*e.g.* a laser pointer based equipment) will be vital.

In order to assess the performance of the acoustic model a comparison between this model and the model used in [Peremans et al., 1998b] and [Kim et al., 2000] was done (figure 7.10). The comparison was performed using some of the reflector configurations given by the GA in [Kim et al., 2000] for 3, 5 and 10 reflectors but using the same transducer orientation as in figure 7.9. With this orientation, because there is no direct echo reception by the transducer, it was much easier to distinguish the effects that each reflector introduced in the final wave. Then, the GA was modified for optimising the current model criteria.

In any reflector system, the echo from the target will reach each reflector at a different time and therefore the path lengths from the reflectors to the receiver will be different for each case. Since the the position of the reflectors of figure 7.10 were evolved for the previous model, differences in performance between the two models were expected to be found. In figure 7.10, the solid line is the total summation of the signals from each reflector. As can be seen, for the previous model (left column) all the reflected signals are in same phase while in the current model (right column), because of phase cancellation, the total summation is reduced.

An evaluation of the new model was also performed. Figure 7.11 shows 5 (left) and 10 (right) reflector configurations (top) given by the GA for the current model and the final wave (bottom) resulting from each reflector's contribution. The important point here is the better performance of the final wave (solid line) compared to the same cases in figure 7.10 (right column). As seen in figure 7.11, the final wave has higher amplitude because of the lack of phase cancellation in both cases and, therefore, improves with respect to figure 7.10.

At this point, as seen in figure 7.10, the significant differences between the current spherical wave model and the point-like wave proposed in [Peremans et al., 1998b] are clear. Moreover, the successful simulation results of the reflector systems evolved for the current model (figure 7.11) suggest the importance of using a more realistic model of wave propagation such as the one proposed in this work.

7.5 Discussion and conclusions

This work started replicating and improving the results obtained in [Peremans et al., 1998b] in which artificial pinnae in the form of three reflectors surrounding the two receiver transducers of the biomimetic sonarhead — which spatial coordinates were evolved using a GA — were used for improving echolocating behaviours such as arc scanning and IIDs. The solutions given

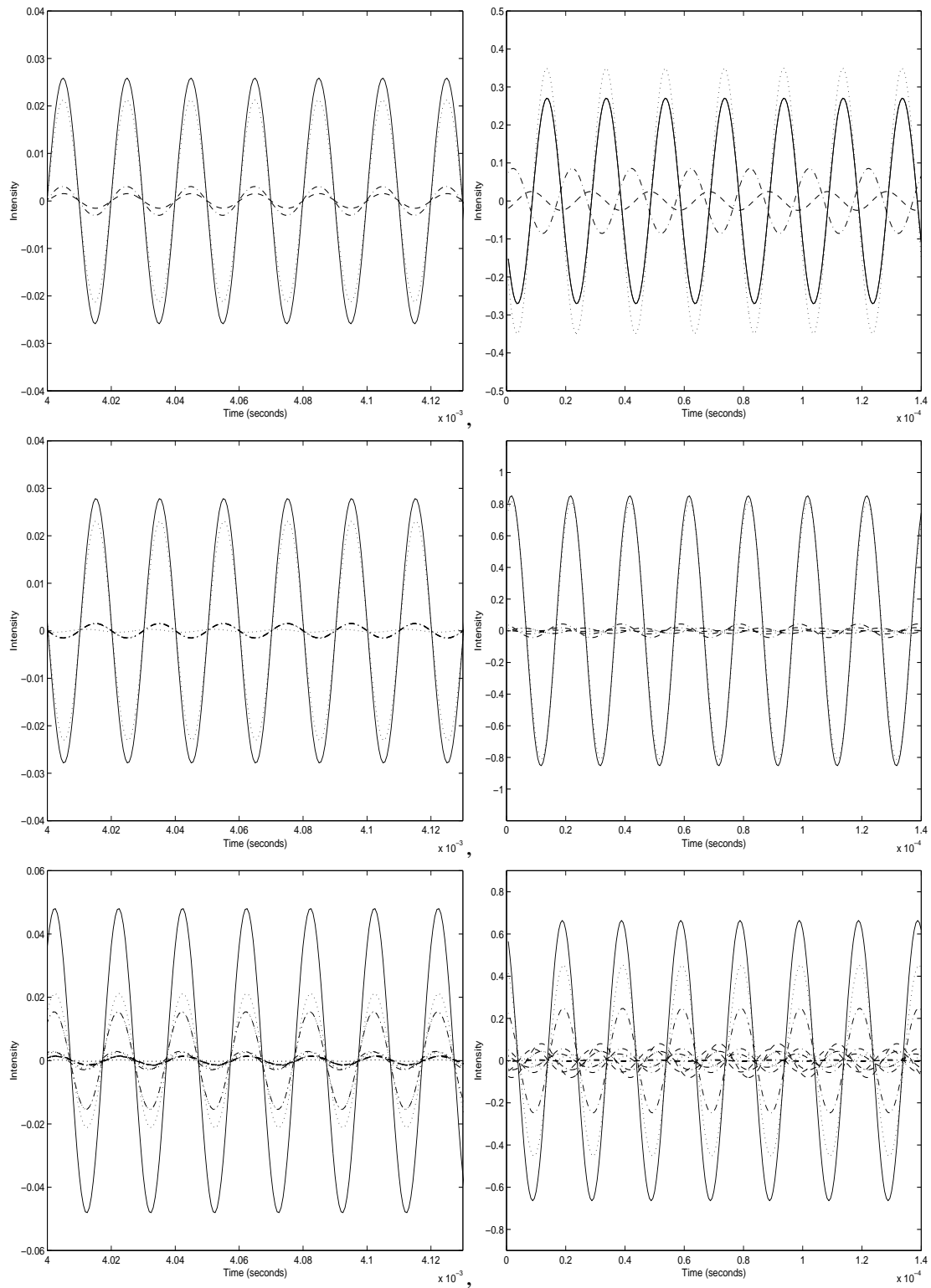


Figure 7.10: **Comparison between previous acoustic model (left columns) and current model (right columns) for 3 (top), 5 (middle) and 10 (bottom) reflectors. Final wave (solid) is the sum of each reflector's (non solid) contribution.**

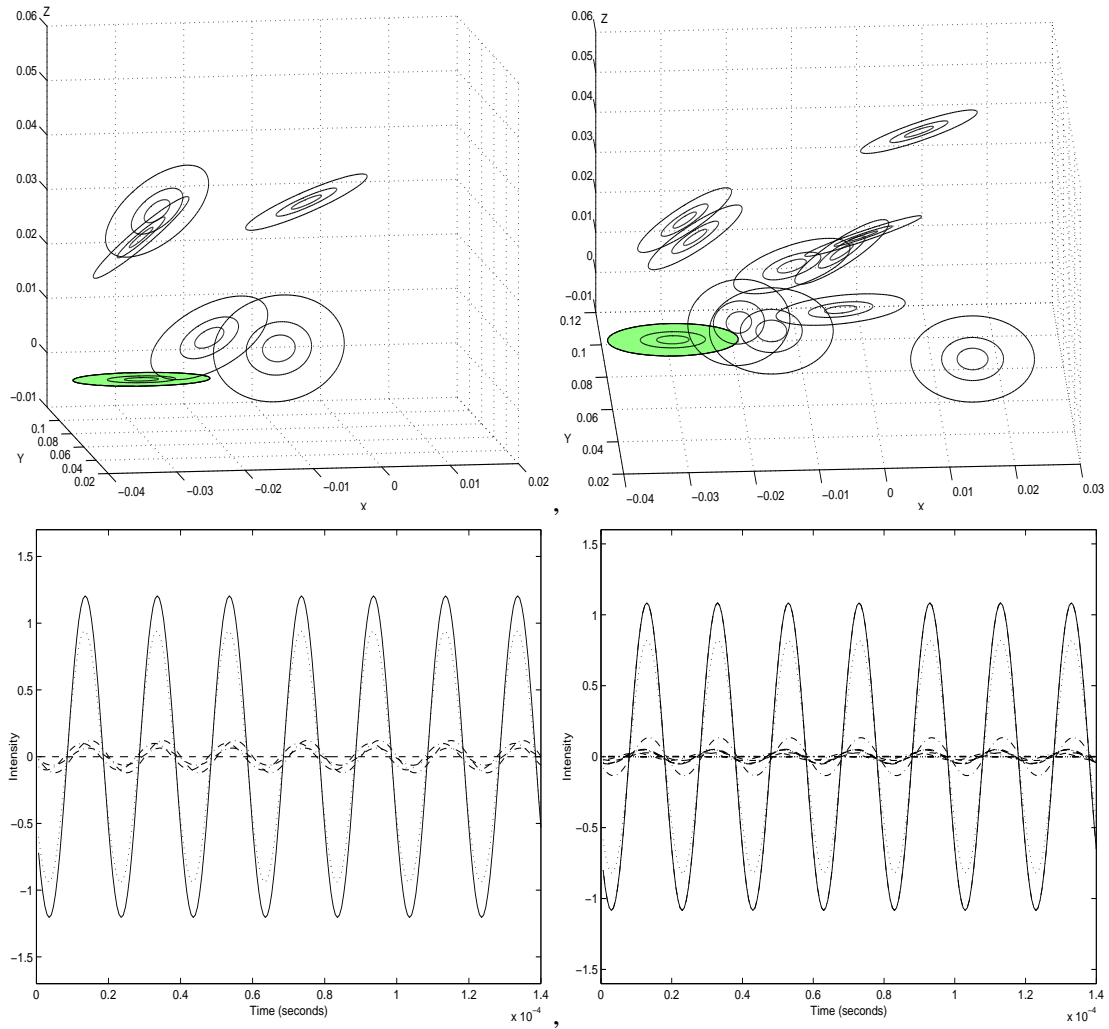


Figure 7.11: **Evaluation of the new model.** Top plots: Evolved configurations of 5 (left) and 10 (right) reflectors for the plane wave model. Bottom plots: Evaluation of the configurations. Final wave (solid) is the sum of each reflector's (non solid) contribution.

by the GA were evaluated using the *3D Echolocation Simulator* [Walker, 1997].

As a first step, a region coverage method was used to evolve pinna shapes of up to ten reflectors. From the results obtained, we realised that increasing the number of reflectors from three to ten does not improve performance enough, because of the adverse effect of multipath *phase cancellation* phenomena. Experiments with one and three reflector showed how the effect of phase cancellation for a fixed reflector configuration varies for different target positions. Our conclusion from these results was that we were using too simple a model of the pinnae, *i.e.* using small reflectors instead of surfaces and, therefore, evolving an optimal reflector configuration for improving performance for every target position using such a simple model seemed to be a very difficult task.

Thus we addressed the importance of using a more realistic model of the bat's pinna before extending the work with complex surfaces, focusing on an acoustic model inspired by a physical model of sound diffraction and reflections in the human concha [Lopez-Poveda and Meddis, 1996]. From the significant differences between models and, moreover, the successful simulation results of the reflector systems evolved for the new model (figure 7.11), the importance of using a more realistic model of wave propagation, such as the one proposed in this work, was demonstrated.

Regarding the experiments in the real world, the results showed the plausibility of the theoretical model despite physical differences between the real transducer and the simulated transducer as seen in figure 7.9. These differences, such as the transducer box with sharp edges and corners as well as the grid covering the transducer may be the cause of the energy offset found in the interval between 30 and 10 degrees.

At this point we were ready to jump from multiple reflectors to real surfaces. For further work we proposed to design long run-time experiments evolving different surfaces such as paraboloids (see figure 7.12) in which, because of the inherent properties of the parabola equation, all the reflections will direct to the focus, *i.e.* the transducer.

7.6 Further work: From multiple reflectors to surfaces

As mentioned at the beginning of the chapter, this section summarises the continuation of the work proposed in section 7.5 by Kämpchen as a Master's project.

First, the model described in section 7.4 was revisited. In the upgraded model, the grid covering the receiver box was removed and the transducer was raised up to the same level as the side of the box as suggested in section 7.2⁴. Also, Kämpchen improved the FE model by

⁴These changes were implemented into the simulator. However it is also possible to apply them to RoBat.

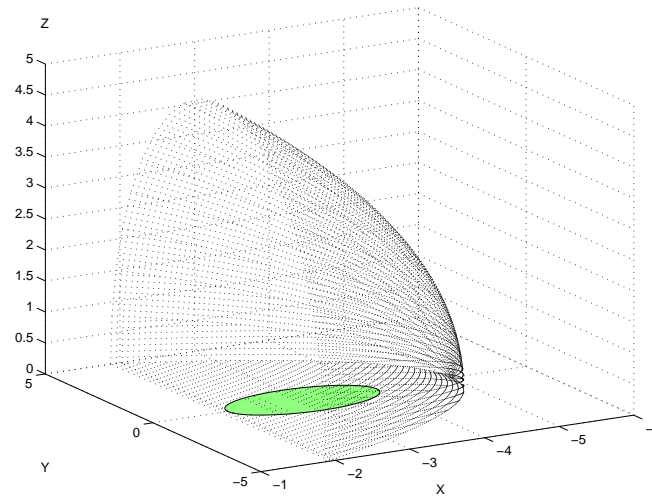


Figure 7.12: **Example of paraboloid surface** with transducer at focus position.

increasing its accuracy (see figure 7.13), and reducing the number of FE by up to 50%, thus reducing computation time.

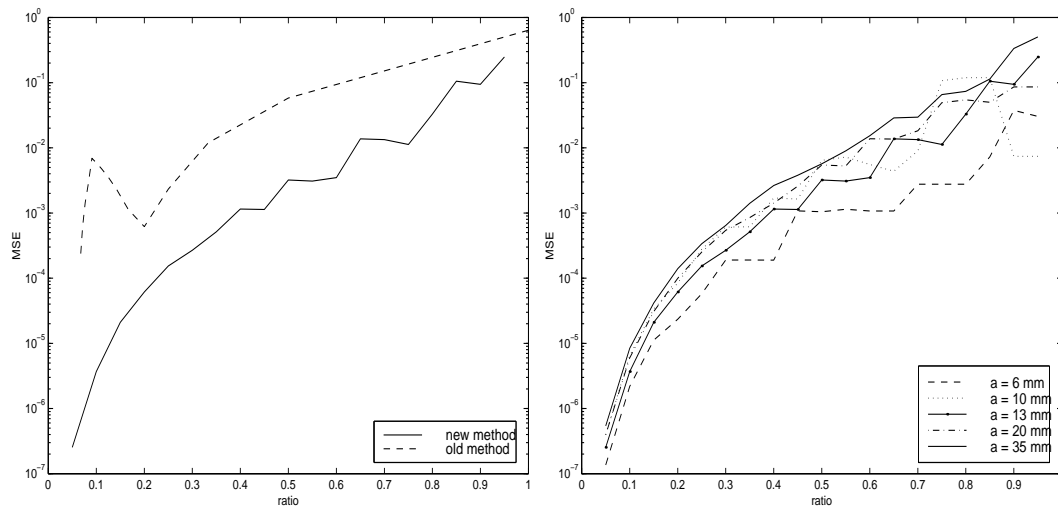


Figure 7.13: **Comparison between old and new finite element model** (transducer radius $a = 13\text{mm}$) (left). Accuracy for different transducer radii and finite element sizes (right). (Reproduced from [Kämpchen, 2000]).

During his work Kämpchen focussed in evolving conical and a paraboloid shapes, after preliminary experiments with cylindrical shapes gave unfavourable results. Both shapes were defined by four parameters (a fifth parameter, the displacement in x direction, was rejected for being almost redundant). These parameters, together with the two angles of the orientation of the receivers defined the six parameters to evolve. Three fitness functions — maximising

the gain, vertical target localisation (arc scanning), and horizontal target localisation (IIDs) — were used by Kämpchen. For specific details on the GA see [Kämpchen, 2000].

The gain was defined by the difference of the maximal sound pressure received with and without the added pinna. The gain of a pinna-transducer configuration depended on two parameters: the ability of the pinna to focus the incident sound wave on the transducer surface, and the transducer area — *i.e.* smaller transducers receive less sound pressure than larger ones.

In the experiments, the conical and paraboloid pinnae were evolved as well as the null position of the bare transducer. Two receiver disc sizes were used: 4 and 13 mm radius. This is summarised in the following table [Kämpchen, 2000]:

	max pressure with pinna (dB)	max pressure without pinna (dB)	gain (dB)
conical, 4 mm	-12.21	-20.46	8.25
paraboloid, 4 mm	1.10	-20.46	21.56
conical, 13 mm	-0.16	-0.03	-0.13
paraboloid, 13 mm	4.31	-0.03	4.34

Table 7.1: **Comparison of received sound pressure with and without pinna.** (Reproduced from [Kämpchen, 2000]).

As seen in the table, though the maximal amplitude is obtained by the paraboloid with a receiver disc radius of 13 mm, the best gain results from the combination of a paraboloid with the smaller transducer of 4 mm radius.

The experiments were performed by both tilting the neck — the head was moved towards the direction where the loudest echo came from and then oscillated around that direction in order to estimate the target's elevation — and arc scanning. In the former, the azimuth is estimated by the IID of the loudest received echo throughout a period of head movement.

For a bare transducer without pinnae there is a tradeoff between the steepness and the broadness of the IID. If the broadness is enlarged the maximal values of the IID decrease and the curve becomes less steep. For the paraboloid, the results in figure 7.14 show that it is able to produce an almost linear IID curve which is even steeper (on average) than that of the bare transducer.

The results of arc scanning for the bare transducer and the transducer with a paraboloid pinna configurations are shown in figures 7.15 and 7.16. In part (a) of the figures the directivity of the pinna alone, without the emitter directivity, is shown. If the ears are rotated and not the whole head, the elevation estimation only depends on the pinna and not the emitter directivity. The difference between the main peak and the highest side peak, when arc scanning is performed, is shown in Fig. 7.15(b). Sub-plot (e) in the figure shows the elevation for the

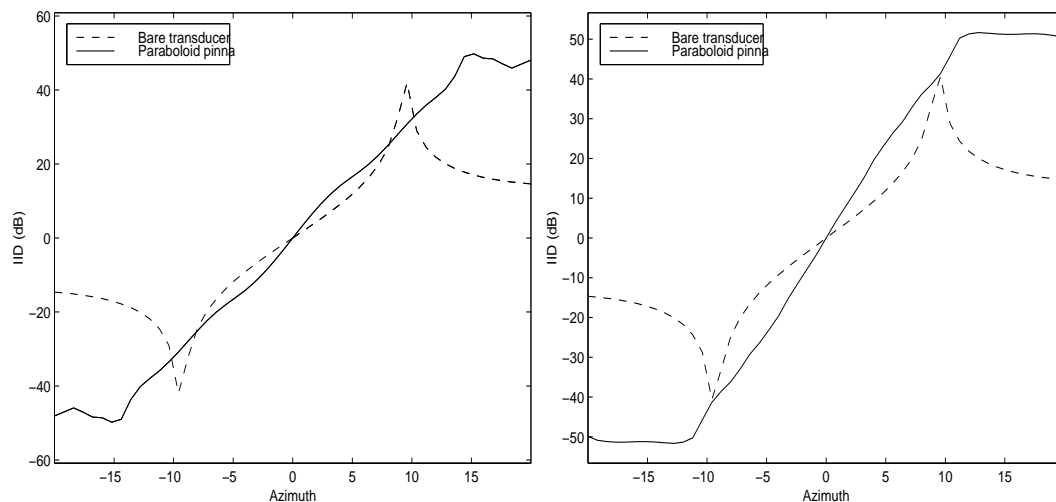


Figure 7.14: **IID performance comparison between paraboloid pinna and bare transducer** for the tilting-the-neck (left) and arc scanning (right) experiments. (Reproduced from [Kämpchen, 2000]).

highest sensitivity. As the bare transducer has an axis of highest sensitivity at 0° elevation (Fig. 7.15(e)), the IID is independent of the target's elevation (Fig. 7.15(c)). Wider regions of one grey level correspond to a flatter part of the IID curve (d) and the thinner a region is, the steeper is the IID at that position. The maximal pressure for a bare transducer with the steep IID is -0.47 dB and -23.9 dB for the 4 mm receiver configuration [Kämpchen, 2000].

Figure 7.16 shows the results of arc scanning using paraboloid pinnae. Though the steepness of the IID in Fig. 7.16(d) is on average equal to that of the IID of the bare transducer in Fig. 7.15(d), it is very linear and therefore much steeper in the center of view (resolution of $0.21^\circ \text{dB}^{-1}$ in comparison to 1.1°dB^{-1}). Due to a slightly irregular maximum sensitivity in elevation (see Fig. 7.16(e)) the IID map in shows some divergences from the linear pattern for high elevations. The maximal pressure which is received with this pinna shape is -8.9 dB [Kämpchen, 2000].

Improvement with paraboloid pinnae Kämpchen's results suggest that paraboloid reflector shapes are able to improve the directivity of the receiver configuration. For echolocation tasks where the target's elevation is estimated by sweeping the head or only the pinnae, the IID and the elevation directivity were enhanced. Conical reflectors, however, exhibited a lower gain and therefore a flatter IID. Kämpchen also points out the necessity of proving that the results obtained in the simulations coincide with measurements on real reflector shapes mounted on RoBat. Figure 7.17 shows one of the paraboloid shapes evolved for maximising the gain.

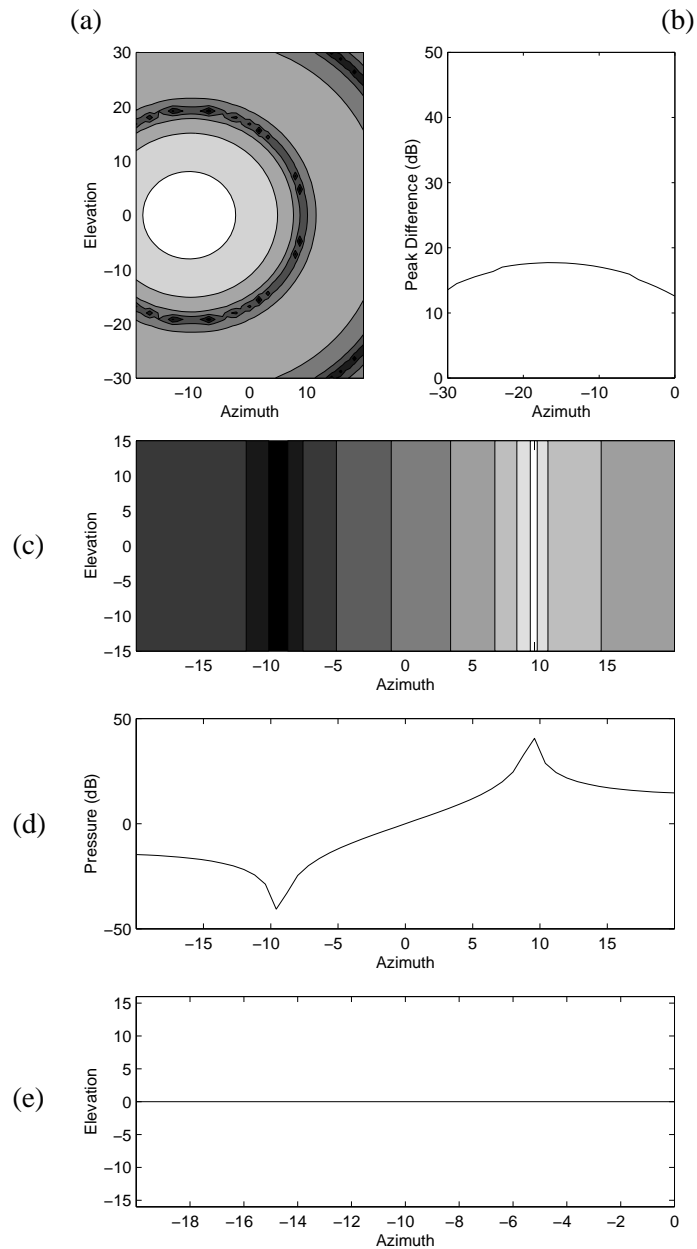


Figure 7.15: Performance of arc scanning applied to the bare transducer configuration. **Emitter radius of 4 mm and receiver radius of 13 mm.** (a) Directivity of pinna (only receiver). White 3 dB acceptance region. All other regions cover 10 dB. (b) Difference between main and side peak. (c) IID map. (scaling as in (a)). (d) IID curve at 0° elevation. (e) Elevations of maximal amplitude. (Reproduced from [Kämpchen, 2000]).

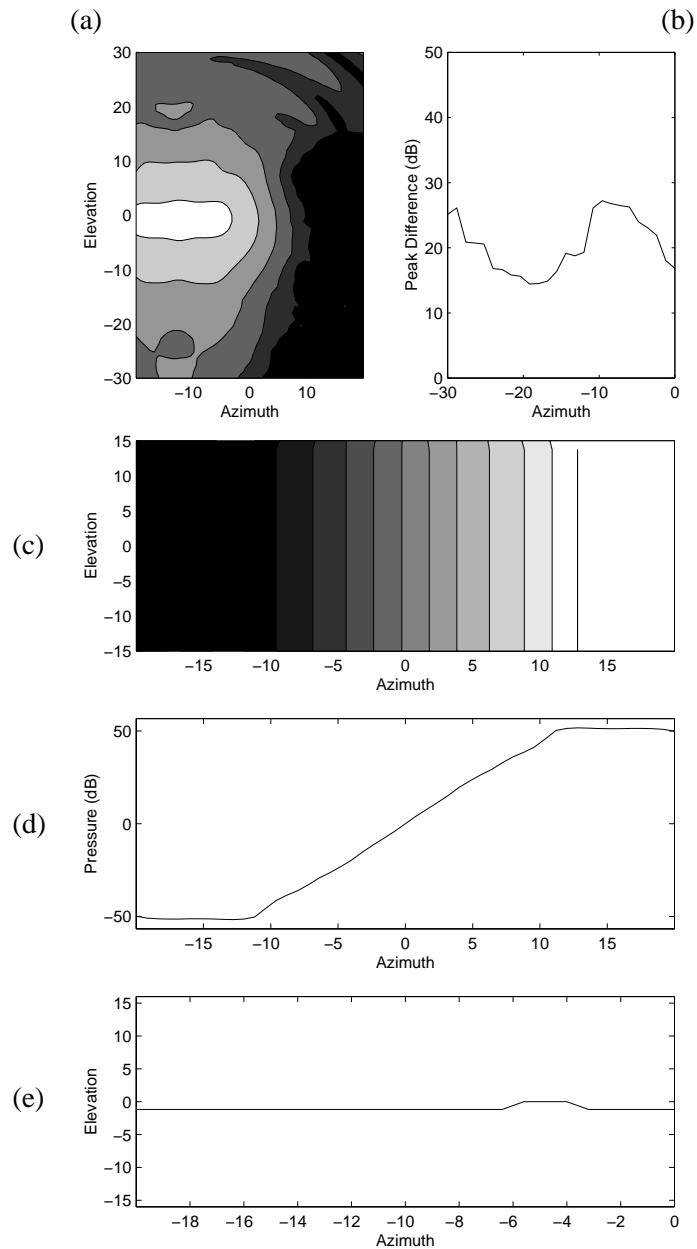


Figure 7.16: Performance of arc scanning using paraboloid pinnae. **Emitter and receiver radius of 4 mm.** (a) Directivity of pinna (only receiver). White 3 dB acceptance region. All other regions cover 10 dB. (b) Difference between main and side peak. (c) IID map. (scaling as in (a)). (d) IID curve at 0° elevation. (e) Elevations of maximal amplitude. (Reproduced from [Kämpchen, 2000]).

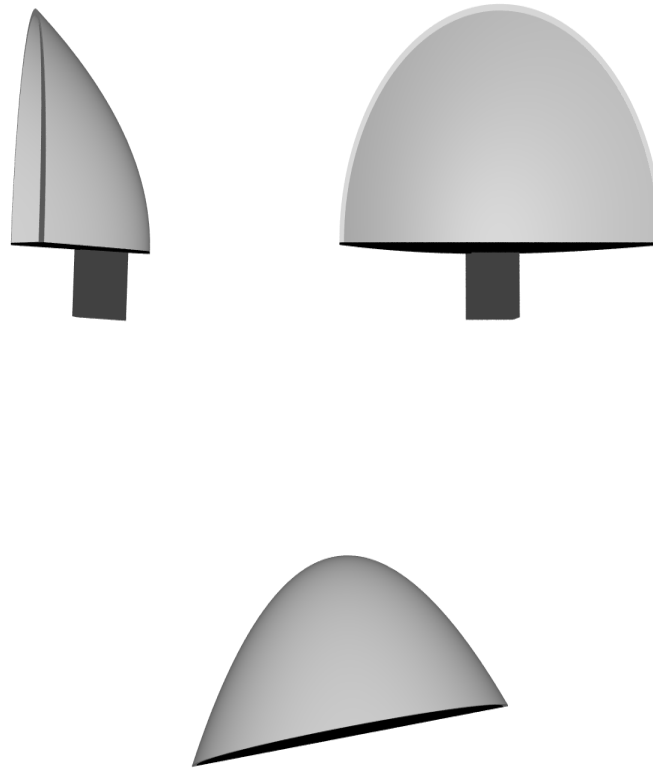


Figure 7.17: **Paraboloid shape** which maximises the gain to 21.56 dB. (Reproduced from [Kämpchen, 2000]).

Comparison with bat pinnae The big differences of the IID maps among bats make it difficult to make comparison. However, as pointed out by Kämpchen [2000], some common features were observed: “The model bat *Rhinolophus ferrumequinum* has a HIID (highest IID) of 40 dB, therefore slightly lower than the HIIDs of the paraboloid pinnae of 42 — 55 dB, depending on the IID range. The maximal steepness of the bat’s IIDs (0.6°dB^{-1} in one study, in others 0.1°dB^{-1} [Obrist et al., 1993]) is comparable to that of the evolved reflectors ($0.21 - 0.8^\circ \text{dB}^{-1}$, depending on the scope of view). However the gain of bats’ pinnae tend to be much higher (*e.g.* 24 dB in *Rhinolophus rouxi*). A maximal gain of 21.6 dB with a paraboloid pinna was only achieved if the fitness function had no other optimisation criterium. The gain of evolved shapes which were useful for the echolocation task did not exceed 11.6 dB. This could be caused by an inappropriate acoustic model. Other models approximate the cavity of the bat’s pinna with an acoustic horn which has a circular or elliptic entrance [Walker, 1997]. The absolute gain and the changes of gain with frequency for those models coincides well with the observations on bat’s pinnae [Obrist et al., 1993]”. This suggests that evolving horn-like pinnae could be a

fruitful avenue to explore.

Chapter 8

Conclusions

In this last chapter, the final conclusions of the different issues seen in the course of the dissertation are presented. These conclusions are structured in three main parts: first, in section 8.1, the thesis is summarised. This is followed, in section 8.2, by the achievements and contributions of the thesis. Finally, in section 8.3, ideas on further directions of this work are given and discussed.

8.1 Thesis summary

This dissertation has presented biologically inspired engineering on the use of narrowband Sonar in mobile robotics. We have replicated, using robotics as a modelling medium, several aspects of echolocation in bats aiming to improve the design and use of narrowband ultrasonic sensors for mobile robot navigation.

As seen in chapter 2, most research on ultrasonic sensors for mobile robots has suffered from the ‘ultrasonic sensor = Polaroid range sensor’ fallacy. As a result, the use of ultrasonic sensors for mobile robot navigation has been under-rated for many years. Even worse, as these sensors operate only on the first echo whose amplitude exceeds a threshold value, most of the information present in the echo signal, such as Doppler shifts and incoming echoes from further reflectors, is discarded.

Hence, an obvious natural system worth looking at was bat biosonar. So-called CF-FM bats are highly mobile creatures that emit long calls in which much of the energy is concentrated in a single frequency. It is our belief that these bats face sensor interpretation problems very similar to those of mobile robots provided with ultrasonic sensors, while navigating in cluttered environments: forests for bats and laboratories for robots. A better understanding of such biosonar systems can provide helpful insights for the design of Sonar sensors for mobile

robots if biological tasks are analysed carefully and the underlying principles are tested for their applicability to the engineering problems of mobile robots.

To that effect, we followed the biomimetic approach to Robotics — *i.e.* implementing in a robotic model ideas taken from Biology — focusing on how the constant frequency part of the call emitted by CF-FM bats is used for several tasks which depend on temporal (*e.g.* TOF), frequency (*e.g.* Doppler-shift) and dynamic (*e.g.* arc scanning) cues.

The robotic model used as the experimental platform for this work is RoBat, described in chapter 3. RoBat is the biomimetic sonarhead designed by Peremans and Hallam, mounted on a commercial 3 DOF mobile platform. System integration, including signal processing capabilities inspired by the bat's auditory system and closed loop control of both sonarhead and mobile base movements, was designed and implemented. RoBat allows the study of ultrasonic perception in realistic dynamic environments. This tool visualises a biologically plausible representation, *i.e.* the outputs of the cochlear model, of the acoustic flow field in real-time as the biomimetic platform moves through its environment, thereby making it much easier for human experimenters to detect the salient features in these acoustic images and investigate their relationship with the environmental features. The usefulness of RoBat as a biomimetic platform is related to four essential features: its mobility allows the study of sequences of echoes in the context of different behaviours; the active sonarhead allows the study of active sensing strategies; the biologically plausible representation of the echoes allows the cross-fertilisation of biology and robotics; and real-time operation allows the study of acoustic flow fields.

In chapter 4 we investigated how continuous estimates of Doppler-shifts can be derived from physical echoes seen through two different models of a cochlear representation of the CF-FM bat. Doppler-shifts are a rich source of information not exploited by the robotics community (partially because the commercial ultrasonic range sensors do not provide Doppler estimates), hence our interest in addressing its utility for robotics. Two parsimonious models of the auditory fovea of these bats based on filterbanks — sets of bandpass filters followed by full-wave rectification and low-pass filtering — were implemented. One filterbank used Butterworth filters whose centre frequencies vary linearly across the set. The alternative filterbank used gammatone filters, with centre frequencies varying non-linearly across the set. Two methods for estimating Doppler-shift from the output of these models were implemented: a novel neural network-based technique and a simple energy-weighted average of filter centre frequencies.

Each method was tested with each of the cochlear models, and evaluated in the context of several dynamic tasks in which RoBat was moved at different velocities towards stationary echo sources such as walls and posts. Overall, the performance of the linear filterbank was

more consistent than the gammatone. The same applies to the ANN, which had consistently better noise performance than the weighted average. It was interesting to see how Doppler-shift can be reliably estimated despite the low velocity of the robot compared to real bats.

The effect of multiple reflections contained in a single echo was also analysed in terms of error in Doppler-shift estimation assuming a single wider reflector, *i.e.* how much our Doppler-shift estimation deteriorates when another signal is introduced in the echo, investigating how likely the problem applies to robotics provided with Polaroid electrostatic transducers and up to what extent the problem can be ignored when assuming a single dominant frequency echoes in indoor environments.

In chapter 5 we saw how Doppler-shifts can be used in several ways in a robotic context. Bat behaviours such as target recognition through frequency signatures, Doppler-shift compensation, and acoustic flow were implemented in Robat and discussed. From Doppler-shift compensation, inspiration for a convoy navigation controller following a set of simple Doppler dependent rules was successfully implemented. This controller takes advantage of the flat portion of the cosine curve at small bearing angles which allows small fluctuations in bearing angle around 0° without worsening performance. The performance of the controller was satisfactory despite low Doppler-shift resolution caused by lower velocity of the robot when compared to real bats. On the other hand, an implementation of Müller's hypothesis on acoustic flow for obstacle avoidance resulted, as expected, in a crude estimation of the target's passing distance at small bearing angles which improved as this increased, nevertheless sufficing for avoiding the obstacles of the experiment. The reason for this crude estimation was the low resolution introduced by the large difference in navigating velocities between the robot and the bat.

In chapter 6 we implemented in RoBat a simple and preliminary 3D tracker through the integration of two different methods for object localisation in the horizontal and vertical planes. These methods exploit the physics of narrowband echolocation and the dynamics of the sensor. The first method [Barshan and Kuc, 1992] estimates the azimuth and range of a target located at the intersection of the two ellipses defined by each of the receiver-transmitter TOF, assuming the target is in the same elevation plane as the collinear emitter and receivers. This model was adapted to the sonarhead's geometry which introduces an offset in the z axis. Different TOF estimation methods were tested, the LSE parabola fitting being the most accurate. Then, instead of using a sensor with extra receivers to measure target elevation (as in *e.g.* [Kuc, 1993]), we employed the sensor's motion to create additional virtual receivers. This method, named arc scanning by Walker [1997], was successfully implemented in RoBat using temporal (*i.e.* peak-delay) cues instead of IIDs rates of change. A so-called "echo median" controller was devised for removing spurious TOF and peak-delays estimates. The 3D tracking was performed in

the simplest way, *i.e.* applying both methods independently. A more sophisticated method in which the TOF of both receivers is estimated at the same time as performing arc scanning was proposed. The method, which needs the geometric model to be revisited and a better TOF estimation method, would allow to estimate range, azimuth and elevation in a single scan.

Finally, a joint investigation with Kim, Kämpchen and Hallam on designing optimal ear morphology using genetic algorithms was presented in chapter 7. The long term goal of this investigation, inspired by the CF-FM bat's large *pinnae*, was twofold: to improve the echolocating capabilities of the biomimetic sonarhead by attaching real pinnae to it, and to obtain insights on the role of pinnae in CF-FM bats for specific echolocating behaviours such as arc scanning and IIDs. As a first step, a simple ray light-like model of sound propagation was used to evolve pinna shapes of up to ten reflectors. From the results obtained, we realised that increasing the number of reflectors did not improve performance because of the adverse effect of multipath *phase cancellation* phenomena. Thus a more complete acoustic model inspired by a physical model of sound diffraction and reflections in the human concha [Lopez-Poveda and Meddis, 1996] was devised. Results showed significant differences in performance between models. The results of an experiments in the real world, showed the plausibility of the theoretical model despite physical differences between the real transducer and the simulated transducer. At this point we were ready to jump from multiple reflectors to real surfaces, proposing paraboloids as interesting surfaces to investigate because — from the inherent properties of the parabola equation — all the reflections will direct to the focus, *i.e.* the transducer. In the last stage of this work, some interesting paraboloid shapes were obtained [Kämpchen, 2000], improving performance significantly with respect to the bare transducer.

8.2 Achievements and contributions

The main contribution of this thesis, in a high level of abstraction, is the demonstration of how biologically inspired engineering results in an alternative and useful approach to the use of ultrasound in mobile robots.

More specifically, the achievements and contributions of this thesis can be summarised as:

- RoBat's system integration, including signal processing capabilities inspired by the bat's auditory system and closed loop control of both sonarhead and mobile base movements. The result is a versatile tool for studying the relationship between environmental features, their acoustic correlates and the cues computable from them, in the context of both static, and dynamic real-time closed loop, behaviour [Peremans et al., 2000].

- A comparative study of two models of the signal processing performed by the bat's cochlea — a Butterworth and a gammatone filterbank — with two frequency discrimination methods — a simple energy-weighted average of filter centre frequencies, and a novel neural network-based technique — for Doppler-shift estimation tasks [Carmena and Hallam, 2000, 2001a].
- The design and implementation of Doppler-based behaviours such as Doppler-shift compensation (typical of CF-FM bats), and a controller suitable for collision detection and convoy navigation in mobile robots [Carmena and Hallam, 2001b,c].
- The implementation and testing of Barshan's and Kuc's 2D object localisation method adapted to the geometry of the sonarhead, including different TOF estimation methods. The implementation of arc scanning as a mean of recovering elevation cues, and the integration of both methods in a preliminary narrowband 3D tracker.
- A joint investigation with Kim, Kämpchen and Hallam [Kim et al., 2000; Carmena et al., 2000, 2001] on designing optimal ear morphology for improving the echolocating capabilities of the sonarhead. Genetic algorithms were used for evolving configurations of multiple reflectors around the transducer and for improving in arc scanning and IID behaviours. A simple ray light-like model of sound propagation was used before a more complete acoustic model, inspired by a physical model of sound diffraction and reflections in the human concha [Lopez-Poveda and Meddis, 1996] was devised and used to evolve pinnae surfaces made of finite elements.

8.3 Discussion and future work

In most of the existing robotic sonar systems, the target's azimuth is estimated from the differences in arrival times of the echoes. With respect to binaural systems, such as the biomimetic sonarhead, this method would not be useful for further scaled down versions because the shorter inter-aural separation would be unsuitable for accurate localisation. The approach started by Peremans et al. [1998a] advocates gleaning this information from inter-aural intensity comparisons instead. This will allow us to build arbitrarily small sensors — with inter-aural dimensions and transducer radii corresponding better with those of the bat — whose accuracy depends only upon the sensitivity of the receivers and their relative orientation. These scaled down sensors might be employed in the near future aboard many real-world systems such as automobile cruise control and collision avoidance systems [Jones, 2001].

Also, a smaller, faster robotic sonarhead provided with faster and more accurate motors will allow modelling the movements of the pinnae and the head in CF-FM bats more precisely thereby addressing questions such as how horizontal (*i.e.* panning) movements of the pinnae are combined with the vertical (arc scanning) movements, and how these movements are synchronised with the movements of the head and body while tracking a target. In addition, because it is important to study animal perceptual mechanisms within a feedback control system capable of real-time behaviour, RoBat's signal processing speed must be extended. Neuromorphic cochlear chips can be used for this purpose; however, the main problem lies in how to digitise the n analog output channels of the chip so the system can work in close-loop.

To free the system from the dependence of the host computer and the umbilical is another important issue to be achieved in further versions of RoBat. This will require on-board signal acquisition and processing, as well as power supply. A good example of such self-contained systems can be seen in [Heale and Kleeman, 2000].

Regarding ear morphology design, building and attaching real pinnae to the sonarhead is the next step. Also, it would be interesting to evolve emitter reflector shapes *e.g.*, the nostrils of *Rhinolophus ferrumequinum*. These complex surfaces modify the acoustic properties of echolocation calls to optimize retrieval of information about the environment. By the time this thesis was about to finish, Cook, a Master's student co-supervised with Hallam, was assessing the role of emitter morphology in echolocation cue extraction, providing a parallel object model suitable to be used on Beowulf-class cluster machines [Cook, 2001]. This platform will facilitate further experimental optimisation of acoustic reflecting structures such as pinnae and nostrils.

Finally, an ideal scenario in the future of ultrasonic sensors for robots would be the commercialization of more sophisticated sensors capable of estimating Doppler-shift in addition to TOF. Perhaps this could be done by on-chip signal processing and electronic circuitry avoiding digitisation and therefore the need of expensive and space consuming equipment (*e.g.* acquisition boards). Taking advantage of monaural Doppler properties, this could be imagined as a single sensor outputting two parameters (TOF, Doppler) per return echo instead of one. In such case, a robot provided with a sensor-ring made of these sensors would provide not only range but also motion information of the environment around its body. Also, if new cochlear models are devised so they can improve current Doppler-shift estimates in robots moving at realistic (*i.e.* slow) speeds, the 30° uncertainty introduced by the main lobe of these sensors may be decreased significantly.

Appendix A

Mathematical formulas

A.1 Design of acoustic foveas with variable Q values

Formulas related to acoustic fovea design (N_F is the number of filters, Δf_{fov} the width of the fovea, sf the step factor and ERB being the equivalent rectangular bandwidth [Müller, 1998]):

$$N_F = Q_{max} * \Delta f_{fov} [N_{f1} + N_{f2}] \quad (A.1)$$

$$ERB = \frac{f}{Q} \quad (A.2)$$

$$Q = \frac{Q_{max}}{\frac{|f-f_{fov}|}{\Delta f_{fov}} + 1} \quad (A.3)$$

Applying partial integration we obtain:

$$N_f = \int_{f_1}^{f_2} \frac{1}{ERB * sf} df = \int_{f_1}^{f_2} \frac{1}{\frac{f}{\frac{Q_{max}}{\frac{|f-f_{fov}|}{\Delta f_{fov}} + 1}} - sf} df \quad (A.4)$$

$$\begin{aligned} N_{f1} &= Q_{max} * \Delta f_{fov1} \int_{f_{min}}^{f_{fov}} \frac{1}{(-sf_1 * f_1^2) + (sf_1(\Delta f_{fov1} + f_{fov}) * f_1)} df_1 \\ &= Q_{max} * \Delta f_{fov1} \left[\frac{1}{sf_1(\Delta f_{fov1} + f_{fov})} \ln \frac{f_{fov}(\Delta f_{fov1} - f_{min} + f_{fov})}{f_{min} * \Delta f_{fov1}} \right] \end{aligned} \quad (A.5)$$

$$N_{f2} = Q_{max} * \Delta f_{fov2} \int_{f_{fov}}^{f_{max}} \frac{1}{(sf_2 * f_2^2) + (sf_2(\Delta f_{fov2} - f_{fov}) * f_1)} df_2$$

$$= Q_{max} * \Delta_{fov2} \left[\frac{1}{sf_1(\Delta_{fov2} - f_{fov})} \ln \frac{f_{max} * \Delta_{fov2}}{f_{fov}(\Delta_{fov2} + f_{max} - f_{fov})} \right] \quad (A.6)$$

$$f_{min} = \frac{f_{fov}(\Delta_{fov1} + f_{fov})}{f_{fov} + (\Delta_{fov1} * e^{\frac{N_{f1} * sf_1(\Delta_{fov1} + f_{fov})}{Q_{max} * \Delta_{fov1}}})} \quad (A.7)$$

$$f_{max} = \frac{f_{fov}(\Delta_{fov2} - f_{fov}) * e^{\frac{N_{f2} * sf_2(\Delta_{fov2} - f_{fov})}{Q_{max} * \Delta_{fov2}}}}{\Delta_{fov2} - (f_{fov} * e^{\frac{N_{f1} * sf_1(\Delta_{fov1} + f_{fov})}{Q_{max} * \Delta_{fov1}}})} \quad (A.8)$$

For the broadband examples of chapter 3, a wideband filterbank modelling the portion of the cochlea of the CF-FM bats outside the fovea was devised. In such configuration, the filter quality is constant ($Q = 20$) over center frequency, which ranges from 35kHz-160kHz in our experiments. Keeping filter quality constant implies that bandwidth (f_{bw}) is a linear function of center frequency (f_c): $f_{bw} = f_c/Q$. Additionally, overlap between neighbouring filters is kept constant [Slaney, 1993], which results in a wider spacing of filters as bandwidth increases.

A.2 Derivatives of h with respect to t_r and β

Given equations 6.11, 6.10, 6.13, and 6.12 their derivatives with respect to h are:

$$\begin{aligned} \frac{\partial \alpha}{\partial h} &= \frac{\frac{d(b^2 - a^2)(a^2 + b^2 - 2d^2 - 2h) + 2dh(b^2 - a^2)}{d(a^2 + b^2 - 2d^2 - 2h)^2}}{1 + (\frac{A}{B})^2} \\ &- \frac{\frac{2h(a-b)\sqrt{h(b^2 - a^2)^2 + d(a^2 + b^2 - 2d^2 - 2h)^2} - 2h(a-b)(ab + d^2 + h^2)(b^2 - a^2) - 4d^2(a^2 + b^2 - 2d^2 - 2h)}{2\sqrt{h(b^2 - a^2)^2 + d(a^2 + b^2 - 2d^2 - 2h)^2}}}{h(b^2 - a^2)^2 + d(a^2 + b^2 - 2d^2 - 2h)} \end{aligned} \quad (A.9)$$

$$\frac{\partial r}{\partial h} = \frac{4h(a - d \sin \alpha + h \cos \alpha)(a^2 - d^2 - h^2)(-2d \frac{\partial \alpha}{\partial h} \cos \alpha - 2 \cos \alpha + 2h \frac{\partial \alpha}{\partial h} \sin \alpha)}{2(a - d \sin \alpha + h \cos \alpha)^2} \quad (A.10)$$

$$\frac{\partial \beta}{\partial h} = \frac{\frac{\frac{\partial r}{\partial h} \sin \alpha + \frac{\partial \alpha}{\partial h} r^2 \cos \alpha^2 + h - r \sin \alpha (1 + (\frac{\partial r}{\partial h} \cos \alpha) - r \frac{\partial \alpha}{\partial h} \sin \alpha)}{(h + r \cos \alpha)^2}}{1 + (\frac{r \sin \alpha}{h + r \cos \alpha})^2} \quad (A.11)$$

$$\frac{\partial t_r}{\partial h} = \frac{\frac{\partial r}{\partial h} \sin \alpha + r \frac{\partial \alpha}{\partial h} \cos \alpha \sin \beta + r \sin \alpha \frac{\partial \beta}{\partial h} \cos \beta}{\sin \beta^2} \quad (A.12)$$

A.3 LSE parabola fitting

$$E = \sum_{i=1}^N (ax_i^2 + bx_i + c - Y_i)^2 \quad (\text{A.13})$$

where E is the LSE fitted parabola defined by the parameters a , b , and c , x is the sample index given by $x_i = [-100, \dots, +100]$, and Y_i is the data (echo samples) for $N = 201$.

$$\frac{\partial E}{\partial a} = 2 \sum (ax_i^2 + bx_i + c - Y_i) * x_i^2 = 0 \quad (\text{A.14})$$

$$\frac{\partial E}{\partial b} = 2 \sum (ax_i^2 + bx_i + c - Y_i) * x_i = 0 \quad (\text{A.15})$$

$$\frac{\partial E}{\partial c} = 2 \sum (ax_i^2 + bx_i + c - Y_i) * 1 = 0 \quad (\text{A.16})$$

$$M = \begin{pmatrix} \sum x_i^4 & \sum x_i^3 & \sum x_i^2 \\ \sum x_i^3 & \sum x_i^2 & \sum x_i \\ \sum x_i^2 & \sum x_i & \sum 1 \end{pmatrix} \quad (\text{A.17})$$

$$M \cdot \begin{pmatrix} a \\ b \\ c \end{pmatrix} = \begin{pmatrix} \sum Y_i x_i^2 \\ \sum Y_i x_i \\ \sum Y_i \end{pmatrix} \quad (\text{A.18})$$

$$\begin{pmatrix} a \\ b \\ c \end{pmatrix} = M^{-1} \cdot \begin{pmatrix} \sum Y_i x_i^2 \\ \sum Y_i x_i \\ \sum Y_i \end{pmatrix} \quad (\text{A.19})$$

$$vertex = x_i = \frac{-b}{2a} \quad (\text{A.20})$$

Appendix B

The following are the parameters used to train the different configurations of backpropagation ANNs used in chapter 4. The parameters were obtained using *rbp*, applying the sigmoidal function in all the cases.

B.1 ANN parameters

B.1.1 Linear filterbank (6-3-1)

Filterband	Seed	Learning rate	Momentum	Iterations	Error/unit
40 Hz	38	0.0005	0.0	17106	0.02382
40 Hz, .5 inc	40	0.0058	0.1	25638	0.02650
100 Hz	40	0.005	0.42	9738	0.01951
200 Hz	69	0.0072	0.25	19254	0.01959

Table B.1: ANN parameters for linear filterbank for different configurations.

B.1.2 Gammatone filterbank (9-4-1)

Fovea	Seed	Learning rate	Momentum	Iterations	Error/unit
400 Hz	38	0.0005	0.0	286	0.02541

Table B.2: ANN parameters for gammatone filterbank.

B.2 Example of the GA's encoding for a 3-reflector configuration

Table B.3 shows the data of a 3-reflector configuration after running the GA for 1000 generations. The 15 genes of the chromosome (5 genes per reflector) are transformed into the reflector's spatial coordinates and normal vector.

	SPATIAL COORDINATES			NORMAL VECTOR		
Reflector	X	Y	Z	\vec{n}_x	\vec{n}_y	\vec{n}_z
0	0.077500	0.000000	-0.030000	0.000000	1.000000	0.000000
1	0.064000	0.014000	-0.008000	0.261445	-0.913546	0.311578
2	0.088000	0.036000	-0.026000	0.000000	-0.743145	0.669131
3	0.078000	0.022000	0.010000	0.000000	-0.970296	0.241922

Table B.3: **GA encoding for a 3-reflector configuration.** (Reflector 0 is the transducer.)

Appendix C

C.1 Noise removal

Figure C.1 shows an example of a 50 kHz echo reflected upon a stationary flat surface oriented towards the sonarhead with the mobile platform halted, *i.e.* no Doppler-shift expected, before pre-filtering (top), after band-pass filtering (middle) and after pick-up removal (bottom). The left column shows the time domain plot of the echo acquired by one of the receivers. The right column shows the frequency analysis (via FFT) of the echo.

The origin of the big glitch in the top-left plot was unknown during a certain amount of time. This glitch generates frequency components at 12.35 kHz and lower frequencies as seen in the top-right plot. The possibility of the 12.35 kHz being a sub-harmonic of the call frequency (due to its close value to 12.5 kHz) was discarded after the transmitter was set to send a higher frequency (55 kHz) with no shift in the noise frequency.

The source of noise was located in the DC/DC converter of the sonarhead's power supply. When powering off the sonarhead (except for the bias voltage), the frequency analysis of the acquired weak signal sent by the D/A card showed no energy at 12.35 kHz nor at lower frequencies. For removing this noise component, a 2nd order Butterworth band-pass filter with cut-off frequencies at 45 and 55 kHz was used. This can be seen in the middle plots of figure C.1. Later on, it was discovered that the origin of this noise was in the commuting power supply. Replacing this unit by a linear power supply eliminated the noise and therefore the bandpass filter was of no further use.

The signal pick-up is purely electronic, *i.e.* the acoustic pick-up due to the proximity of the receivers to the emitter is minimum or inexistent. To arrive at this conclusion we acquired samples from the receivers while the transmitter was emitting and RoBat was moving. If the cause of the noise was acoustic pick-up, its echo should be Doppler-shifted because of the robot motion. The frequency analysis of the acquired samples showed all the energy located at the call frequency discarding any possible acoustic pick-up.

This pick-up is harmless if no frequency information from the echoes is needed. However, because of our interest in Doppler, it was impossible to obtain meaningful data from Doppler-shifted echoes in which the estimated Doppler-shift value has been pulled down by the 50 kHz pick-up. Taking advantage of the high speed of the processor (AMD Athlon 1GHz), and given the known frequency of the pickup (50 kHz), a software strategy for getting rid of it without introducing a critical delay in the *sense-and-act* loop was implemented as follows.

Every time RoBat is switched on, a calibration process obtains the amplitude of the pick-up for each of the receivers. Next, a synthetic signal with this amplitude and length equal to the length of the call is created and stored in memory. As soon as the echoes are converted into the digital domain (*e.g.* the echo in figure C.1 (middle)), a phase-lock routine finds the phase of the pick-up, which is invariant along the length of the echo. Finally, the synthetic signal is subtracted to the echo resulting in decrease of the noise as seen in the bottom plots of figure C.1. The amplitude of the noisy part of the bottom-left plot is clearly smaller than the middle-left. Likewise, the 50 kHz component of the bottom-right plot is greater than the middle-right. This is because of the pick-up interfering (no phase coherence) with the echo.

C.2 Servomotor synchronisation

The servomotors of the sonarhead are controlled by the *Mini SSC II Serial Servo Controller* [Jameco, 1999]. This electronic module controls eight pulse-proportional servos according to instructions received through the serial port of a PC at 2400 or 9600 baud.

These servos [Futaba, 2001] are pulse-proportional. They receive pulses ranging from 1 to 2 ms long, repeated 60 times a second. The servo positions its output shaft in proportion to the width of the pulse [Jameco, 1999]. The servos can operate at 90° or 180° range of motion modes. In the former, a 1-unit change in position value produces a 4- μ s change in pulse width. Positioning resolution is 0.36°/unit (90°/250). In the latter, a 1-unit change in position value produces a 8- μ s change in pulse width. Positioning resolution is 0.72°/unit (180°/250).

Servos are not provided with shaft encoders for indicating the position of the servo at a specific time. This results in the servos operating in open-loop, which is an inconvenience for tasks such as arc scanning in which the ears move synchronously with call emission.

In order to solve this problem, the receiver's tilting servos were connected from the controller board to the Data Carrier Detect (DCD) and Clear To Send (CTS) lines of the serial port previous voltage conversion to RS232 standard and disabling the handshake protocol interruption flag. Since DCD and CTS are input lines the status of each servo can be monitored as convenient, it is possible to write a simple routine for synchronising the servos with call

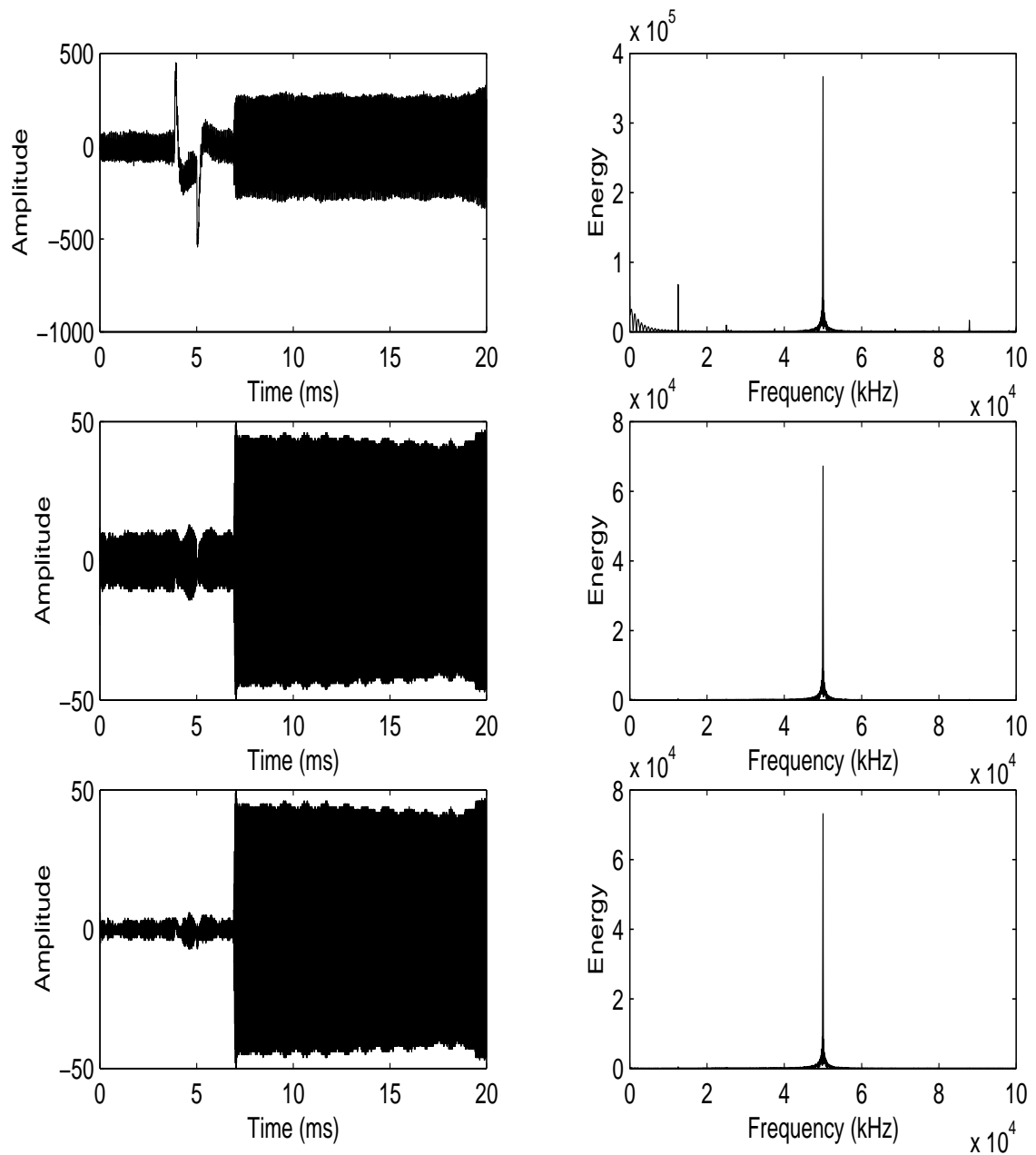


Figure C.1: **Example of noise removal** in a single echo in time (left column) and frequency (right column) domains. Noisy echo (top), after band-pass filtering (middle) and after pick-up subtraction (bottom).

emission. See [Sweet, 1999] for more details on serial programming for POSIX operating systems.

Bibliography

- Adams, M. D. (2000). Lidar Design, Use, and Calibration Concepts for Correct Environmental Detection. *IEEE Trans. on Robotics and Automation*, 16(6):753–761.
- Akbarally, H. and Kleeman, L. (1995). A sonar sensor for accurate 3d target localisation and classification. In *Proceedings of the IEEE International Conference on Robotics and Automation*, pages 3003–3008, Nagoya (Japan).
- Anke, D. (1974). Luftschallwandler nach dem sell-prinzip fur frequenzen von 50 kHz bis 100 kHz. *Acustica*, 30:30–39.
- Arkin, R. C. and Hobbs, J. D. (1993). Communication and social organization in multi-agent systems. In *From Animal to Animats: International Conference on Simulation of Adaptive Behaviour*, pages 486–493. MIT Press.
- Audenaert, K., Peremans, H., Kawahara, Y., and Campenhout, J. V. (1992). Accurate Ranging of Multiple Objects using Ultrasonic Sensors. In *Proceedings of the 1992 IEEE International Conference on Robotics and Automation*, pages 1733–1738.
- Barshan, B., Ayruolu, B., and Utete, S. W. (2000). Neural-Network-Based Target Differentiation Using Sonar for Robotics Applications. *IEEE Trans. Robotics and Automation*, 16(4):435–442.
- Barshan, B. and Kuc, R. (1990). Differentiating Sonar Reflections from Corners and Planes by Employing an Intelligent Sensor. *IEEE Trans. Pattern Anal. Machine Intell.*, 12(6):560–569.
- Barshan, B. and Kuc, R. (1992). A Bat-Like Sonar System for Obstacle Localization. *IEEE Trans. Syst. Man, Cybern.*, 22(4):636–646.
- Bass, H., Bauer, H., and Evans, L. (1972). Atmospheric absorption of sound: Analytical expressions. *J. Acoust. Soc. Amer.*, 52(3):821–825.
- Bear, M. F., Connors, B. W., and Paradiso, M. A. (1996). *Neuroscience*. William and Wilkins.
- Beer, R., Chiel, H., Quinn, R., and Ritzmann, R. (1998). Biorobotic approaches to the study of motor systems. *Current Opinion in Neurobiology*, 8:777–782.
- Behrend, O., Kössl, M., and Schuller, G. (1999). Binaural influences on Doppler shift compensation of the horseshoe bat *Rhinolophus rouxi*. *J Comp Physiol A*, 185:529–538.
- Berkowitz, editor (1965). *Modern RADAR: analysis, evaluation and system design*. John Wiley & Sons, Inc., New York.

- Biber, C., Ellin, S., Shenk, E., and Stempeck, J. (1980). The Polaroid Ultrasonic Ranging System. In *Proceedings of the 67th Convention of the Audio Engineering Society*, New York.
- Blanes, F., Benet, G., Martínez, M., and Simó, J. (1998). Grid Map Building from Reduced Sonar data. In *IFAC International Symposium on Intelligent Autonomous Vehicles*, Madrid.
- Blanes, J. F. (2000). *Percepción y Representación del Entorno en Robótica Móvil*. PhD thesis, Universidad Politécnica de Valencia.
- Bøe, S. and Kristoffersen, K. (1995). Predictive Analog to Digital Conversion of Doppler Ultrasound signals. *IEEE Transactions on Biomedical Engineering*, 42(3).
- Borenstein, J., Everett, B., and Feng, L. (1996). *Navigating Mobile Robots: Systems and Techniques*. A. K. Peters, Ltd., Wellesley, MA.
- Borenstein, J. and Koren, Y. (1989). Real-time Obstacle Avoidance for Fast Mobile Robots. *IEEE Trans. Syst. Man, Cybern.*, 19(5):1179–1187.
- Borenstein, J. and Koren, Y. (1990). Real-time Obstacle Avoidance for Fast Mobile Robots in Cluttered Environments. In *Proceedings of the 1990 IEEE International Conference on Robotics and Automation*, pages 572–577.
- Bozma, O. and Kuc, R. (1991). Building a Sonar Map in a Specular Environment Using a Single Mobile Sensor. *IEEE Trans. Pattern Anal. Machine Intell.*, 13(12):1260–1269.
- Braddick, H. J. J. (1965). *Vibrations, Waves and Diffraction*. McGraw-Hill, London.
- Brooks, R. A. (1986). A robust layered control system for a mobile robot. *IEEE Trans. Robotics and Automation*, 2(1):14–23.
- Brooks, R. A. (1991). New approaches to robotics. *Science*, 253:1227–1232.
- Burdic, W. (1968). *Radar Signal Analysis*. Prentice-Hall, Inc., Englewood Cliffs, N.J.
- Carmena, J. and Hallam, J. (1999). Improving performance in a multi-robot task through minimal communication. In *Proceedings of the 7th International Symposium on Intelligent Robotic Systems (SIRS)*, pages 329–337, Coimbra, Portugal.
- Carmena, J. M. (1998). Cooperative tasks need versatile inter-robot communication systems? Master's thesis, Department of Artificial Intelligence, University of Edinburgh.
- Carmena, J. M. and Hallam, J. C. T. (2000). Estimating Doppler-shift with a coarse cochlear filterbank. In *Proceedings of the IEEE/RSJ International Conference on Intelligent Robots and Systems (IROS)*, volume 1, pages 221–226.
- Carmena, J. M. and Hallam, J. C. T. (2001a). A comparison of methods for estimating Doppler-shift using bat-inspired cochlear filterbank models. In *Fourth European workshop on advanced mobile robots (EUROBOT'01)*, pages 9–16.
- Carmena, J. M. and Hallam, J. C. T. (2001b). Doppler-based motion controller for an echolocating mobile robot. In *Towards Intelligent Mobile Robots. Technical Report Series, Department of Computer Science, Manchester University*.

- Carmena, J. M. and Hallam, J. C. T. (2001c). Exploiting the physics: towards Doppler-based navigation with a bat-inspired mobile robot. In *Proceedings of the 9th International Symposium on Intelligent Robotic Systems (SIRS)*, pages 467–476, Toulouse, France.
- Carmena, J. M., Kämpchen, N., Kim, D., and Hallam, J. C. T. (2001). Artificial Ears for a Biomimetic Sonarhead: From Multiple Reflectors to Surfaces. *Artificial Life*, 7(2):147–169.
- Carmena, J. M., Kim, D., and Hallam, J. C. T. (2000). Designing artificial ears for animal echolocation. In *From Animals to Animats 6*, Proceedings of the 6th International Conference on Simulation of Adaptive Behaviour, pages 73–80. MIT press.
- Carpenter, G. A., Grossberg, S., Markuzon, N., Reynolds, J. H., and Rosen, D. B. (1992). Fuzzy artmap: A neural network architecture for incremental supervised learning of analog multidimensional maps. *IEEE Transactions on Neural Networks*, 3(5):698–712.
- Cavaco, S. and Hallam, J. C. T. (1999). A biologically plausible acoustic motion detection neural network. *International Journal of Neural Systems*, 9(5):453–459.
- Cook, D. L. (2001). A Parallel Object Model for Evolution of Echolocating-Enhancing Acoustic Structure in a Robotic Bat. Master's thesis, School of Artificial Intelligence, University of Edinburgh.
- Delepaute, C., Vandendorpe, L., and Eugène, C. (1986). Ultrasonic three-dimensional detection of obstacles for mobile robots. In *Proceedings 8th International Conference on Industrial Robot Technology*, pages 483–490, Brussels (Belgium).
- Dooley, S. R. and Nandi, A. K. (1999). Adaptive time delay and Doppler shift estimation for narrowband signals. *IEE Proc.-Radar, Sonar Navig.*, 146(5):243–250.
- Durá, E. and Malcolm, C. (2000). Cooperating LEGO Robots in the 1999 Five Universities “Volleyball” Competition at Sheffield. In *Proceedings of the 8th International Symposium on Intelligent Robotic Systems (SIRS)*, pages 239–244, Reading (UK).
- Ecemis, M. I. and Gaudiano, P. (2000). Object recognition system using sonar. In McKee, G. and Schenker, P., editors, *Proceedings of SPIE: Sensor Fusion and Decentralized Control in Robotics Systems III*, volume 4196, pages 180–188.
- Elfes, A. (1987). Sonar-Based Real-World Mapping and Navigation. *IEEE Trans. Robotics and Automation*, 3(3):249–265.
- Elfes, A. (1989). Using occupancy grids for mobile robot perception and navigation. *IEEE Computer*, 22:47–56.
- Elfes, A. (1992). Dynamic control of robot perception using multi-property inference grids. In *Proceedings of the IEEE International Conference on Robotics and Automation*, pages 2561–2567, Nice.
- Erwin, H., Wilson, W., and Moss, C. F. (2000). A computational sensorimotor model of bat echolocation. *Submitted to J. Acoust. Soc. Amer.*
- Fay, R. and Popper, A. (1996). *Hearing by bats*. Springer-Verlag.

- Ferguson, I. A. (1992). *Touring Machines: an Architecture for Dynamic, Rational, Mobile Agents*. Technical Report 273, University of Cambridge, Computer Laboratory.
- Firby, R. J. (1989). *Adaptive Execution in Complex Dynamic Domains*. PhD thesis, Yale University.
- Flieger, E. and Schnitzler, H.-U. (1973). Ortungsleistungen der Fledermaus *Rhinolophus ferrumequinum* bei ein- und beidseitiger Ohrverstopfung. *J. Comp. Physiol.*, 82:93–102.
- Futaba (2001). Servos list. <http://www.futaba-rc.com/servos/futm0029.html>.
- Gaioni, S. J., Riquimaroux, H., and Suga, N. (1990). Biosonar behaviour of mustached bats swung on a pendulum prior to cortical ablation. *J. Neurophysiol.*, 64:1801–1817.
- Gilkerson, P. and Probert, P. (1999). A Diffuse Reflection Model for Time-of-Flight Sonar. In *Proceedings of the IEEE International Conference on Robotics and Automation*, Detroit.
- Goldman, L. J. and Henson, O. W. (1977). Prey recognition and selection by the constant frequency bat, *Pteronotus p. parnellii*. *Behav. Ecol. Sociobiol.*, 2:411–419.
- Gorlinsky, I. A. and Konstantinov, A. I. (1978). Auditory localization of ultrasonic source by *Rhinolophus ferrumequinum*. In Olembo, R., Castelino, J., and Mutere, F., editors, *Proc. of the Fourth Int. Bat Research Conf.*, pages 145–153.
- Grasso, F. W., Consi, T. R., Mountain, D. C., and Atema, J. (1999). Chemo-orientation in Turbulence with a Biomimetic Robot Lobster. *Journal of Robotics and Autonomous Systems*. Accepted (in press).
- Griffin, D. R. (1958). *Listening in the Dark: The Acoustic Orientation of Bats and Men*. Yale University Press.
- Griffin, D. R., Dunning, D. C., Cahlander, D. A., and Webster, F. A. (1962). Correlated orientation sounds and ear movements of horseshoe bats. *Nature*, 196:1185–1186.
- Groover, M. P., Weiss, M., Nagel, R. N., and Odrey, N. G. (1986). *Industrial Robotics. Technology, Programing and Applications*. McGraw-Hill.
- Hallam, J. (1984). *Intelligent Automatic Interpretation of Active Marine Sonar*. PhD thesis, University of Edinburgh.
- Hallam, J. (1991). *Autonomous Robots: from Dream to Reality*. DAI Technical Paper 526, Department of Artificial Intelligence, University of Edinburgh.
- Hallam, J. (1997). *Experimental Methodology*. AI1Bh lecture notes. Department of Artificial Intelligence, University of Edinburgh.
- Hallam, J., Forster, P., and Howe, J. (1989). Map-Free Localisation in a Partially Moving 3d World: the Edinburgh Feature-based Navigator. In *Proceedings of the International Conference on Intelligent Autonomous Systems*, volume 2, pages 726–736.
- Hallam, J. and Hayes, G. (1997). Benchmark for mobile robotics? In *Towards Intelligent Mobile Robots, TIMR 97*. Technical Report Series, Dept. of Computer Science, Manchester University. ISSN 13616161.

- Han, Y., Han, M., Cha, H., Hong, M., and Hahn, H. (2001). Tracking of a moving object using ultrasonic sensors based on virtual ultrasonic image. *Robotics and Autonomous Systems*, 36:11–19.
- Handel, S. (1989). *Listening, An introduction to the Perception of Auditory Events*. A Bradford Book, MIT Press.
- Harper, N. L. and McKerrow, P. J. (1995). Discriminating between plants with CTFM range information using a backpropagation learning algorithm. In Yao, X., editor, *Eighth Australian Joint Conference on Artificial Intelligence*, pages 227–234. World Scientific.
- Harrison, R. R. and Koch, C. (1999). A Robust Analog VLSI Motion Sensor. *Autonomous Robots*, 7:211–224.
- Haugeland, J. (1985). *Artificial Intelligence: the very idea*. Bradford Books, MIT Press.
- Heale, A. and Kleeman, L. (2000). A real time DSP sonar echo processor. In *Proceedings of the IEEE/RSJ International Conference on Intelligent Robots and Systems*, volume 2, pages 1261–1266.
- Heffner, R. S., Koay, G., and Heffner, H. E. (1999). Sound localization in old-world fruit bat *Rousettus aegyptiacus*: acuity, use of binaural cues and relationship to vision. *J. Comp. Psychology*, 113(3):297–306.
- Hong, M. and Kleeman, L. (1995). A low sample rate 3D sonar sensor for mobile robots. In *Proceedings of the IEEE International Conference on Robotics and Automation*, pages 3015–3020, Nagoya (Japan).
- Horiuchi, T. (2000). <http://www.isr.umd.edu/Labs/CSSL>. The Computational Sensorimotor Systems Laboratory, U. Maryland, College Park.
- Jameco (1999). *Mini SSC II Serial Servo Controller*. Scott Edwards Electronics, Inc. v2.1 <http://www.seetron.com/ssc.htm>.
- Jones, G. (1999). Scaling of echolocation call parameters in bats. *J. Exp. Biology*, 23:3359–3367.
- Jones, W. D. (2001). Keeping cars from crashing. *IEEE Spectrum*.
- Kämpchen, N. (2000). Evolving pinna-like surfaces for a biomimetic sonar head. Master’s thesis, School of Artificial Intelligence, University of Edinburgh.
- Kay, L. (1980). Air sonars with acoustical display of spatial information. In Busnel, R. and Fish, J., editors, *Animal SONAR Systems (NATO ASI Series)*, pages 769–816. Plenum Press.
- Kay, L. (1999). A CTFM acoustic spatial sensing technology: its use by blind persons and robots. *Sensor Review*, 19(3):195–202. ISSN:0260-2288.
- Keating, A. W., Henson, O. W., Henson, M. M., Lancaster, W. C., and Xie, D. H. (1994). Doppler-shift compensation by the mustached bat: quantitative data. *J. Exp. Biol.*, 188:115–129.

- Kim, D., Carmenta, J. M., and Hallam, J. C. T. (2000). Towards an artificial pinna for a narrow-band biomimetic sonarhead. In *ICES'2000: From Biology to Hardware*, Lecture Notes in Computer Science 1801, pages 113–122. Springer-Verlag.
- Kleeman, L. (1992). Optimal estimation of position and heading for mobile robots using ultrasonic beacons and dead-reckoning. In *Proceedings of the IEEE International Conference on Robotics and Automation*, pages 2582–2587, Nice (France).
- Kleeman, L. and Kuc, R. (1995). Mobile Robot Sonar for Target Localization and Classification. *The International Journal of Robotics Research*, 14(4):295–318.
- Kober, R. and Schnitzler, H.-U. (1990). Information in sonar echoes of fluttering insects available for echolocating bats. *J. Acoust. Soc. Amer.*, 87:882–896.
- Kobler, J. B., Wilson, B. S., Henson, O. W., and Bishop, A. L. (1985). Echo intensity compensation by echolocating bats. *Hearing Research*, 20:99–108.
- Kortmann, R., Postma, E., and van den Herik, J. (2001). Evolution of Visual Resolution Constrained by a Trade-off. *Artificial Life*, 7(2):125–145.
- Kuc, R. (1993). Three-dimensional tracking using qualitative bionic sonar. *Robotics and Autonomous Systems*, 11:213–219.
- Kuc, R. (1994). Sensorimotor model of bat echolocation and prey capture. *J. Acoust. Soc. Amer.*, 94(6):1965–1978.
- Kuc, R. (1996). Biologically motivated adaptive sonar system. *J. Acoust. Soc. Amer.*, 100(3):1849–1854.
- Kuc, R. (1997). Biomimetic Sonar Locates and Recognizes Objects. *IEEE Journal of Oceanic Engineering*, 22(4).
- Kuc, R. and Barshan, B. (1989). Navigating vehicles through an unstructured environment with sonar. In *Proceedings of the 1989 IEEE International Conference on Robotics and Automation*, pages 1422–1426.
- Kuc, R. and Siegel, M. W. (1987). Physically based simulation model for acoustic sensor robot navigation. *IEEE Trans. Pattern Anal. Machine Intell.*, 9(6):766–778.
- Kuc, R. and Viard, V. B. (1991). A physically based navigation strategy for sonar-guided vehicles. *Int. Journal of Robotics Research*, 10(2):75–87.
- Lee, D. (1996). *The Map-Building and Exploration Strategies of a Simple Sonar-Equipped Mobile Robot*. Distinguished Dissertations in Computer Science. Cambridge University Press.
- Lee, D. N., Simmons, J. A., Saillant, P. A., and Bouffard, F. (1995). Steering by echolocation: a paradigm of ecological acoustics. *J Comp Physiol A*, 176:347–354.
- Lee, D. N., van der Weel, F. R., Hitchcock, T., Matejowsky, E., and Pettigrew, J. D. (1992). Common principle of guidance by echolocation and vision. *J Comp Physiol A*, 171:563–571.
- Leonard, J. J. and Durrant-Whyte, H. F. (1991). Mobile Robot Localization by Tracking Geometric Beacons. *IEEE Trans. Robotics and Automation*, 7(3):376–382.

- Leonard, J. J. and Durrant-Whyte, H. F. (1992). *Directed Sonar Sensing for Mobile Robot Navigation*. Kluwer Academic Publishers.
- Liese, A., Polani, D., and Uthmann, T. (2001). A Study of the Simulated Evolution of the Spectral Sensitivity of Visual Agent Receptors. *Artificial Life*, 7(2):99–124.
- Lopez-Poveda, E. A. and Meddis, R. (1996). A physical model of sound diffraction and reflections in the human concha. *J. Acoust. Soc. Amer.*, 100(5):3248–3259.
- Lund, H., Webb, B., and Hallam, J. (1998). Physical and temporal scaling considerations in a robot model of cricket calling song preference. *Artificial Life*, 4(1):95–107.
- Lund, H. H. (1999). Robot Soccer in Education. *Advanced Robotics*, 13(8):737–752.
- Lyon, R. F. and Mead, C. (1988). An Analog Electronic Cochlea. *IEEE Transactions on Acoustics, Speech and Signal Processing*, 36(7):1119–1134.
- Marr, D. (1982). *Vision*. W.H. Freeman and Company.
- Martin, K. D. (1995). A computational model of spatial hearing. Master's thesis, Department of Electrical Engineering and Computer Science, Massachusetts Institute of Technology.
- Maslin, G. D. (1983). A simple ultrasonic ranging system. In *102nd Convention of the Audio Engineering Society*, Cincinnati.
- Matia, F. and Jimenez, A. (1998). Multisensor fusion: an autonomous robot model. *Journal of Intelligent and Robotic Systems*, 22:129–141.
- Matthies, L. and Elfes, A. (1988). Integration of Sonar and Stereo Range Data Using a Grid-Based Representation. In *Proceedings of the 1988 IEEE International Conference on Robotics and Automation*, pages 727–733.
- McCormick, F. (2000). A Software Model of the Mammalian Cochlea. Final Year Project Report, School of Artificial Intelligence, University of Edinburgh.
- McKerrow, P. J. (1991). *Introduction to Robotics*. Addison-Wesley.
- McKerrow, P. J. (1993). Echolocation - From Range to Outline Segments. *Robotics and Autonomous Systems*, 11(4):205–211.
- McKerrow, P. J. and Hallam, J. C. T. (1990). An introduction to the physics of echolocation. In *Third National Conference on Robotics*, pages 198–209, Melbourne.
- McKerrow, P. J. and Harper, N. L. (2001). Acoustic density profile model of CTFM ultrasonic sensing. *IEEE Sensors Journal (submitted)*.
- Melhuish, C., Holland, O., and Hoddell, S. (1999). Convoying: using chorusing to form travelling groups of minimal agents. *Robotics and Autonomous Systems*, 28:207–216.
- Mogdans, J., Ostwald, J., and Schnitzler, H.-U. (1988). The role of pinna movement for the localization of vertical and horizontal wire obstacles in the greater horseshoe bat, *Rhinolophus ferrumequinum*. *J. Acoust. Soc. Amer.*, 84(5):1676–1679.

- Möller, R., Lambrinos, D., Pfeifer, R., Labhart, T., and Wehner, R. (1998). Modeling ant navigation with an autonomous agent. In *From Animals to Animats 5, Proc. Fifth International Conference on Simulation on Adaptive Behaviour*, pages 185–194. MIT Press.
- Moravec, H. P. (1979). Visual Mapping by a Robot Rover. In *Proceedings of the 6th IJCAI*, pages 589–601.
- Moravec, H. P. and Elfes, A. (1985). High Resolution Maps from Wide Angle Sonar. In *Proceedings of the IEEE International Conference on Robotics and Automation*, pages 116–121.
- Müller, R. (1998). *The concept of acoustic flow in cf-bats*. PhD thesis, University of Tübingen.
- Müller, R. (2000). Biomimetic sonar: Why, How and What? In *Proceedings of the Workshop on Biomimetic Ultrasound*, page 5, Edinburgh.
- Müller, R. and Kuc, R. (2000). Foliage echoes: a probe into the ecological acoustics of bat echolocation. *J. Acoust. Soc. Amer.*, 108(2):836–845.
- Müller, R. and Schnitzler, H.-U. (1999). Acoustic flow perception in cf-bats: Properties of the available cues. *J. Acoust. Soc. Amer.*, 105(5):2958–2966.
- Müller, R. and Schnitzler, H.-U. (2000). Acoustic flow perception in cf-bats: extraction of parameters. *J. Acoust. Soc. Amer.*, 108(3):1298–1307.
- Nachtigall, P. and Moore, P., editors (1988). *Animal SONAR Processes and Performance (NATO ASI Series)*. Plenum Press.
- Nehmzow, U., Hallam, J., and Smithers, T. (1989). Really Useful Robots. In *Proceedings of the Intelligent Autonomous Systems conference*, volume 2, pages 284–293, Amsterdam.
- Nilsson, N. (1984). Shakey the Robot. Technical note 323, SRI International.
- Nilsson, N. J. (1994). Teleo-reactive programs for agent control. *Journal of Artificial Intelligence Research*, pages 139–158.
- Nowak, R. M. (1994). *Walker's Bats of the World*. Johns Hopkins University Press.
- Obrist, M. K., Fenton, M. B., Eger, J. L., and Schlegel, P. A. (1993). What ears do for bats: A comparative study of pinna sound pressure transformation in chiroptera. *J. exp. Biol.*, 180:119–152.
- Oriolo, G., Venditelli, M., and Ulivi, G. (1995). On-line map building and navigation for autonomous mobile robots. In *Proceedings of the IEEE International Conference on Robotics and Automation*, volume 3, pages 2900–2906.
- Ostwald, J. (1987). *Encoding of natural insect echoes and sinusoidally modulated stimuli by neurons in the auditory cortex of the greater horseshoe bat, Rhinolophus ferrumequinum*, pages 483–487. NATO ASI Series.
- Pagac, D., Nebot, E. M., and Durrant-Whyte, H. (1998). An evidential approach to map-building for autonomous vehicles. *IEEE Trans. Robotics and Automation*, 14(4):623–629.

- Papadopoulos, G. (1997). Evolving Ears for Echolocation. Master's thesis, Department of Artificial Intelligence, University of Edinburgh.
- Peremans, H. (1994). *Tri-aural perception for mobile robots*. PhD thesis, University of Gent.
- Peremans, H. (2000). Historic overview of ultrasonic sensing in mobile robotics. In *Proceedings of the Workshop on Biomimetic Ultrasound*, page 6, Edinburgh.
- Peremans, H., Audenaert, K., and Campenhout, J. M. V. (1993). A High-Resolution Sensor Based on Tri-aural Perception. *IEEE Trans. Robotics and Automation*, 9(1):36–48.
- Peremans, H., Müller, R., Carmenta, J. M., and Hallam, J. C. T. (2000). A biomimetic platform to study perception in bats. In McKee, G. and Schenker, P., editors, *Proceedings of SPIE: Sensor Fusion and Decentralized Control in Robotics Systems III*, volume 4196, pages 168–179.
- Peremans, H., Walker, A., and Hallam, J. C. T. (1997). A biologically inspired sonarhead. Technical Report 44, Dep. of Artificial Intelligence, U. of Edinburgh.
- Peremans, H., Walker, A., and Hallam, J. C. T. (1998a). 3D object localisation with a bionic sonarhead: inspirations from biology. In *Proceedings of the 1998 IEEE International Conference on Robotics and Automation*, volume 4, pages 2795–2800, Leuven, Belgium.
- Peremans, H., Walker, V. A., Papadopoulos, G., and Hallam, J. C. T. (1998b). Evolving Batlike Pinnae for Target Localisation by an Echolocator. In *Proceedings of the Second International Conference on Evolvable Systems: From Biology to Hardware*, pages 230–239. Springer.
- Pickles, J. O. (1982). *An introduction to the physiology of hearing*. Academic Press, London.
- Polaroid (1982). *Ultrasonic range finders*. Polaroid Corporation.
- Politis, Z. and Probert, P. J. (2001). Classification of Textured Surfaces for Robot Navigation Using Continuous Transmission Frequency-Modulated Sonar Signatures. *The International Journal of Robotics Research*, 20(2).
- Popper, A. and Fay, R., editors (1995). *Hearing by Bats*. Springer Verlag.
- Proakis, J. G. and Manolakis, D. G. (1996). *Digital Signal Processing. Principles, Algorithms and Applications*. Prentice-Hall International.
- Pye, J. D., Flinn, M., and Pye, A. (1962). Correlated orientation sounds and ear movements of horseshoe bats. *Nature*, 196:1186–1188.
- Pye, J. D. and Roberts, L. H. (1970). Ear Movements in a Hipposiderid Bat. *Nature*, 225:285–286.
- Quinn, R. D. and Ritzmann, R. (1998). Construction of a hexapod robot with cockroach kinematics benefits both robotics and biology. *Connection Science*, 10(3-4).
- Ratner, D. and McKerrow, P. J. (1998). Extracting Features from CTFM Sonar. In Chugani, M., Samat, A., and Cerna, M., editors, *LabVIEW Signal Processing*, pages 124–131. Prentice Hall.

- Ratner, D. and McKerrow, P. J. (2000). Recognition experiments with a narrow beam CTFM sonar mounted on the Titan outdoor 4WD mobile robot. In *SIRS'00, Proceedings of the 8th International Symposium on Intelligent Robotic Systems*.
- Roverud, R. C. and Grinnell, A. D. (1985). Frequency tracking and Doppler shift compensation in response to an artificial CF-FM echolocation sound in the CF-FM bat, *Noctilio albiventris*. *Journal of Comparative Physiology A*, 156:471–475.
- Rucci, M., Edelman, G. M., and Wray, J. (1999). Adaptation of Orienting Behaviour: From the Barn Owl to a Robotic System. *IEEE Trans. Robotics and Automation*, 15(1):96–110.
- RWI (1994). *B12 Base Manual (version 2.4)*. Real World Interface, Inc.
- Sabatini, A. and Benedetto, O. (1994). Towards a robust methodology for mobile robots localization using sonar. In *Proceedings of the IEEE International Conference on Robotics and Automation*, San diego, CA.
- Sabatini, A. M. (1992). Active hearing for external imaging based on an ultrasonic transducer array. In *Proceedings of the International Conference on Intelligent Robots and Systems (IROS)*, pages 829–836.
- Schnitzler, H.-U. and Flieger, E. (1983). Detection of oscillating target movements by echolocation in the greater horseshoe bat. *J. Comp. Physiol. A*, 153:385–391.
- Schnitzler, H.-U. and Grinnell, A. D. (1977). Directional sensitivity of echolocation in the horseshoe bat, *Rhinolophus ferrumequinum*. I. directionality of sound emission. *J. Comp. Physiol. A*, 116:51–61.
- Schnitzler, H.-U. and Ostwald, J. (1981). *Adaptations for the detection of fluttering insects by echolocation in horseshoe bats*, volume 56, pages 801–827. NATO ASI Series.
- Schroeder, M. R. and Hall, J. L. (1974). Model for mechanical to neural transduction in the auditory receptor. *J. Acoust. Soc. Amer.*, 55:1055–1060.
- Shaw, E. (1974). The external ear. In Keidel, W. and Neff, W., editors, *Handbook of Sensory Physiology*. Springer-Verlag.
- Slaney, M. (1993). An efficient implementation of the Patterson-Holdsworth auditory filter bank. Technical Report 35, Apple Computer Inc.
- Snyder, D. L., O'Sullivan, J. A., and Miller, M. I. (1989). The Use of Maximum-Likelihood Estimation for Forming Images of Diffuse Radar Targets from Delay-Doppler Data. *IEEE Trans. Info. Theory*, 35(3):536–548.
- Srinivasan, M., Zhang, S., Altwein, M., and Tautz, J. (2000). Honeybee navigation: nature and calibration of the 'odometer'. *Science*, 287:851–853.
- Stanley, B. and McKerrow, P. (1997). Measuring Range and Bearing with a Binaural Ultrasonic Sensor. In *Proceedings of the International Conference on Intelligent Robots and Systems (IROS)*, pages 565–571.
- Suga, N. (1990). Biosonar and neural computation in bats. *Scientific American*, pages 60–68.

- Suga, N. and Jen, P. H.-S. (1977). Further studies on the peripheral auditory system on 'CF-FM' bats specialized for fine frequency analysis of doppler-shifted echoes. *J. Exp. Biol.*, 69:207–232.
- Suga, N., Niwa, H., and Taniguchi, I. (1981). *Representation of biosonar information in the auditory cortex of the mustached bat, with emphasis on representation of target velocity information*, volume 56, pages 829–867. NATO ASI Series.
- Sweet, M. R. (1999). *Serial Programming Guide for POSIX Operating Systems*, 5th edition. <http://www.easysw.com/mike/serial/>.
- Teimoorzadeh, K. (1995). Seeing in the dark with artificial bats. In *3rd. European Conference on Artificial Life*, Granada, Spain.
- Tian, B. and Schnitzler, H.-U. (1997). Echolocation signals of the greater horseshoe bat (*Rhinolophus ferrumequinum*) in transfer flight and during landing. *J. Acoust. Soc. Am.*, 101(4):2347–64.
- Urdiales, C., Bandera, A., Arrebola, F., and Sandoval, F. (1998). Multi-level path planning algorithm for autonomous robots. *Electronic letters*, 2(34):223–224.
- Urdiales, C., Bandera, A., Ron, R., and Sandoval, F. (1999). Real time position estimation for mobile robots by means of sonar sensors. In *IEEE International Conference on Robotics and Automation*.
- van Schaik, A., Fragniere, E., and Vittoz, E. (1995). Improved silicon cochlea using compatible lateral bipolar transistors. In *Advances in Neural Information Processing Systems 8*, pages 671–677. MIT Press.
- Walker, V. A. (1997). *One tone, two ears, three dimensions: An investigation of qualitative echolocation strategies in synthetic bats and real robots*. PhD thesis, University of Edinburgh.
- Walker, V. A., Peremans, H., and Hallam, J. C. T. (1998a). Good vibrations: Exploiting reflector motion to partition an acoustic environment. *Robotics and Autonomous Systems*, 24(1-2):43–55.
- Walker, V. A., Peremans, H., and Hallam, J. C. T. (1998b). One tone, two ears, three dimensions: A robotic investigation of pinnae movements used by rhinolophid and hipposiderid bats. *J. Acoust. Soc. Amer.*, 104(1):569–579.
- Walter, G. W. (1950). An Imitation of Life. *Scientific American*, 182(5):42–45.
- Walter, S. A. (1987). The Sonar Ring: Obstacle Detection for a Mobile Robot. In *Proceedings of the 1987 IEEE International Conference on Robotics and Automation*, pages 1574–1579.
- Watts, L., Kerns, D., Lyon, R., and Mead, C. (1992). Improved Implementation of the Silicon Cochlea. *IEEE J. Solid State Circuits*, 27:692–700.
- Webb, B. (1995). Using robots to model animals: a cricket test. *Robotics and Autonomous Systems*, (16):117–134.

- Webb, B. (1999). A framework for models of biological behaviour. *International Journal of Neural Systems*, 9(5):375–381.
- Webb, B. (2000). Are ‘biorobots’ good models of biological behaviour? *Behavioural and Brain Sciences*, 24(6).
- Webb, B. H. (1993). *Perception in real and artificial insects: A robotic investigation of cricket phonotaxis*. PhD thesis, University of Edinburgh.